INTERACTIONS BETWEEN TECTONISM AND MAGMATISM AT SANTORINI: INSIGHTS FROM AN ACTIVE SOURCE SEISMIC EXPERIMENT

by

BEN HEATH

A DISSERTATION

Presented to the Department of Geological Sciences
and the Graduate School of the University of Oregon
in partial fulfillment of the requirements
for the degree of
Doctor of Philosophy

December 2019

DISSERTATION APPROVAL PAGE

Student: Ben Heath

Title: Interactions Between Tectonism and Magmatism at Santorini: Insights from an Active Source Seismic Experiment

This dissertation has been accepted and approved in partial fulfillment of the requirements for the Doctor of Philosophy degree in the Department of Geological Sciences by:

Emilie E. E. Hooft	Chair
Ilya Bindeman	Core Member/Coordinator
Leif Karlstrom	Core Member
Hank Childs	Institutional Representative

and

Kate Mondloch	Interim Vice Provost and Dean of the Graduate School

Original approval signatures are on file with the University of Oregon Graduate School.

Degree awarded December 2019

© 2019 Ben Heath
All Rights Reserved

DISSERTATION ABSTRACT

Ben Heath

Doctor of Philosophy

Department of Geological Sciences

December 2019

Title: Interactions Between Tectonism and Magmatism at Santorini: Insights from an Active Source Seismic Experiment

In extensional volcanic arcs, tectonic and magmatic processes control the evolution of eruptive centers and their surrounding regions. Faulting, which increases crustal permeability, can focus magmatism and preferentially localize eruptive edifices near intersecting fault zones. In turn, magmatic diking and volcanic edifice growth/collapse can change both the regional and local stress/strain in the crust altering the style and amount of faulting. The relative importance of these magmatic and tectonic processes as well as how these processes coevolve are still poorly known. Here we study magmatic and tectonic interactions at Santorini Volcano, focusing on the localization of magmatism in the highly extended terrain and the subsequent influence of this magmatism on the evolution of tectonic activity. We use the dense PROTEUS active source seismic dataset, collected in a 120 km x 45 km region around the volcano, to perform both P-wave anisotropic traveltime tomography inversions and full waveform inversions, imaging the upper crust down to ∼4 km depth. Integrating our results with the well-studied volcanic and geologic history of Santorini, we show evidence for strong tectonic control on the evolution of Santorini's magmatic system. In Chapter II and V, this interaction is recorded as i) the alignment of volcanic features parallel to tectonic features, ii) the localization of volcanism within a tectonic basin, and iii) the strong influence of tectono-magmatic lineaments on both regional volcanic evolution and localization

of caldera collapse. In Chapter III we show that the magnitude of small-scale local faulting is uncorrelated to regions of magmatic activity indicating that magmatism is neither focused in areas of higher fracturing nor is accommodating substantial extensional strain. Rather both magmatism and small-scale faulting are strongly correlated with regional stress. In Chapter IV we hypothesize that the broad distribution of deformation (>40 km wide) currently observed results from magmatic activity. In contrast, a narrower episode of localized deformation (<20 km wide) preceded initiation of regional magmatism. This highlights the impact of regional magmatism on tectonic evolution. This works shows that magmatic and tectonic processes interact on a variety of temporal and spatial scales.

This dissertation includes both previously published and co-authored material.

CURRICULUM VITAE

NAME OF AUTHOR: Ben Heath

GRADUATE AND UNDERGRADUATE SCHOOLS ATTENDED:

University of Oregon, Eugene, OR, USA
Northwestern University, Evanston, IL, USA

DEGREES AWARDED:

Doctor of Philosophy, Geological Sciences, 2019, University of Oregon
Master of Science, Geological Sciences, 2014, University of Oregon
Bachelor of Arts, Earth and Planetary Sciences, 2012, Northwestern University

AREAS OF SPECIAL INTEREST:

Geophysics/Seismology
Volcanology
Tectonophysics

PROFESSIONAL EXPERIENCE:

Graduate Student, University of Oregon 2015-2019
ORISE Fellow, NETL-Albany 2015-2015
Graduate Student, University of Oregon 2012-2014

GRANTS, AWARDS AND HONORS:

Johnston Memorial Fellowship, 2012
Johnston Geology Fund, 2015, 2016, 2017
Weiser Memorial Scholarship, 2016, 2017
Outstanding Student Presentation Award, IAVCEI 2017
GSA Student Research Grant, 2017

PUBLICATIONS:

Heath, B. A., Hooft, E. E. E., Toomey, D. R., Papazachos, C. B., Nomikou, P., Paulatto, M., Morgan, J.V., & Warner, M.R. (2019). Tectonism and its relation to magmatism around Santorini volcano from upper crustal P-wave velocity. *Journal of Geophysical Research: Solid Earth* DOI: https://doi.org/10.1029/2019JB017699

Hooft, E.E.E., Heath, B.A., Toomey, D.R., Paulatto, M., Papazachos, C.B., Nomikou, P., Morgan, J.V., & Warner, M.R. (2019). Seismic imaging of Santorini: Subsurface constraints on caldera collapse and present-day magma recharge. *Earth and Planetary Science Letters*, 514, 48-61. DOI: https://doi.org/10.1016/j.epsl.2019.02.033

Hooft, E. E. E., Nomikou, P., Toomey, D. R., Lampridou, D., Getz, C., Christopoulou, M. E., O'Hara, D., Arnoux, G. M., Bodmer, M., Gray, M., Heath, B. A., & VanderBeek, B. P. (2017). Backarc tectonism, volcanism, and mass wasting shape seafloor morphology in the Santorini-Christiana-Amorgos region of the Hellenic Volcanic Arc. *Tectonophysics*, 712, 396-414. DOI: https://doi.org/10.1016/j.tecto.2017.06.005

Heath, B. A., Hooft, E. E., & Toomey, D. R. (2018). Autocorrelation of the seismic wavefield at Newberry Volcano: Reflections from the magmatic and geothermal systems. *Geophysical Research Letters*, 45(5), 2311-2318. DOI: https://doi.org/10.1002/2017GL076706

Mark-Moser, M. K., Rose, K. K., Schultz, J. D., Schultz, A., Heath, B., Urquhart, S., & Vincent, P. (2015). *A Conceptual Geologic Model for the Newberry Volcano EGS Site in Central Oregon: Constraining Heat Capacity and Permeability Through Joint Interpretation of Multifaceted Geophysical and Geological Data Sets* (No. NETL-PUB-20152). NETL.

Heath, B. A., Hooft, E. E., Toomey, D. R., & Bezada, M. J. (2015). Imaging the magmatic system of Newberry Volcano using joint active source and teleseismic tomography. *Geochemistry, Geophysics, Geosystems*, 16(12), 4433-4448. DOI: https://doi.org/10.1002/2015GC006129

ACKNOWLEDGEMENTS

I would first like to acknowledge my parents who have been supportive of me throughout my graduate career. Without their help, I am not sure how I would have finished this degree.

I would like to thank my advisor Emilie Hooft for both giving me an opportunity to work on the PROTEUS dataset as well as for providing me the space to develop and test my ideas. I would also like to thank my collaborators during this experiment including: Emilie Hooft, Joanna Morgan, Paraskevi Nomikou, Costas Papazachos, Michele Paulatto, Doug Toomey and Mike Warner. Their feedback throughout this process has been invaluable. I am indebted to Kajetan Chrapkiewicz and Brennah McVey for helpful conversations regarding Santorini.

I would like to thank my committee which consists of Emilie Hooft, Ilya Bindeman, Leif Karlstrom, and Hank Childs. I appreciate the support they provided, their honest and open feedback, and their constructive criticism which has helped me to become a better scientist.

My views on and understanding of magmatic systems has been shaped by conversations with a wide range of people. The patience displayed by the volcanology community in explaining concepts to a young scientist is greatly appreciated.

I would like to thank my roommates, labmates and friends over the past few years for their support. I feel honored to have gone through my graduate career with so many bright people by my side.

Much of my research has used super-computers present on the University of Oregon campus. I am constantly amazed by both my ability to make mistakes

in the job submission process and the responsiveness of the ACISS/talapas high performance computing team to my frantic cries for help. Without this team, I would still be submitting “hello world” jobs to as many computer nodes as possible.

Finally, I would like to thank the Department of Earth Sciences (formerly the Department of Geological Sciences or DoGS), especially the office staff, Marla, Sandy and Dave.

To my parents, thank you for always supporting me and helping me to become a better person

TABLE OF CONTENTS

Chapter Page

I. INTRODUCTION 1

II. TECTONISM AND ITS RELATION TO MAGMATISM AROUND SANTORINI VOLCANO FROM UPPER CRUSTAL P-WAVE VELOCITY 5

2.1. Introduction 5

2.2. Background 6

2.2.1. Tectonic background 6

2.2.2. Volcanic Background 11

2.3. Experiment Geometry and Data Acquisition 12

2.3.1. Seismic experiment 12

2.3.2. Data return and data quality 13

2.4. Data processing and tomographic inversion 14

2.4.1. OBS relocation 14

2.4.2. Pg travel time data 15

2.4.3. Tomographic Inversion 16

2.5. Results and Interpretation 19

2.5.1. Upper crustal velocity variations 19

2.5.2. Comparison of tomographic velocity model with seismic reflection images 20

2.5.3. Mapping geometry and thickness of sedimentary basins from the tomography model 23

2.5.4. Western side of Santorini: Christiana Basin and Christiana Ridge 24

2.5.5. Eastern side of Santorini: Anydros Basin, Anafi Basin and Anydros Horst 27

2.5.6. Structures associated with Santorini 28

2.6. Discussion 29

2.6.1. Differences between the east and west sides of Santorini and relationship to faulting 29

2.6.2. Tectonic evolution of the basins and Christiana-Santorini-Kolumbo magmatism: Localization of magma in a proto-Anydros Basin 32

2.6.3. Volcano-tectonic lineaments 35

2.7. Conclusions 36

2.8. Bridge 37

III. RELATIONSHIP BETWEEN FAULTING AND MAGMATISM AROUND SANTORINI: SEISMIC ANISOTROPY RESULTS FROM A REFRACTION EXPERIMENT . . 39

3.1. Introduction 39

3.2. Background 41

3.2.1. Geologic Background of the Aegean 41

3.2.2. Regional Volcanism and its Relation to Tectonics 43

3.2.3. Current State of Tectonic and Magmatic Activity 45

3.3. Methods 46

3.3.1. Tomography 46

3.3.2. Forward Modeling 48

3.4. Results 51

3.4.1. Tomographic Results 51

3.4.2. Forward Modeling Anisotropy Results 57

3.5. Discussion 63

3.5.1. Source of Anisotropy on the eastern side of Santorini 63

3.5.2. Modeling the fraction of different aspect ratio fractures . . . 66

3.5.3. Magmatism and its relationship to faulting/fracturing around Santorini - Local-scale/Regional Scale Interactions 68

3.5.4. Implications for Sources of Faulting and Fault Damage Zones on the Eastern Side of Santorini 73

3.5.5. Understanding the Regional Tectonic and Magmatic Interactions 77

3.6. Conclusions 79

3.7. Bridge 80

IV. TECTONISM AND THE INFLUENCE OF INHERITED STRUCTURAL DEFORMATION AROUND SANTORINI FROM P-WAVE TOMOGRAPHY 81

4.1. Introduction 81

4.2. Background 83

4.3. Methods 86

4.4. Results 91

4.4.1. Overview of seismic anisotropy results from travel-time tomography 91

4.4.2. Overview of FWI results 93

4.4.3. Comparison of FWI results to isotropic travel-time tomography results 97

4.4.4. Comparison of FWI to seismic reflection results 99

4.5. Discussion 100

4.5.1. Seismic anisotropy and the record of ductile deformation . . . 100

4.5.2. Tomographic evidence of brittle behavior in the Christiana Basin 105

4.5.3. Distribution of faulting within and outside the basin proper 108

4.5.4. Ductile and brittle deformation: controls on the localization of deformation, comparison between east and west 114

4.6. Conclusions 118

4.7. Bridge 121

Chapter Page

V. SEISMIC IMAGING OF SANTORINI: SUBSURFACE CONSTRAINTS ON CALDERA COLLAPSE AND PRESENT-DAY MAGMA RECHARGE 122

5.1. Introduction 122

5.2. Santorini volcano 124

5.3. Seismic experiment and data 129

5.4. Tomographic inversion and results 130

5.4.1. Inversion 130

5.4.2. Synthetic tomography resolution tests 133

5.4.3. Tomography results 134

5.5. Calculation of physical properties 135

5.6. Discussion 139

5.6.1. Collapse plug filled with volcanic deposits 143

5.6.2. Phreatomagmatic rock breakup 144

5.6.3. Multistage, nested caldera collapse 145

5.6.4. Present day magma recharge 147

5.7. Conclusions 150

VI. CONCLUSIONS 152

APPENDICES

A. APPENDIX CHAPTER II: TECTONISM AND ITS RELATION TO MAGMATISM AROUND SANTORINI VOLCANO FROM UPPER CRUSTAL P-WAVE VELOCITY 155

A.1. Description of Synthetics 155

A.2. Attenuation of caldera centered data 168

A.3. First motions of signals 168

A.4. 1-D velocity profile comparison 168

A.5. Investigations of roughness/smoothing values vs RMS of travel time residuals 168

A.6. Dv analysis as function of penalty and smoothing 168

A.7. Checkerboard test: 5x5x2 km checkers 168

A.8. Checkerboard test:5x5x1 km checkers 168

A.9. Checkerboard test: 3x3x1 km checkers 168

A.10. MCS comparison Supplement 1 168

A.11. MCS comparison Supplement 2 168

A.12. Contouring basin depth using various different velocities 168

A.13. Evidence for anisotropy in traveltime residuals 168

A.14. RMS of travel times for various different parameters 168

B. APPENDIX CHAPTER III: RELATIONSHIP BETWEEN FAULTING AND MAGMATISM AROUND SANTORINI: SEISMIC ANISOTROPY RESULTS FROM A REFRACTION EXPERIMENT 169

B.1. Calculation of Resolution of Anisotropy 169

B.2. Applicability of Anisotropy Assumptions 169

C. APPENDIX CHAPTER IV: TECTONISM AND THE INFLUENCE OF INHERITED STRUCTURAL DEFORMATION AROUND SANTORINI FROM P-WAVE TOMOGRAPHY 172

C.1. Modeling Anisotropy 172

C.2. Modeling Styles of Extension 176

D. APPENDIX CHAPTER V: SEISMIC IMAGING OF SANTORINI: SUBSURFACE CONSTRAINTS ON CALDERA COLLAPSE AND PRESENT-DAY MAGMA RECHARGE . 178

D.1. Temperature and pressure corrections for velocity 178

D.2. Checkerboard resolution test 179

D.3. Cylindrical low-velocity anomaly resolution test 179

D.4. Comparison of shallow tomography velocity model with seismic reflection profiles 179

D.5. Comparison of shallow tomography velocity model with seismic reflection profiles 179

Chapter Page

D.6. Interpretation of the low VP anomaly if porosity were filled with partial melt 179

REFERENCES CITED 184

LIST OF FIGURES

Figure		Page
2.1.	Tectonic setting of the Aegean	7
2.2.	Experiment geometry and regional tectonic structures	10
2.3.	Example of seismic data from two basins	14
2.4.	Regional 1-D P-wave velocity-depth profiles	18
2.5.	Tomographic velocity anomalies	19
2.6.	Regional cross section locations	21
2.7.	Comparison with seismic reflection profiles	23
2.8.	Analysis of regional basin depths	25
2.9.	Cross sections through the velocity model	26
2.10.	Comparison between caldera centered geology and tomographic velocity anomalies	30
2.11.	Model of tectonic evolution	33
3.1.	Regional tectonic setting and experiment geometry	42
3.2.	Azimuthal distribution of travel-time residuals: evidence for anisotropy	52
3.3.	Anisotropic structure of the eastern portion of the experiment	54
3.4.	Anisotropic depth distribution	55
3.5.	Anisotropy magnitudes across the experiment	57
3.6.	Calculation of the effect of dikes on seismic velocity	59
3.7.	Calculation of the effect of fractures on seismic velocity	61
3.8.	Calculation of the effect of dipping faults on seismic velocity	63
3.9.	Calculation of combined fracture-induced anisotropy with metamorphic-structure derived anisotropy	64
3.10.	Regional overview of fracture distribution	68

Figure Page

3.11. Hypotheses relating tectonism and magmatism 71

3.12. Interpretations of regional structure 74

4.1. Recorded and modeled waveforms 88

4.2. Phase residual comparison between final and starting model 92

4.3. Comparison of ideal and actual coverage for FWI inversions 93

4.4. Anisotropic travel-time tomography for various depths 94

4.5. FWI results for various depth slices 95

4.6. Cross sections through the FWI models 96

4.7. Overview of cross sections and regions used for averaging velocities . . 98

4.8. Comparison between FWI and traveltime tomography 99

4.9. Comparison of FWI to seismic reflection studies: example 1 101

4.10. Comparison of FWI to seismic reflection studies: example 2 102

4.11. Anisotropy resulting from metamorphic horst properties 106

4.12. Anisotropy distribution for various geologically motivated blocks . . . 110

4.13. Orientation of anisotropy throughout the experiement 111

4.14. Hypothesis 1: Wide rifting from thermal perturbations 117

4.15. Hypothesis 2: Accommodation zones and their effect on distributed faulting 119

4.16. Model of regional evolution 120

5.1. PROTEUS seismic experiment map 124

5.2. The geological and volcanic features of Santorini 127

5.3. Maps of P-wave seismic velocity at Santorini 131

5.4. Cross-sections of seismic velocity along profile A-A' and B-B' 132

5.5. Predicted porosity for the northern caldera low-velocity anomaly and the reference metamorphic profile. 136

5.6. Conceptual model for the evolution of the LBA eruption and formation of the low-velocity anomaly. 142

5.7. Comparison of the low-velocity anomaly with magma recharge during the 2011-2012 unrest and predicted lithostatic pressure at 4 km depth. 149

A.1. Attenuation of caldera centered data 156

A.2. First motions of signals 157

A.3. 1-D velocity profile comparison 158

A.4. Investigations of roughness/smoothing values vs RMS of travel time residuals 159

A.5. Dv analysis as function of penalty and smoothing 160

A.6. Checkerboard test: 5x5x2 km checkers 161

A.7. Checkerboard test:5x5x1 km checkers 162

A.8. Checkerboard test: 3x3x1 km checkers 163

A.9. MCS comparison Supplement 1 164

A.10. MCS comparison Supplement 2 165

A.11. Contouring basin depth using various different velocities 166

A.12. Evidence for anisotropy in traveltime residuals 167

B.1. Approximating anisotropy using a weak elastic assumption 170

B.2. Predicted velocities and travel-times as a function of azimuth for various different magnitudes of anisotropy 171

D.1. Checkerboard resolution test 180

D.2. Cylindrical low-velocity anomaly resolution test 181

D.3. Comparison of shallow tomography velocity model with seismic reflection profiles. 181

D.4. Comparison of shallow tomography velocity model with seismic reflection profiles. 182

D.5. Interpretation of the low VP anomaly if porosity were filled with partial melt 183

LIST OF TABLES

Table Page

4.1. Data Processing Steps 87

4.2. Model Parameters 89

4.3. Inversion Parameters 90

A.1. RMS of travel times for various different parameters 168

C.1. Extensional Style Parameters 177

CHAPTER I

INTRODUCTION

Globally, magmatic centers are found to strongly correlate with areas of tectonic activity on a variety of spatial scales. Volcanic cones form linear alignments that parallel the local kilometer-scale fault orientations, larger volcanic edifices often lie near the intersection of multiple fault zones and at volcanic-arc scales magmatic eruption volume is found to correlate with extension rate (e.g. Muirhead et al., 2015; MacLeod and Sherrod, 1988; Acocella and Funiciello, 2010). This interaction is commonly attributed to tectonic faults providing pathways for the ascent of both magma and magmatic fluids as well as due to tectonic stresses localizing magmatic activity (e.g. Kokkalis and Aydin, 2013; Magee et al., 2013). Magmatism can then change tectonic activity by i) accommodating extensional strain and modifying crustal stresses, which change fault density and orientation and ii) weakening the crust through thermal and physical effects (e.g. Parsons and Thompson, 1991; Parsons and Thompson, 1993; Casey et al., 2006; Ebinger and Casey, 2001, Corti et al., 2013). However, despite strong evidence for interaction, in many volcanic systems it is not clear whether tectonic or magmatic stresses dominate regional evolution. This is further complicated because the interaction between these two processes evolves through both time and space, as the thermal and physical properties of the crust change through the addition of magma/magmatic fluids.

While there is a substantial body of work investigating these tectonic and magmatic interactions, studies have historically been limited by several issues. Geologic studies, which are limited to the surface expression of faults and volcanic deposits, have been biased against features that exist at depth and are limited to rocks present in exposures. Geophysical methods, which are designed to probe the

current state of upper crustal continental magmatic systems, have been historically of too poor resolution to sufficiently resolve local-scale tectonic and magmatic interactions and have only been able to image regional faults. Due to the ease of data collection in marine settings over land settings, the best studied volcanoes from a seismic tomography perspective are preferentially located in the ocean. It is precisely these oceanic regions that are inherently undersampled in geologic studies due to limited outcrops and as a results are few volcanoes that are well studied both geophysically and geologically. Therefore, few studies are able to combine well-mapped geologic observations with dense geophysical constraints without sacrificing resolution from either technique.

Here I probe upper crustal tectonic and magmatic interactions in the marine setting of Santorini Volcano, Greece by combining both anisotropic P-wave travel-time tomography and Full Waveform Inversions (FWI) with a well-studied geologic history. Santorini, which sits on extended Aegean crust, is a prime location to study tectonic and magmatic interactions because it has experienced multiple episodes and styles of tectonic extension that were both accompanied and unaccompanied by magmatism, it has a well-studied geologic and geochemical record and history outlining episodes of both tectonism and magmatism and it is located in a marine setting enabling the collection of dense active source seismic experiment which provides unprecedented resolution of the continental upper crust. By combining the geophysical results with geological and geochemical studies, we are able to resolve deeper features, record subtle interactions between tectonic and magmatic activity and build/test conceptual models of the timescales, length-scales and styles of tectonic and magmatic interactions.

Chapter II provides a regional overview of faults and magmatic features imaged using a dense marine-land seismic experiment. In this chapter, I conducted

isotropic P-wave travel-time tomography inversions to resolve seismic velocity and ultimately resolve crustal structure beneath Santorini and the surrounding region. This chapter validates the structures interpreted in later chapters, outlines broad tectonic and magmatic interactions around Santorini including volcano-tectonic lineaments that have focused regional volcanism and proposes a regional model for tectonic evolution. This chapter was published with coauthors E. E. E. Hooft, D. R. Toomey, C.B. Papazachos, P. Nomikou, M. Paulatto, J.V. Morgan, M.R. Warner in *Journal of Geophysical Research* in a paper titled "Tectonism and its relation to magmatism around Santorini volcano from upper crustal P-wave velocity."

Chapter III discusses anisotropic travel-time inversion results for the Santorini-Kolumbo region, a region inclusive of both the large Santorini caldera and the nearby, submerged Kolumbo volcano. Here I investigate the localization of magmatism in this region from local and regional faults. Anisotropic travel time results resolve local, small, kilometer-scale fault structure, providing the first tomographic insight into small-scale interaction between magmatism and tectonic activity at Santorini. Using a model that relates observed seismic velocity and anisotropy to fault fraction and orientation, I show that regions of magmatism have no correlation to the magnitude of local-scale faulting but do have a strong relationship to regional-scale faulting, indicating that small scale faults are not a first order control on magmatic activity. These results show that the regional structure on the eastern side of Santorini is characterized by pervasive local faulting and that regional extension has provided a favorable stress regime to allow the rise of magmatic fluids.

Chapter IV investigates the largely amagmatic Christiana basin (western side of Santorini) using anisotropic travel-time tomography and FWI, outlining the style of extension in the Christiana basin in order to understand a transition

from narrow amagmatic extension within the basin to broader magmatic extension observed regionally. I investigate sources of seismic anisotropy here and show that it results from a variety of different processes including various oriented faults from differing extensional episodes as well as ductile-deformation-derived metamorphic stretching lineations that record prior Oligo-Miocene extension. Using FWI, I outline the regional tectonic fault structure of the Christiana basin and investigate localization of faulting within the basin proper, inferring changes in the orientation of faulting through time. The differences between older amagmatic localized faulting within the Christiana basin and younger, distributed NE-SW oriented faults associated with magmatism (discussed in Chapters II and III) is hypothesized to be caused by thermal perturbations to the crust resulting from initiation of magmatism. I provide an overview of different extensional modes and their evolution through time.

Chapter V consists of a focused P-wave travel-time tomography study of the structure of the Santorini caldera, highlighting the localization of vents around a newly discovered region of isolated caldera collapse which in turn is localized between two long-lived tectono-magmatic structures. This chapter, titled "Seismic imaging of Santorini: Subsurface constraints on caldera collapse and present-day magma recharge" was written by EEE Hooft, and coauthored by Heath, B.A., Toomey, D.R., Paulatto, M., Papazachos, C.B., Nomikou, P., Morgan, J.V. and Warner, M.R. and is published in the journal *Earth and Planetary Sciences*. This work is included in this dissertation as B. A. Heath collected all the travel-times used in this project, conducted all tomographic inversions and contributed to the development of ideas presented.

CHAPTER II

TECTONISM AND ITS RELATION TO MAGMATISM AROUND SANTORINI VOLCANO FROM UPPER CRUSTAL P-WAVE VELOCITY

This chapter was published in *Journal of Geophysical Research: Solid Earth*, under the title "Tectonism and its relation to magmatism around Santorini volcano from upper crustal P-wave velocity." This publication was co-authored with E. E. E. Hooft, D. R. Toomey, C.B. Papazachos, P. Nomikou, M. Paulatto, J.V. Morgan, M.R. Warner. Ben Heath picked the data used in this chapter, conducted all the inversions, wrote the paper and drafted all figures. All co-authors contributed to discussion of ideas and provided extensive edits to the document.

2.1 Introduction

In extensional volcanic arcs, the crust is often composed of a patchwork of interacting faults that control the localization of magmatism and development of sedimentary basins. Analogue models have shown that magma may be localized within basins in different extensional regimes (Corti et al., 2003). In turn magma bodies can alter the stress state of the crust. In addition to weakening the crust through thermal effects, magmatism can facilitate the formation of low angle faults (Parsons & Thompson, 1993), inhibit the formation of through-going normal faults (e.g., Faulds & Varga, 1998), and accommodate extensional strain.

Santorini is one of the most active volcanoes in the Hellenic Volcanic arc (e.g., Le Pichon & Angelier, 1979) (Figure 2.1), resulting from the subduction of the African plate under the Aegean microplate. Regional extension, since the Oligocene-Miocene, has been accommodated both on older E-W oriented faults and on younger NE-SW oriented normal faults that remain tectonically active to present day. As a consequence of this extension, the crust has been thinned and

multiple fault systems of differing orientations intersect Santorini (Figures 2.1 and 2.2). The link between tectonics and magmatism across Santorini, however, is currently not well constrained, in part because many of these features are buried under sedimentary and volcanic deposits.

In this study we use seismic data, acquired in the marine-land active-source PROTEUS (Plumbing Reservoirs Of The Earth Under Santorini) seismic experiment, to obtain a tomographic P-wave velocity model of the upper-crustal structure across Santorini volcano and the surrounding region. Seismic velocity is sensitive to fracturing, porosity, and composition and, here, we use it to delineate the structure and evolution of faults, extensional basins, as well as volcanic features in the Santorini region. We draw on our tomographic images, and results from previous seismic reflection and other studies, to delineate basins and faults. The combined datasets, as well as results from prior studies, are used to investigate differences between the upper crust to the west and east of Santorini, build a geologic model of fault evolution, and explore the relationship between tectonism and magmatism.

2.2 Background

2.2.1 Tectonic background

The Aegean has undergone multiple episodes of extension from at least the Oligocene-Miocene to present that were driven by slab roll-back of the Hellenic subduction zone (Le Pichon & Angelier, 1979), westward extrusion of Anatolia (McKenzie, 1972), and gravitational collapse of continental crust (McKenzie, 1972). These extensional events have led to thinned crust (Makris, 1976, 1978), exhumed and rotated metamorphic blocks (e.g. Walcott & White, 1998), and localized

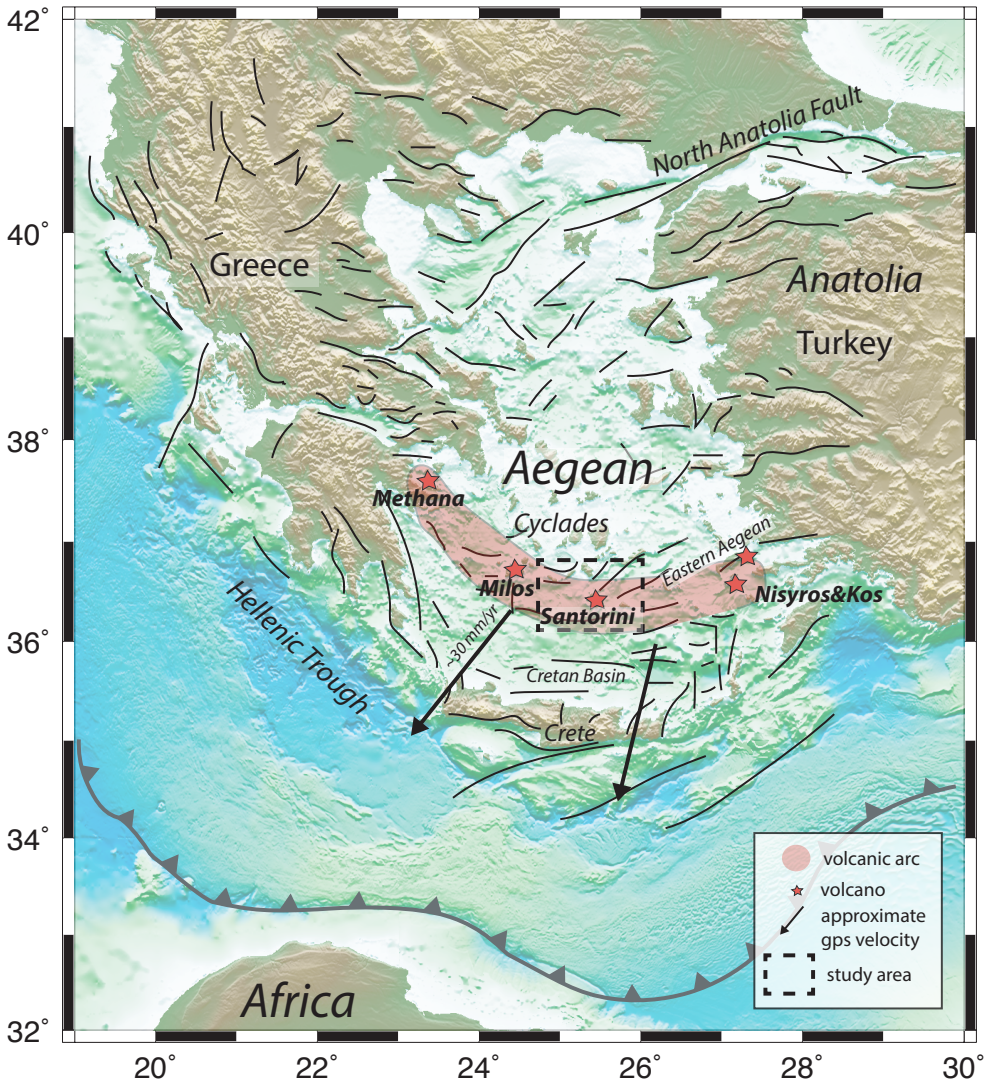

Figure 2.1. Tectonic setting of the Aegean. Topographic/bathymetric map of the broader Aegean/Hellenic subduction zone (bold grey line with triangles) where the African plate subducts under the Aegean microplate showing the volcanic arc (red region) and main volcanic centers (stars and bold names). The study area is indicated with a dashed box. Faults in the overriding Aegean microplate (black lines, after Caputo et al., 2012) result from subduction rollback and extrusion along the North Anatolia Fault. The Santorini study area is located between the Cyclades to the northwest and the Cretan Basin to the south, within an actively faulted region. The GPS-derived velocity vectors relative to Eurasia (black arrows) reflect differential motion between regions east and west of Santorini (Reilinger et al., 2010).

deformation along zones of crustal weakness (Jolivet et al., 2013 and citations therein), creating a variety of deforming terrains.

Geological studies show that the Cyclades (Figure 2.1) were extended, thinned, and rotated throughout the Miocene, but have behaved as a single rotating block since the late Miocene-early Pliocene (Walcott & White, 1998) and currently exhibit little internal deformation. Santorini and the surrounding region lies at the southeastern margin of this Cycladic block (Le Pichon & Kreemer, 2010) (Figure 2.1).

During the Miocene to Pliocene, E-W-striking normal faults and related basins formed under ~N-S extension (Anastasakis & Piper, 2005; Piper et al., 2007). One of these basins is the Christiana basin in the western part of the study area. The Christiana basin has been mapped using seismic reflection imaging (Tsampouraki-Kraounaki & Sakellariou 2018, Piper et al., 2007 and citations therein) and is thought to have been truncated against N-S-striking transfer faults (Piper & Perissoratis, 2003). This E-W-striking basin is filled with Messinian and younger sediments (Piper & Perissoratis, 2003, Tsampouraki-Kraounaki & Sakellariou 2018). The main faults bounding the Christiana basin ceased activity ~1 Ma during the Pleistocene (Piper and Perissoratis, 2003) but some activity continues to present day as evidenced by small-offset, active faults observed in seismic reflection data (Tsampouraki-Kraounaki & Sakellariou, 2018).

In the latest Pliocene or early Pleistocene, the regional stress direction rotated resulting in NE-SW trending faults and subsequent basin inversion (Piper and Perissoratis, 2003; Piper et al., 2007) as well as the formation of new basins such as the Anydros and Anafi Basins on the eastern side of our study area (e.g., Hübscher et al., 2015; Nomikou et al., 2016). Following the change in

faulting orientation, volcanism in the region began (Perissoratis, 1995), with initial volcanism sourced at Christiana and Akrotiri (SW Santorini) (Piper et al., 2007).

Faults striking NE-SW continue to be active to present day (e.g., Dimitriadis et al., 2009, Bohnhoff et al., 2006) and are thought to be predominately extensional to trans-tensional (Hubscher et al., 2015, Hooft et al., 2017, Nomikou et al., 2016, Nomikou et al., 2018), but a component of strike-slip behavior is observed (Sakellariou et al., 2010). The NE-SW-striking Santorini-Amorgos fault zone (e.g. Stiros et al., 1994), which includes the Anydros Region on the eastern side of the study area (Figure 2.2), is one of the most active in the Aegean and regionally is the margin between the seismically quiet Cycladic block and the diffuse seismicity observed in the eastern Aegean (Bohnhoff et al., 2006). This is consistent with GPS studies showing that the eastern Aegean moves to the SE relative to the Cylcadic block (McClusky et al., 2000; Reilinger et al., 2010).

Metamorphosed sediments of the Attico-Cycladic complex, which were exhumed during Miocene and younger extension (Piper et al., 2007; Piper & Perissoratis, 2003; Xypolias et al., 2010), highlight the role of tectonics in the evolution of the southern Aegean. These exhumed rocks compose most of the regional islands (e.g. Ios, Amorgos) (Lister et al., 1984; Forster et al., 1999), including a portion of SW Santorini itself (Heiken & Mccoy, 1984). Moreover, these metamorphic fault blocks often extend as horsts into the Aegean sea, as seen in sea bathymetry and seismic reflection profile images (Perissoratis, 1995; Hübscher et al., 2015; Nomikou et al., 2016; 2018; Hooft et al., 2017). Metamorphic basement lithics, found in the erupted ignimbrite products from Santorini, reveal that the metamorphic complex must underlie Santorini's caldera (Druitt, 2014) and it is thought that Santorini sits on a NE-SW oriented fracture network (Budetta et al., 1984).

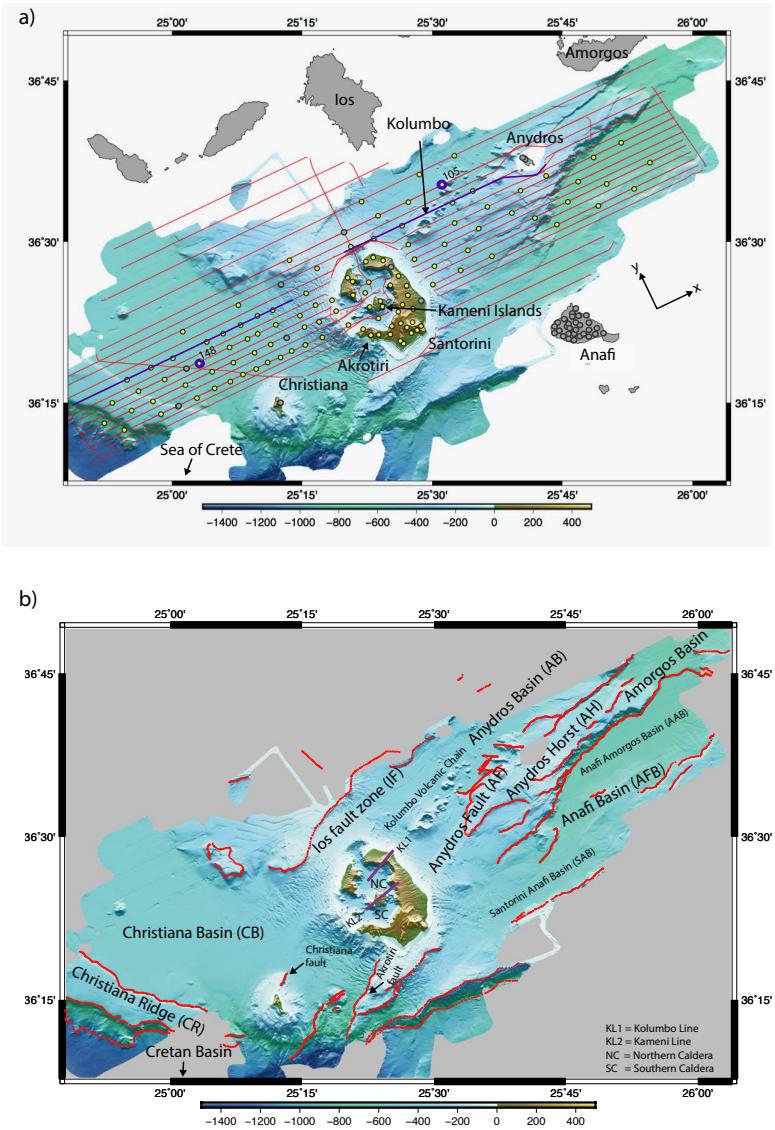

Figure 2.2. The Santorini region showing the PROTEUS active seismic experiment and the main morphotectonic features. (a) Topographic/bathymetric map of Santorini and the surrounding islands showing seafloor and island seismic stations (yellow circles are stations used in inversion, grey circles are stations that were not used) and the seismic shot profiles (small red circles). Data from seismic lines recorded on stations 148 and 105 (blue/purple) are shown in Figure 2.3. (b) Topographic/bathymetric map with the main basins, horsts/ridges, and faults (red lines, from Hooft et al., 2017). Abreviations used are: CB-Christiana Basin, CR - Christiana Ridge, IF - Ios Fault, Anydros Horst, AB - Anydros Basin, AFB -Anafi Basin, SAB - Santorini-Anafi Basin, AAB - Amorgos-Anafi Basin. Kolumbo and Kameni lines (KL1 and KL2, respectively) are after Pfeiffer (2001).

2.2.2 Volcanic Background

Regional volcanism has been localized in three areas: Christiana Island, Santorini volcano and the Kolumbo volcanic chain, arranged roughly in a NE-SW direction (Nomikou et al., 2013) (Figure 2.2). The oldest of the regional volcanic deposits results from Christiana volcanism (active during late Pliocene) and from early volcanic centers at the SW edge of Santorini near Akrotiri (~0.6 Ma) (Piper et al., 2007). Volcanism at Santorini itself began roughly 650 ka (Druitt et al., 1999), with explosive volcanism beginning around 360 ka. At least 4 major caldera-forming eruptions have occurred at Santorini (Druitt, 2014), the most recent of which, the 30-86 km3 (dense rock equivalent) Late Bronze Age (LBA) "Minoan" eruption, occurred 3.4 ka (Druitt, 2014 and citations therein; Johnston et al., 2014; Friedrich et al., 2006).

Post-LBA effusive eruptive vents are located along the Kameni line, a NE-SW-trending line of vents in the caldera (Nomikou et al., 2014; Pyle & Elliott, 2006) that results from either a deep seated fault focusing magmatism, a caldera ring fault, or a region of diking (Konstantinou et al., 2013; Newman et al., 2012; Papadimitriou et al., 2015; Saltogianni et al., 2014; Tassi et al., 2013). The Kolumbo line, a similarly oriented lineament north of the Kameni line (see Figure 2.2), is observed as a linear alignment of older volcanic centers in the NE caldera and is thought to strike toward the Kolumbo volcanic chain NE of Santorini. The Kolumbo volcanic chain is a NE-striking alignment of submarine seamounts (e.g., Hooft et al., 2017; Nomikou et al., 2012; 2013), the largest of which is Kolumbo Seamount (Hübscher et al., 2015; Nomikou et al., 2016).

The interaction between magmatism at Santorini and Kolumbo is still debated. Petrologic studies indicate that their respective crustal magmatic systems are not linked (Klaver et al., 2016), though earthquake tomography suggests a

possible connection below 5 km depth (Dimitriadis et al., 2010). The NE-SW strike of regional volcanism, combined with NE-SW striking fault zones, has led other researchers to suggest an interaction between magmatism and tectonic stresses (e.g., Dimitriadis et al., 2009; Feuillet, 2013). Similar NE-SW trending faults are also present at other large Aegean volcanoes (Papazachos & Panagiotopoulos, 1993; Nomikou & Papanikolaou, 2011).

2.3 Experiment Geometry and Data Acquisition

2.3.1 Seismic experiment

In November and December of 2015, a three-dimensional, active-source seismic tomography experiment was conducted in the broader Santorini volcano area of the southern Aegean Sea. The experiment covered an area roughly 120 km x 45 km centered on Santorini, with the goal of imaging the crustal magmatic plumbing system beneath the volcano (Figure 2.2). Data were collected on 91 ocean bottom seismometers (OBSs) and 65 land seismometers distributed around Santorini's caldera, as well as on Anafi, Christiana, and Anydros islands. The OBSs included 30 Woods Hole Oceanographic Institution (WHOI) instruments (4.5 Hz Geospace 3-axis geophone) and 61 Scripps Institute of Oceanography (SIO) instruments (4.5 Hz Sercel L-28 3-component geophone). Both OBS types also had a High Tech HTI-90-U hydrophone. The land seismometers included 60 Mark 1-Hz geophones from the German Research Center for Geosciences Geophysical Instrument Pool in Potsdam and 5 CMG-40T and Trillium compact (120s) seismometers from the Aristotle University of Thessaloniki. All OBS instruments had a 200-Hz sampling rate and all land stations used a 100-Hz sampling rate. There were over 14,300 active-source marine shots using a 6600 in3 36-component airgun array towed at 12 m depth. Average shot spacing was ~150 m along ENE-

WSW-oriented shot lines spaced at 1-2 km intervals and included shot-receiver offsets up to ~115 km. Additional azimuthal coverage was achieved using a lower shot-density NW of Santorini and stations located on the neighboring Anafi island (Figure 2.2a).

2.3.2 Data return and data quality

The OBS data return was sufficient with 1 OBS lost and an additional 10 OBSs with noisy and/or poor-quality records on both the hydrophone and vertical channels. A sporadic ~6 Hz ringing noise was observed on several SIO stations that did not correlate to any external processes such as wind, lightning, boat traffic, etc. This noise was of variable amplitude and occurred randomly on all 4 channels. Figure 2.3 provides an example of good quality OBS data for two stations located in the Christiana and Anydros basins. Differences between the basins are clearly observed, with large, rather impulsive first arrivals with short coda in the Christiana basin and more chaotic arrivals with a "ringy" character and longer coda in the Anydros basin.

Santorini land stations had variable quality data. Those located on metamorphic rocks and exposed bedrock had great return; in contrast those situated on volcanic deposits were noisy and difficult to pick. Clear impulsive arrivals were seen on Anafi stations, as all these stations were installed on metamorphic basement, providing good longer-range azimuthal coverage to the experiment. However, the Anafi stations were located outside the velocity model used in this paper and thus picks for these stations were not included.

For upper crustal Pg waves crossing the caldera area, arrivals were highly attenuated and travel times for these stations were difficult to pick due to emergent waveforms (Figure A.1). For seismic waveforms that did not travel within the

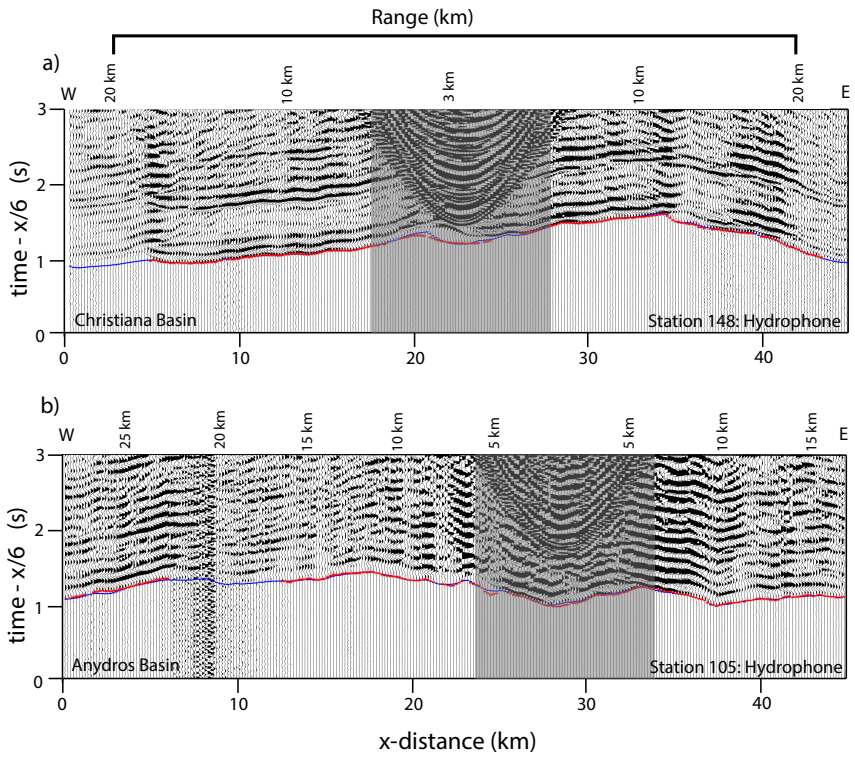

Figure 2.3. Seismic data recorded in basins east and west of Santorini. Seismic record sections (hydrophone) for shot lines in the Christiana (top) and the Anydros Basins (bottom) shown with a reduction velocity of 6 km/s. Shots in the Christiana Basin are characterized by a large impulsive first motion in contrast to the more 'ringy' character of those in the Anydros Basin. There is good agreement between travel time picks (red) and predicted travel times through our preferred model (blue). Regions shaded grey correspond to near shot ranges (0-6 km) which were excluded from the inversion (see text for details).

footprint of the volcano, clear, impulsive arrivals were observed, indicating that any attenuative structure was located beneath the caldera.

2.4 Data processing and tomographic inversion

2.4.1 OBS relocation

The OBSs were relocated on the seafloor by minimizing the misfit between predicted and observed acoustic water-wave arrival times (Creager & Dorman, 1982) for short range arrivals (0-2 km) (longer ranges were included when

necessary). A constant water velocity of 1.52 km/s (determined from expendable bathythermographs) was used and a pick error of 5 ms was estimated. Station locations were fixed to the seafloor using the bathymetric map from Hooft et al. (2017). OBS depths ranged from ~30 m to ~890 m, with typical depth uncertainties of 10 m and horizontal uncertainties less than 4 m. Using the precision of the water-wave arrivals (most stations were fit to water-wave travel-time RMS values of ~5 ms), we were able to identify and correct several errors in the dataset including origin time offsets and mis-located shots. In addition, a non-linear response at short ranges (typically < 0.8 km) was observed on the hydrophone for many instruments, especially shallow stations. This effect did not influence picking of the first motion of water-waves, although it did affect the resulting waveform shape (Figure A.2). Finally, we were able to identify and correct for a linear drift in the OBS clock for one instrument that had not been accounted for in the initial data processing.

2.4.2 Pg travel time data

We picked over 200,000 Pg first arrivals using two approaches. Initial picking was conducted using an autopicker from the open-source opendTect software (https://www.dgbes.com/). Several tens of thousands of arrivals with high signal to noise ratio (SNR) traces (e.g. short ranges, predominately less than 20 km range) were collected using this approach. The picking error for these arrivals was assigned a value of 10 ms, following visual inspection of the automatic picks. After this first step, arrivals were picked manually. Errors were visually assigned during the picking process and ranged from 5 ms (high SNR, exceptional quality data) to 30 ms (low SNR); the median error was 10 ms with standard deviation of 13 ms. The difference in assigned errors resulted from both variability in the noise level, as well as differences in waveform shape and arrival time due to surface and subsurface

complexity. Data were picked on the hydrophone, vertical, and/or a scaled linear stack of the hydrophone and vertical channels. All picks (manual and automatic) were made on the first negative to positive zero crossing (using the polarity convention of the hydrophone channel, Figure 2.3) as it is the easiest portion of the first arrival pulse to pick. This zero-crossing followed a small negative first motion that was only easily observed in the highest quality data. All picks were made on waveforms filtered with a 4th order causal Butterworth filter of 5-25 Hz, for shots with distance ranges between 0 and 65 km. Picking resulted in a high-quality dataset for distances between 4 and 30 km at most stations.

2.4.3 Tomographic Inversion

We inverted the Pg travel time first arrivals using the approach of Toomey et al. (1994), minimizing the squared residual between observed and predicted travel times while also penalizing against both the magnitude and roughness of model perturbations (roughness measured using Laplacian smoothing). The slowness model was defined on a 120 km x 45 km x 12 km (x, y, and z dimensions) rotated rectangular grid for the forward problem, with a grid spacing of 200 m for both horizontal (x and y) and vertical (z) dimensions, and bathymetry reflected by vertical shearing of the grid (Toomey et al., 1994). The grid was rotated 25.5^o counter-clockwise from north, to align the x-axis with the shot-line orientation (Figure 2.2a). Travel times through the crust were calculated using the graph theory approach of Moser (1991), with the water-wave segment of the travel-time (shot to seafloor) calculated on a grid with a 50 m x 50 m horizontal spacing, using a constant water-wave velocity of 1.52 km/s. For the linearized model inversion, a perturbational grid of 400 m x 400 m x 200 m in the horizontal and vertical directions, respectively, was used, inverting for slowness perturbations. Updated

slowness values were then linearly interpolated onto the forward problem grid. Iterating on this linearized inversion strategy allowed for an accurate approximation to the non-linear travel time tomographic problem (see Toomey et al., 1994 for additional details) A number of inversions were conducted to create a smooth 3-D VP starting model, so that large velocity contrasts resulting from the metamorphic horsts and sediment-filled grabens were included in the starting model. To first obtain the best 1D velocity model for the region (Figure 2.4), a 3D inversion was conducted using a 1-D VP starting model derived from a combination of prior gravity, seismic refraction, and receiver function studies (Bohnhoff et al., 2006) (blue line in Figure A.3). The 3-D output velocity model was averaged at each depth and the new 1-D model was used as an updated starting model. This process was repeated and allowed for the migration to an optimized regional 1-D velocity model (black line Figures 2.4 and A.3). To obtain the smooth 3-D VP starting model, we used this regional 1-D velocity model and inverted for 3-D isotropic velocity variations, which were then spatially smoothed with a median filter of 5 km by 5 km by 2 km in the horizontal (x and y) and vertical (z) directions, respectively. For the final inversion we used horizontal and vertical smoothing parameters of 200 and 100, respectively, and penalized model perturbations relative to the previous model iteration using a penalty of 1 (see Toomey et al., 1994 for more detail). Each inversion consisted of 5 model iterations, ensuring the convergence of the RMS travel time misfit (Figure A.4). We conducted tens of trial inversions and the main model features presented in this paper were insensitive to reasonable variations of the inversion parameters (Table A.1, Figures A.4 & A.5). Ranges shorter than 6 km were poorly fit in the initial inversions, a result of the lack of short-range travel-time picks and a large grid spacing (200 x 200 x 200 m) relative to the ranges. Picks associated with these ranges were therefore

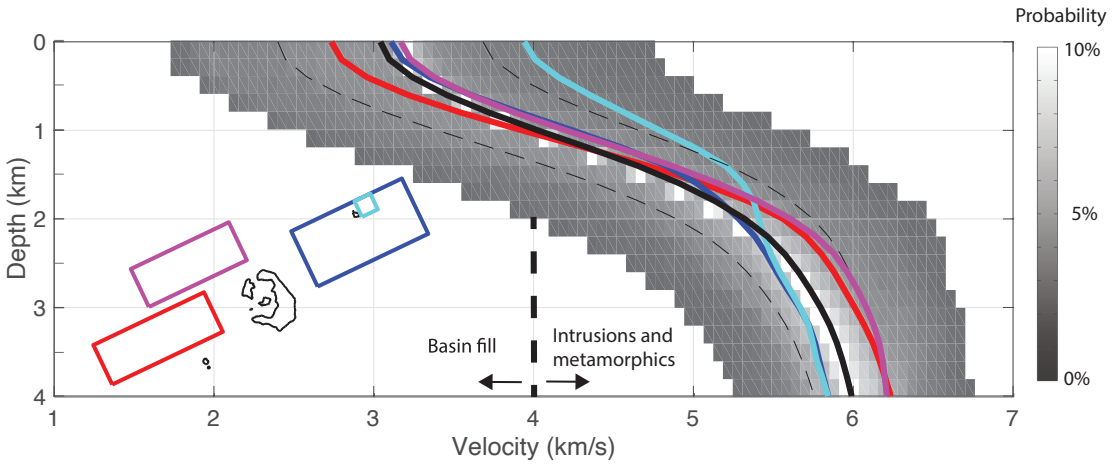

Figure 2.4. 1-D P-wave velocity-depth profiles. Averaged 1-D velocity depth profile of four selected areas around Santorini (outlined in subfigure), compared to the average regional velocity profile (black line). Basin fill is assumed for velocities less than 4 km/s and metamorphic rocks and intrusives for velocities faster than 4 km/s - this corresponds to a steep gradient in the velocity-depth curve. The light blue curve highlights the P-wave velocity for the Anydros metamorphic horst (Fig. 2.2), showing faster than average velocities of the metamorphic rocks at shallow depths (0-2 km). At $>$ 2 km depth, areas on the western side of Santorini (red and magenta) are systematically faster than those on the eastern side (dark blue and light blue). Background grey-scale shows the probability density function distribution of all 1-D velocities of the tomography model.

removed from the inversions. The model presented here (Figure 2.5) was fit to an RMS travel-time misfit of 15 msec, which corresponds to a χ^2 of 2.2. To ensure the accurate recovery of structures, initial inversions only used the higher quality, often shorter-range data ($<$ 15 km). By predicting expected (theoretical) arrival times through this initial tomographic model, we were able to identify mis-picked arrivals and facilitate the manual picking of noisy first arrivals, which were skipped in the initial picking effort. Using this approach, we extended the picked dataset from $<$ 15 km (high signal-to-noise) to $>$ 30 km (often lower signal-to-noise).

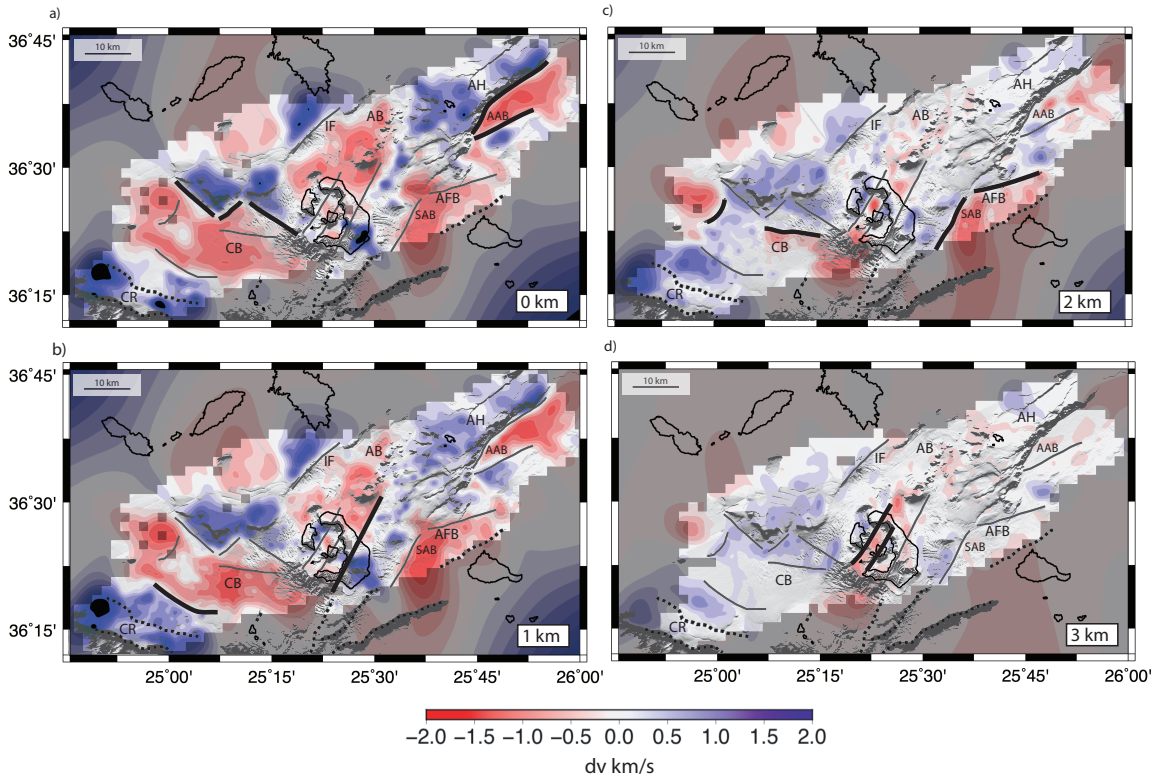

Figure 2.5. Velocity anomalies relative to the 1-D average velocity-depth profile at 0, 1, 2, and 3 km depth. Background is illuminated bathymetric map from Hooft et al. (2017). Grey lines are faults defined using the seismic tomography images. These faults are colored black on the depth slice on which they were defined. Dashed black lines are large faults outside the region of resolution. Abbreviations as in Figure 2.2b.

2.5 Results and Interpretation

2.5.1 Upper crustal velocity variations

The tomographic model shows substantial P-wave velocity variations in the upper crust of the study area, with lateral differences in velocity exceeding 3 km/s near the surface (Figure 2.5). In the top-most kilometer, regions of anomalously high (+1.5 km/s) and low (-1.5 km/s) relative velocity correspond to mapped metamorphic basement and sedimentary basins, respectively (Figures 2.2 & 2.5a-b). At depths greater than 2 km, the velocity west of Santorini is higher and

spatially more uniform compared to the eastern side of the Santorini volcano, where velocities are both lower and more variable (Figures 2.4 & 2.5b). At 3 km depth, the overall lateral velocity variability across the study area is still ~2 km/s (± 1 km/s) (Figure 2.5d). The reliability of the recovered longer wavelength lateral velocity variations is validated by checkerboard resolution tests (Text A.1, Figures A.6, A.7 & A.8), which show that features with length scales of 5 km and greater are well recovered throughout the model, while features with length scales of 3 km are well recovered within the higher-velocity areas, mainly metamorphic basement.

Rapid velocity changes between the low-velocity sedimentary basins and higher velocity metamorphic basement rocks are interpreted as faults. Near-surface faulting, delineated by sharp velocity changes observed in the 0- and 1-km-depth slices (heavy black lines in Figure 2.5a&b) is in good agreement with faults observed in the topographic-bathymetric map (Figure 2.2). At the depth of 2 and 3 km, we interpret similar sharp spatial velocity gradients as faults within or beneath the basins (heavy black lines in Figure 2.5c-d).

2.5.2 Comparison of tomographic velocity model with seismic reflection images

In general, first order geotectonic features, such as large-scale sedimentary basins and their bounding faults, are well resolved in both tomographic and prior seismic reflection datasets and show similar geometries and structures. Figure 2.6 shows the location of 7 cross-sections where detailed model evaluation and interpretation were performed, of which profiles A-A', B-B' and C-C' have associated seismic reflection results (Figure 2.7).

Figure 2.7a compares the seismic tomography cross-section to a multi-channel seismic (MCS) profile that crosses the Anydros Basin, Anydros Horst, and Anafi-Amorgos Basin from NW to SE (Nomikou et al., 2018) (Figure 2.6).

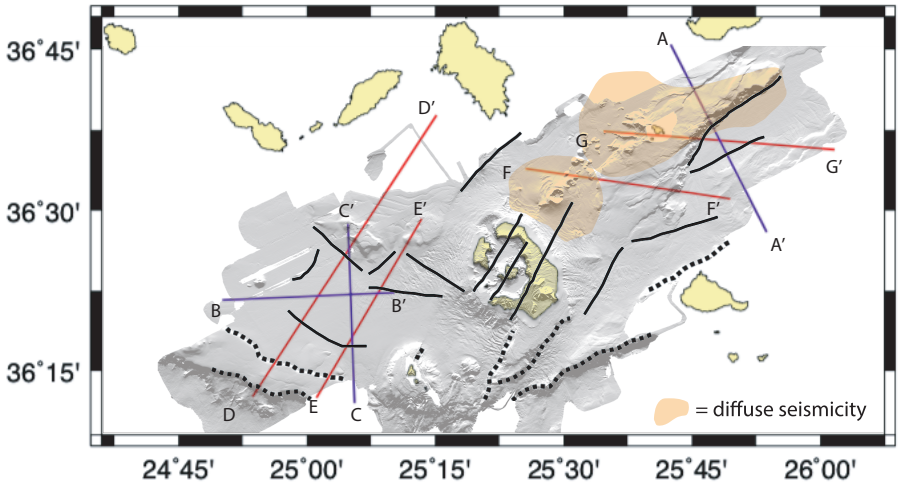

Figure 2.6. Map showing the location of seismic cross-sections. A-A', B-B' and C-C' (purple lines) indicate the locations of the three seismic reflection profiles (from prior studies) and corresponding velocity cross-sections (this study) that are shown in Figure 2.7. D-D', E-E', F-F' and G-G' (red lines) show the locations of the four interpreted tomography cross-sections through regional basins shown in Figure 2.9. Tomographically defined faults (black lines) are after Figure 2.5. Orange regions mark areas of diffuse micro-seismicity (Bohnhoff et al., 2006; Brüstle et al, 2014).

The transition across a large-offset normal fault into the Anafi-Amorgos basin accurately coincides with an abrupt change from high to low velocities in the tomographic image. A smaller basin bounded by secondary faults is similarly expressed tomographically in the Anydros Horst footwall. The transition from sediment to the underlying basement of the Anafi-Amorgos basin corresponds approximately to the 4 km/s velocity contour. Additional comparisons with the MCS results (Nomikou et al., 2016) in the vicinity of Kolumbo submarine volcano are presented in Figures A.9 and A.10.

A seismic tomography comparison to a W-to-E seismic reflection profile within the Christiana Basin (Tsampouraki-Kraounaki & Sakellariou 2018) is presented in Figure 2.7b. In the reflection image, the basin is filled by sediments (Units 1 -5, Figure 2.7b) intercalated with pyroclastic flows (Roman numerals),

with Unit 6 proposed to be Messinian evaporites, a late Miocene marker (Tsampouraki-Kraounaki & Sakellariou 2018). In the center of our tomographic velocity profile, elevated seismic velocities relative to the surrounding sediments (3 - 4 km/s versus 1.5 - 3 km/s) correlate with an updoming of the Messinian evaporites, an observation consistent with research showing that evaporites are seismically faster than sediments and pyrolastic flows (e.g., Zong et al., 2017). Small-offset faults within the sediments on the eastern end of the reflection profile correlate with underlying variations in basement structure in the tomography images.

Figure 2.7c shows a S-N seismic reflection profile through the Christiana Basin (Tsampouraki-Kraounaki & Sakellariou 2018) and its comparison with tomographic results. Generally, the main basin is seismically slow, whereas the basement rock (Unit 7 in top figure) is seismically fast (~3.5 to 5.5 km/s). In the northern portion of the basin the dip of the margin is well recovered. An old buried basin margin on the southern edge of the Christiana basin, thought to have become inactive ~1 Ma (Tsampouraki-Kraounaki et al. 2018), is also tomographically identified as seismically faster than the main portion of the basin. Near-vertical faults observed in the reflection images (red lines) appear to spatially correlate with variations in the underlying basement, similar to Figure 2.7b. These faults have been proposed to be strike-slip features associated with a prior episode of deformation, which ceased activity ~1 Ma, as evidenced by the undisturbed sediments overlying the faults (Tsampouraki-Kraounaki et al. 2018).

While the travel time tomographic velocity model is less detailed than the seismic reflection images with respect to structure and deposition sequence, it provides valuable velocity and depth constraints, as well as fuller three-dimensional spatial coverage than the existing reflection imaging. The tomographic images also

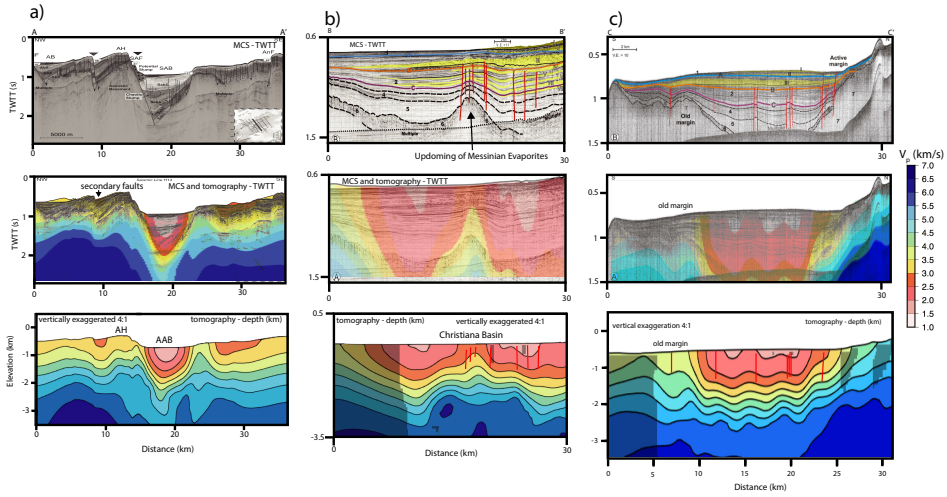

Figure 2.7. Comparisons of tomography velocity model with seismic reflection profiles. Upper panels depict seismic reflection profiles from previous studies (locations shown in Figure 2.6). Middle panels show seismic velocity from this study overlain on the seismic reflection image, after converting depth into a Two-Way Travel Time (TWTT). Bottom panel is the same seismic velocity cross-section shown as a function of depth. (a) Seismic reflection profile (H14) from Figure 6 of Nomikou et al. (2018) across the Anydros Ridge showing tomographic recovery of the Anafi-Amorgos Basin (AAB) as well as recovery of secondary faulting on the Anydros Horst (AH) (b) E-W seismic reflection profile across the east-central Christiana basin (Figure 7 of Tsampouraki-Kraounaki & Sakellariou 2018) showing the correlation between the seismic velocity structure and faults in the seismic reflection data. The authors interpret Unit 6 as Messinian evaporites and the region of up-doming of this layer correlates with higher seismic velocities. Red lines in bottom panel are faults from the seismic reflection data. (c) S-N seismic reflection profile across the eastern portion of the Christiana basin (Figure 5 of Tsampouraki-Kraounaki & Sakellariou 2018) showing thin sediments over an old basin margin. Shallow faults from seismic reflection studies (red lines) correlate well with deeper undulations of basement structure.

reveal deeper features such as faults that ultimately control the shallower structures observed in the seismic reflection images.

2.5.3 Mapping geometry and thickness of sedimentary basins from the tomography model

We outline basin depth using a velocity of 4 km/s throughout the model and map both the two-way travel-time (TWTT) and the depth to the 4 km/s

iso-velocity contour (Figure 2.8). Visual comparison between seismic reflection images and tomography results indicates that this value typically corresponds to the sediment-basement interface (e.g. Figure 2.7 & A.11). The 4 km/s velocity also corresponds to the midpoint of a rapid increase in average seismic velocity with depth (Figure 2.4), interpreted as the transition from seismically slow sediments to the underlying, seismically fast metamorphic basement rocks. We contour the depth to the 4 km/s iso-velocity to delineate the 3D geometry and thickness of the sedimentary basins across the entire study area (Figure 2.8a), and not just the profiles that were mapped using TWTT from seismic reflection studies (e.g. Nomikou et al., 2016).

Figure 2.8 shows how the faults identified in Figure 2.5 correlate with, and control, the geometry and internal structure of the basins. Cross-sections through the tomography results on two SW-NE cross-sections through the Christiana Basin west of Santorini and two WNW-ESE cross-sections through the Anydros and Anafi Basins east of Santorini are shown in Figure 2.9 (with locations of the profiles in Figure 2.6). This figure validates and elucidates the faults identified in the map views (Figure 2.5) and their relationship to basin structure (Figure 2.8).

2.5.4 Western side of Santorini: Christiana Basin and Christiana Ridge

The anomalously low P-wave velocities at 0-2 km depth in the western part of the model coincide with the NW-SE striking Christiana Basin (Figures 2.2 & 2.5). Low-velocity anomalies associated with the basin extend to ~1 km depth in the basin center and down to 2 km in its SE and NW parts, indicating the presence of two deeper sub-basins (Figure 2.5 and 2.9). The SE sub-basin is deepest close to Santorini, near Christiana island (Figure 2.5d). Results from previous seismic reflection studies suggest that these sub-basins formed in the Early to Middle

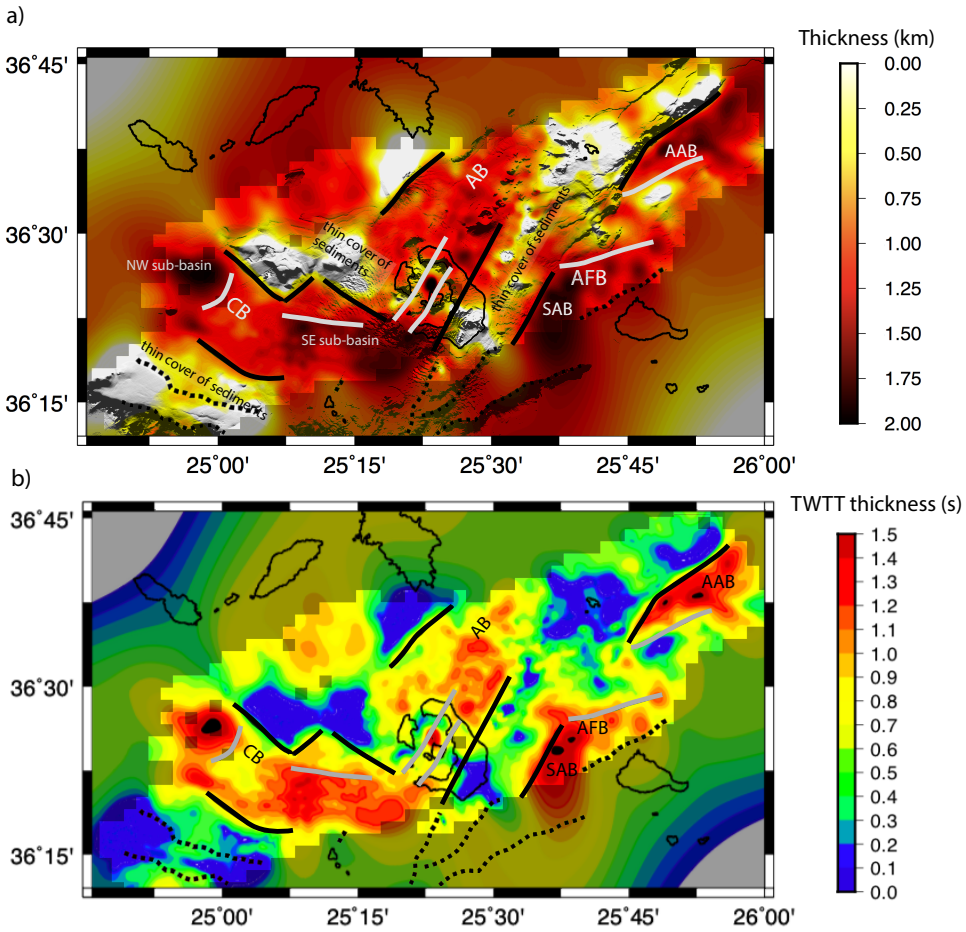

Figure 2.8. Sedimentary basin thickness maps from the seismic tomography model. (a) Basin thickness, determined using the 4 km/s velocity contour as the sediment-basement transition, with relevant geological features labeled. (b) Tomographic basin thickness converted to TWTT for comparison with seismic reflection studies. The Anydros basin, despite being a prominent tectonic feature on bathymetric maps, has relatively shallow sediment fill (1-1.5 km). In contrast, the Amorgos-Anafi Basin and the Santorini-Anafi basins as well as the relatively inactive Christiana basin contain thick sediment fill (>2 km). Faults after Figure 2.5, with deeper faults (2-3 km depth) shown in light grey and shallower faults (0-1 km) in dark grey. Dark shading indicates areas with poor resolution of sediment thickness. Labels as in Figure 2.2.

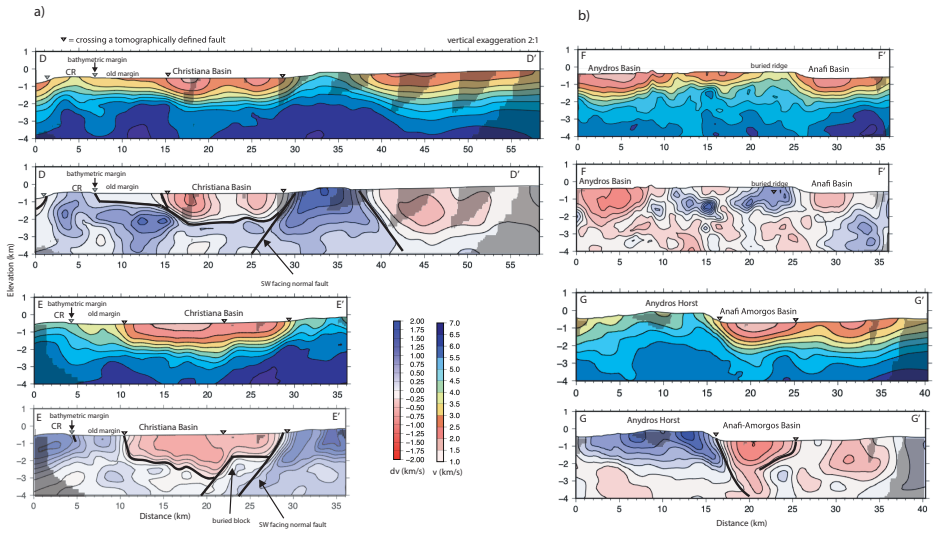

Figure 2.9. Seismic velocity cross-sections through the Christiana and Anydros basins. (a) Profiles D-D' and E-E' through the Christiana basin in velocity (v) and velocity anomalies (dv) with interpretations of main fault geometries shown in black on dv cross-sections. The open triangles mark where the profiles cross the black faults shown on Figure 2.6. These profiles show evidence for down-dropped blocks within the Christiana basin. (b) Profiles F-F' and G-G' through the Anydros and Anafi basins, following conventions described above. These two basins show thinner sedimentary fill than the Christiana basin, more pervasive faults at depth, and are regionally characterized by a seismically slower basement velocities than the profiles through the Christiana basin (D-D' and E-E') (see also Figure 2.4).

Pleistocene, before continued expansion was accommodated by wider faults in the north and south (Tsampouraki-Kraounaki & Sakellariou 2018).

The Christiana basin is separated from the Sea of Crete to the south by the Christiana ridge (Tsampouraki-Kraounaki & Sakellariou 2018) (Figures 2.2 & 2.5). The northern, bathymetrically expressed margin of the ridge proper (dashed black line north of CR in Figures 2.5a and 2.5b) has little tomographic expression, showing a minor velocity contrast across the fault (Figure 2.9a). The tomographically expressed fault margin (solid black line above CR in Figure 2.5b) is located basin-ward (north) of the ridge proper, striking NW-SE, and reflecting the presence of an old basin margin, buried under a thin veneer of sediments

(Tsampouraki-Kraounaki & Sakellariou 2018, see also Figure 2.7c). This fault, which dips at an angle of 25-40°, marks the deepening of the basin to km-scale depths (Tsampouraki-Karounaki et al., 2018) (Figures 2.8 & 2.9a).

The northern margin of the Christiana basin is marked by a large SW-facing normal fault. While this fault is clearly evident in Figures 2.8 & 2.9a, it has little bathymetric expression close to Santorini (Figure 2.2), most likely because it is covered by volcanic deposits. On the contrary, in the western part of the model away from Santorini, it is identified in both the tomography model and the seafloor bathymetry as seen in the D-D' and E-E' model cross-sections and their proposed interpretation (Figure 2.9a). At ~2 km depth, and basin-ward of the northern basin-bounding fault, there is a large buried normal-fault block, dipping to the SSW at an angle of 25-40° (solid black line north of CB in Figure 2.5 and solid black line labelled buried block in Figure 2.9a). This fault forms the northern margin of the SE sub-basin.

2.5.5 Eastern side of Santorini: Anydros Basin, Anafi Basin and Anydros Horst

The two large NE-SW trending basins on the eastern side of Santorini, the Anydros (AB) and Anafi (AFB) basins, are tomographically identified at 0-1 km depths as seismically slow regions (Figures 2.5a and b and Figure 2.9b). The Pliocene/Quaternary-aged Anydros Basin has thin basin fill and appears to be only ~1.5 km thick (Figures 2.8 & 2.9b). The similarly aged Anafi basin is divided into two sub-basins by a buried ridge at <1 km depth (Figure 2.5), the Anafi-Amorgos basin (AAB) to the north and the Santorini-Anafi basin (SAB) to the south. Both sub-basins are up to 2 km thick. The buried ridge dividing these sub-basins has an ENE-WSW orientation (Figure 2.5b).

On the eastern side of Santorini, we observe tomographically resolved variations in the strike of basin margins of up to 20° from a mean NE-SW direction. For example, the northern margin of the Anydros basin, the Ios fault (IF in Figure 2.5), strikes approximately N40^oE, whereas the southern margin of the Anydros basin strikes roughly N25^oE. Similarly, the large dipping fault on the northern margin of the Anafi-Amorgos basin (the Santorini-Amorgos fault) is curved and has strikes ranging from N25^oE to N60^oE (Figure 2.5), a pattern consistent with sea-floor morphology (e.g. Hooft et al., 2017, Nomikou et al., 2018) (Figure 2.2b).

The Anydros and Anafi basins are separated by the Anydros Horst (AH), which has typical bedrock velocities of 5-6 km/s at shallow depths (<1 km), in contrast to the low velocities in the basins (2-4 km/s) (Figure 2.9b). Close to Santorini, this horst is buried under a thin cover of sediments, possibly by volcanic eruption deposits, as suggested by the presence of a relatively flat bathymetry but a strong high-velocity tomographic signature.

2.5.6 Structures associated with Santorini

Several NE-SW striking faults extend from the western side of the study area (e.g. Christiana basin region), through Santorini, to the eastern side (Anydros Horst and Anafi basin region). At shallow depths, metamorphic blocks that are part of the pre-existing volcanic basement and that outcrop in southern Santorini are well recovered as seismically fast regions (Figures 2.5a and 2.10). The NE-SW striking Akrotiri fault on the western side of Santorini, which is identified in the bathymetry south of Santorini (Figure 2.2) (Hooft et al., 2017), is tomographically observed at 0-1 km depth as a prominent velocity contrast that strikes through Santorini and out to the east toward the Anydros Horst region (Figure 2.5a-b)

juxtaposing the seismically slow basin sediments of the Anydros Basin to the north against the seismically fast metamorphic basement to the south. This fault, which extends from the southwestern termination of the Christiana basin, through Santorini, to the margin of the Anydros Horst on the east, is subparallel to the regional alignment of volcanic centers (Figures 2.5a and 2.5b). At deeper depths (2-3 km), a tomographically defined fault strikes through the northern caldera basin, passing through NE Santorini. This fault may also be connected to a bathymetrically expressed fault extending NE from Christiana island (Figure 2.2b). From Santorini's northern caldera, the fault extends northeast toward Kolumbo volcano (Figures 2.5c & A.10).

At 1-2 km depth a large circular, low-velocity anomaly is observed in the center of the northern caldera basin, which has been proposed to be related to caldera collapse (Hooft et al., 2019) (Figure 2.10). This anomaly directly overlies the inflation source from a 2011-2012 unrest period (inferred source depth of ~4 km) (Parks et al., 2015) and is bounded by the two dominant tectono-magmatic lines on Santorini, the Kameni and Kolumbo lines (Pfeiffer, 2001). The southern margin of the anomaly marks the location of recent volcanism (Kameni lavas, Figure 2.10) (Pyle and Elliott, 2006). Its shape matches that of the shallow basin-fill of about 100 m thick, observed in previous seismic reflection images and inferred to correspond to LBA eruption deposits (Johnson et al., 2015).

2.6 Discussion

2.6.1 Differences between the east and west sides of Santorini and relationship to faulting

The area east of Santorini is seismically active and exhibits ongoing, distributed faulting including a MS = 7.4 normal-faulting event on the Santorini-

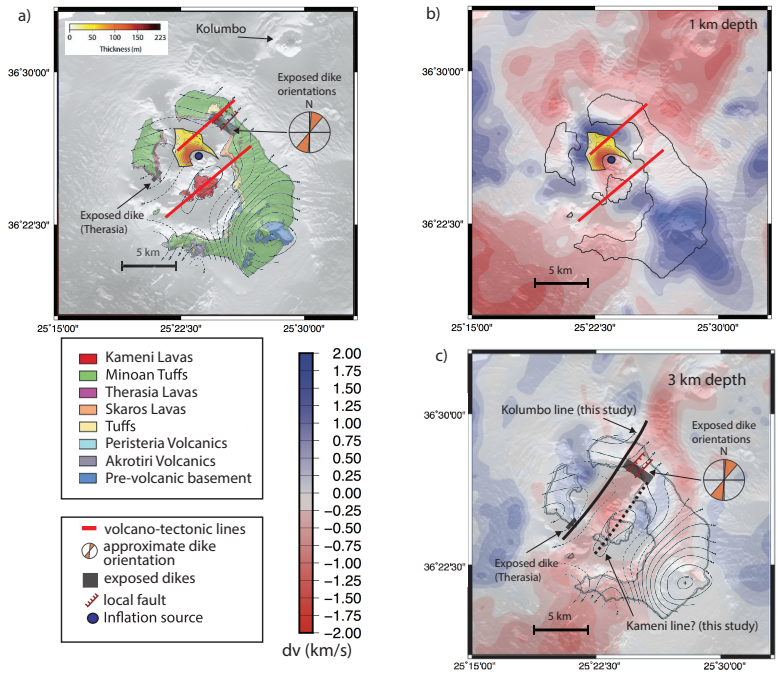

Figure 2.10. Comparison of the seismic velocity beneath Santorini with volcanic features and exposed geology. (a) Geologic map of Santorini (modified from Druitt et al., 2016) with dike locations and orientations (Browning et al., 2015; Fabbro et al., 2013), the Kolumbo and Kameni tectono-magmatic lineaments (defined by prior studies), locations of small-scale faulting (Druitt et al., 1999), location of the 2011-2012 inflation source (Parks et al., 2015), long wavelength gravity data (black contours at 2 mGal intervals; Budetta et al., 1984), and a LBA (Late Bronze Age) deposit thickness map from seismic reflection data (modified from Johnston et al., 2015). (b) Comparison of previously proposed tectono-magmatic lineament locations (red lines), 2011-2012 inflation point source (blue dot), and Late Bronze Age (LBA) deposit thickness (modified from Johnston et al., 2015) with relative velocity (dv) at 1 km depth. An increase in the LBA deposit thickness directly overlies a decrease in velocity associated with caldera collapse (Hooft et al., 2019) and also overlies the 2011-2012 inflation point source at ~4 km depth (Parks et al., 2015). (c) Comparison of locations of exposed dikes, their orientations, faults, and long wavelength gravity with dv at 3 km depth. The Kolumbo line (labelled) is clearly observed in the tomography, dividing slower seismic velocities to the SE from faster velocities to the NW. The orientation of the NE-SW striking line parallels exposed dike orientations and matches the strike of regional faults. The Kameni line (labelled) is also observed in the tomography, paralleling the Kolumbo line.

Amorgos fault in 1956 (Brüstle et al., 2014; Konstantinou, 2010; Okal et al., 2009; Papadopoulos & Pavlides, 1992). There are also two regions of small earthquakes: those around Kolumbo that are thought to result from magmatic processes (Bohnhoff et al., 2006; Dimitriadis et al., 2009) and clustered earthquakes around the Anydros Horst (AH) that may reflect upward migration of fluids within a zone of tectonic weakness or the development of volcanic activity (Bohnhoff et al., 2006) (e.g. Figure 2.6). In contrast, the west side is characterized by the seismically quiet, older Pliocene faulting of the Christiana Basin (e.g. Bohnhoff et al., 2006). These differences have led to the interpretation that the AH is part of a boundary that accommodates the relative motion between a competent Cycladic block and a less-competent eastern Aegean region, dividing the Aegean into a seismically quiet west and more active east (e.g., Bohnhoff et al., 2006; McClusky et al., 2000; Reilinger et al., 2010).

At ~3 km depth the basement east of Santorini has a lower average seismic velocity than to the west of Santorini by ~0.4 km/s (7%) (Figures 2.4 and 2.5), which can be attributed to the presence of dense, distributed faulting in AH region, reducing rock competency. Preliminary plots of travel time misfit as a function of azimuth show NE-SW-oriented seismic anisotropy which results from a fracture network in this region (Figure A.12). Focal mechanisms of shallow earthquakes from the AH area (Friederich et al., 2014; Dimitriadis et al. 2009) are also consistent with normal faulting due to NW-SE 130-155° extension, indicating ongoing NE-SW fault activity in this region.

An alternative explanation for the difference in average velocity on the east and west sides of Santorini is that it is generated by differences in composition. While the presence of carbonates, flyschs, greenschists, blueschists, and granites (Kilias et al., 2013) indicates that variable seismic velocities due to compositional

differences should exist, the orientation of the geological units is mainly controlled by N-S-dipping regional detachments, which is unlikely to produce significant NE-SW velocity variations. We conclude that the association of the lower P-wave velocities east of Santorini with active deformation and pervasive fracturing of the basement is the most plausible scenario.

2.6.2 Tectonic evolution of the basins and Christiana-Santorini-Kolumbo magmatism: Localization of magma in a proto-Anydros Basin

Using the delineated faults and basin structures, we refine an existing model for the tectonic evolution of the Santorini region from the Miocene-Pliocene to present (Piper et al., 2007) and investigate how tectonism interacts with, and localizes, magmatism (Figure 2.11). While the tomographic velocity images provide information on the strike and style of faults, absolute time constraints on fault activity rely on other studies, mainly seismic reflection imaging.

The earliest stage of faulting in the region, during the Miocene-Pliocene (Figure 2.11a), resulted in WNW-ESE-oriented faults that define the Christiana Basin and likely the buried ENE-WSW faults that divide the Anafi basin (Anastakis and Piper, 2005; Piper et al., 2007) (hereafter these faults will be referred to as E-W to be consistent with the literature). The offset between these two sets of tomographically resolved faults (Figures 2.5 and 2.11a) supports the inference of Piper et al., (2007) that a transfer zone may have existed striking approximately N through the area where Santorini currently resides.

In the late Pliocene to Pleistocene (Figure 2.11b), these predominately E-W structures were cross-cut by NE-SW striking faults (Piper et al., 2007). This may have occurred as a result of NW-SE extension due to differences in motion between the Cycladic and eastern Aegean blocks (e.g. Reilinger et al.,

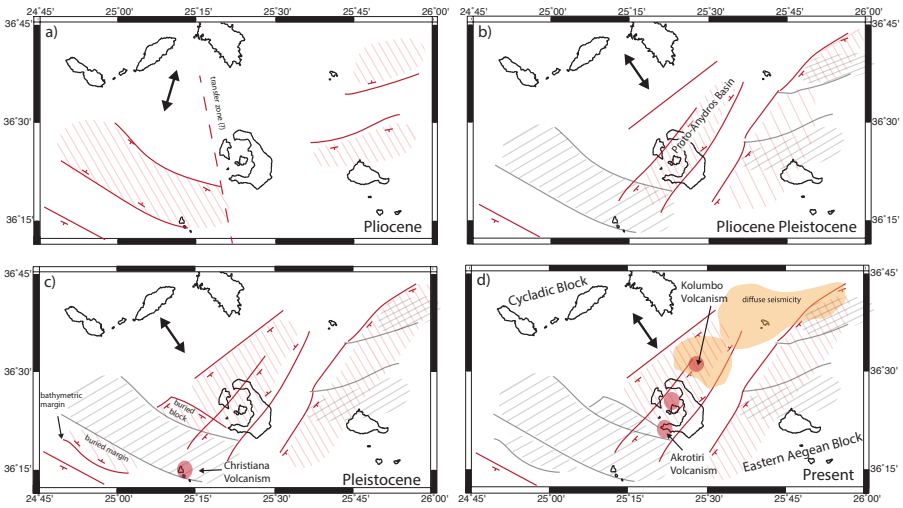

Figure 2.11. Fault evolution and its relationship to magmatism: Sketch of the evolution of faulting and volcanism in the Santorini area using the faults defined from the tomographic model (Figure 2.5) and building on the tectonic evolution model of Piper et al. (2007). Temporal constraints are taken from previous studies (Piper et al., 2007). Red lines and red shading show active faults during each time period, hatched areas indicate basins, red circles indicate regions of volcanic activity, black arrows indicate approximate extension direction for each period. (a) Formation of the Christiana Basin as a full-graben structure in the Pliocene under NNE-SSW extension. (b) Transition to NW-SE extension leading to Anydros Horst formation from the Pliocene-Pleistocene on, with initial formation of a proto-Anydros Basin. (c) Initiation of Christiana volcanism in the Pleistocene. (d) Volcanism at Santorini and Kolumbo developed in the Quaternary within the proto-Anydros Basin. Current diffuse seismicity (orange region; Bohnhoff et al., 2006, Brüstle et al, 2014) occurs predominately on the eastern side of Santorini.

2010). These faults formed primarily on the eastern side of Santorini (Figures 2.5, 2.11b) and the earlier E-W fault systems became mostly inactive (e.g. Piper et al., 2007). The tomographic results indicate that a proto-Anydros basin formed by progressive normal faulting along parallel to subparallel NE-SW-trending faults near the current Anydros basin and extending further to the SW through Santorini toward Christiana island (Figure 2.11b). A substantial portion of the proto-basin is currently filled by the Santorini volcanic edifice (bold black line,

Figure 2.4c) and the Kolumbo volcanic field (Figure 2.11b, 2.11d). Gravity and magnetic data support the presence of a NE-SW-oriented fault zone underlying the caldera (Figure 2.10) (Budetta et al., 1984). We infer that the proto-Anydros basin intersected the Christiana basin in the region of the SE Christiana sub-basin, potentially contributing to deepening of the SE portion of this sub-basin (Figure 2.8).

During the Pleistocene (Figure 2.11c), volcanism initiated at Christiana Island (~1.2 Myr) (Piper et al., 2007) and was roughly localized at the intersection of the proto-Anydros basin with the Christiana basin (Figure 2.11c). Because the proto-Anydro basin is filled by the Santorini and Kolumbo edifices (Figure 2.11d), the NW-SE extension that formed this basin must have preceded the majority of these volcanic eruptions. Volcanism at Santorini began around the Middle Pleistocene (650 ka) (Figure 2.11c) (Druitt et al., 1999). Seismic reflection data show that the present-day Anydros basin opened in six tectonic pulses (Hübscher et al., 2015; Nomikou et al., 2016), creating the basin that is currently observed to the NE of Santorini. The exact relationship between Santorini volcanism and Anydros basin formation is not known though the seismic reflection data indicate that eruptions from nearby Kolumbo seamount started after Anydros basin initiation (Nomikou et al., 2018). Because all of the regional volcanism falls within the proto-Anydros basin (Figure 2.11d), it is likely that this basin has played a role in localizing volcanism. Such interaction between extension and volcanism is readily observed in analog models where volcanism is localized in rift basins during oblique extension (Corti et al., 2003).

The above interpretations, where proto-Anydros basin formation precedes major local volcanism, are consistent with previous models that inferred that the rotation from older NNE-SSW extension to the current NW-SE extension in the

early Pliocene was associated with an increase in volcanism in the area (Piper et al., 2007). Across the Hellenic arc, volcanism is dominantly associated with NE-SW striking features (i.e. NW-SE extension) (e.g., Budetta et al., 1984) and only secondarily with NW-SE strikes (Kokkalas & Aydin, 2013).

2.6.3 Volcano-tectonic lineaments

At Santorini we recover and improve on the geometry of the well-known Kameni and Kolumbo volcano-tectonic lineaments, using information inferred from the seismic tomography images (Figures 2.5, 2.8 and 2.10). The northern margin of the low-velocity anomaly (LVA) within the Santorini caldera is bordered by the Kolumbo line, initially identified as an alignment of volcanic edifices in the northern portion of Santorini. It has been suggested that one of the vents of the LBA eruption was located along this line (Pfeiffer, 2001). In our study, the Kolumbo line is tomographically imaged at 3 km depth as a linear feature that divides a seismically fast region to the north from a lower velocity region to the south, oriented more northerly than suggested by previous studies and sub-parallel to the regional NE-SW trending faults (Figures 2.2 and 2.10). The tomographically defined Kolumbo lineament is associated with faulting observed in MCS profiles north of Kolumbo volcano (Figure A.10) (Nomikou et al., 2016). This line is also aligned with exposed dikes in the northern portion of the caldera walls and with a similarly oriented dike exposed on Therasia on the western side of the caldera (Browning et al., 2015; Fabbro et al., 2013). The joint interpretation of these observations suggests that (at depth) the Kolumbo line is controlled by regional tectonism and that it plays a dominant role in localizing magmatic and volcanic features, both within, and close to, Santorini.

In contrast to the Kolumbo line, the Kameni line has a weaker tomographic signature. This line, which is thought to have focused vents of prior explosive eruptions (Druitt et al., 1989), has previously been defined using the orientation of post-LBA eruption vents on the Kameni islands (Pyle and Elliott, 2006). Moreover, it was re-activated seismically in the recent 2011-2012 seismo-volcanic crisis (e.g. Newman et al., 2012), verifying its active character. Our study shows that the line is associated with a NE-SW trending region of limited lateral extent that divides anomalously slow velocities to the NW from faster velocities to the SE (Figure 2.10) and lies parallel to the tomographically recovered Kolumbo line.

The Kameni and Kolumbo lines border the caldera LVA, a region of collapse in the northern caldera (Hooft et al., 2019). This isolated region of deepened caldera collapse, which overlies a recent influx of magma (e.g. Newman et al., 2012; Parks et al., 2015), seems to have been limited in extent by these tectono-magmatic lineaments. Similarly, the majority of exposed dikes and vents associated with Santorini volcanism also fall between the Kolumbo and Kameni lines. It is clear these lineaments have helped to control the tectonic evolution of the volcanic system and, given their association with eruptive vents, they have likely shaped magma input into the upper crust.

2.7 Conclusions

We used the seismic velocity model to outline faults and basins (Figure 2.5) and to correlate magmatic and tectonic processes. In the Santorini region, we find that the tomographic results compare well with previous seismic reflection studies and geological outcroppings on Santorini (Figure 2.10). Geologically observed dikes and volcanic chains around the volcano directly overlie tomographically observed faults and tectono-magmatic lineations. Inside the caldera, volcanic vents and

deposits from the Late Bronze Age eruption correspond to a seismically slow region of caldera collapse. Our results and interpretations, combined with those from other studies, support the following conclusions: 1. Resolved tomographic structures, specifically orientations of faults and basins, are consistent with a previously proposed tectonic evolution model consisting of NNE-SSW extension during the Miocene-Pliocene transitioning to NW-SE extension in the Late Pliocene-Pleistocene that predominates on the eastern side of Santorini (Figure 2.11). This present-day extension is associated with pervasive faulting east of Santorini. 2. The Christiana, Santorini, and Kolumbo volcanic centers are found to lie in a NE-SW-trending basin-like structure, the proto-Anydros basin (Figure 2.5). These results are in agreement with models that suggest volcanism initiated after the transition to NW-SE extension in the Pleistocene. 3. Two tectono-magmatic lineaments control magma emplacement at Santorini. These lineaments border a NE-SW trending region of low velocity, are associated with dikes in the caldera walls, and strike parallel to active NE-SW trending regional faults and sub-parallel to regional volcanic chains. The two lineaments also bound a region of localized caldera collapse within Santorini's northern caldera, verifying the strong relationship between tectonics and magmatism.

2.8 Bridge

In Chapter II I outlined regional tectonic and magmatic features around Santorini Volcano, emphasizing that the magmatic features, which generally have a NE-SW orientation, have been localized in a buried NE-SW elongate basin. I proposed a simplified conceptual model for regional tectonic evolution and its association with this localized magmatism. In Chapter III, I discuss whether this localized magmatism results from small scale (km) faulting or regional tectonic

stresses. In addition, I investigate pervasive regional fracturing of the crust in this extensional tectonic environment.

CHAPTER III

RELATIONSHIP BETWEEN FAULTING AND MAGMATISM AROUND SANTORINI: SEISMIC ANISOTROPY RESULTS FROM A REFRACTION EXPERIMENT

This chapter is being prepared for future publication. Ben Heath conducted all inversions, drafted all figures (excluding portions of those credited to other sources) and wrote the manuscript. Emilie Hooft provided edits to a previous version of this chapter. Michele Paulatto and Joanna Morgan aided anisotropy interpretations as well as provided suggestions on the modeling of anisotropy.

3.1 Introduction

Investigations of magmatic centers and their evolution show strong evidence that extensional tectonic and magmatic processes interact on regional ($\geq \mathcal{O}\left(10^1\right)$ km) and local ($< \mathcal{O}\left(10^1\right)$ km) scales. For example, volcanoes are often found to be located in areas of increased faulting near first-order, regional fault zones. In rifts, magmatism is often focused in regional-scale basins and vents are arranged in linear lines paralleling the orientation of fault zones (e.g. Casey et al., 2006; Muirhead et al., 2015). For areas such as the Basin and Range and the Aegean, magmatism is often found to focus at accommodation zones, complex zones of intermeshed faults (Faulds & Varga, 1998). In such regions, major normal faults often terminate in magmatic centers, either due to pre-existing magmatism inhibiting fault propagation or due to tectonic-induced stress distributions favorable to magma body development (Faulds & Varga, 1998). These observations all support a strong correlation between extension in faulted continental crust and magmatic activity.

Despite this strong correlation, understanding of exactly how these processes are related remains enigmatic. For example, faults and fractures are thought

to represent permeability pathways through the crust and/or represent zones of crustal weakness characterized regionally by damaged host rock. In these models, dikes and their associated melt follow preexisting fracture networks, and therefore are focused to regions dominated by extensive fracturing, extensive damage and higher permeability (Kokkalas & Aydin, 2013). Other models suggest that magmatism accommodates extensional strain, inhibiting faulting (Parsons & Thompson, 1991) and that magmatism should therefore be associated with lessened faulting. Stress-based models suggest that dikes open approximately in the direction of least compressive stress, a direction that need not be associated with the shear-based faulting (Anderson, 1951; Gudmundsson, 1995). In these models, dikes follow solely a stress-based path and, therefore, a regional correlation between faulting and magmatism represents the shared dependence of both processes on stress. These processes are further complicated by the fact that magmatism and tectonism iteratively impact each other. For example, dikes can alter a tectonic stress field, leading to shallower angle faulting (Parsons & Thompson, 1993), which in turn alters the stress field leading to altered dike orientations. From observations it is clear that tectonism and magmatism are related, however why they are related is still an area of active research with models proposing multiple styles of interaction between tectonic and magmatic features.

Here we use anisotropic P-wave travel-time tomography to investigate local and regional interaction between tectonism and magmatism at Santorini Volcano Greece. We investigate tectonic and magmatic sources of anisotropy, modeling the role of each in our observations. We highlight the relationship between local faults/fractures, regional tectonic features and magmatic features. Our results show how pervasive regional faulting has shaped the Aegean crust around Santorini. These results support the hypothesis that regional scale tectonic processes

dominate the relationship between tectonism and magmatism in extensional volcanic arcs such as the Aegean and that local-scale surface faulting neither controls, nor is controlled by, regional magmatic activity and is rather a product of local stress variations in the upper crust.

3.2 Background

3.2.1 Geologic Background of the Aegean

The Aegean is characterized by extension dominated tectonic structures resulting from Oligocene/Miocene to present slab roll-back of the Hellenic subduction zone (Pichon & Angelier, 1979), westward extrusion of Anatolia (McKenzie, 1972), and gravitational collapse of continental crust (McKenzie, 1972). These structures weakened the crust, localizing deformation (Jolivet et al., 2013, and citations therein) and magmatism in the Cyclades (Kokkalas & Aydin, 2013) (Figure 3.1).

Extensional detachments and NNE-trending strike-slip faults controlled Aegean pluton emplacement during the middle Miocene (Kokkalas & Aydin, 2013). In many cases, this pluton emplacement was associated with structural complexities that enhanced local permeability. This regional pluton emplacement, which occurred along zones of contemporaneous deformation, arrested in the late Pliocene when internal deformation of the Cycladic region ceased. Santorini lies at the margin of this non-deforming region (e.g. Le Pichon & Kreemer, 2010).

Around Santorini during the Miocene to Pliocene, N-S extension created E-W-striking normal faults (Anastasakis & Piper, 2005; Piper et al., 2007). Activity on the main bounding faults of the basin ceased 1 Ma during the Pleistocene (Piper & Perissoratis, 2003) but some regional tectonic activity continues to present day as evidenced by small-offset faults (Tsampouraki-Kraounaki & Sakellariou,

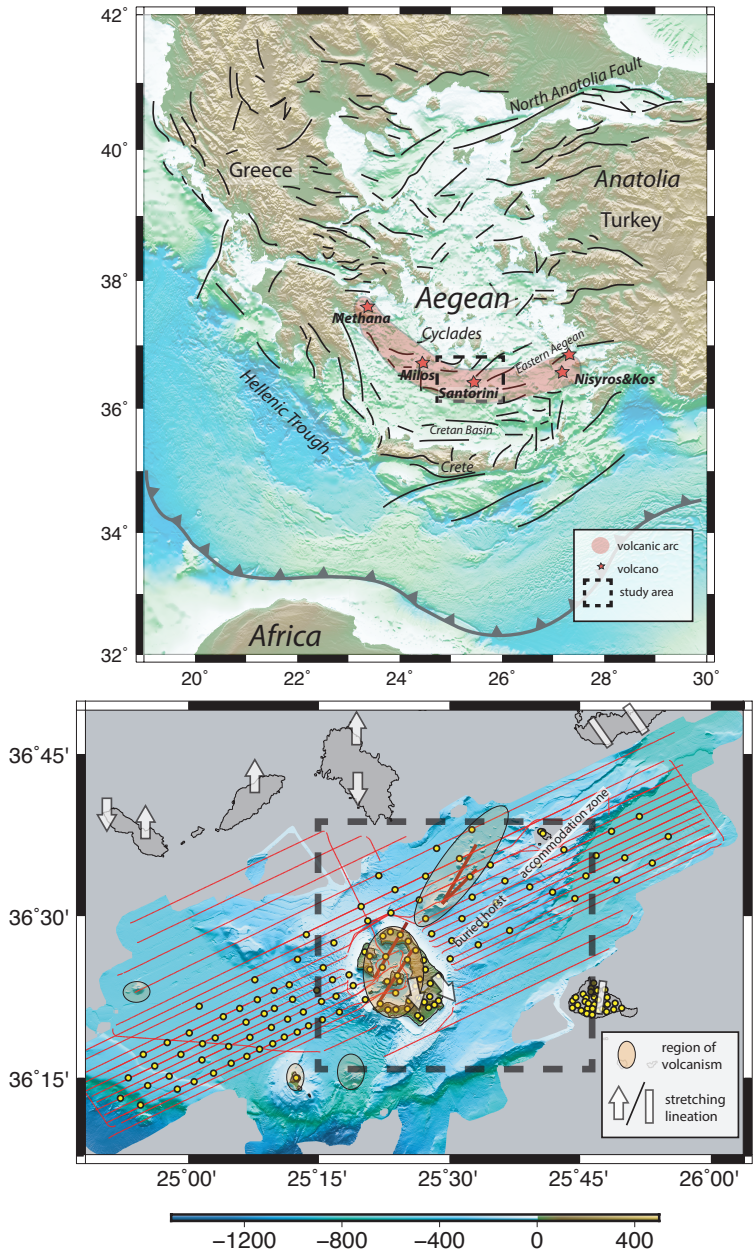

Figure 3.1. a) Regional map of the Aegean showing the Hellenic subduction zone, Hellenic volcanic arc, as well as the Santorini study area, from Heath et al. (2019). Bold black lines represent regional faults. b) Topographic/bathymetric map showing the experiment geometry, shot locations (red dots) and seismic stations(yellow). Orange shaded regions mark regions of magmatism. White shaded arrows and lines represent stretching lineations recorded in metamorphic rocks from prior episodes of deformation (after Schneider et al. (2018). Red lines mark tectono-magmatic lineaments.

2018). These E-W striking normal faults are to first order unassociated with magmatism.

In the late Pliocene or early Pleistocene, the regional stress direction rotated resulting in NE-SW trending faults (e.g. Hübscher et al., 2015; Nomikou et al., 2016) forming a regional basin largely located on the eastern side of the experiment, within which volcanism is focused (Heath et al., 2019). It is thought that this volcanism in the region began only after stress direction rotation and subsequent basin formation (Perissoratis, 1995; Piper et al., 2007).

3.2.2 Regional Volcanism and its Relation to Tectonics

The regional volcanic centers of Christiana, Santorini, and Kolumbo are aligned in a NE-SW orientation, within an elongate NE-SW trending basin (Heath et al., 2019), following approximate regional stresses. Initial volcanism was sourced at Christiana, active during the late Pliocene (Piper et al., 2007), which is situated near the intersection of older E-W and younger NE-SW striking faults SW of Santorini (Heath et al., 2019; Piper et al., 2007). Early Santorini volcanic centers, occurring 0.6 Ma near the SW edge of Santorini (Piper et al., 2007), are located near a NE-SW trending fault that divides the island into two halves.

Volcanism then migrated NE into the present day Santorini caldera. This caldera-centered Santorini volcanism has a clear tectonic control. Santorini's edifice, which is thought to lie on a NE-SW oriented fracture network (Budetta et al., 1984), is dominated by a NE-SW fault striking through the island composed of the elevated footwall as well as a hanging wall whose surface expression is covered by volcanic deposits. Nearly all of the known eruptive vents at Santorini are located within the hanging wall portion of the fault zone. Explosive volcanism at Santorini,

which started 360 ka, records this hanging wall as basement lithics observed in erupted ignmibrites (Druitt, 2014).

At least 4 major caldera-forming eruptions that have occurred at Santorini were sourced within this hanging wall (Druitt, 2014). The most recent eruption, the 30-86 km^3 (dense rock equivalent) Late Bronze Age (LBA) Minoan eruption, occurred only 3.4 ka (Druitt, 2014; Friedrich, 2006; Johnston et al., 2014, and citations therein). The majority of vents for these eruptions were further localized to be within two distinct NE-SW trending tectono-magmatic lines, the Kameni an Kolumbo lines (Heath et al., 2019; Hooft et al., 2019). Historically, the Kameni line has been the more active of the two tectono-magmatic lineaments. This lineament, commonly defined by a NE-SW-trending linear arrangement of post-LBA vents in the center of the caldera (Nomikou et al., 2014; Pyle & Elliott, 2006) results from either a deep-seated fault focusing magmatism, a caldera ring fault, or a region of diking (Konstantinou et al., 2013; Newman et al., 2012; Papadimitriou et al., 2015; Saltogianni et al., 2014; Tassi et al., 2013) and has survived multiple caldera forming eruptions. The Kolumbo line, the other NE-SW lineament, is located north of the Kameni line (see Figure 3.1) and is recorded as a linear alignment of older volcanic centers in the NE caldera that strikes toward the Kolumbo volcanic chain NE of Santorini (Heath et al., 2019; Heiken & Mccoy, 1984; Pfeiffer, 2001). This line is thought to have focused one of the large eruptive phases of the LBA eruption (Pfeiffer, 2001). Collectively, these two tectono-magmatic lineaments also bound i.) a region of NE-SW diking in the caldera (Browning et al., 2015; Fabbro et al., 2013; Heath et al., 2019), ii.) a region of isolated caldera collapse (Hooft et al., 2019), and iii) a deeper magma NE-SW elongate magma body (McVey et al., 2019).

The most NE of the regional volcanics is the Kolumbo volcanic chain, a NE-striking alignment of submarine seamounts (e.g. Hooft et al., 2017; Nomikou

et al., 2012, 2013), the largest of which is Kolumbo Seamount (Hübscher et al., 2015; Nomikou et al., 2016). This alignment of volcanoes is located within the NE-SW striking Anydros Basin. Volcanism in this region post-dates Anydros Basin formation, however an exact age of initial Kolumbo volcanism is not known but is thought to have first erupted in the late Pleistocene and last erupted 1650 AD (Hübscher et al., 2015). The interaction between magmatism at Santorini and Kolumbo is still debated. Petrologic studies indicate that their respective crustal magmatic systems are not linked (Klaver et al., 2016), though tomography suggests a possible connection occurring along an NE-SW elongate magma body that stretches from Santorini towards Kolumbo (Dimitriadis et al., 2010; McVey et al., 2019) .

The NE-SW strike of regional volcanism, combined with NE-SW striking fault zones, has led other researchers to suggest an interaction between magmatism and tectonic stresses (e.g. Dimitriadis et al., 2009; Feuillet, 2013; Nomikou et al., 2012). This interaction between NE-SW faults and NE-SW striking volcanism spans a variety of scales, from the NE-SW locations of regional volcanic centers down to the NE-SW localization of individual vents and dikes. At other Aegean volcanoes, regional volcanic centers are situated along similar NE-SW trending faults (Nomikou & Papanikolaou, 2011; Papazachos & Panagiotopoulos, 1993).

3.2.3 Current State of Tectonic and Magmatic Activity

Large-scale tectonic activity continues to present day as evidenced by the 1950 M 7 earthquake near the Anydros Ridge, hosting a NE-SW striking focal plane. Microseismic activity associated with NE-SW striking faults (e.g. Bohnhoff et al., 2006; Dimitriadis et al., 2009) is thought to result from extensional to trans-tensional stresses (Hooft et al., 2017; Hübscher et al., 2015; Nomikou et al., 2018,

2016), with a minor component of strike-slip (Sakellariou et al., 2017). This region marks an approximate boundary between the seismically quiet stable Cycladic block and diffuse seismicity observed in the eastern Aegean (Bohnhoff et al., 2006).

Effusive volcanic activity which post-dates the LBA eruption has been centered in the caldera and formed the Kameni islands, which erupted as recently as 1950 (Georgalas, 1953; Pyle & Elliott, 2006). In 2011-2012, Santorini inflated, with a modeled intrusion depth of 4 km in the center of the northern caldera (Newman et al., 2012; Parks et al., 2012, 2015; Saltogianni et al., 2014; Tassi et al., 2013). Associated earthquakes were laterally offset from the intrusion by 2 km, occurred beneath the Kameni islands along the Kameni line (Konstantinou et al., 2013; Newman et al., 2012).

While Santorini is seismically quiet and only exhibits microseismicity associated directly with the 2011-2012 crisis, Kolumbo volcano is seismically active. Microseismicity beneath Kolumbo Volcano is thought to result from interaction between magmatic processes and extension (Dimitriadis et al., 2010). A vertical alignment of earthquakes near Anydros Island may result from migration of fluids and potentially developing volcanism (Bohnhoff et al., 2006).

3.3 Methods

3.3.1 Tomography

Using an expanded version of the travel-time dataset from Heath et al. (2019), we invert travel times for both velocity structure and anisotropy following the method of Toomey et al. (1994) and Dunn et al. (2005). The forward problem of calculating travel times is conducted on a 200 m by 200 m by 200 m slowness grid, following the method of Moser (1991). This grid is sheared to incorporate topography and bathymetry. The inverse problem is defined on a grid with

dimensions of 400 m by 400 m in the horizontal and 200 m in the vertical. Further elaboration on the travel-time technique for this study is present in Heath et al. (2019) and further elaboration on the method is present in Toomey et al. (1994). For the inversion of anisotropy, we follow Dunn et al. (2005) and parameterize anisotropy using the following equation:

$$v\Big[\mathbf{r},\theta\Big] = v_{iso}\Big[\mathbf{r}\Big] * \Bigg(1 + m/2 * cos[2\theta]\Bigg) \tag{3.1}$$

Equation 3.1 defines a surface that is nearly elliptical in shape, where $v_{iso} = [v(\mathbf{r}_{\theta=0}) + v(\mathbf{r}_{\theta=90})]/2$, θ describes the angle between the symmetry axis which is oriented at $\mathbf{r}_{sym}$ and the direction of propagation $\mathbf{r}_{propagation}$, and m describes the magnitude of anisotropy where $m = \Big(v(\mathbf{r}_{\theta=0}) - v(\mathbf{r}_{\theta=90})\Big)$ From equation 3.1 it is clear that $v(\mathbf{r}_{\theta=0}) = v_{iso} + v_{iso} * m/2$ and $v(\mathbf{r}_{\theta=90}) = v_{iso} - v_{iso} * m/2$. Collectively, $v(\mathbf{r}_{\theta=0})$ and $v(\mathbf{r}_{\theta=90})$ describe the fast and slow velocities; whether $\theta = 0$ corresponds to the fast or slow axis depends on the sign of m. Equation 3.1, often described as elliptic anisotropy (after Thomsen, 1986), is valid for describing weakly anisotropic media (e.g. $|v(\mathbf{r}_{\theta=0}) - v(\mathbf{r}_{\theta=90})| \ll v(\mathbf{r}_{iso})$). We invert for parameters that relate to the magnitude and orientation of anisotropy (see Dunn et al. (2005) for a full discussion on the inversion for anisotropy).

In principle, the symmetry axis ($\mathbf{r}_{sym}$) can be oriented in any direction, however for the inverse problem we assume horizontal transverse isotropy (HTI) which requires the symmetry axis to lie in the horizontal plane. Using this HTI assumption in the anisotropic inversion, one can map the orientation and approximate density of subvertical fractures and dikes within the crust and/or the bulk alignment of minerals that have an anisotropic seismic signature.

The tomographic code allows for cases where $v(\mathbf{r}_{\theta=0}) > v(\mathbf{r}_{\theta=90})$ and where $v(\mathbf{r}_{\theta=0}) < v(\mathbf{r}_{\theta=90})$. The former case is where the symmetry axis corresponds to the fast direction such as seismic anisotropy caused by the alignment of olivine (ellipsoid looks like a football) and the latter is where the symmetry axis corresponds to the slow direction such as anisotropy resulting from fractures (ellipsoid looks like a frisbee standing on its side). For an HTI system as defined in equation 3.1, the azimuthal velocities for $v(\mathbf{r})_{m=m_0,\mathbf{r}_{sym}=[x_0,y_0,0]}$ (e.g. former case fast axis symmetry axis for $m_0 > 0$ with symmetry axis oriented at some angle $\tan^{-1} y/x$ in the horizontal plane) and $v(\mathbf{r})_{m=-m_0,\mathbf{r}_{sym}=[-y_0,x_0,0]}$ (e.g. latter, slow symmetry axis case with the horizontal symmetry axis rotated 90° relative to the former case) will produce the exact same azimuthal (horizontal) velocities (e.g. a frisbee on its side can look like a football). It is only through analysis of vertical velocities that we can distinguish between these two cases (e.g., with the correct viewing angle a football will not look like a frisbee). For an active source refraction dataset where waves propagate predominately in the horizontal direction, the vertical velocity is not well constrained and therefore distinguishing the style of anisotropy is largely based on the geologic plausibility of the possible interpretations.

3.3.2 Forward Modeling

We employ two techniques for forward modeling of possible anisotropy scenarios: one based on modeling anisotropy resulting from numerous oriented ellipsoids and one based on modeling anisotropy from a finely layered medium. We assume neither elliptic nor weak anisotropy in the forward modeling of anisotropy using ellipsoidal inclusions, in contrast to the tomographic inversion. This enables

us to test these assumptions in addition to accurately modeling the physics of various anisotropic sources for waves propagating in all directions.

We use GASSDEM from (Kim et al., 2019), which uses a differential effective media technique (Mainprice, 1997) to model anisotropic variations due to ellipsoidal inclusions embedded within a background medium. The background medium can have an arbitrary defined pre-existing anisotropy. Individual ellipsoidal inclusions are iteratively added into a background medium and after the addition of each new inclusion a new effective medium is characterized. These ellipsoidal inclusions are defined by:

$$1 \geq (x_1/a_1)^2 + (x_2/a_2)^2 + (x_3/a_3)^2 \tag{3.2}$$

where x_1, x_2 and x_3 are used to define the orientation of the inclusion and a_1, a_2 and a_3 are used to define the size and shape of the inclusions. These inclusions can be assigned properties to effectively model a variety of geologic scenarios including oriented melt, oriented porosity as well as preferred alignment of minerals. We assume that all inclusions are of the form that $a_1 = a_2$ and $a_1, a_2 > a_3$ (e.g. frisbees), a sufficient condition for modeling dikes and fractures.

From GassDem we can obtain the Christoffel matrix (C_{IJ}) which relates the stress (σ) to the strain (ϵ) through

$$\sigma = C_{IJ}\epsilon \tag{3.3}$$

From symmetry constraints the relationship between the stress σ and strain ϵ can be reduced from 9 by 9 elements to 6 by 6 elements (in practice further symmetry constraints reduce the number of independent elements to 5) . From equation 3.3, we can obtain $v(\mathbf{r}, \theta)$. We can then obtain v_{iso}, m and $\mathbf{r}_{sym}$ by assuming a weak anisotropy.

We also employ a technique used to model finely layered media composed of two distinct solids, where fine is defined such that the layer thickness is much smaller than the seismic wavelength. Following Backus (1962), we can define C_{IJ} such that it is only a function of the Lamé parameters of the two components, yielding $C_{IJ} = C_{IJ}(\lambda_1, \mu_1, \lambda_2, \mu_2)$, a transversely isotropic solid of the form:

$$C(\lambda_1, \mu_1, \lambda_2, \mu_2) = \begin{bmatrix} C_{11} & C_{11} - 2C_{66} & C_{13} & 0 & 0 & 0 \\ C_{11} - 2C_{66} & C_{11} & C_{13} & 0 & 0 & 0 \\ C_{13} & C_{13} & C_{33} & 0 & 0 & 0 \\ 0 & 0 & 0 & C_{44} & 0 & 0 \\ 0 & 0 & 0 & 0 & C_{44} & 0 \\ 0 & 0 & 0 & 0 & 0 & C_{66} \end{bmatrix}$$

For transverse isotropy, analytic solutions are known that describe $v(\theta_{propagation})$ as:

$$v = \Big(0.5\Big(C_{33} + C_{44} + (C_{11} - C_{33})sin(\theta)^2 + D\Big)/\bar{\rho}\Big)^{0.5} \tag{3.4}$$

where

$$D = (C_{33} - C_{44})^2 + 2sin^2(\theta)\Big(2(C_{13} + C_{44})^2 - (C_{33} - C_{44})(C_{11} + C_{33} - 2C_{44})\Big) + \Big((C_{11} + C_{33} - 2C_{44})^2 - 4(C_{13} + C_{44})^2\Big)sin^4(\theta) \tag{3.5}$$

and $\bar{\rho}$ is the mean density.

We use these equations to model the effect of vertical intrusions (dikes) in a homogenous medium.

3.4 Results

3.4.1 Tomographic Results

The dataset consists of over 200,000 P wave picks for >14,000 active source shots as recorded on over 150 seismic stations. These picks are recorded on 50 land stations located on the islands of Thera, Therasia, Anafi, and the Kameni islands, as well as 90 ocean bottom seismometers located regionally around Santorini volcano. Several land stations were also located on the islands of Anydros and Christiana but were not included in this inversion. Further information on picking strategies is included in Heath et al. (2019). This dataset is different from Heath et al. (2019) in that it includes picks from Anafi as well as a greater number of picks from OBS instruments, specifically focused around the caldera.

We investigate the travel-time residuals from the isotropic model of Heath et al. (2019), looking for an anisotropic signal that is not fit by the isotropic inversion (Figure 3.2). Here we bin the travel time residuals in azimuthal bins and subset based on ray turning depth as well as location of shots. These residuals, $t_{observed} - t_{predicted}$, show a clear $cos(2\theta)$ pattern indicating the presence of seismic anisotropy. This distribution of residuals is similar to those expected from equation 3.1 when $|m/v_{iso}| \ll 1$, and indicate the presence of weak HTI symmetry anisotropy.

From Figure 3.2, we see that the distribution of residuals on either side of the experiment is different, mostly in orientation but also in magnitude. The fast axis orientation (minimum in residual) has an orientation of 30° (blue lines) on the east side, and an orientation of 0° on the west side (red lines). The orientation also seems to rotate slightly with depth on both the east and west sides, varying about 30° degrees between orientations measured at the surface and orientations measured at depth. The magnitude of anisotropy for rays turning at shallow depths is larger

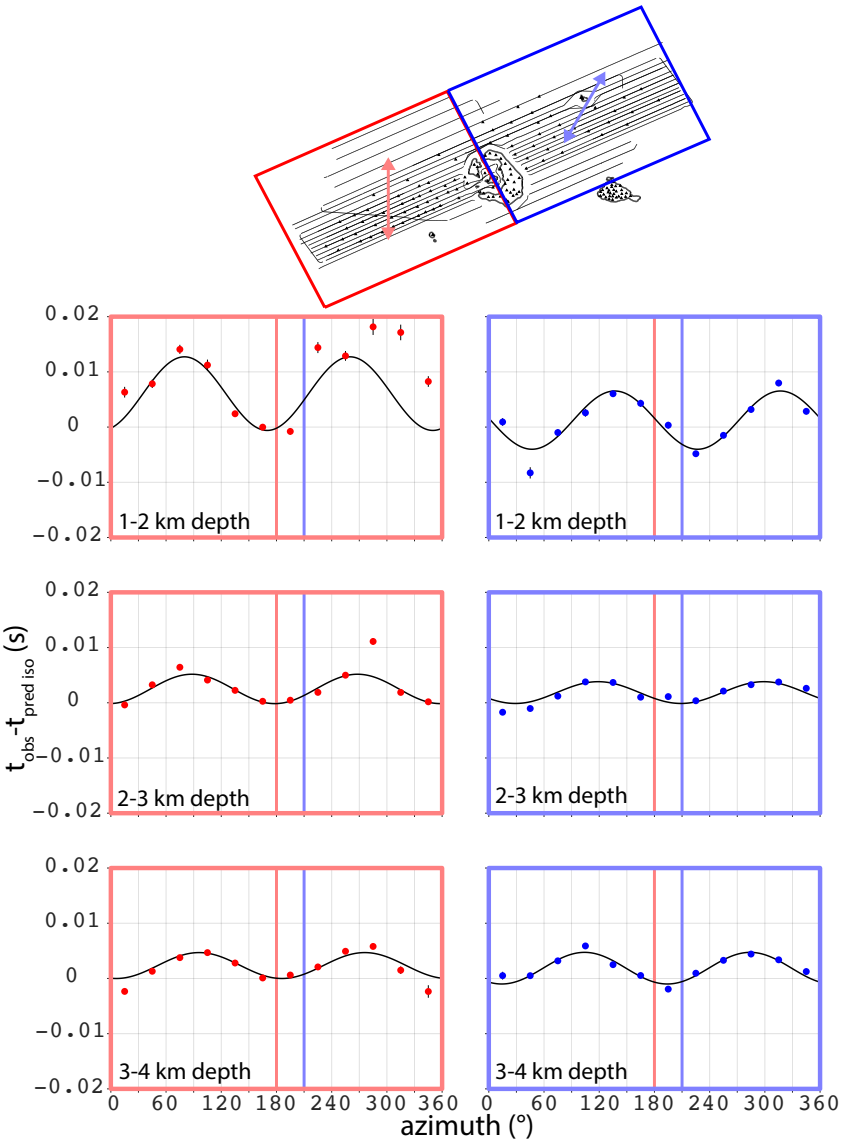

Figure 3.2. a) Overview of experiment geometry showing shot locations (black dots), seismic stations (black triangles) islands (bold black lines) as well as boxes (red/blue) denoting regions of binned travel-times and inferred anisotropy fast direction (arrows). b)Travel-time residuals for an isotropic model binned by azimuth on two sides of the experiment. We only use travel-time residuals for rays traveling entirely in the red box (left hand side) or blue box (right hand side) respectively Depth of each travel-time measurement is selected as the turning depth of the ray associated with each travel-time. Black lines represent a best fit anisotropy (e.g. $\cos(2\theta)$ signature). Vertical red and blue lines represent the approximate respective fast directions for the western and eastern sides of the experiment. These directions are recorded as the arrows in the top plot.

than that for rays turning at deeper depths, showing that anisotropy magnitude is likely to decrease with depth.

To resolve this anisotropic signature, we performed anisotropic travel-time tomography inversions. For the inversions, we smoothed perturbations to model parameters (smoothing parameters of 200 and 100), penalizing both anisotropic and isotropic perturbations to the velocity model (see Arnoux et al. (2019) for further elaboration on this method). Isotropic perturbations compared well with those from Heath et al. (2019), showing the same regional features and structures. Below we investigate the spatial variability in the magnitude of anisotropy and the orientation of anisotropy.

Regional resolution of anisotropy is assessed by looking at the number of rays in a given area and the azimuthal distribution of those rays (see Appendix for further details). Regions that exhibit a large azimuthal gap in coverage or have an insufficient number of total rays are characterized as having a poor resolution and hence anisotropy results from these areas are not further discussed. Checkerboard tests with 90° variation in anisotropy magnitude suggest excellent regional resolution (Appendix material), although they a priori assume an HTI, weakly anisotropic medium.

Anisotropy magnitude slightly decreases with depth transitioning from 7% to 5% over 3 km depth (Figure 3.4). Differences in anisotropy magnitude are observed on either side of the experiment, correlating with differences in tectonic activity (Figure 3.4). The west side of the experiment is largely characterized by fast axis oriented at 0 degrees and the east side of the experiment is characterized by a fast axis oriented at 30 degrees, consistent with the azimuthal distribution of residuals observed in Figure 3.2. Average anisotropy magnitudes are larger

at shallow 0-2 km depth on the Santorini-Amorgos region as compared to the Christiana region (Figure 3.4).

Figure 3.3 shows the recovery of seismic anisotropy over the region from the anisotropic tomographic inversion, where the black lines point in the direction of the fast axis of anisotropy. Here we focus on the eastern side of the experiment. Regionally on the eastern side of the experiment we find that the local orientation of anisotropy is approximately parallel to the orientation of regional faults. This is true even on the Anydros Ridge where changes in fast-axis orientation correlate with changes local fault orientation (Figure 3.3).

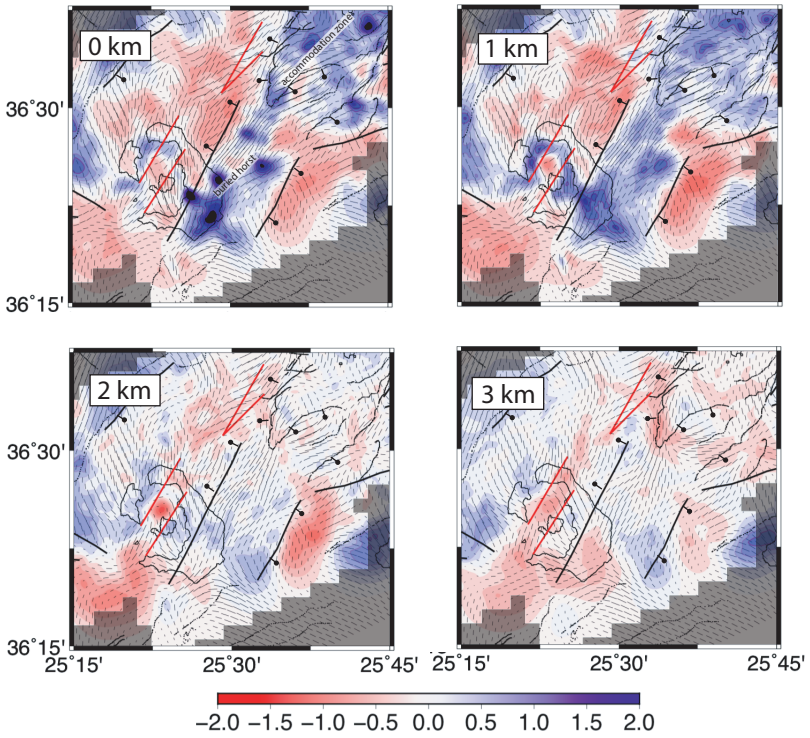

Figure 3.3. Plot showing isotropic velocity variation and associated anisotropy fast direction for 0,1,2, and 3 km depth. The size of the anisotropy bars is directly proportional to the magnitude of anisotropy. Black lines and red lines show tectonic and magamatic features respectively.

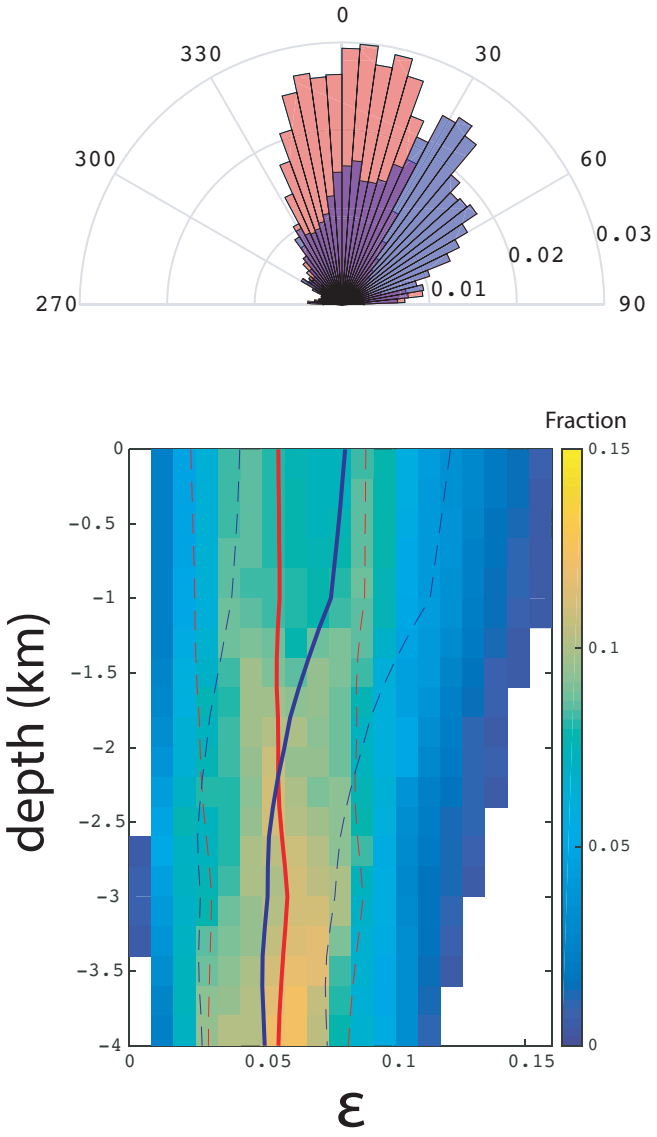

Figure 3.4. a) Rose plot showing the fractional distribution of azimuthal fast direction of anisotropy on the western side of the experiment (red) and the eastern side of the experiment (blue). b) Anisotropy (ϵ) as a function of depth. Red and blue represent the average anisotropy on the western and eastern sides of the experiment respectively, with associated standard deviations shown by dashed line. Background colors represent a fractional probability density function for recovery of a given value of anisotropy for each depth.

Structurally, the deep basins such as the Amorgos basin exhibit less HTI anisotropy than surrounding regions (Figure 3.3). The basins are largely filled with layers of sediments which should produce a transversely isotropic signature

with the symmetry axis pointing in the vertical direction (VTI system). These VTI systems produce no azimuthal velocity variation. The VTI anisotropic signature is unlikely to be resolved using our refraction dataset, where most energy propagates in the horizontal direction. It is expected that basins should exhibit no HTI anisotropy, and should produce a VTI anisotropy signal; the former is consistent with the results from this experiment and the latter expected based on geologic consideration.

The Anydros Basin, which hosts Kolumbo Volcano and other volcanic features, does exhibit seismic anisotropy. The anisotropic alignment is predominately parallel to the alignment of dikes in the caldera wall as well as the alignment of cones associated with the Kolumbo volcanic complex and the alignment of regional faults.

At 0 and -1 km depth, the metamorphic blocks bounding the basins, especially regions that are extensively faulted such as the horst near Santorini show the highest magnitudes of anisotropy (Figure 3.5). Here the anisotropy direction is almost exactly parallel to the fault zone. Seismic reflection experiments show extensive faults which are buried beneath sediments (Hübscher et al., 2015; Nomikou et al., 2016). At deeper -2 and -3 km depths, the anisotropy magnitude tends towards more uniform values across the area, indicating that neither magmatic features such as eruptive centers nor tectonic features such as horsts/basins are localizing small-scale aligned anisotropic fractures/faults. We highlight that the orientation of anisotropy however does parallel both known faults/fractures as well as volcanic features.

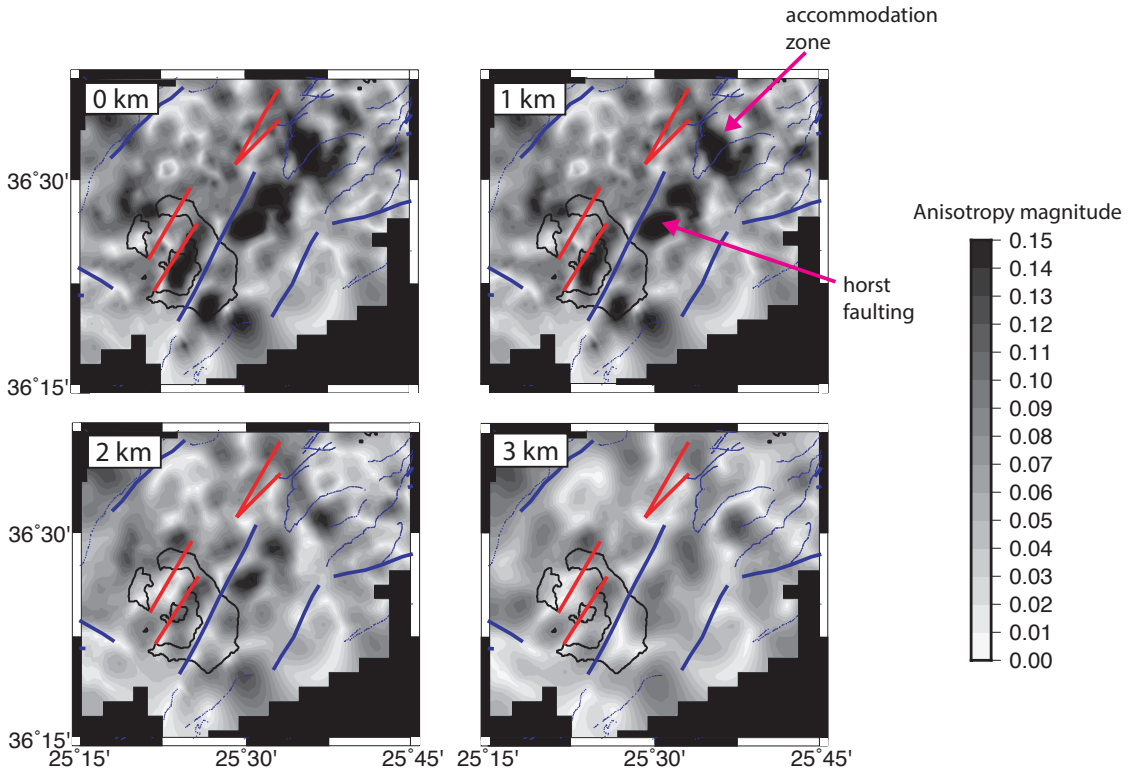

Figure 3.5. Recovered anisotropy magnitude from anisotropic travel-time P-wave tomography across the eastern portion of the experiment at 0,1,2 and 3 km depth. Red and blue lines after Figure 3.3

3.4.2 Forward Modeling Anisotropy Results

We model the anisotropy and seismic velocity from a series of dikes oriented vertically that extend to the surface, assuming their thickness is much less than the seismic wavelength. These dikes, which are assigned a constant velocity of $v_p = 6\,km/s$ with a v_p/v_s ratio of 1.7 and a density ρ from the Nafe-Drake equation (Brocher, 2005), are embedded at some fraction ϕ in the crust. The crust has a velocity profile where seismic velocity increases with depth, shown in Figure 3.6.

These modeling efforts show two interesting features: 1.) At a constant dike volume fraction throughout the crust, dike-induced anisotropy is greatest at shallow depths and 2.) Anisotropy increases with increased dike volume fraction.

We investigate these observations by varying background medium properties as well as fraction of dikes.

Variations in velocities of the background medium effect both the recovered mean velocity and recovered anisotropy (Figure 3.6). For background media that are similar in bulk physical properties to the dike (e.g., dikes deeper in the crust), low anisotropies and low deviations in mean velocity are recovered. In contrast, for background media substantially different from the dikes (e.g., dikes in the shallow crust), we see both a strong anisotropic and a strong mean velocity effect. The overall sign of the deviation in mean velocity is dependent on the sign of the velocity difference between dike and medium, where areas with dikes that are seismically faster than the background medium characterized by a positive mean velocity deviation.

These results, when combined, show that dikes in the seismically slow, shallow crust have a large characteristic positive velocity signature and are dominated by large anisotropy percentages. In contrast, at deeper 4 km depths, where the background velocity is approximately that of the dikes, the dikes have neither a characteristic seismic signature in the mean velocity nor in anisotropy. Solidified dikes extending at some constant volume fraction from the mid-crust to the surface would therefore have a prominent seismic signature for both $+dv_p$ and $+\epsilon$ in the shallow upper crust where the background seismic velocity is much less than that of the dike, and would have a weaker signature at 4 km depths where the dike structure is more representative of the background velocity structure and would have a $-dv_p$ and $+\epsilon$ signature deeper in the crust if the crust is seismically faster than the dike.

We also investigate the effect of fractures on recovered seismic velocity and anisotropy by assuming oriented water-filled penny-shaped cracks (frisbees) where

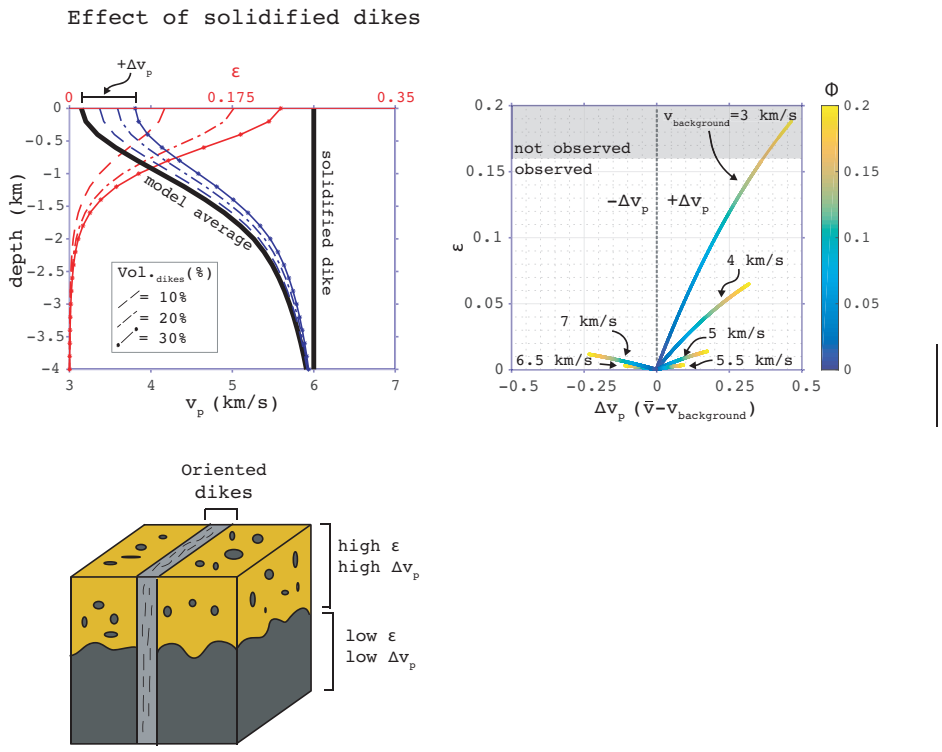

Figure 3.6. a) Effect of inducing a certain fraction of vertical, aligned, solidified dikes within the model. Here we assume dikes are vertically oriented within the crust, have velocity properties defined by the black line labeled "solidified dike" and are introduced into a backgound medium labeled "model average". Introducing aligned dikes induces anisotropy and induces a net shift in bulk azimuthal velocity. b) Effect of imposing dikes at some fraction ϕ within a crust defined by a constant seismic velocity. Here we investigate the deviation in average azimuthal velocity ($\bar{v}$) from the background velocity as well as the anisotropy ϵ. The larger the velocity contrast between dike and background, the greater the induced anisotropy and change in the bulk velocity. c) Conceptual model showing that dikes intruding shallow basin structures induce strong anisotropy and strong velocity signature and dikes intruding basement induce weak anisotropy and have a weak velocity signature.

$a_1 = a_2$ and $a_3 < a_1$. In Figure 3.7, mean recovered velocity and anisotropies are plotted as a function of different volume fractions for different crack aspect ratios where the background medium is fixed at 6 km/s and the cracks are assumed to be water filled with a velocity of 1.52 km/s. We find that, holding aspect ratio constant ($\alpha = a_3/a_1 = constant$), mean velocity decreases with increasing fracture

volume (in this scenario, the inclusion is seismically slower than background medium). For aspect ratios $\mathcal{O}(10^{-1}$ to $10^{0})$, the decrease in velocity with increasing volume fraction is approximately linear. For aspect ratio $\mathcal{O}(\leq 10^{-1})$, the rate of decrease in velocity is greatest for small volume fractions, and overall the decrease in velocity at a given volume fraction is greater than for larger aspect ratio cracks. Similarly, anisotropy values are lowest for $\mathcal{O}(10^{0})$ cracks which are approximately linearly related to inclusion volume fraction. For aspect ratio $\mathcal{O}(\leq 10^{1})$, the anisotropy values are high, increasing rapidly at small volume fractions, and quickly exceed the tomographically recovered anisotropy values.

Figure 3.7 shows where different aspect ratios fall in a mean velocity vs. anisotropy magnitude space, the space informed by anisotropic travel time tomography. For low volume fractions, aspect ratios $\mathcal{O}(\leq 10^{-1})$ all plot in the same area, suggesting that uniquely resolving such cracks at small volume fractions is not possible without additional parameters. This overlap in the same area in Figure 3.7c is still consistent with separation of different α as a function of volume fraction ϕ (Figure 3.7a-b), as Figure 3.7c is showing that $\bar{v}_{\alpha=\alpha_1}(\phi_1) \approx \bar{v}_{\alpha=\alpha_2}(\phi_2)$ and $\epsilon_{\alpha=\alpha_1}(\phi_1) \approx \epsilon_{\alpha=\alpha_2}(\phi_2)$. Aspect ratio $\mathcal{O}(10^{0})$ cracks fall in different areas in this plot, signifying that we can uniquely resolve these features from our seismic tomography results if only one set of faults/fractures is present. In Figure 3.7d we show a histogram of absolute dv ($v_{observed} - v_{unaltered}$)and anisotropy in a region defining a faulted area. We see that overall, this region is characterized by largely below average seismic velocities. In addition, negative excursions in dv are in general associated with higher anisotropy values, as would be predicted for velocity decrease due to consistent orientation of fractures. It is unclear what the aspect ratio of these potential fractures is, however, as the bulk of the anisotropy dv

values fall in the region of unresolvability where multiple different aspect ratios (at different fractions) are able to produce the same observations.

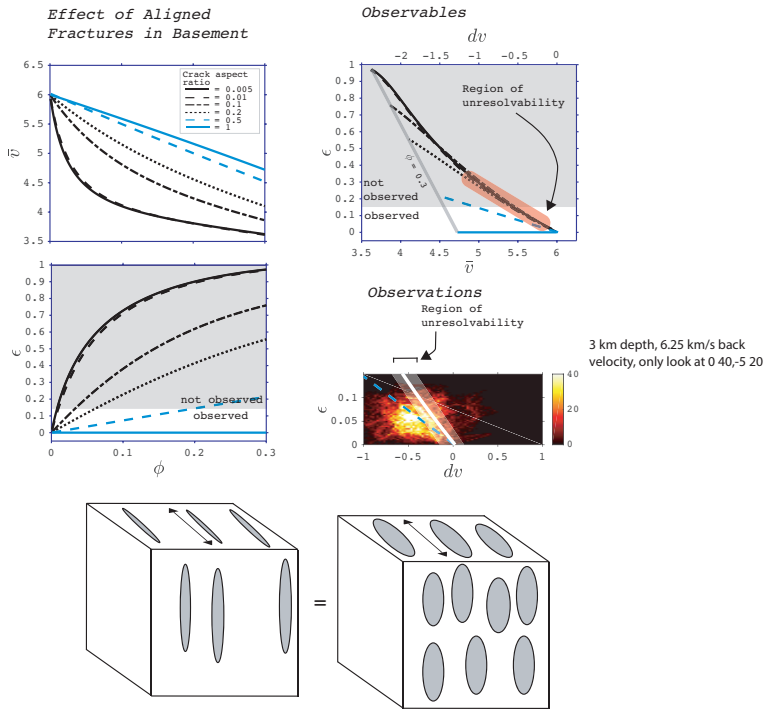

Figure 3.7. a-b) Plots showing average azimuthal velocity as well as anisotropy for different fractions of ellipsoidal inclusions of various aspect ratios. Anisotropy magnitudes greater than 0.16 were not observed. c) Plot of magnitude of azimuthal anisotropy as function of mean azimuthal velocity shows that several aspect ratios sample the same observable space, marked as region of unresolvability. dv is marked as the difference between $\bar{v}_{\phi=0}$ and $\bar{v}_{\phi}$. Probability of dv (change in velocity) and anisotropy (ϵ) for an area on the eastern side of the experiment show high azimuthal anisotropy values associated with lower velocities, as would be predicted by fracture-induced anisotropy in basement.

We investigate the role of dipping cracks on the measure of azimuthal anisotropy (Figure 3.8). Synthetic tests reveal that the tomography experiment is largely insensitive to the vertical velocity and is most sensitive to azimuthal variations in velocity. We find that the recovered mean velocity ($\bar{v}$) and the recovered anisotropy (ϵ) from dipping faults/fractures are largely invariant for steeply dipping faults/fractures and small volumes fractions, but the effects

are non-negligible for shallower dipping faults/fractures, where the measured azimuthal anisotropy would tend towards zero. Similar to aspect ratios, a region of unresolvability exists for steeply dipping faults when plotted in the $\bar{v} - \epsilon$ space. Here faults with steep dips ranging from 45° to 90° span similar ranges of $\bar{v}$ and ϵ over the range of observed ϵ. In contrast, shallow dipping faults $<45^o$ extend into a space marked by lowered anisotropy values, analogous to the region spanned by higher aspect ratio cracks. Nomikou et al. (2018), using seismic reflection technique, have measured the dip of several of the larger faults. Kolumbo fault dip at 70°, SAF dips at 30-50°. For secondary faults they tend to find dips of 54-81°, however the larger faults have dips of 30°. This suggests that the dip of faults in the region could lead to under-prediction of fracture distribution, especially around the larger shallower dipping faults if the respective dips of associated faults/fractures is neglected.

We investigate the role of a pre-existing metamorphic anisotropic fabric assumed to be hexagonal, on recovered anisotropy magnitude of a fractured medium (Figure 3.9). We find that the overall magnitude of anisotropy is strongly affected at small fracture volume. A metamorphism-induced anisotropy of 0.12 can, for the same fraction of fractures, yield a difference of $>.20$ observed anisotropy depending on whether the fractures parallel the fast-axis of the metamorphic anisotropy (add constructively) or are perpendicular to the metamorphic anisotropy (add destructively). The recovered mean velocity, in contrast drops strongly with increased fracture volume and is largely unaffected by a background anisotropy. By assuming hexagonal symmetry for both the fractures and the metamorphic horst, the combined medium exhibits hexagonal symmetry. More complicated anisotropy symmetries will not necessarily behave as simply. We map the change in anisotropic fast-axis orientation relative to the metamorphic fast-axis for a variety of different

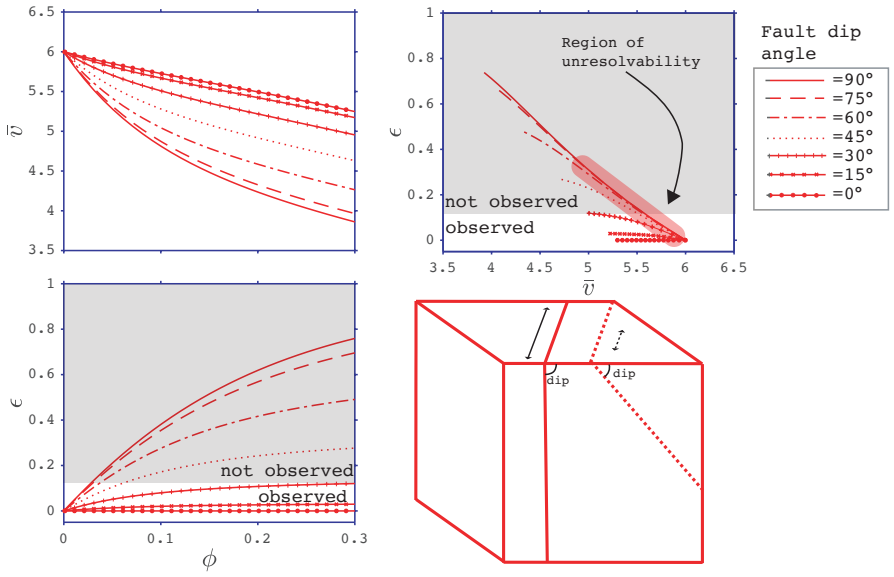

Figure 3.8. Effect of fault dip on faults with aspect ratio 0.1 superimposed in a media. The mean azimuthal velocity and mean azimuthal anisotropy are strongly effected by fault dip, where faults with shallow dip become more azimuthally isotropic. Variations in fault dip from 45-90°, which are observed across the experiment (e.g. Nomikou et al. (2016)) could produce a factor of 2 difference in $\bar{v}$ and ϵ at constant crack fraction and aspect ratio.

fracture orientations. We find that by about 0.05 fraction, the predicted anisotropy has largely assumed the orientation of the fracture. For fractions less than this, the orientation is approximately a linear function between the background orientation and the fracture orientation.

3.5 Discussion

3.5.1 Source of Anisotropy on the eastern side of Santorini

The seismic anisotropy follows the bulk orientation of extensional tectonic structures which are approximately perpendicular to the inferred extension direction. Such favorable orientation to current extensional structures is indicative

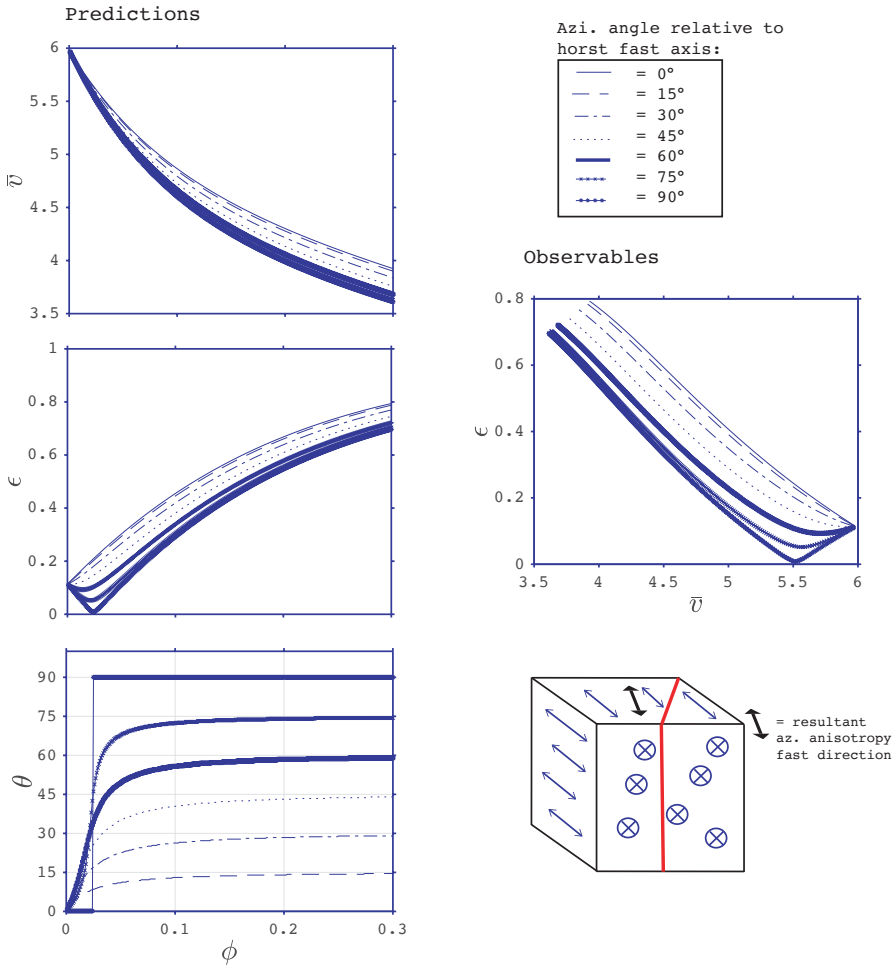

Figure 3.9. a-c) Plot of predicted azimuthal velocity, predicted magnitude of azimuthal anisotropy and predicted fast direction angle for an azimuthally anisotropic medium with aspect ratio 0.1 cracks introduced, as a function of crack fraction. Unfractured anisotropy of the metamorphic horst is 0.15, assumed to be an horizontal transverse isotropic medium with a azimuthal fast axis oriented at 0 degrees. As crack fraction increases, the bulk anisotropy takes on the orientation of crack induced anisotropy instead of bulk background anisotropy. Introduction of a small fraction of aligned cracks in an anisotropic media can lead to a local decrease in anisotropy magnitude, depending on the respective orientations of azimuthal fast-axes.

of fracture and/or dike dominated sources of seismic anisotropy. The anisotropy orientation is distinct from inherited metamorphic orientations from prior Oligo-Miocene extension. The metamorphic fabric on rocks outcropping on Santorini is oriented in a N-S direction with foliations dipping to the E (Schneider et al., 2018,

and citations therein) which should both tend to produce N-S oriented anisotropy. These N-S dominated orientations are not observed on this side of the experiment, but do dominate on the western side of the experiment (Figure 3.2).

Below we discuss the relative plausibility of contribution to anisotropy from solidified dikes, molten dikes and fractures. Solidified magmatic features such as dikes may induce seismic anisotropy and are present on the eastern side of the experiment, but they are unlikely the regional source of the bulk anisotropy at deeper depths. At these depths the bulk velocity difference between dike and basement decreases, yielding a decreasing effect of dikes on anisotropy even at large (e.g. >0.2 volume fractions). As a result, solidified dikes located at 3-4 km depth are unlikely to produce anisotropy values >0.02. In contrast, dikes located in basin and in the shallow upper crust (e.g. >2 km) can produce >0.15 fraction anisotropy because of the bulk velocity difference between seismically fast solidified dike and seismically slow basin/upper crust. Therefore, the explanation of solidified dikes as the source of observed anisotropy magnitudes is only plausible at shallow depths. Magmatic features seem to be predominately limited to the Anydros Basin and Santorini, and interpretations involving diking as a source of anisotropy will be limited to these areas.

In contrast to solidified dikes, molten dikes could be a prominent source of anisotropy at deeper depths. In this case, these molten dikes would have similar characteristics to the fractures discussed below. Because molten magmatic features are not thought to be currently prominent at the depth ranges we are investigating (0-3 km depth) and instead are thought to lie deeper (e.g. McVey et al., 2019), we do not discuss this option further.

As a result, we conclude fracturing is the main mechanism for driving anisotropy on the eastern side of Santorini, which is also more seismogenic

than the western side of Santorini (e.g. Bohnhoff et al., 2006), hosting on going deformational episodes. An orientation so strongly controlled by current active deformation highlights the general structural differences between the east and west sides of Santorini, where the eastern side is more tectonically active and has higher microseismic activity. A discussion on the structure of the faults, inherited damage zones as well as the superposition of faulting on an already anisotropic metamorphic horst structure is presented below.

3.5.2 Modeling the fraction of different aspect ratio fractures

To model the fraction of randomly and consistently oriented fractures, we make the following simplifying assumptions. We assume that there are only two types of fractures present, "random" fractures with aspect ratio 1 and vertical fractures with a consistent orientation and aspect ratio of 0.1. The former fractures are meant to encompass any sets of fractures that collectively exhibit no anisotropic signature; the choice of spherical shape (e.g. $\alpha = 1$) was to ensure no net anisotropy and this choice has no other physical basis. The selection of 0.1 aspect ratio cracks represents a plausible thick crack orientation (e.g. Kim et al., 2019); we discuss the effect of different crack aspect ratios below.

After assuming an unaltered velocity and anisotropy of v_{p0} and anisotropy ϵ_0, we can write the following equation:

$$v_p = v_{p0} + \frac{\partial v_p}{\partial \phi_{\alpha=1}}\phi_{\alpha=1} + \frac{\partial v_p}{\partial \phi_{\alpha=0.1}}\phi_{\alpha=0.1} \tag{3.6}$$

$$\epsilon = \epsilon_0 + \frac{\partial \epsilon}{\partial \phi_{\alpha=1}}\phi_{\alpha=1} + \frac{\partial \epsilon}{\partial \phi_{\alpha=0.1}}\phi_{\alpha=0.1} \tag{3.7}$$

The linear superposition of anisotropy magnitudes shown in Equation 3.7 is only valid for consistently oriented structures (e.g. only one orientation). In

our model we are assuming $\epsilon_0 = \frac{\partial \epsilon}{\partial \phi_{\alpha=1}} = 0$, which means that only $\phi_{\alpha=0.1}$ cracks contribute to the observed anisotropy and therefore the assumption is valid. We can then solve for δv_p, defined as $v_p - v_{p0}$ and $\delta\epsilon$, defined as $\epsilon - \epsilon_0$. Substituting in for the partial derivatives these equations can be written as:

$$\begin{bmatrix} \delta v_p \\ \delta \epsilon \end{bmatrix} = \begin{bmatrix} \frac{\partial v_p}{\partial \phi_{\alpha=1}} & \frac{\partial v_p}{\partial \phi_{\alpha=0.1}} \\ \frac{\partial \epsilon}{\partial \phi_{\alpha=1}} & \frac{\partial \epsilon}{\partial \phi_{\alpha=0.1}} \end{bmatrix} \begin{bmatrix} \phi_{\alpha=1} \\ \phi_{\alpha=0.1} \end{bmatrix} \tag{3.8}$$

Using the plots of v_p and ϵ as function of ϕ as calculated in figure 3.7 and the fact that at small fractions the variation in v_p and ϵ is linear with ϕ, we can rewrite the partial derivative matrix in equation 3.8 as:

$$\begin{bmatrix} \frac{\partial v_p}{\partial \phi_{\alpha=1}} & \frac{\partial v_p}{\partial \phi_{\alpha=0.1}} \\ \frac{\partial \epsilon}{\partial \phi_{\alpha=1}} & \frac{\partial \epsilon}{\partial \phi_{\alpha=0.1}} \end{bmatrix} = \begin{bmatrix} -4 & -66 \\ 0 & 16 \end{bmatrix} \tag{3.9}$$

We show the results of this modeling in Figure 3.10, which outlines the lateral variation in fraction of the two sets of fractures across the eastern side of the experiment. Figure 3.10 should be considered in terms of lateral variation in respective fracture fractions and not the relative ratio between the two different aspect ratio fractures. For example, because $\alpha = 0.1$ fractures fall in the region of unresolvability, the selection of $\alpha = 0.01$ fractures instead would yield a similar spatial pattern of fracture distribution, but would require fewer fractures overall due to the stronger effect of these fractures on reducing v_p and increasing ϵ. Therefore, the ratio between random and oriented fractures is influenced by our assumption of crack aspect ratios whereas the lateral variation in fracture fraction only requires the assumption of a laterally uniform aspect ratio.

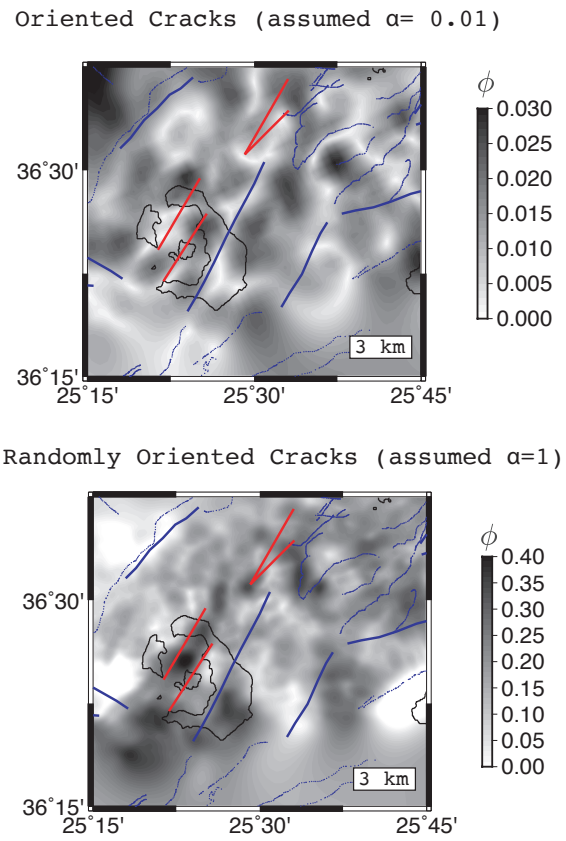

Figure 3.10. Anisotropy fraction for oriented cracks with aspect ratio of $\alpha = 0.01$ and randomly oriented cracks (here assume to have $\alpha = 1$). for 3 km depths These are predicted from observations of dv and ϵ, using equations 3.8 and 3.9. The combination of anisotropy inducing, velocity reducing $\alpha = 0.01$ aspect ratio cracks and velocity reducing randomly oriented cracks can explain all velocity and anisotropy observations, however different choices crack aspect ratio can also explain our observations. While the randomly oriented cracks are of highest fraction in areas near magmatism, anisotropy inducing aligned fractures are not correlated to regions of magmatism.

3.5.3 Magmatism and its relationship to faulting/fracturing around Santorini - Local-scale/Regional Scale Interactions

There is strong geologic evidence for a tectonic control on magmatism around Santorini across a variety of different scales. For example the regional volcanic centers of Christiana, Santorini and Kolumbo are collectively oriented

NE-SW (Nomikou et al., 2012), following the regional stress direction, and are located in a similarly oriented elongate basin-like structure (Heath et al., 2019). The vents that form the Kolumbo volcanic chain to the NE of Santorini also share this NE-SW orientation, forming a line >10 km long. . At local scales, the Kameni line, one of the tectono-magmatic lineaments that has controlled the emplacement and rise of magma throughout Santorini's history, has a NE-SW orientation (Pyle & Elliott, 2006) and represents a fault in the basement (Druitt et al., 1999; Fytikas et al., 1990; Pyle & Elliott, 2006). The Kolumbo line, the other prominent tectono-magmatic lineament that has controlled Santorini magmatism has a similar orientation (Heiken & Mccoy, 1984; Pfeiffer, 2001). A local region of diking in the NE caldera wall bounds these lineaments and overlies the low velocity anomaly, sharing a similar strike (Browning et al., 2015). At depths of 3 km, a >10 km long elongate low velocity trending NE-SW from Santorini towards the Kolumbo volcanic field represents a region of partially molten dikes and increased fractures that is bounded by the Kameni and Kolumbo lines (Heath et al., 2019; McVey et al., 2019). Together, these observations which span a variety of scales support the idea of a strong tectonic control on magmatism.

It is clear and well established in multiple volcanic arcs that regional faulting relates to regional magmatic features. However, it is not clear how local faulting should correlate with magmatic processes. Here we hypothesize possible relationships between local scale faulting and magmatism, make simple predictions these processes would have on the observations of fracture/fault fraction and test these hypotheses against observed magnitudes of oriented and randomly oriented fracture/faults.

If local faulting/fracturing provided a weakness through the crust for magma to rise, one might expect an observation of increased local oriented faults/fractures

in the vicinity of the magmatic system, as these features would enable magma ascent (Hypothesis 1 in Figure 3.11). This would manifest itself as an increase in the fraction of consistently oriented fractures, and likely an increase in randomly oriented fractures that are associated with damage zones as a result of increased fracturing. In contrast, one might assume that substantial regional strain is accommodated by diking. In this case, one would expect a decrease in faulting associated with regions of magmatic activity as magmatism would accommodate the regional strain (Hypothesis 2 in Figure 3.11). This strain accommodation would be observed as a decrease in the density of orientated faults and likely a local decrease in randomly oriented faults (resulting from the necessity of fractures to be oriented to accommodate regional strain) and smaller associated fault/fracture damage zones. Finally, one might assume that local scale faults/fractures do not strongly impact nor are impacted by broad magmatic trends, but that both faults/fractures and vents follow a similar alignment due to a shared dependence on the regional stress state. In this case, one would expect no correlation between oriented fault density and regions of magmatism, but would potentially expect an increase in randomly oriented faults, a result of local stress perturbations associated with magmatism (Hypothesis 3 in Figure 3.11).

From our observations of the fracture fraction for different aspect ratio fractures at 3 km depth (Figure 3.10), it is clear that the magnitude of local-scale oriented faulting on the eastern side of Santorini in general shows no correlation to specific regions of magmatism, even though the faults/fractures share the same strike as magmatic features. This suggests that Hypothesis 3 in Figure 3.11 is accurate. One might expect that Hypothesis 2 (lessened faulting through strain accommodation from diking) is still possible if oriented diking in turn produced its own seismic anisotropy signature that counteracted the decrease in faulting

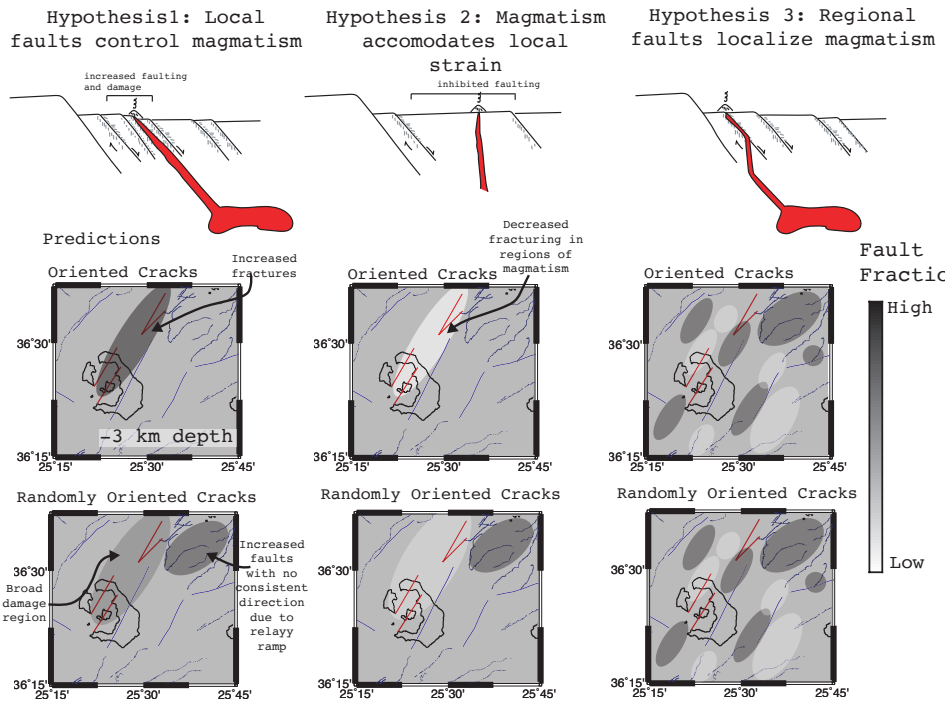

Figure 3.11. Three hypotheses of relationships between tectonism and magmatism. Hypothesis 1 predicts that there should be a strong relationship between increased faulting and magmatism, with increased fault fraction in areas of magmatic activity. Hypothesis 2 predicts that magmatism should accommodate local strain, lessening faulting in areas of magmatic activity. Hypothesis 3 predicts that magmatism is not strongly affected by local faults and is most affected by regional larger-scale faulting features. Here local fault fractions are not correlated to magmatic activity, but local fault orientations and regional scale structures should parallel tectono-magmatic lineaments.

anisotropy. However, synthetic tests show that at -3 km depth the anisotropic signature of dikes compared to anistropy from faulting is virtually negligible (Figures 3.6, 3.7). In addition, from observations of diking in the caldera walls, we calculate that there are too few dikes to accommodate the regional strain. For example, the amount of extension that may have been accommodated by the 50 known NE-SW dikes in the caldera that have an average thickness of 0.7m (Browning et al., 2015) is approximately 35 meters. In contrast, assuming a boundary fault dip of 50 degrees (Nomikou et al., 2016) and a vertical offset of 1 km (Heath et al., 2019), the Anydros basin has accommodated ∼0.8 km

of extension. It is clear that while dikes may be responding to extension and producing their own anisotropic signature, they are not nearly voluminous enough to be a first order influence on regional extension accommodation nor on the observed anisotropy at 3 km depth. We therefore conclude that there is no correlation between the magnitude of local scale oriented faulting and magmatism.

We do record a correlation between the fraction of randomly oriented fractures/faults and magmatism (Figure 3.10). Therefore, the magnitude of local-scale faulting is only correlated to magmatism through chaotic and random fracturing of host-rock near magmatic centers. Whether this is due to random injection of magma, magmatic fluids, hydrothermal systems or gases is beyond the scope of this work; the importance of this observation is only that such randomly oriented fractures are unrelated to regional tectonics. These results are in contrast with Dimitriadis et al. (2009) who found earthquakes near the Kolumbo Volcanic field to be dominantly related to the general tectonic stress field, which should be reflected in our experiment as a correlation between the oriented seismogenic faults and magmatism. These differences can be resolved by noting that earthquakes are sensitive to the current stress regime whereas seismic anisotropy resulting from fracturing is sensitive to the integrated faulting history and hence time-integrated stress regime. Therefore, there can be a seismogenic medium responding to regional tectonic stresses that is also composed of dense, randomly oriented cracks.

There is one exception to the lack of a correlation between oriented local fault magnitude and magmatism, the tectono-magmatic Kameni line. This line, thought to represent a deep seated fracture in the basement, is observed as an increase in the magnitude of NNE-SSW striking faults/fractures at -1 km depth (Figure 3.5). However, at deeper -3km depths, there is a much weaker anisotropic signature associated with this region, suggesting that the anomalous anisotropy

feature is not prominent at deeper depths. It is also curious that the apparent strike of the faults (NNE-SSW) does not parallel the orientation of the inferred Kameni line ($\sim 30^o$).

The regional lack of a correlation between magmatism and oriented local scale fault fraction suggests that such local-scale features do not control the structure of magmatic features at Santorini and also that the magmatic system does not control the structure of local-scale oriented faulting. However, tectonic stresses at some scale clearly play a role in localizing magmatic activity, given the strong association with regional NE-SW oriented fracture network that is seen in the orientation of both local and regional-scale faults, indicating that a shared process must drive both the orientation of local-scale faults and magmatism. Given evidence for large extensional stresses, the correlation between magmatism and tectonics in general, but the lack of a correlation between oriented local-scale fault and magmatism, we conclude that regional-scale tectonic features and stresses must be the dominant control on localization of magmatic activity (Figure 3.12). These results suggest that relationship between tectonism and magmatism reflects an interaction over a regional area and that local kilometer-scale interaction between faulting and magmatism does not dominate the location of either of these two features and is likely of second-order importance. This likely reflects that regional structures and stresses act over a deeper range, decaying at a slower rate than local structures.

3.5.4 Implications for Sources of Faulting and Fault Damage Zones on the Eastern Side of Santorini

Observations of oriented fractures on the eastern side of the experiment suggest that these features are predominately focused at metamorphic horsts

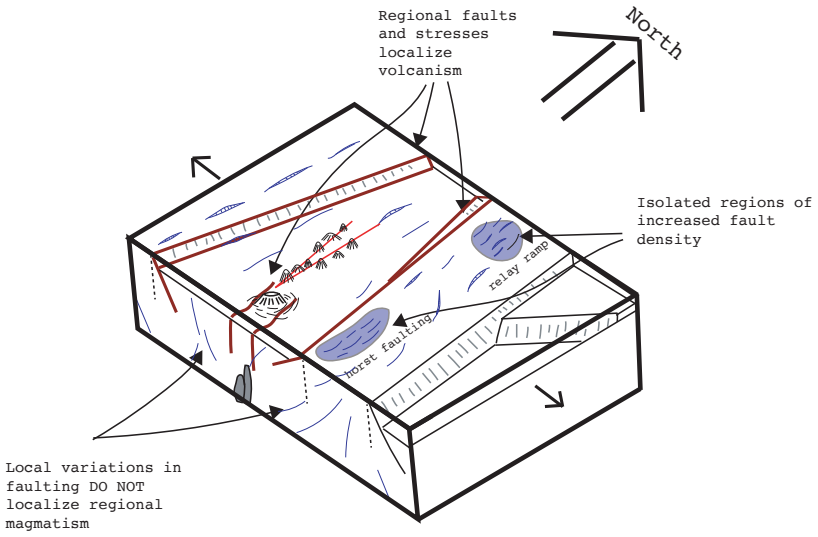

Figure 3.12. Outline of regional results. While increased local fracturing is observed across the study area, it is not correlated with volcanic activity and instead occurs near a accommodation zone and along an extensively faulted portion of the metamorphic horst. All volcanic activity is located in a basin-like structure that and is correlated with regional tectonic activity and regional extension. While local faults might accommodate local magmatism, regional magmatism is most strongly influenced by regional-scale tectonic features and regional extension.

at shallow depths, but are also pervasive at deeper depths (Figure 3.10). To understand this observation, we investigate the effect of faulting and associated damage zones on anisotropy.

Strain from individual faults is often focused along a region only tens of centimeter wide fault core, features that individually are well below seismic resolution. However, hundreds-of-meter-scale zones of lowered seismic velocities are often observed around faults and are thought to represent damage zones near the high strain fault core (e.g. Ben-Zion et al., 2003; Cochran et al., 2009). These damage zones represent the accumulation of micro- and macro-fractures associated with deformation that have a width that is determined by both amount of slip as well as lithology (e.g. Faulkner et al., 2010). As each fault has its own region of

damage, fault zones which consists of multiple individual fault strands collectively have damage zones that span a large region on the order of kilometers (e.g. Savage & Brodsky, 2011). Depending on the overall structure and linearity of the faults, these damage zones may consist of oriented micro-fractures and macro-fractures that are oblique to the fault zones and extend hundreds of meters from the fault core (e.g. Kim et al., 2004). The zones can be located along the fault wall and can take the form of wedges, narrow zones of faulting or asymmetric fault zones (Kim et al., 2004). Additional fracturing may be located at fault tips, due to tensile stresses and/or at relay ramps that relieve stress (Kokkalas & Aydin, 2013).

Due to the consist preferential alignment of fractures and their pervasive nature, these damage zones are likely seismically anisotropic and potentially exert a large influence on the seismic structure of fault zones, potentially inducing anisotropy in orientations oblique to the strike of the main fault. Therefore, the measurement of seismic anisotropy and mean seismic velocity, which collectively inform local scale features, should inform the structure and orientation of the small fractures.

The Santorini-Amorgos fault zone represents an area of pervasive faulting and fault damage. The region is marked by an accommodation zone where the average strike of the faults rotates (Hooft et al., 2017; Nomikou et al., 2016). Accommodation zones are often thought to be associated with local increases in fault density as a result of motion and stress being distributed across a number of different structures. Correspondingly, at shallow depths high anisotropy is observed near Anydros, associated with high fault density, in the middle of this accommodation zone-like structure. Regionally, the accommodation zone area is also associated with higher seismicity, however, locally the areas of highest anisotropy magnitude have not been recently seismogenic.

The strongest anisotropy signature is recorded on the metamorphic horst at shallow 0 and -1 km depths near Santorini and reflects faults oriented parallel to a straight section of fault, a feature that might be expected to have little damage as such portions of the footwall are the least likely to fail after initial graben fault formation and hence should have fewer faults (Melosh & Williams, 1989). Seismic reflection profiles do however confirm the presence of pervasive faulting of the metamorphic horst in this region (termed the Anydros Fault Zone). These faults have varaible dips from 48-82 degrees where some faults break through overlying sediment packages and others arrest within them (Nomikou et al., 2016; Sakellariou et al., 2017). Given the parallel nature of the anisotropy to regional faults, the observed anisotropy may represent the development of wall damage zones associated with normal faults, which can produce en echelon parallel fractures associated with normal fault development (Manighetti et al., 2004). Such features are common features in other tectonic environments (Kim et al., 2004) (Figure 3.12).

Overall, at deeper -2 and -3 km depths, there is little evidence individual that large tectonic features such as horsts, grabens and accomodation zones affect the regional magnitude of anisotropy and fault fraction, although slight decrease in fault fraction occurs near larger regional faults. These results suggest that at depth there is a pervasive and relatively consistent fracture distribution across the eastern side of the experiment. A thorough discussion of this distributed style of deformation and the processes driving it is presented in the following dissertation chapter.

3.5.5 Understanding the Regional Tectonic and Magmatic Interactions

Analogue models show a strong correlation between regional tectonism and magmatism (Corti et al., 2003, and citations therein). Models of extension in horst and graben structures suggest that if rifting is orthogonal to the principle stress direction, then magmatism is focused towards the horst, opposite to the basin centered magmatism observed around Santorini. If in turn there is slightly oblique rifting, such as what one might expect in the transtensional Anydros area (Bohnhoff et al., 2006; Sakellariou et al., 2017), then magmatism can be localized in the graben, leading to the partial inhibition of the development of external normal faults. If there are two episodes of extension consisting of orthogonal rifting followed by to oblique rifting, magmatism is ultimately localized along en echelon faults within the graben. Therefore, the localization of vents within the proto-Anydros basin (e.g. Heath et al., 2019) supports a transtensional tectonic regime localizing magmatism at Santorini. Further support for this argument comes from the relative dips of the Kolumbo and Kameni lines. These features are thought to be subvertical (Newman et al., 2012; Nomikou et al., 2016), a fault feature unlikely to exist in a purely extensional environment. Similar transtension has been found in the Main Ethiopian Rift where graben faults and fractures do not always follow the orientation of extension, a feature attributed to basement anisotropies and/or complicated dynamics associated with transfer zones (Acocella & Korme, 2002). Analogue studies also highlight the impact lateral distribution of magma has on regional deformation. Laterally distributed magma produces faulting along numerous graben shaped structures over the region spanned by magma, whereas small narrow magma bodies localize deformation to magma body boundaries, thereby altering the style of extensional features (Corti et al., 2003). The net result

is a complex interplay between magmatism and tectonics that drives the evolution of the area.

It is possible that the bulk tectonic stress at Santorini has been underpredicted. Studies predicting the location of volcanic vents based on the ratio between tectonic stresses and caldera stresses find vents at Santorini to be disproportionately located within the caldera, a feature they predict may be due to an underestimation in the magnitude of tectonic extension (Rivalta et al., 2019). The parallel orientation of dikes and regional faults also suggest a strong tectonic environment. Dikes in weak tectonic environments often form circumferential and/or radial patterns in close proximity to the volcanic edifice (Acocella & Neri, 2009), such dikes are not dominant features in outcrops around Santorini (Browning et al., 2015).In contrast, Hooft et al. (2019) suggest that a low velocity low density region of chaotic caldera collapse nested within the northern caldera at Santorini may aid the eruption of magma along the margins of this chaotic caldera collapse through the alteration of local stresses within the topographic caldera, favoring the development of radial and circumferential fissures. While strong evidence for a regional effect of this feature is not observed, it is likely that the effect of such a feature would be limited laterally because it is approximately a point a source and that its role in localizing magmatic activity would be dependent on the stage of Santorini magmatism (e.g. whether Santorini was in a dome forming, caldera filling episode or caldera forming, void creating episode) and its effect would therefore vary throughout Santorini's geologic history. It is worth highlighting, however, that this region of isolated collapse is controlled and bounded by the Kameni and Kolumbo tectono-magmatic lineaments (Heath et al., 2019) and so even this feature has a tectono-magmatic connection.

In summary, it is the regional extension and its orientation of faults that focuses the emplacement of magma at Santorini. Local-scale faulting to first order does not control, nor is to controlled by, the emplacement of magma within the shallow crust. Rather both these features are predominately controlled by larger scale tectonic stresses and extensional features. We highlight a qualification to the above conclusions. Seismic anisotropy as a measure of faulting and diking is sensitive only to pervasive structures that are are thinly spaced with respect to the seismic wavelength, but that persist over an area larger than the seismic wavelength. This means that these results do not strongly inform isolated faults/dikes and associated damage that have a width smaller than the seismic wavelength.

3.6 Conclusions

We used anisotropic P-wave travel-time tomography to elucidate local and regional scale tectonic and magmatic structures around Santorini. We find that magmatism is localized in a regional basin, with the strike of regional faults paralleling the strike of regional dikes and regional volcanic chains. We find that local fracture magnitude is not correlated with magmatic activity, while local fracture strike parallels local magmatic system orientation. These results support the conclusion that regional scale tectonic structures and regional scale tectonic extension control the localization of magmatism around Santorini. Such a result between regional tectonism and magmatism is observed at a variety of volcanic arcs. Local variations in local faulting are observed at shallow depths 0 and 1 km depths and result from wall damage as well as increased faulting and fault damage near an accommodation zone, relieving regional stress. At deeper depths 2 and 3

km depths fault magnitude is not correlated to horsts and basins suggesting that faults are pervasive.

3.7 Bridge

In Chapter III, I showed that the regional stresses control magma emplacement, not local-scale fractures. I emphasized that the eastern side of Santorini is regionally characterized by pervasive fracturing. In Chapter IV, I investigate the western side of Santorini, which is thought to record an older tectonic episode unassociated with magmatism. I show localization of faulting within the western basin and compare it to the pervasive distributed faulting currently active on the eastern side of Santorini. I discuss the role of magmatism in altering the thermal state of the crust, changing this style of deformation from localized to distributed faulting.

CHAPTER IV

TECTONISM AND THE INFLUENCE OF INHERITED STRUCTURAL DEFORMATION AROUND SANTORINI FROM P-WAVE TOMOGRAPHY

This chapter is being prepared for future publication. Ben Heath conducted all the inversions, drafted all the figures and wrote the chapter. Joanna Morgan, Michele Paualatto and Emilie Hooft aided interpretations of FWI results. Emilie Hooft provided minor edits on a previous version of the Chapter.

4.1 Introduction

In extensional terrains, the thermal state and strength of the lithosphere are reflected in the style and mode of deformation (Buck, 1991; England, 1983). For example, hot, thickened crust often experiences core complex mode extension where large faults and shear zones accommodate the doming up of the lithosphere. Thinned cold crust, in contrast, often forms narrow rifts where extension is localized in one location. Hot and thin crust forms wide rifts where faulting strengthens the crust favoring the progressive migration of faulting over wide regional areas. These styles of extension then, in turn, impact the thermal state and strength of the lithosphere. How the modes of extension evolve and transition through time and how they are influenced by external processes such as magmatism remains enigmatic.

For extending subduction zones, thinning and cooling of thickened lithosphere as the slab rolls back may favor transitions between modes of extension, where lithosphere initially in a core complex mode may transition to a wide mode after having undergone sufficient extension and crustal thinning. These transitions between modes inform perturbations to the thermal state of the crust as well as changes in crustal thickness. Regions such as the Basin and Range and

Aegean have undergone multiple transitions between these different extensional modes. For example, the Basin and Range has undergone core complex mode of extension with low angle normal faults accommodating upwards of 10s of km of displacement, leading to the exhumation of mid-crustal rocks (Smith & Bruhn, 1984). Subsequent deformation has been distributed across the region forming the pervasive horst and (half-)graben style deformation that gives the Basin and Range its name and distinctive characteristics. The Aegean has also undergone large scale extension, with top to the S and top to the N detachment faults thinning the crust and exhuming ductile metamorphic rocks and their associated fabrics (Jolivet et al., 2013; Lister et al., 1984; Ring et al., 2010). Plate-scale wide rift extension then thinned and cooled the crust. This thinning ultimately led to coherent block formation in the Cyclades, which limited deformation to the block margins, localizing this extension in a more narrow rift style. Regional subduction-driven magmatism has added heat back into the crust, leading to elevated crustal temperatures.

Each tectonic event that acts on the crust leaves an imprint on the crustal structure, often in ways that impact later styles of extension. For example, large thrust faults that juxtapose different terrains may be reactivated under extension (Smith & Bruhn, 1984), nappe stacked structures may localize low angle normal faults (Huet et al., 2011), and steeply dipping tension fractures and faults may rotate, localizing later deformation along shallow dipping features (Angelier & Colletta, 1983). To understand the tectonic history therefore requires an understanding of the state of the crust, processes acting on the lithosphere, how these processes influence the state of the lithosphere, and how the structural state of the lithosphere was influenced by prior episodes of tectonic activity.

Here we use a combination of anisotropic travel-time tomography and full waveform inversion (FWI) to image the subsurface of the Christiana basin near Santorini down to 3 km. This region of the Aegean is characterized by a metamorphic fabric that records prior ductile deformation from the Oligocene-Miocene due to core complex mode extension as well as brittle faulting from the Miocene to present that records extension in both a wide rift style of deformation and narrow rift style of deformation. As a result of the large scale extension, most of the Aegean crust is covered by the Aegean sea, limiting exposures to the outcropping Cycladic islands and therefore limiting structural studies of regional tectonic evolution. By combining the observations on the outcropping Cycladic islands with structural constraints from the seismic imaging technique we are able to better constrain the current overall structure of the basin as well as better relate these structures to prior extensional episodes, which enable building of a coherent model of the evolution of the regional styles of extension.

4.2 Background

The Hellenic subduction zone and associated Aegean plate consists of complicated series of stacked terrains that were thrust upon and accreted to the overriding crust and that have been subsequently extended and thinned for tens of millions of years. Plate scale extension has led to the development of core complexes, low angle normal faults and subsequent exhumation of buried metamorphosed terrains. The current Hellenic Volcanic Arc is situated within in this highly extended region. Because of the exhumation of these metamorphic terrains there is a substantial record of the ductile behavior of the Aegean crust throughout the past 50 Million years. Multiple extensional episodes from approximately the Miocene to present are recorded by brittle faulting and

fracturing of the Aegean upper crust, successively overprinting each other. The regional upper crust therefore records an integrated 50 million-year history of tectonic activity.

Plate-scale extension in the Aegean began in at least the Oligocene-Miocene (Gautier & Brun, 1994; Lister et al., 1984), and potentially earlier in the Eocene-Oligocene (Forster & Lister, 2009; Ring et al., 2010), likely a result of slab roll-back of the subduction zone. There is a general consensus that extension was predominately N-S, however there is substantial disagreement over whether extension had a top to the north sense of shear(e.g. Gautier & Brun, 1994; Huet et al., 2009), bivergent top to the N and top to the S sense of shear (Thomson et al., 2009) or a top to the south sense of shear (Forster & Lister, 2009; Lister et al., 1984). The differences within these models result from different perceptions of the geometry of various faults and detachment surfaces, which have been overprinted by later tectonic episodes.

Top to the N extension is thought to dominate within the northern portion of the Cyclades during the Miocene. Models of top to the N style extension suggest reactivation of prior thrust faults that were developed during nappe stacking orogenesis, leading to the extension within the accreted terrains of the Aegean microplate (Jolivet et al., 2013). In these models, differences in rheological properties of these nappes favored the development of core complexes, highlighting the effect inherited structures may have on regional tectonic evolution (Huet et al., 2011). Such models are unable to explain the development of top to the S senses of shear observed in the southern Cyclades and it is not known in what conditions this top to the S sense of shear would be favored (Jolivet et al., 2013).

The northernmost island that records a top to the S sense of shear is Ios (north of Santorini) which records both N and S senses of shear during the

Oligocene-Miocene (Forster & Lister, 2009; Huet et al., 2009; Lister et al., 1984; Thomson et al., 2009). The surrounding islands around Santorini, including Santorini itself, all record extensional events which suggest a top to the S sense of shear (Schneider et al., 2018; Soukis & Papanikolaou, 2004) (Figure 3.1). This S sense of shear is thought to have dominated the ductile and brittle-ductile crust around Santorini during the Oligocene-Miocene (Forster & Lister, 2009; Lister et al., 1984; Schneider et al., 2018).

In the late Miocene-Pliocene, N-S extension drove the formation of the Christiana basin, creating the oldest of the brittle-dominated tectonic structures observed around Santorini today. This N-S extension is thought to have created E-W trending normal faults within the Christiana basin which can be observed in both seismic reflection profiles of the basin (Piper et al., 2007; Tsampouraki-Kraounaki & Sakellariou, 2018) as well as in seismic tomography results which show old buried tectonic blocks within the Christiana basin (Heath et al., 2019). It is currently debated whether these basement faults are extensional or strike-slip in nature (Heath et al., 2019; Tsampouraki-Kraounaki & Sakellariou, 2018). Later basin enlargement occurred on faults striking more NW-SE (approximately 120°), leading to abandonment and subsequent burial of the narrower basin margins (Tsampouraki-Kraounaki & Sakellariou, 2018). Recent tomographic work suggests that younger, 30° NE-SW striking faults, which are orthogonal to the older faults and are associated with magmatism at Santorini, extend into the Christiana basin leading to further extension of this basin (Heath et al., 2019) While the general structure of the basin is known from seismic reflection and seismic tomography results (e.g. Heath et al., 2019; Perissoratis, 1995; Piper et al., 2007; Tsampouraki-Kraounaki & Sakellariou, 2018), substantial uncertainty exists as to how extension has been accommodated, whether full graben or half-graben behavior dominates

and whether the basin margins are taking advantage of pre-existing weaknesses inherited from prior deformational episodes such as the top to the S sense of ductile shear. Recent tomographic studies suggest that the style of extension that formed the Christiana basin produced more localized faulting than the extension that formed currently active NE-SW striking faults associated with magmatism (Heath et al., 2019). These results suggest therefore a progressive change in ways in which extension is accommodated.

4.3 Methods

We employ two methods to interrogate the role of inherited structures on deformation. The first method, anisotropic travel-time tomography, was outlined in the prior dissertation chapter. This method uses travel-time information to invert for isotropic velocity variation as well as for azimuthal velocity variation, informing orientation and structure of metamorphic lineations, metamorphic foliations, as well as the orientation of folded geologic layers and orientations of local and regional faults (e.g. Brocher & Christensen, 1990; Brownlee et al., 2017; Cao et al., 2013; Dempsey et al., 2011; Okaya et al., 2018). From this, we are able to deduce the metamorphic fabric derived from older ductile deformation as well as the orientation of local scale faults resulting from later brittle deformation. The second method, which we elaborate on here is Full Waveform Inversion (FWI). This method uses aspects of the seismic waveform other than the initial arrival time to image the subsurface, and is here used in a refraction experiment to better image the isotropic structure of tectonic features. FWI is an ideal tool for studying the Christiana basin using a dense active source experiment because it theoretically can image structures down to half the seismic wavelength (Virieux & Operto, 2009; Warner et al., 2013), enabling the imaging of fault blocks and kilometer scale

Table 4.1. Data Processing Steps

Data Parameters	
window length	max(0.7, $TWTT^{*1}_{seafloor}$) s
filter frequency min	3 Hz
filter frequency max	7 Hz

[1] $TWTT^{*} = 2(stationdepth/v_{seawater}) + 0.6$

tectonic features. Currently, this method does not inform the anisotropic structure of the crust. At mid-ocean-ridges, FWI on similar-scale datasets has yielded high resolution images of hydrothermal systems (Arnoux et al., 2017; Morgan et al., 2016) and theoretical studies show possible resolution of upper crustal magmatic systems (Morgan et al., 2013). In the Nankai trough, FWI has been shown to image crustal scale features that show deforming tectonic structures associated with subduction (Górszczyk et al., 2016).

We process the observed data for use in FWI. This processing includes resampling the seismic data from the initial sample interval of 5 ms to 3 ms and filtering the data with a butterworth filter from 3-7 Hz . Because we wish to model primarily the well-constrained first arriving energy we window the observed data around both the first arrival and the later arriving receiver side water-wave reverberation (Figure 4.1). This window is approximately 1s in length, but the exact values is depth dependent. The receiver side reverberation is included because it is usually well recorded, it occurs a relatively short time after the first arrival due the relatively shallow bathymetry ($<$ 500 m in most cases) and would therefore be difficult to exclude, and because it provides additional information on the subsurface structure. Inversions that exclude this reverberation in general show slightly noisier tomographic images due to the shorter available time windows, but show similar first-order structures. The exact parameters used in our inversions are shown in Table 4.1.

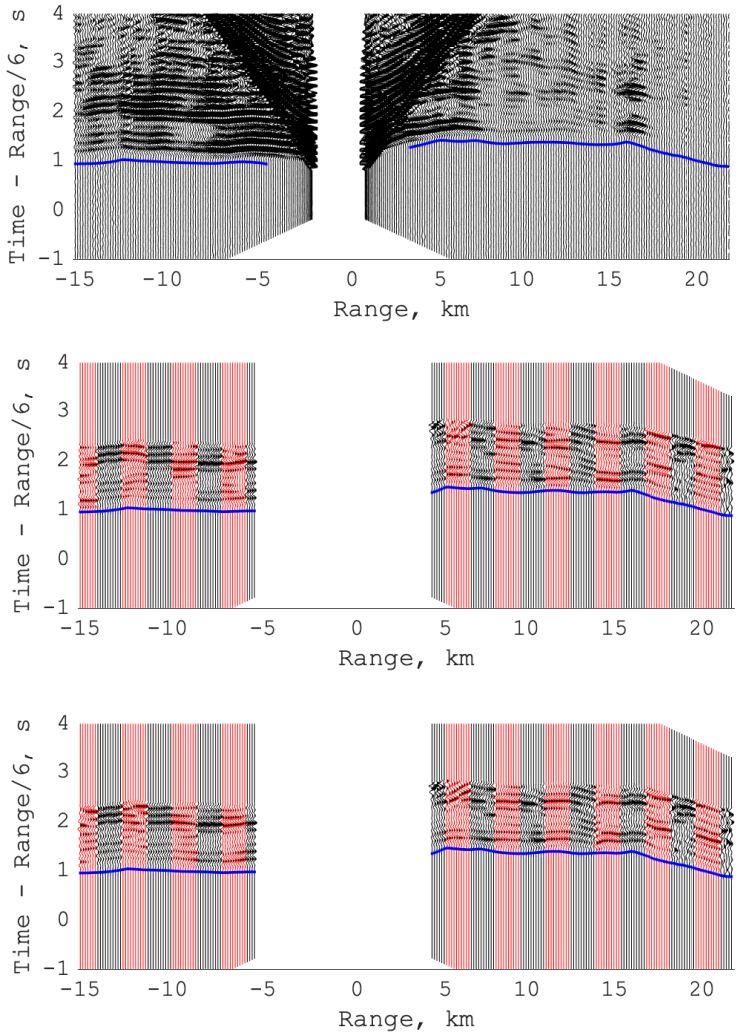

Figure 4.1. Top: Plot of observed data (magnitudes are range normalized) for station 188 line 24. Blue lines indicate predicted first arrivals from our model. Middle and Bottom:Plot of observed seismic waveforms (black) and synthetic seismic waveforms (red) for the starting model (middle) and after 40 iterations (bottom). The updated model (iteration 40) has a better fit to the observed waveforms than the starting model. Data has been windowed, filtered and energy normalized (see text for details). Ranges less than 5 km were excluded to ensure no waterwave contamination and ranges greater than 25 km were excluded due to poor signal to noise.

For the initial velocity grid used in full-waveform inversions we adapt the model of Heath et al. (2019) using a smaller grid (see Table 4.2). To model the acoustic propagation of seismic waveforms (e.g. no shear waves) , a finite difference

Table 4.2. Model Parameters

dx	$50m$
nx	20
dy	$50m$
ny	191
dz	$50m$
nz	121

scheme is employed, using a synthetic source to approximate the air gun array. To accurately model both the water-seabed interface and the station depth, neither of which necessarily falls on a grid node, we vertically resample the model grid at a finer scale placing the seabed at the accurate location, smooth the seabed interface over an area approximately equivalent to two times the preferred grid spacing, and then resample this grid at the initial scale. This method induces artificial velocities at the water-rock interface that are a proportional average of the rock velocity and water velocity, which allows us to approximately match the travel-time to a correctly placed seismic station for both the direct arrival and receiver side reverberation while also limiting erroneous secondary reflections that result from a discretized water-seabed interface that would otherwise be artificially restricted to fall on a grid node.

For the inversion, we model waveforms through the velocity model . The difference between the processed observations and synthetic modeled waveforms is then backpropagated through the model and cross correlated with forward modeled waveforms. This produces gradients that drive perturbations to the initial model (Virieux & Operto, 2009; Warner et al., 2013). An iterative approach, using lower frequencies (longer wavelengths) and then gradually introducing higher frequencies has been show to lessen the likelihood of cycle-skipping. This cycle-skipping results from the gradient trending towards a local minima in waveform misfit reduction instead of the global minima (Virieux & Operto, 2009; Warner et al., 2013) and an

Table 4.3. Inversion Parameters

Frequency(Hz)	Iterations
3.2	20
3.6	20
4.0	20
4.5	20
5.0	20

example of this phenomena can be found in Warner et al. (2013). The number of iterations and frequencies used is show in Table 4.3. This technique is described in Virieux and Operto (2009); Warner et al. (2013) and the model development presented here is described in (Morgan et al., 2016).

Because of variable quality data, we performed substantial quality control measures. The volume of data precluded looking at observations and synthetics on an event by event, or even a line by line basis. To broadly assess data quality we looked at the phase of the observed and synthetic data as well as the phase residual between the two (Figure 4.2). Here, phase is termed to represent the phase of the Fourier transform of gaussian windowed data. Broadly, the phase increases linearly with distance (wrapping around from $-\pi$ to $+\pi$), producing approximately concentric circles. These concentric circles result from an increase in arrival time of the waveforms with increased range. Additional complexity in the phase residuals results from complicated waveform interactions that alter waveform shape and hence alter the phase. By looking at the observations and the phase residual we can identify data of anomalously poor quality by identifying areas of complicated non-concentric phase of observations that are also characterized by large and chaotic phase residuals. By excluding areas based on these criteria, we are excluding data that are both not fit by the synthetics (e.g. high residual) and also likely noisy (chaotic phase residual combined with non-concentric phase of observations). Areas of uniformly high residual are retained as they represent areas

that are not currently fit by the model, but that likely have clean data. After data processing, we find good coverage in the Christiana basin (Figure 4.3).

4.4 Results

4.4.1 Overview of seismic anisotropy results from travel-time tomography

Regional anisotropy patterns show two distinct trends.. The western side of Santorini is characterized regionally by a N-S orientation whereas the eastern side of Santorini is characterized by a NE-SW orientation. This is confirmed both in the residual travel-times from the experiment for an isotropic model (Figure 3.2) as well as the overall structural orientation of anisotropy from tomographic inversions (Figures 3.4 and 4.4).

The NE-SW orientation of anisotropy, discussed in the previous chapter, results from pervasive faulting on the eastern side of Santorini. It is in this tectonically active portion of the experiment that volcanism has been focused. We refer the reader to the previous chapter for an in-depth discussion of seismic anisotropy resulting from faulting and the association between tectonism and magmatism at Santorini.

The predominant N-S anisotropy orientation on the western side of Santorini originates mostly from the metamorphic horsts north of Santorini and follows the approximate orientation of stretching lineations as recorded on Ios and other neighboring islands (Figures 3.1). Regions away from this horst are characterized by anisotropy with different orientations. Within the basement of the Christiana basin, anisotropy tends to follow the approximately NE-SW orientation that characterizes the eastern side of Santorini. The Christiana Ridge, located south of the basin, has an approximately NW-SE orientation, following the approximate orientation of the regional faults in this area. Thus, we find a variable anisotropy

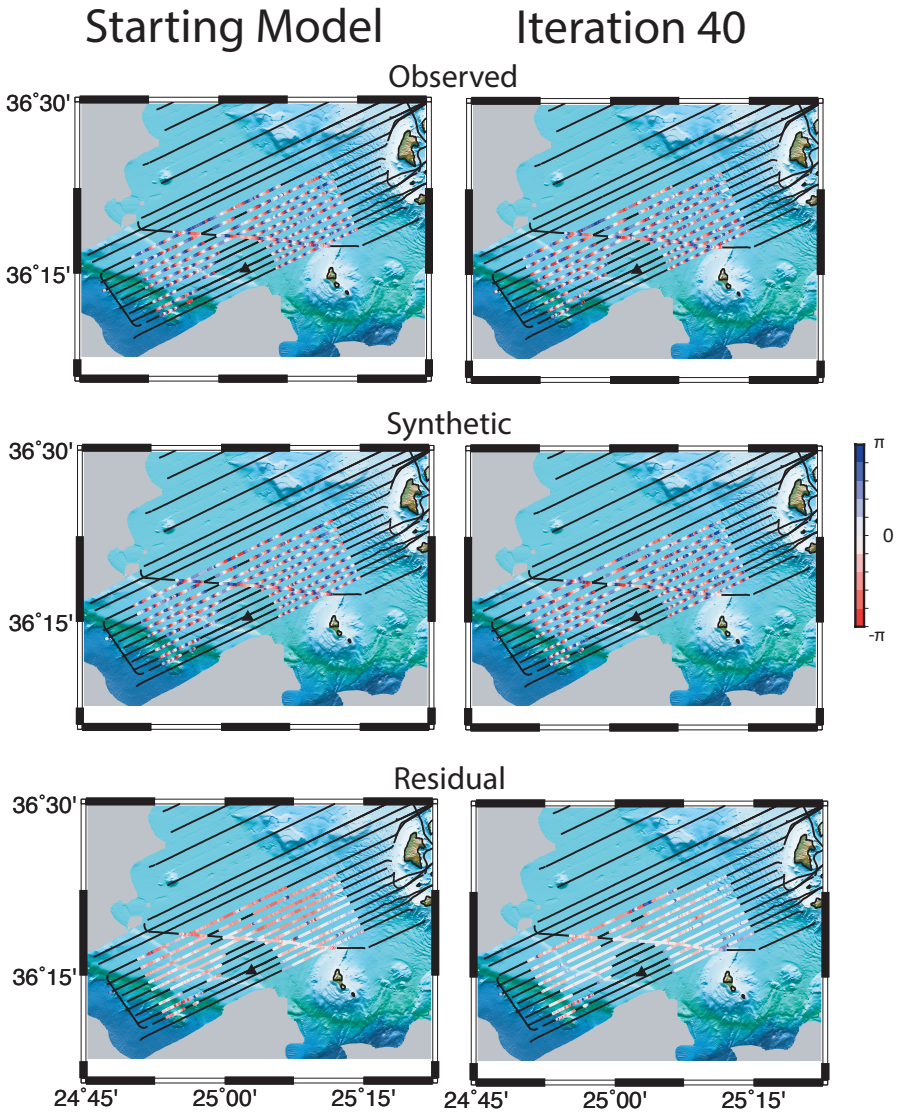

Figure 4.2. Comparison between synthetic and observed phases and associated residuals ($phase_{synthetic} - phase_{observed}$) for the starting model and iteration 40. Phases are based on gaussian windowed data, with start time chosen from the first synthetic waveform arrival (differences in observed phase between the starting model and model from iteration 40 result from differences in the first synthetic waveform arrival between these models). On average, the phase residual for iteration 40 are less than the phase residuals for the starting model resulting in the removal of long wavelength trends in phase residual.

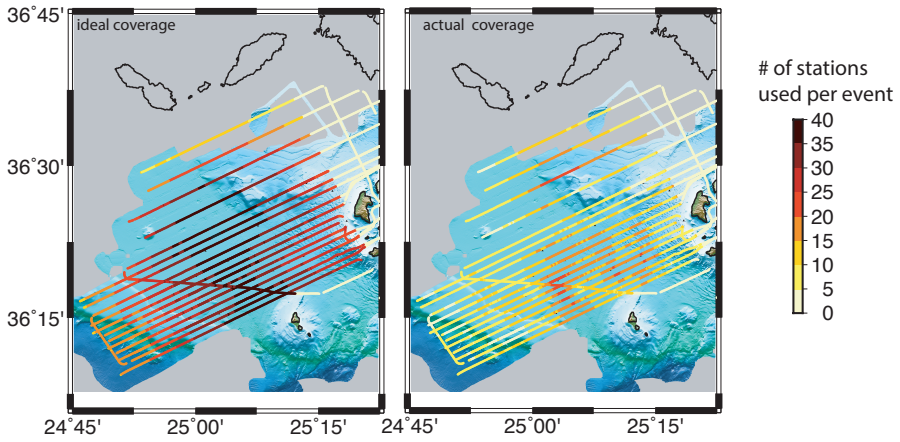

Figure 4.3. Plots of ideal and actual coverage for FWI, shown as the number of stations recording an individual event. Ideal coverage is calculated by assuming all shots within 5-25 km of each station are used. Actual coverage is based on the data used based on the same range limitation, but excluding poor quality data, as measured by phase residuals. The highest coverage is within the Christiana Basin indicating that structures within this area should be best resolved.

field that may reflect lateral differences in sources of anistropy from inherited metamorphic fabrics to local-scale faulting.

4.4.2 Overview of FWI results

Because FWI is able to image sharper velocity gradients and smaller features, FWI results better highlight observed and known faults, bringing out additional characteristics of the basin (Figure 4.5). The regional shallow upper crust (0-1 km depths) is characterized by respective fast velocities of metamorphic horsts and the slow velocities of the sedimentary basins. Two metamorphic horsts are prominent in this region, the Christiana Ridge south of the Christiana basin and a horst north of the basin. The Christiana ridge is found to extend N of the topographic ridge into the basin, representing an old basin margin that is buried under a thin veneer of sediments (Heath et al., 2019; Tsampouraki-Kraounaki & Sakellariou, 2018). The northern horst separates the Christiana basin from another

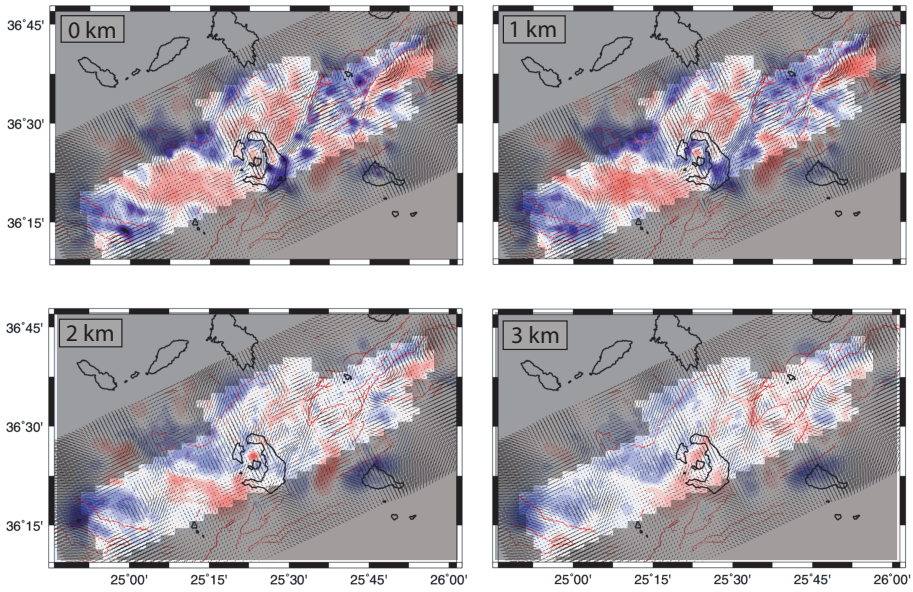

Figure 4.4. Travel-time tomography celocity perturbations as well as azimuthal anisotropy magnitude and orientation across the experiment. We show 0, 1, 2 and 3 km depths. While the azimuthal anisotropy on the eastern side of Santorini correlates strongly with fault orientation, the anisotropy on the western side of Santorini varies strongly and compares well with the metamorphic stretching lineations shown in Figure 3.1.

basin located closer to Ios and Sikinos that is not well resolved by this study. The faults at these shallow depths are characterized by NW-SE trends. Both the northern and southern margins of the Christiana basin consist of left stepping NW-SE faults, however it is not clear how these two sets of fractures formed.

At deeper 2-3 km, the northern margin of the Christiana basin is characterized by a large NW-SE striking, SW dipping normal fault that dips at an angle of approximatly 30°. This normal fault separates the competent seismically fast northern metamorphic horst from the seismically slower basin and sub-basin basement. Similar dips of large normal faults associated with different deformational episodes are found on the eastern side of Santorini (Nomikou et al., 2018). A large buried tectonic block is observed in the northern portion of the

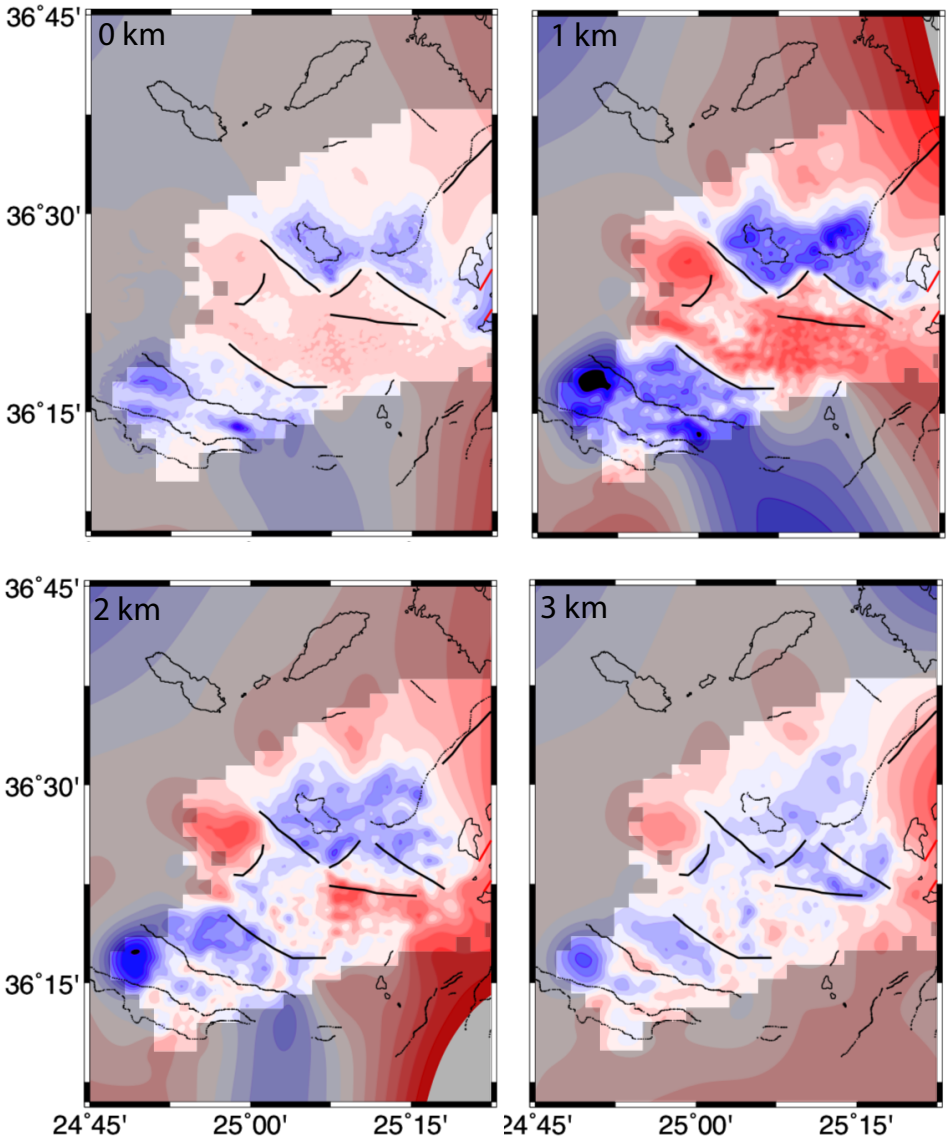

Figure 4.5. Full waveform inversion results at 0,1,2 and 3 km depth. Tectonic lines (bold black) are from Heath et al. (2019). Bathymetric features (thin black lines) are from Hooft et al. (2017). These results show lowered velocities within the basin and lowered velocities in the sub basin basement. At 2 km and 3 km depth, decreases in velocity near the Christiana ridge correlate with known fault locations, showing the effect faulting and associated fault damage has on reducing rock competency.

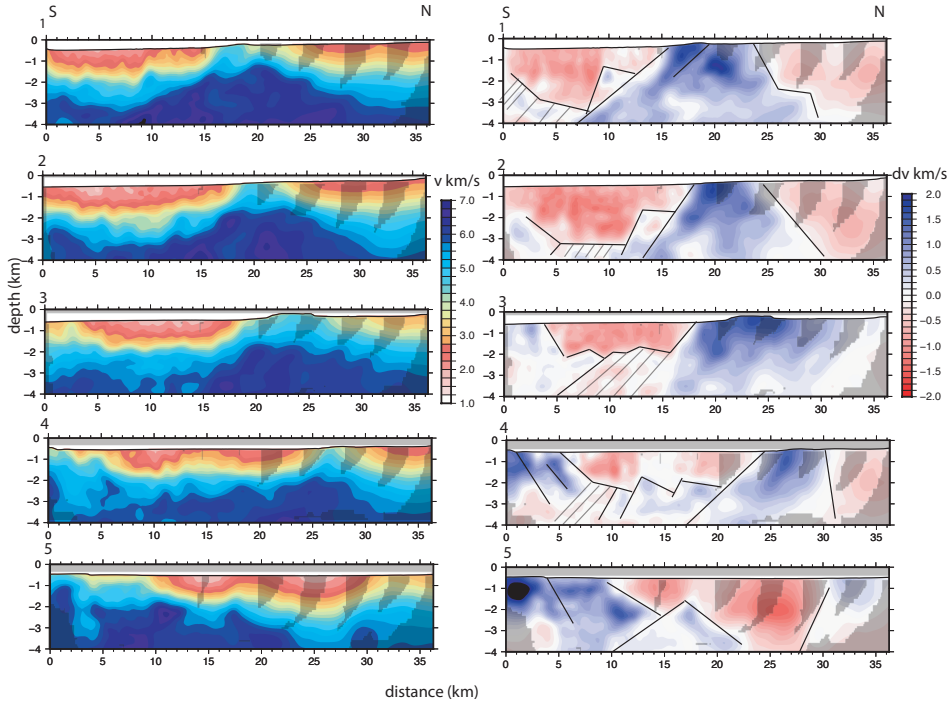

Figure 4.6. Cross sections through the FWI model shown in velocity and dv. Cross section locations shown in Figure 4.7.

Christiana basin whose strike is approximately E-W and whose extent is truncated against a N-S trending boundary, and has a similar seismic signature to the old buried basin margin seen to the south (Figure 4.6).

The deeper N-S and E-W faults that characterize the buried tectonic block outline one of three deeper subbasins recorded in the Christiana basin (Tsampouraki-Kraounaki & Sakellariou, 2018). The other subbasin imaged in this study (one of the three subbasins is outside the scope of the experiment geometry) is observed in the NW and is bounded by a curvilinear fault with NE-SW strike. These subbasins are separated by a region of thinned basin fill (Heath et al., 2019).

Regional basement velocities beneath the basin proper (the region bounded by the old buried margin and the buried tectonic block) are slower than those beneath metamorphic horsts by approximately 0.5 km/s, in contrast to the buried basin margin and buried tectonic block which are characterized by velocities similar

to the metamorphic horst (Figure 4.5). Within the basin proper basement, there is evidence for small fault blocks that dip to the S or SW (Figure 4.6). Due to the prominent shallow dip of the regional faults and their associated offset, these faults are likely extensional in nature (Heath et al., 2019) and no unambiguous evidence for previously hypothesized strike-slip behavior (Tsampouraki-Kraounaki & Sakellariou, 2018) is observed.

Local decreases in velocity of the Christiana Ridge at deeper 2-3 km depths correspond well with the bathymetric margins of the Christiana Ridge. These decreases in velocity are approximately 0.5 km/s and together represent strong evidence that faulting along the Christiana Ridge may lower the seismic velocity around faults on a kilometer scale. It is hypothesized that a similar velocity drop in the basement of the basin proper results from such fault-driven velocity reduction.

4.4.3 Comparison of FWI results to isotropic travel-time tomography results

Overall, FWI images show great agreement with isotropic travel-time tomography results (Figure 4.8, profile shown in Figure 4.7). We show a profile that highlights several structural differences between the two inversion strategies. In general the delineation of faults and their orientation suggest similar features, however for the profile below we do see areas of substantial differences in dip of 20° for the SW dipping normal fault between the two inversion methods (differences this large are only seen in a few profiles). The structure of the basins is also somewhat different, where the FWI results suggest a more prominent transition from slower seismic velocity of basin sediments to the faster velocities of the basement. This results from FWI being sensitive to features such as scattering and reflections off the basin basement where as travel-time tomography is sensitive to only the integrated and hence smoothly varying travel-time of the first arrival.

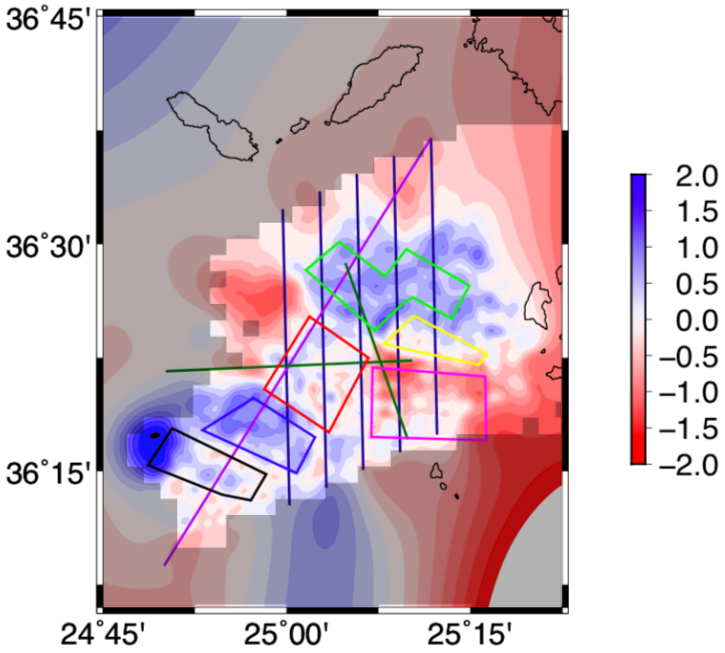

Figure 4.7. Plot of dv at 2 km depth from the FWI model. Colored boxes represent regions of averaging in Figure 4.13. Blue lines show areas of cross sections show in Figure 4.6. Magenta line represents region of cross section for the comparison of FWI and travel-time tomography models, show in Figure 4.8 . Green lines represent cross sections for comparisons between seismic reflection and FWI tomography, shown in Figure 4.9 and 4.10.

In Figure 4.8, we can clearly see the basin basement in *dv* plots for FWI as a transition from anomalously slow to anomalously fast velocities. In the travel-time tomography, this is much less prominent and the basin (black lines) is not easily observed. In addition, the FWI results show greater variability in velocity anomalies, showing both a greater regional standard deviation as well as less smooth velocity perturbations, features expected in the heterogeneously faulted Christiana basin.

FWI-derived basin centered structure confirms the presence of SSW dipping normal faults that control the structure of the basement as recorded in travel-time tomography. The similar dip direction of regional faults to the SSW within the

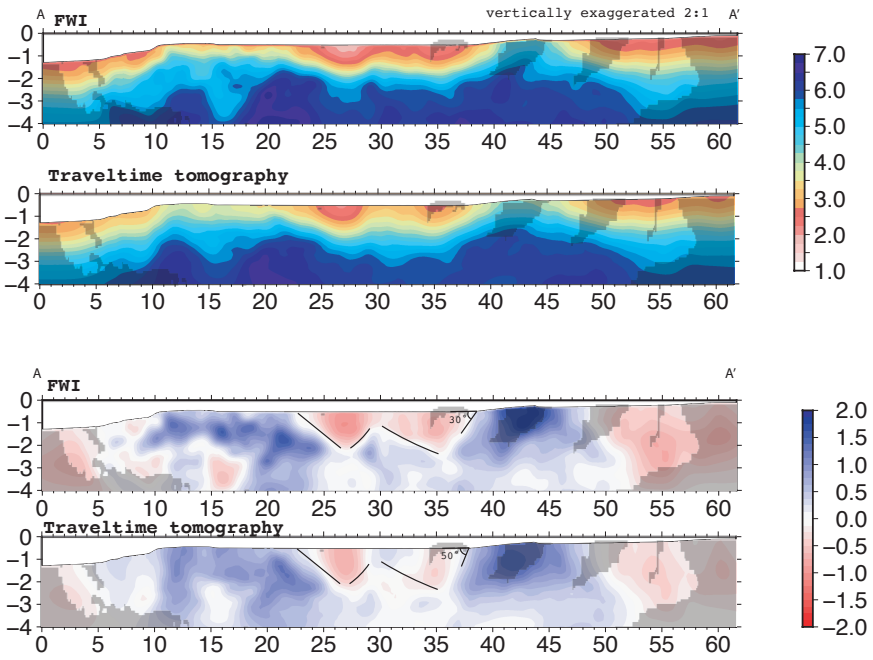

Figure 4.8. Comparison between travel time tomography results and FWI results, shown in v and dv. Location of cross section shown in Figure 4.7. The FWI recovers a slightly shallower dip in the large normal fault forming the northern boundary of the Christiana basin. Lowered basin velocities across the Christiana basin are better recovered by FWI.

basement suggests a half-graben behavior. Such half-graben behavior is prominent at other extending regions such as the Basin and Range.

4.4.4 Comparison of FWI to seismic reflection results

Comparison between FWI images and seismic reflection results enables the validation of the FWI images. We investigate two seismic reflection profiles crossing through the Christiana basin, focusing on faults observed in the basin on seismic reflection profiles and their deeper structural counterparts observed in FWI results (Figures 4.9 and 4.10).

For profile AA - AA' (Figure 4.9) we find that the shallowing of the basin center as seen in the seismic reflection profile corresponds to a rise in the basement

as seen in the FWI. Faults observed in the basin fill on the seismic reflection profile similarly correspond to deeper undulations in basement topography. These seismic reflection profiles show a general increase in layer thickness in the center of the unfaulted portion of the basin, with a general thinning and upwarping of the respective layers above the decrease in basin thickness in the middle of the profile, suggesting an active component of tectonism during (or after) basin sedimentation. Regions of thickest sediment packages correspond to the regions of lowest overall velocities.

In profile BB-BB' (Figure 4.10) seismic reflection results show an overall increase in the thickness of the sediment package to the N. These seismic reflection images show that individual layers are characterized by a concave up pattern, bounded by small fault zones, where the respective maximum thickness is achieved at points farthest from any of the local fault zones, suggesting again that there was active tectonism either syn- or post- basin formation. The basin proper is characterized by lowered seismic velocities (2-3 km/s) where as the old relict basin margin is characterized by faster velocities (3-4 km/s). Faults recorded in the basins from seismic reflection images are found to relate to deeper undulations in the basement (see 5 km/s iso-velocity contour) at 2-3 km depth, showing that the basin centered features are ultimately controlled by deeper tectonic structures.

4.5 Discussion

4.5.1 Seismic anisotropy and the record of ductile deformation

The western side of Santorini is characterized by approximately N-S oriented bulk anisotropy fast-axes (Figures 3.2, 3.4, and 4.4). The regional broad average anisotropy direction parallels metamorphic lineations, but does not follow the direction of known faults, current maximum stress direction or locations

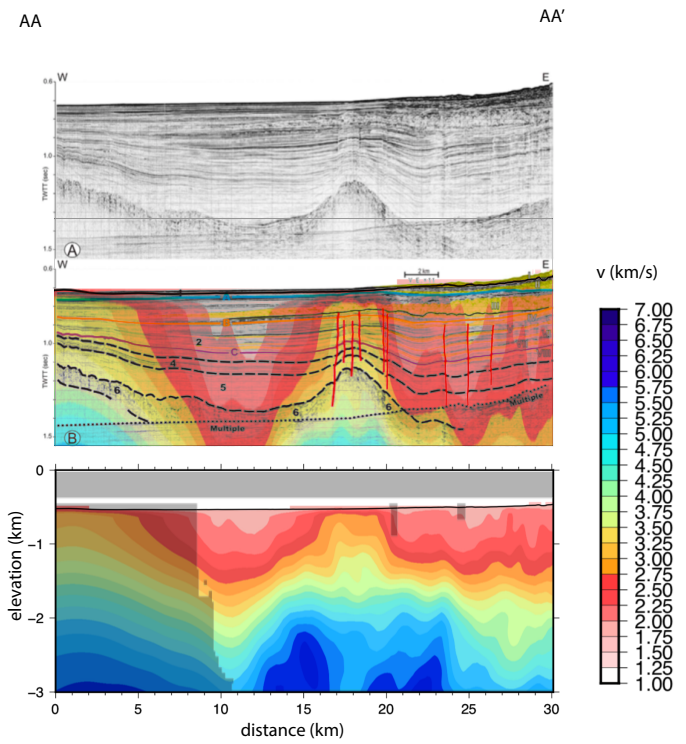

Figure 4.9. Comparison between multi-channel seismic (MCS) results and FWI results, through the Christiana Basin. MCS results are from Figure 7 of Tsampouraki-Kraounaki and Sakellariou (2018). We convert tomography results to two-way traveltime to overlay our results on MCS profiles. Faults in the shallow subsurface as recorded by MCS profiles correlate with deeper structural variations as recorded by FWI, supporting the conclusion that the basin basement is faulted.

of magmatism, indicating that it results from metamorphic properties of the host rock. This observation, where fractures are not the dominant contributor of anisotropy, has been noted in other metamorphic areas and highlights the complexity of interpreting anisotropic results in the continental crust (Brocher & Christensen, 1990). The metamorphic fabric was formed in a ductile or brittle-ductile setting in the crust, and hence must have resulted from, and therefore records, a prior history of deformation that preceded its exhumation.

The largest general contributor to azimuthal seismic anisotropy of metamorphic fabric is the preferential alignment of minerals in planes, or foliation, of the metamorphic rock. Rocks such as schists are often dominantly controlled

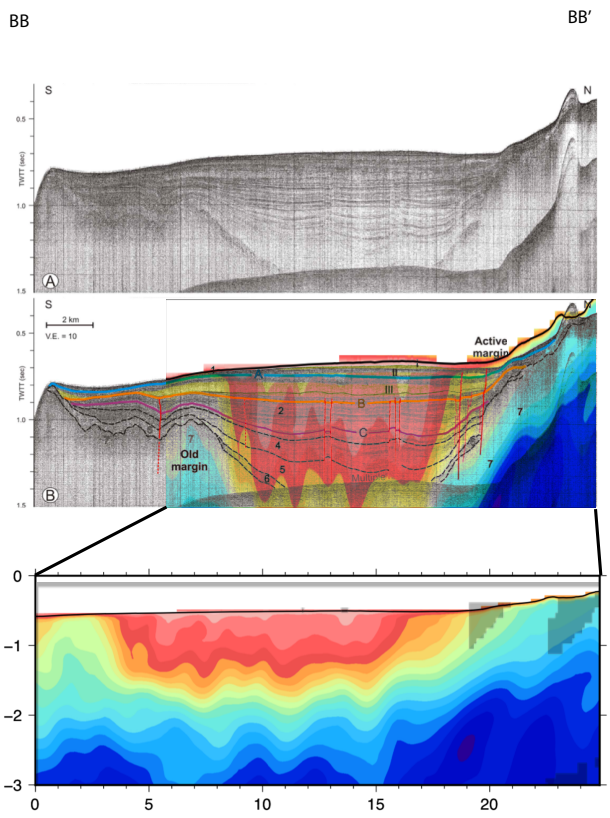

Figure 4.10. Comparison between multi-channel seismic results and FWI results, through the Christiana Basin. MCS results are from Figure 5 of Tsampouraki-Kraounaki and Sakellariou (2018). An old buried basin margin is recorded as a seismically fast block in the travel-time tomography. MCS results show evidence for faulting within the basin that correlates with the deeper structural faulting observed in the FWI results.

by micas which have slow-axis hexagonal symmetry, where the foliation plane exhibits approximately uniform fast velocities as compared to the slow velocities perpendicular to foliation. Detailed studies do show minor velocity variation in the foliation plane, producing minor azimuthal anisotropy (5%) in horizontally layered media. In contrast, dipping foliation in the upper crust produces strong azimuthal anisotropy due to the preferential alignment of mica layers, where the strike of the plane of foliation parallels the fast-axis, and the slow horizontal direction parallels the direction of dip (e.g. Brownlee et al., 2017; Cossette et al., 2015).

This azimuthal anisotropy is at a maximum when the dip angle of the mica planes is 90°, analogous to the maximum in azimuthal anisotropy for vertically oriented cracks.

Stretching lineations may also produce azimuthal anisotropy. These stretching lineations result from shearing of rock which leads to preferential alignment of quartz rods, micas and phyllosillicates and/or other minerals (e.g. Huet et al., 2011) in direction of maximum stretch. The exact orientation of this azimuthal anisotropy is complicated. Assuming a horizontal lineation direction and a vertical pole of foliation, the azimuthal anisotropy contribution from mica is negligible. In contrast, other minerals such as quartz, glaucophane, sillimanite and amphibole will produce larger azimuthal anisotropy. Quartz, amphibole, sillimanite and glaucophane all tend to line the mineral c-axis with shearing direction, producing a velocity maximum in the lineation direction (Cossette et al., 2015; Ji et al., 2015; Mainprice & Casey, 1990). Experimental studies show that, when considering the bulk aggregate of all these minerals, blueschists often have a foliation fast-axis oriented parallel to the lineation direction producing an anisotropy magnitude of $\tilde{0}.15$ (Cao et al., 2013; Cossette et al., 2015; Ji et al., 2015). The Aegean crust and mantle exhibits an azimuthal anisotropy direction consistent that parallels the Miocene extension direction (Cossette et al., 2016, 2015).

Geologic structures in anisotropic metamorphic rocks such as folds, monoclines and shear zones can also produce different styles of anisotropy, provided these structures are much smaller than the seismic wavelength. Features such as folds can alter slow-axis vertical symmetry systems such as those associated with foliations with a vertical pole into fast axis parallel to fold axis symmetry systems

(Okaya et al., 2018) inducing azimuthal anisotropy into a system that previously had none.

These series of observations outline the complicated nature of metamorphism on seismic anisotropy. Below we outline observations of geology on Santorini and surrounding islands and discuss the plausibility of foliations, stretching lineations and geologic structures as the source of observed N-S azimuthal anisotropy that occurs on the western side of the experiment (Figure 4.11).

On Santorini, foliations in the footwall of the detachment fault tend to have a N-S strike and dip towards the east. The stretching lineations are also oriented N-S for these footwall layers with E-W trending fold-axes (Schneider et al., 2018)(Figure 4.11). Both the foliation and stretching lineations of the footwall should produce a N-S oriented fast axis, consistent with fast-axis observations at Santorini, whereas the fold-axis should produce an E-W fast axis.

Structurally higher up, the Santorini detachment is dominated by a NNW-SSE sense of shear, with foliation dipping towards the SE and a fold axis oriented approximately NE-SW (Schneider et al., 2018) (Figure 4.11). The stretching lineations in the detachment should produce a NNW-SSE trending fast axis, compared to the SW anisotropy predicted by foliation and fold axis. We find a fast axis for this portion that parallels the NNW orientation of the stretching lineation.

In contrast, on Ios poles of foliation are approximately vertical (Figure 4.11). Stretching lineations point towards a N-S orientation and the fold axis for anticlines and synclines tends to be approximately N-S. For these structures, the foliation should produce no azimuthal anisotropy as it has only a very slight dip to the N and to the S (Mizera & Behrmann, 2016), the stretching lineations should produce N-S azimuthal anisotropy and the folds should induce N-S anisotropy. Again, we

find a correlation between observed N-S azimuthal anisotropy and N-S stretching lineations (Figure 4.11).

From these results we see that inherited metamorphic signatures have influenced the seismic anisotropic structure in and around Santorini. The feature most consistent with the observed azimuthal anisotropy is the stretching lineations, which parallels the observed anisotropy in all 3 cases. The observed regional stretching lineations (Figure 3.1) results from a pervasive N-S sense of shear under ductile conditions. There is substantial debate over whether N-S shear was top-to-the-N or top-to-the-S. We cannot uniquely distinguish top to the N or top to the S senses of shear from the ductile derived N-S stretching lineations as both could produce a N-S stretching lineation. Overall, these results support previous evidence of regional detachment faults active during the Oligo-Miocene that had a N-S sense of shear that has subsequently been exhumed. Because these fabrics formed under older, deeper, hotter more ductile conditions, they do not record current deformation and instead represent an inherited structural recorder of prior deformation.

4.5.2 Tomographic evidence of brittle behavior in the Christiana Basin

In contrast to the older ductile deformation described above, we now discuss the younger brittle faults that have resulted from Miocene/Pliocene to present deformation. The Christiana basin is dominated by a large top to the SSW normal fault that dips at an angle of 35° that defines the northern margin of the basin. A large buried normal fault is also observed buried in the northern portion of the basin near Santorini, having an E-W strike and a slightly steeper dip angle (Figures 4.5 and 4.6). Similar but smaller scale features are pervasive within the basement. Because these basin-centered faults seem to in general parallel

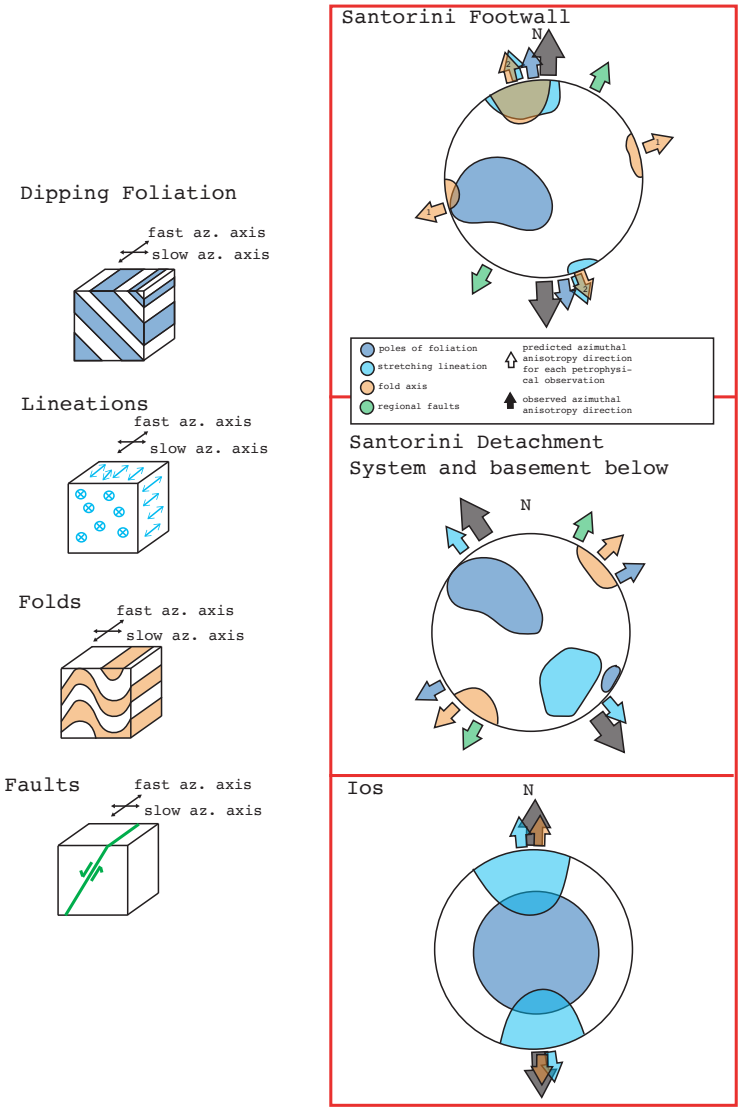

Figure 4.11. Polar plots showing the comparison between predicted anisotropy directions and observed anisotropy directions for metamorphic blocks in the Santorini Footwall, Santorini Detachment and on Ios. Observed azimuthal anisotropy directions are shown as black arrows. We predict azimuthal anisotropy orientations that result from metamorphic foliation (dark blue), stretching lineations (light blue), regional folds (orange) and region faults (green). The poles of foliation/lineations/fold axes/fault orientations are shown on polar plots where appropriate and the predicted azimuthal anisotropy directions are shown by the colored arrows. The correlation between fast-axis orientation and each of these properties is shown by the side panel. Overall, metamorphic stretching lineations seem to correlate best with observed azimuthal anisotropy directions, although a number of different parameters can impact azimuthal anisotropy.

extension dominated faults, we presume that these faults are strongly correlated with extension, as compared to the strike-slip dominated sense of motion inferred by Tsampouraki-Kraounaki and Sakellariou (2018). The shallow dip of the faults, much less than the 60° predicted by Andersonian fault theory, is consistent with studies of extension dominated regimes, especially core-complex forming domains such as the Basin and Range. In such environments progressive rotation of fault boundaries as result of increased extension can lessen the dip of faults. Such rotation may explain steepened faulting within the basin proper. In contrast to the eastern portion of the experiment (e.g. Anydros Basin and Anafi Basin), where syn-tectonic deposition of sediments is recorded within the basins by increase in the dip of strata with depth , the strata within the Christiana basin is relatively flat (Tsampouraki-Kraounaki & Sakellariou, 2018) (Figures 4.9 and 4.10), indicating either a faster opening of the basins (relative to sediment infilling) or a difference in timing between tectonism and sediment infilling . Small undulations in the flat strata which correlate with deeper faults suggests that some minor fault activity has occurred basin basement faults after sediment deposition. It is also possible part of the extension was accommodated without fault rotation, and therefore deposition within the basin could have occurred over longer timescales , however such faults are thought to not be significant in accommodating large extension (Wernicke & Burchfiel, 1982) and the shallow dip of the beds of the basin-centered tectonics blocks indicates some net rotation resulting from extension.

The southern margin of the Christiana basin is characterized by a NW-SE striking old buried basin margin that is offset from a topographic basin margin (Heath et al., 2019; Tsampouraki-Kraounaki & Sakellariou, 2018). This older basin margin is extensively faulted in a NW-SE manner. The southern margin

of the Christiana Ridge proper is also characterized by faults with a more E-W orientation.

It is thought that deformation associated with basin formation began on the inner boundary faults and migrated outward toward the more northern and southern boundaries respectively (Tsampouraki-Kraounaki & Sakellariou, 2018). Lowered velocities in the basin proper and not within the old buried margins, suggests pervasive fracturing within the basin center.

While the northern horst strongly exhibits the N-S anisotropy discussed earlier, the Christiana basin and Christiana Ridge exhibit differing anisotropy orientations. The buried northern block tends to exhibit an anisotropy fast axis that parallels the regional fault orientation and therefore is likely due to fracturing. The Christiana basin tends to exhibit a more NE-SW oriented fracturing, suggesting the NE-SW faults from the eastern side of the experiment do extend into the Christiana basin. The Christiana Ridge and associated old basin margin are characterized by NW-SE to E-W style anisotropy, likely a result of fracturing of these blocks associated with extension.

4.5.3 Distribution of faulting within and outside the basin proper

To investigate the role of, distribution of, and styles of faults, lineations and fracturing associated with deformation, we model the observed anisotropy and velocity assuming three a priori geologically motivated fault orientations, an a priori defined metamorphic lineation as well as a "random" fracture network (Figure 4.12). The 3 assumed fault orientations are 90°, 120° and 30°. 90° oriented fractures characterize the E-W faulting inferred to be present in the Christiana basin from prior episodes of tectonism. 120° fractures characterize the NW-SE faults that define the current margin of the widened Christiana basin. 30° fractures

characterize anisotropy resulting from the NE-SW faults that control regional volcanism and are thought to define a proto-basin in which Santorini sits (Heath et al., 2019). An increase in any of the respective faults/fractures is inferred to lower the bulk velocity as well as to induce anisotropy with a fast-axis orientation in the direction of the respective faults. Metamorphic lineations are assumed to have a 0° orientation, enabling the modeling of their effect on anisotropy. This 0° matches the direction of stretching lineations on Ios and many of the surrounding islands. Local variations in the stretching lineation which are seen on both Santorini and Anafi (Figure 3.1) are not incorporated into this model. The 0° lineations are assumed to not impact seismic velocity (unlike fractures) and therefore only contribute to anisotropy. In contrast, the "randomly" oriented faults lower seismic velocity without increasing anisotropy and are used to highlight tectonic complexity with no preferential orientation. These faults can result from distinctly non-random sets of orthogonal faults which independently produce an anisotropic signature but that destructively add together, or due to truly random faults that have no consistent orientation but that generate porosity. From the above array of fault orientations and lineation directions, we can decompose any arbitrary azimuthal anisotropy and velocity signal and calculate the contribution of each of the above defined fracture sets. A thorough discussion of this modeling effort method is given in the Appendix.

We examine the fracture distribution within 6 parts of the study area to better understand the formation and deformation within the Christiana basin, focusing on: the southern Christiana Ridge, the old buried southern basin margin, the eastern portion of the Christiana Basin, the western portion of the Christiana basin, the buried basin block near the northern margin of the Christiana Ridge and the northern margin of the Christiana Basin (Figures 4.13 and 4.12). For

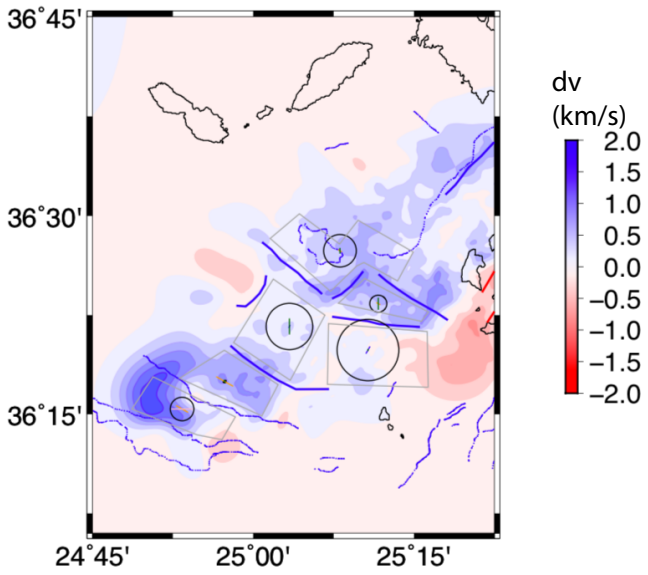

Figure 4.12. Anisotropy magnitudes (and orientations) for the regions outlines in gray, based on inversion of $\delta v, A$ and B parameters. Here we attribute all variations in velocity, anisotropy magnitude and anisotropy direction to result from a combination of N-S stretching lineations (green lines), 30° faults/fractures that characterize current faulting (blue lines), E-W fractures that characterize inherited faults thought to underlie the basin (pink lines), 130° fractures that define the current basin bounding faults (orange lines) and random faults that account for a drop in velocity without a corresponding increase in anisotropy (black circles).The length/diameter of each line is proportional to the anisotropy magnitude. The regions averaged over were selected based on shared physical characteristics and include the east and west portions of the Christiana basin, northern and southern buried basin blocks within the basin as well as the Christiana Ridge and northern bounding ridge. The largest drop in velocity is uncorrelated to anisotropy ("random" fractures) and is located in the center of the basins. 30° faulting is seen within the basin, outlining the region defining a proto-Anydros basin (discussed in a previous chapter).

each of these areas, we produce an average anisotropy and velocity profile and then decompose this into the relative contributions from the faults and lineations described above.

A strong N-S anisotropy is present in the western Christiana basin as well as the northern buried block, a minor component is present in the the northern

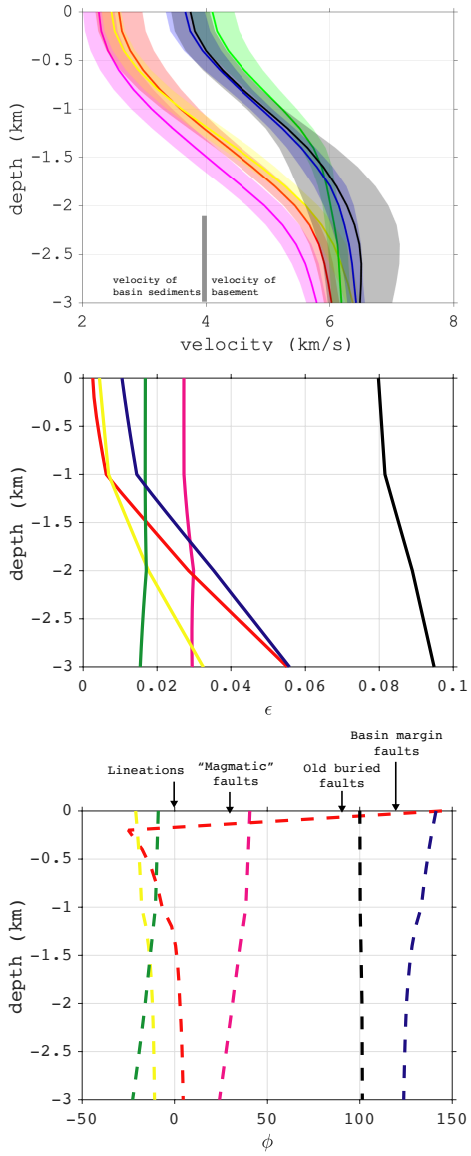

Figure 4.13. Plot of mean velocity, bulk anisotropy magnitude and bulk anisotropy orientation as a function of depth, for various different areas on the western side of the experiment. The anisotropy for the northern bounding horst (green) is consistently oriented in the N-S direction, consistent with metamorphic lineations. Anisotropy in the basins (red/magenta/yellow) tends towards a direction between N-S and the "magmatic" 30° faults. Anisotropy in and near the Christiana Ridge (blue/black) follows a more E-W orientation that parallels older buried faults and basin margin faults. Color-coded regions used for averaging shown in Figure 4.7.

horst and a very minor component in the eastern basin, the southern old buried basin margin and the Christiana Ridge (Figure 4.13). This N-S anisotropy is due to metamorphic stretching lineations as discussed above, although a portion may be due to N-S oriented faults in the Christiana basin.

NW-SE oriented fractures are observed everywhere except within the basin proper (eastern and western Christiana basin) and are strongest in the southern old buried basin margin. As the NW-SE faults are associated with widening of the basin, they likely post-date basin formation.

A NE-SW anisotropy is observed in the basin proper and is strongest in the eastern basin. This seems to confirm the suggestion of Heath et al. (2019) that NE-SW striking faults extend into the Christiana basin as part of a proto-Anydros basin. Such faulting is bathymetrically-expressed near the Christiana Islands.

The only portion of the region that is required to have E-W faults is the Christiana Ridge which does have faults with an E-W orientation. Curiously, the Christiana basin basement, which numerous studies suggest should have E-W faults (Heath et al., 2019; Piper et al., 2007; Tsampouraki-Kraounaki & Sakellariou, 2018) is not required to have pervasive such E-W faults by the anisotropy. This anomaly, where the basin basement is not required to have E-W faults, may be resolved by the "random faults" discussed below.

The largest fraction of random faults/porosity is present in the basement beneath the basins, and these faults, more than any individual fault orientation, can be used to explain the bulk of the lowered basin basement velocity. We do not know the orientation of these faults, just that cumulatively they don't have a consistent orientation. Two end member cases include a.) a pair of mutually orthogonal faults that are otherwise equal in all other properties and b.) truly random fault orientations. Despite being entirely different tectonically, both of

these cases will not produce azimuthal anisotropy and will produce the same constant velocity field. We can explain the lack of E-W anisotropy and the drop in velocity if we assume a.) is true and that any E-W anisotropy is cancelled out by either N-S stretching lineations and/or N-S faulting. Such an explanation allows us to preserve the notion that the basin is underlain by faults of a consistent orientation and that the orientation of these faults is similar to that of basin bounding faults.

We combine the observations of a strong 30° SSW dipping fault that forms the northern boundary of the basin, lowered basin velocities, faults observed in the basin basement, a general half-graben character of the basins and low seismic anisotropy to build an understanding of the style of extension occurring within the basin. It is worth noting that these random faults represent proportionally the greatest fraction of faults within the basin. Therefore, we can appeal to pervasive faulting within this basin if it is cancelled out by pervasive faults or fractures of an orthogonal orientation.

Here the lowering of velocities basement velocities beneath the basins is attributed to small scale faulting, analogous to shearing of a pack of cards (e.g. Angelier & Colletta, 1983; Smith & Bruhn, 1984). Studies suggest that up to 40% of net extension may be accommodated on faults with displacements less than 100 m, a result of the high density of low displacement faults (Marrett & Allmendinger, 1992; Walsh et al., 1991). This displacement is well below the seismic tomography detection threshold for this study, suggesting a bulk order estimate of the amount of extension would be severely underestimated. This domino-style shearing based extension is analogous to that observed in analogue studies of extension, which find localization of extension in the hanging wall of the faults (Berg & Skar, 2005). Such analogue studies are able to produce both half-graben as well as full graben

behavior and find that the orientation of faults varies throughout its lifetime and therefore records an integrated history of deformation (McClay, 1989).

Additional lowering of velocities can result from fault damage. While damage around fault cores is often though to only extend meters to tens of meters (Kim et al., 2004), the superposition of different fault strands can extend the damage zone to much wider length scales (Savage & Brodsky, 2011). Tomographically observable lowered seismic velocities ($> 50\%$ reduction) associated with damage zones can be seen at the San Andreas and Calico fault zones and these damage zones can have widths of hundreds of meters to kilometers (e.g. Cochran et al., 2009; Li et al., 2004). While we can't conclusively attribute lowered basin velocities to fault damage, damage can be observed in the metamorphic horst at the Christiana Ridge, where lowered seismic velocities within the metamorphic horst correlate with the Christiana Ridge fault, correlating with a drop in velocity of 0.5 km/s ($\sim 10\%$ reduction) (Figure 4.5).

Due to the dominance of the SSW dipping normal fault, it's shallow angle and the subsequent localization of deformation within the basin, we conclude that the Christiana basin formed from half-graben style deformation. This then transitioned to a full graben style extension with the subsequent widening of the basin margins.

4.5.4 Ductile and brittle deformation: controls on the localization of deformation, comparison between east and west

In the region around Santorini, we have a unique ability to interrogate constraints on the styles of extension and subsequent progression of extension through time due to the variety of different high resolution datasets present in the region combined with the fact that these differing time periods of extension

effected different parts of the region. N-S ductile behavior associated with Oligo-Miocene extension is recorded in stretching lineations in metamorphic rocks. Progressive, brittle, half-graben extension is recorded in the Christiana basin, with the localization of faulting and damage predominately in the basin center. Subsequent basin enlargement is accommodated on NW-SE striking faults. Finally, pervasive NE-SW striking normal faulting has facilitated magmatism and volcanism at Santorini and the surrounding region.

It is difficult to link together N-S ductile deformation that transitions to E-W striking brittle half-graben behavior, despite both potentially resulting from a N-S directed extension. This difficulty arises due to the fact that the most recent detachment faulting is thought to be top to the N which would likely produce N-dipping half-grabens, where as the half-graben behavior recorded in the Christiana basin suggests a top to the S sense of shear. While surrounding islands do record this top to the S sense of shear in ductile fabrics, it is thought to have preceded the top to the N sense of shear (Forster & Lister, 2009) and thus the shearing cannot have transitioned simply from top to the S ductile behavior to top to the S brittle behavior. Whatever the cause, faulting within the Christiana basin tends to have a E-W strike and tends to exhibit a top-to-the-S style half-graben behavior.

The subsequent localization of faulting within the Christiana basin is curious. This is not observed in the NE-SW striking faults predominately on the eastern side of Santorini that post-date Christiana basin formation. Rather, the eastern side of Santorini exhibits a uniform sense of faulting within basins and beneath horsts (see previous chapter). Localization of faulting is often thought to be driven by the relative weakening of the crust with extension (e.g. narrow rifting or complex mode of extension), whereas regions where the crust exhibits strengthening in regions of faulting tend to develop multiple fault zones and wide

rifts (Buck, 1991). Localized extensional features, with large normal faults that transition to basin centered half grabens, are found in analogue models that restrict regions of basal stretching, artificially limiting regions of deformation (McClay, 1989). This can be compared to models that do not restrict basal stretching which produce pervasive half-grabens and pervasive lateral faulting. Transitions between this localized narrow mode of extension as seen in the Christiana basin and larger wide mode of extension seen in the Amorgos-Anydros area could take place spatially within the same region, just from temporally different extensional episodes. For example, we could consider an initial model with isolated tension gashes through out the region (Angelier & Colletta, 1983). The Christiana basin could be in a developing stage with initial basin centered tension gashes being being reactivated as imbricate normal faults through subsequent block rotation (such possible faults are shown in Figure 4.6). This would localize deformation over an isolated area in the basin center. The eastern side of Santorini, then, might be in a later stage version of this, where pervasive tension gashes have all been reactivated as normal faults, facillitating extensive faulting through both basins and horsts, allowing for deformation over a wider area in a more pervasive fashion.

This model, where basin-centered imbricate normal faults are activated on the Christiana side (reflecting Miocene-Pliocene extension) where as broader and pervasive faults are activated on the eastern side of Santorini (reflecting current extension) is consistent with models for the evolution of styles of extension of Buck (1991), transitioning from narrow rifting to wide rifting (see Appendix). The current thermal state of the lithosphere suggests that the Santorini region is currently on the border of narrow rifting style extension (faults weaken the crust localizing deformation) and wide rifting extension (faults strengthen the crust leading to multiple faults) (Figure 4.14). Slight increases in the temperature of the

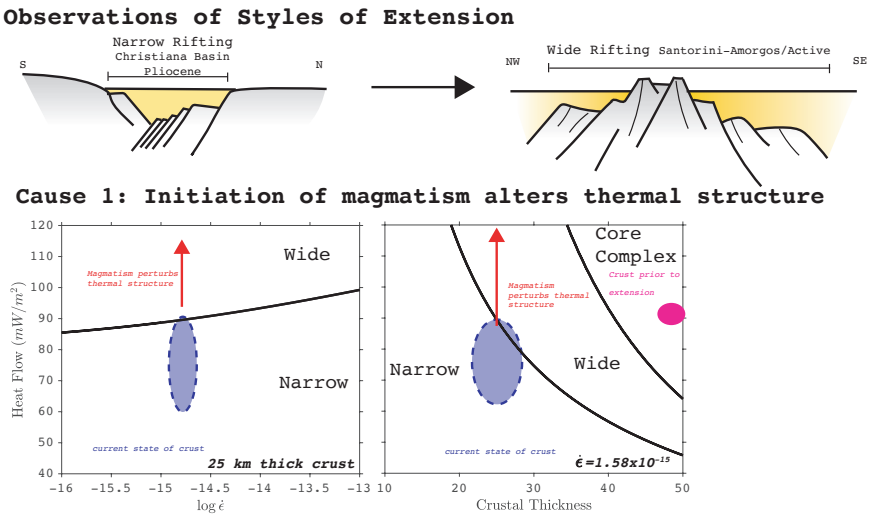

Figure 4.14. Comparison between a narrow style of rifting seen in the Christiana basin and a wider rifting seen on the eastern side of Santorini. This difference may be caused by a thermal perturbation associated with magmatism leading to elevated crustal temperatures and subsequently locally elevated crustal strength near faults, favoring development of new faults. Given the current thermal and physical state of the crust around Santorini, the style of rifting is relatively invariant to small perturbations in both strain rate and crustal thickness, but is highly sensitive to thermal perturbations.

crust will push the crust into a wide rift style of extension. Previous authors have proposed that the transition from E-W to NE-SW styles of faulting led to regional magmatism (Piper et al., 2007), and presumably an altered thermal state of the crust. It is plausible that the initiation of regional magmatism altered the thermal state of the crust sufficiently to alter the style of extension from narrow rifting associated with preferential localization of faulting seen in the Christiana basin to wide rifting associated with pervasive, distributed faulting seen on the eastern side of Santorini. Therefore the differences in styles of deformation may be driven by magmatism more than other factors. The ability to transition across styles of extension due to modest perturbations in the thermal structure results from the unique conditions present at Santorini, situated near the change from narrow to wide rifting.

Alternatively, the difference in faulting styles may result from the fact that the tectonic regime around Santorini supports the idea that Santorini is currently associated with an accommodation zone, where the NE-SW normal faults step-over and slightly change direction (Figure 4.15). Similar accommodation zones are associated with magmatism in the Basin and Range and it is thought the distributed style of faulting at accommodation zones may result from both perturbations to the thermal structure of the crust as well as changes in bulk rheology of the crust due to melt injection associated with magmatism (e.g. Faulds & Varga, 1998).

Both the above models associate changes in the style of faulting with regional magmatism and its effect on physical properties of the crust. Deeper imaging seismic tomography experiments do suggest that there is currently regionally partial melting of the upper mantle as well as a thinned crust (Karagianni et al., 2004), both of which likely impact the physical properties of the crust

4.6 Conclusions

We combined anisotropic travel time inversions with full waveform inversions (FWI) to interrogate the structure of the Christiana basin. Anisotropic travel time inversions inform the overall orientation and fraction of small scale faults within the region as well as the orientation of metamorphic fabric. FWI informs the overall structure and orientation of buried blocks within the Christiana basin.

From the combination of these two methods and geologic observations we are able to resolve the following: 1.) regional metamorphic fabric is characterized by a N-S stretching lineation inherited from ductile behavior in the Oligo-Miocene, 2.) the Christiana basin is defined by a large SW-dipping normal fault, 3.) large

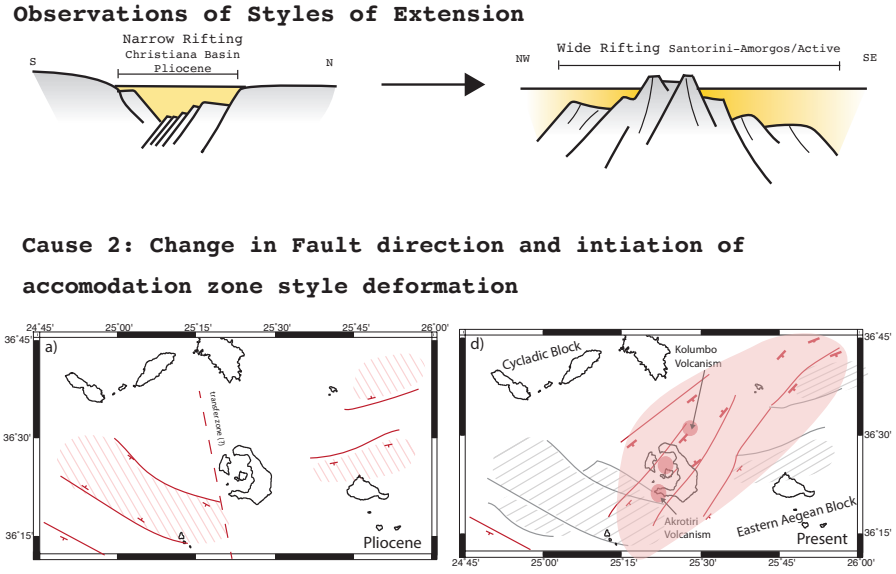

Figure 4.15. Comparison between a narrow style of rifting seen in the Christiana basin and a wider rifting seen on the eastern side of Santorini. Hypothesis 2 is that the difference is related to the fact that broader rifting is associated with an accommodation zone-like structure. These accommodation zone structures can also result from magmatism.

buried E-W striking blocks within the Christiana basin record a prior episode of deformation, 4.) although anisotropy cannot confirm nor exclude the existence of pervasive smaller scale E-W striking faults, lowered velocities within the basin center likely result from the localization of faulting within the basin and the subsequent localization of deformation within basin margins, and 5.) NE-SW striking faults are found to extend into the Christiana basin and reflect the current tectonic environment supporting the hypothesis of a proto-Anydros basin associated with magmatism. Deformation associated with Christiana tectonics shows extensive localization within the basin proper. In contrast, deformation on the eastern side of the experiment associated with current magmatism is broader showing evidence for a more distributed extension. The transition from localized deformation associated

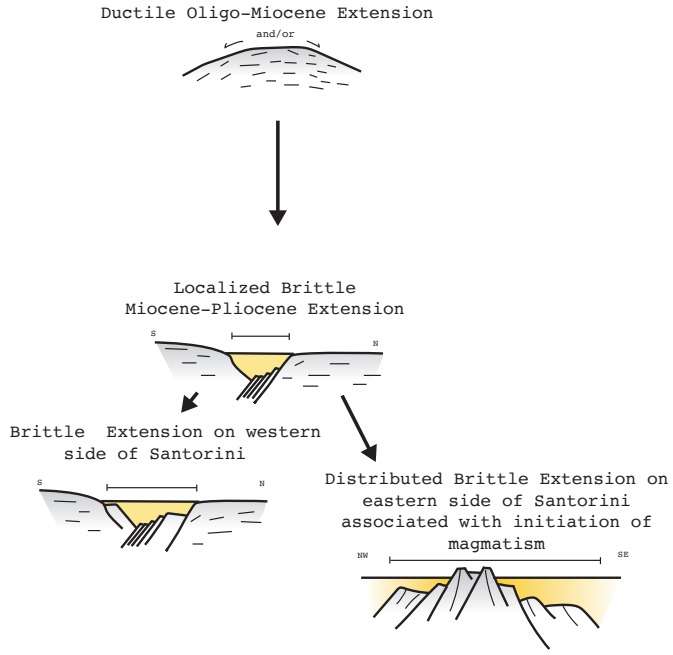

Figure 4.16. Model of the tectonic evolution of the region around Santorini, as recorded in the current upper crustal structure. Ductile extension in the Oligo-Miocene imparted N-S stretching lineations onto the crust. Subsequent Miocene-Pliocene extension was localized in the Christiana basin. Widening of the basin occurred later, creating the structures observed today in the basin. A distributed style of extension associated with the initiation of magmatism is presently observed today, resulting from a change in extension direction that created faults oriented at 30° as well as a change in the crustal thermal structure that may have resulted from magmatism.

with the Christiana basin to the broader deformation that is predominately recorded on the eastern side of the experiment is consistent with numerical models suggesting a transition from narrow rifting to wide rifting due to increased crustal temperatures associated with magmatism (Figure 4.16). Alternative hypotheses include transitions in the style of rifting due to the development of an accommodation-zone-like structure at Santorini, features commonly associated with magmatic activity. In this way, the style of regional tectonism may have been impacted by the initiation of regional magmatism.

4.7 Bridge

In Chapter IV, I investigated causes for the change from localized to distributed extension and discussed the role of magmatism in this process. In Chapter V, I discuss the role of tectono-magmatic lineaments in localizing a long-lived, isolated region of caldera collapse. This isolated caldera collapse is found to enable the stalling of magma at depth beneath this portion of the caldera.

CHAPTER V

SEISMIC IMAGING OF SANTORINI: SUBSURFACE CONSTRAINTS ON CALDERA COLLAPSE AND PRESENT-DAY MAGMA RECHARGE

This chapter was published in *Earth and Planetary Science Letters* with the title "Seismic imaging of Santorini: Subsurface constraints on caldera collapse and present-day magma recharge" and published with co-authors E.E.E. Hooft, D.R. Toomey, M. Paulatto, C.B. Papazachos, P. Nomikou, J.V. Morgan, M. Warner. The first author, E. E. E. Hooft wrote the manuscript and drafted most of the figures. I have included the manuscript in my dissertation because I picked the data, conducted the inversions, and contributed to the development of the ideas presented in the manuscript.

5.1 Introduction

Geological field studies show that calderas are structurally complex and thus formation mechanisms continue to be debated, including multi-event piecemeal collapse (Williams, 1941), piston subsidence of a central plug followed by erosion at the margins (Lipman, 1997; Walker, 1984), nested caldera formation along sets of inward- and outward-dipping ring faults (Roche et al., 2000; Scandone and Acocella, 2007), and funnel-shaped collapse into a cored-out volcanic vent (Aramaki, 1984; Escher, 1929; Yokoyama, 1981). A synthesis of sandbox experiments as well as numerical models of subsurface stresses predict that as deformation and evacuation progress the style of roof collapse evolves from initial reverse faulting to later development of an outer ring of conjugate normal faults (Acocella, 2006; Holohan et al., 2015).

Shallow caldera structure and caldera faults have been seismically imaged at volcanoes revealing low velocities at shallow depths and in a few cases seismicity

along ring faults. Localized low-velocity regions in the uppermost crust (<5 km) at large caldera systems such as Yellowstone (Farrell et al., 2015) and Campi Flegrei (Vanorio, 2005) are interpreted to reflect hydrothermal reservoirs. At Krakatoa (Deplus et al., 1995), Deception Island (Zandomeneghi et al., 2009) and Newberry (Beachly et al., 2012; Heath et al., 2015) volcanoes the caldera is filled with low-velocity material thought to correspond to sediments and brecciated caldera-fill. These low velocities narrow downward and connect to magmatic systems in the upper crust below 2 km depth. At other volcanoes, displacement on caldera ring faults has been inferred from seismicity recorded during diking and eruption episodes. At Bárdarbunga earthquakes beneath the caldera outlined a tall (8-km high), slightly-tilted plug overlying the inferred magma system (M. T. Gudmundsson et al., 2016). While at Axial Seamount conjugate inward- and outward-facing faults were activated during inflation and deflation episodes (Wilcock et al., 2016) providing observational evidence for calderas controlled by conjugate fault structures.

The proposed caldera collapse models predict considerable differences in the structure of the upper portions of volcanoes that may affect the stress state of the edifice and the movement of magma, resulting in distinct styles of magma recharge and post-collapse volcanism. In this paper we use a dense, active source, seismic tomography study of Santorini caldera (Figure 5.1) to image the seismic velocity structure of a collapsed caldera at an arc volcano. We interpret the velocity structure in terms of physical properties and discover an inner shallow low-velocity, high-porosity volume. We then make use of extensive geological studies of the evolution of the volcano and of the latest caldera-forming eruption to explore three models that might explain this feature. In addition, we use the correlation of a recent unrest episode associated with volcano inflation with structures within the

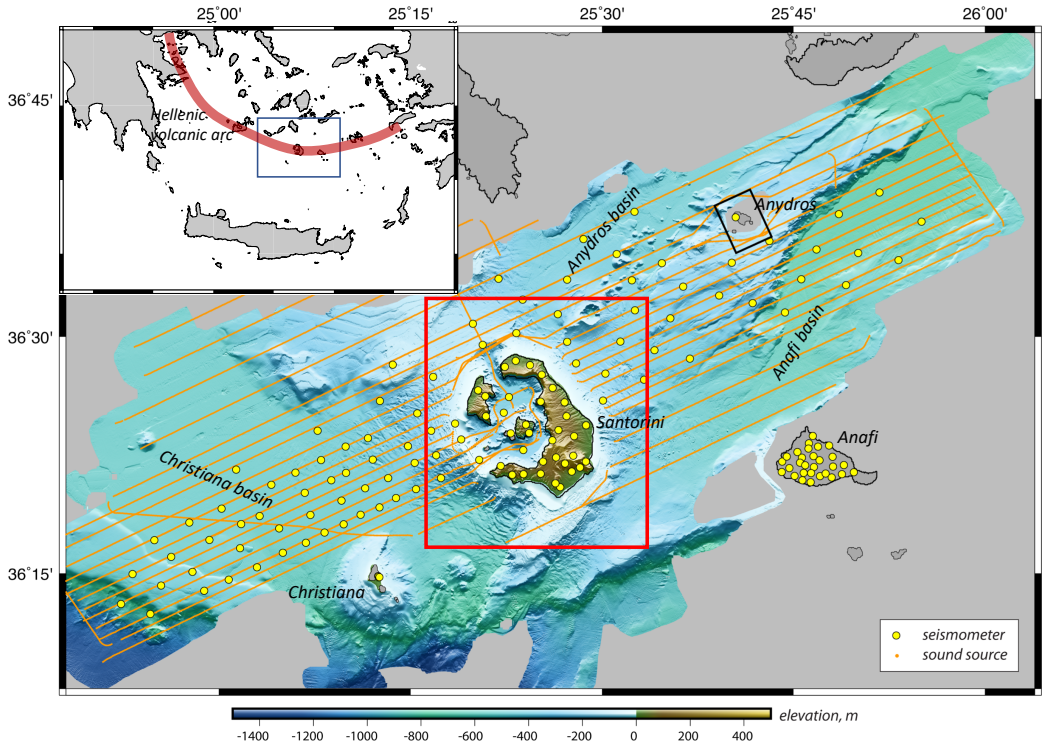

Figure 5.1. PROTEUS seismic experiment. Map of the sea bottom and land topography (Hooft et al., 2017) and the layout of the entire marine-land dataset that was collected in November-December of 2015. The dense marine-land experiment recorded ~14,300 controlled-sound sources (beige dots) from the R/V Marcus Langseth on 90 ocean-bottom and 65 land seismometers (yellow circles). The red rectangle shows the region of this study and the islands and sedimentary basins are labelled. The black rectangle shows the area that was averaged to obtain the velocity-depth curve for the reference metamorphic profile in Figure 5.5a.

caldera to postulate that the sub-surface density anomalies of a caldera may act to localize present-day magma recharge.

5.2 Santorini volcano

Santorini is an arc volcano in the Hellenic subduction zone (Figure 5.1) that has been the subject of numerous geological studies over more than a century. In a regional context, Santorini is located within the sedimentary basins and

metamorphic horsts of the extended Aegean continental crust. Major explosive activity at Santorini began about 360 ka and included up to 12 large explosive eruptions (Druitt, 2014). It has a history of alternating caldera-forming, explosive, Plinian eruptions and caldera-filling, effusive, shield-building periods. This cycle is currently expressed by the explosive Late Bronze Age (LBA) eruption (Also known as the Minoan eruption) that formed the present-day caldera 3.6 kyr ago and was followed by effusive dome-building eruptions to create the Kameni islands within the caldera (Figure 5.2a).

The following episodes established the geological setting of the LBA eruption. A large intra-caldera shield edifice, the 350-m-high Skaros-Therasia complex, was built effusively between 67 and 23 ka (Druitt et al., 1999; Heiken and McCoy, 1984). This shield complex collapsed in the Cape Riva explosive eruption at 22 ka (Fabbro et al., 2013) to form a shallow water caldera located in the northern basin of the present-day caldera (Athanassas et al., 2016). Chemical analysis of the stromatolite lithics show that this caldera was a semi-restricted marine bay no deeper than a few meters (Anadón et al., 2013; Friedrich et al., 1988). Subsequent intra-caldera effusive activity constructed the 2.2-2.5 km^3 Pre-Kameni island inferred from black, glassy andesite lavas found throughout the LBA deposits but not in the present Santorini edifice (Druitt and Francaviglia, 1992; Karátson et al., 2018).

Current models for silicic caldera-forming systems involve trans-crustal magmatic systems that evolve significantly over time with rapid final stages of amalgamation preceding the Plinian caldera-forming eruption (Cashman et al., 2017). At Santorini, melt diffusion profiles in orthopyroxene and clinopyroxene crystals from the LBA rhyodacites indicate prolonged storage and segregation of melts in a sub-caldera pluton (8-12 km depth) prior to the LBA eruption (Flaherty,

2018). Since crystals from all eruptive phases yield similar timescales, the authors infer that, on the timescale of a few centuries to years, a shallow (4-6 km) short-lived chamber formed that held most of the magma erupted in the LBA eruption.

The LBA Plinian eruption occurred in 4 geologically distinct main phases (Figure 5.2c) with a total volume between 30 and 80 $km^3$3 dense rock equivalent (Bond and Sparks, 1976; Druitt, 2014; Heiken and McCoy, 1984; Johnston et al., 2014; Sparks and Wilson, 1990). The first phase was a Plinian pumice fall representative of a subaerial eruption. Isopachs of the pumice deposit and the size-distribution of ejected lithics locate the vent on the Pre-Kameni island 1-2 km west of the modern town of Thira (Bond and Sparks, 1976; Druitt and Francaviglia, 1992; Heiken and McCoy, 1984). The second phase is composed of stratified phreatomagmatic base-surge and Plinian deposits showing that variable magma-water interactions occurred at this time (Bond and Sparks, 1976). A higher concentration of lithic blocks in SE Santorini suggests that the vent migrated along a fissure 2 km SW into the shallow caldera (Heiken and McCoy, 1984; Pfeiffer, 2001). The third phase of the LBA eruption is a massive, weakly stratified, phreatomagmatic ignimbrite. The gradation from well-stratified surge deposits to massive ash-flow deposits (Bond and Sparks, 1976) and low emplacement temperatures (0 to $>$ 250°C) inferred from paleomagnetic data (McClelland et al., 1990) reflect increasing water-magma ratios. Deposition of the low-mobility, wet pyroclastic flows beyond the caldera rim suggest that during phase 3 a large tuff-ring (Bond and Sparks, 1976; Sparks and Wilson, 1990) or a mega-tuff cone grew to fill and overtop the existing caldera (600 m high) (Johnston et al., 2014). Intense magma-water interactions ejected significant lithics up to 10 m in size (Pfeiffer, 2001) including both lavas and tuffs from the caldera floor and black glassy andesites from the Pre-Kameni island (Druitt, 2014). Most of the Pre-Kameni

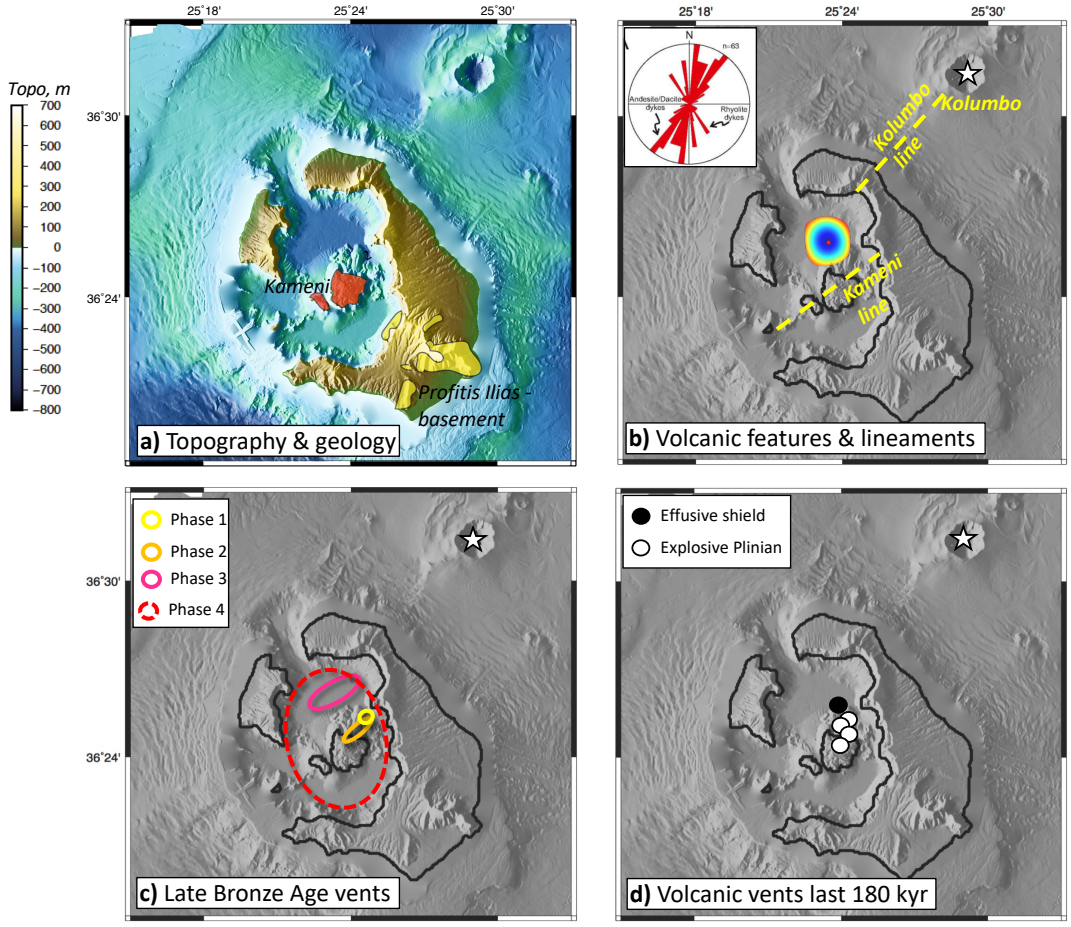

Figure 5.2. The geological and volcanic features of Santorini. (a) Map of the sea bottom and land topography (Hooft et al., 2017) showing outcrops of pre-existing basement (yellow) including at the summit of Profitis Ilias and post-caldera volcanism (red) of the Kameni islands. (b) Gray-scale map of topographic gradient showing the Mogi source at 4.5 km depth from GPS-InSAR inversion of 2011-2012 ground deformation (Parks et al., 2015) (red dot is best fit; colours RMS misfit). Volcanic features include Kolumbo seamount (star), the Kolumbo and Kameni lineaments (dashed blue lines), inset shows dike strikes(Browning et al., 2015) for the Kolumbo lineament. (c) Vent locations for the four phases of the Late Bronze Age explosive Plinian eruption. (d) Vents for the preceding 180 kyr of explosive Plinian eruptions (white) and effusive caldera-filling shields (black).

island is thought to have been ejected as lithics during this phase (Karátson et al., 2018). The presence of stromatolite clasts and distribution of large lithics around the northern part of the caldera (Friedrich et al., 1988) indicate that a large new vent opened in the northern caldera basin (Pfeiffer, 2001) (Heiken and McCoy, 1984). Pfeiffer (2001) argues that the existing phase 1 and 2 vents may have widened and remained active during this time (Figure 5.2c).

The fourth LBA eruption phase is a voluminous, hot ($300 - 500^{o}$C) pyroclastic flow erupted from multiple vents without interaction with water that deposited massive, fine-grained, non-welded ignimbrites in several fans on the coastal plains and in the surrounding sea (Bond and Sparks, 1976; Druitt et al., 1999; Heiken and McCoy, 1984; Sigurdsson et al., 2006; Sparks and Wilson, 1990). The high lithic content in this ignimbrite is considered unusual (Sparks and Wilson, 1990) and it contains metamorphic basement clasts especially in the units that erupted first indicating a deeper fragmentation front (Druitt, 2014). These observations point to caldera formation during this last eruption phase that deepened and expanded the existing caldera but remained isolated from the sea (Druitt, 2014; Heiken and McCoy, 1984).

After the LBA eruption ended the caldera flooded catastrophically when its NW rim breached (Nomikou et al., 2016a). A number of small-volume intra-caldera eruptions in the last 3.4 kyr built the Kameni islands (Nomikou et al., 2014; Pyle and Elliott, 2006) (Figure 5.2a). Seismic reflection imaging of intra-caldera fill reveals three units that thicken to fill a depression in the northern caldera basin (Johnston et al., 2015). An upper layer, Unit 1 is on average 20 m thick and consists of modern sediments deposited after the Kameni islands became subaerial. The underlying unit 2 is about 40-50 m thick and merges with the Kameni volcanics indicating it formed during post-LBA intra-caldera shallow-

water phreatomagmatism. Unit 3 is up to 150-200 m thick in the center of the northern caldera basin and in the southern caldera basin and is internally faulted. The authors interpret this unit to be downfaulted Minoan pyroclastic deposits that overlie pre-Minoan volcanic basement.

Recently, in 2011-2012, Santorini underwent an episode of unrest that included ground inflation consistent with a Mogi source of volume change 0.02 km^3 at 4.5 km depth (Parks et al., 2015) and seismic swarms on the Kameni lineament (Konstantinou et al., 2013; Papadimitriou et al., 2015) (Figure 5.2b). The Kolumbo and Kameni lineaments are alignments of volcanic vents and dikes within the Santorini edifice inferred to relate to tectonic extensional stresses and/or structures (Druitt et al., 1999) (Figure 5.2a) and the Kolumbo line extends from the Santorini volcanic complex toward the nearby Kolumbo seamount (Figure 5.2b).

5.3 Seismic experiment and data

Because Santorini's geological evolution and the latest caldera-forming eruption are well understood it is an ideal target for imaging the magmatic system of an arc volcano. We collected a dense, marine-land active source seismic dataset at Santorini volcano in the November-December of 2015. The PROTEUS experiment recorded ~14,300 controlled-sound sources from the 3600 cubic inch airgun array of the R/V Marcus Langseth on 90 ocean-bottom and 65 land seismometers and covered an area of 120 x 60 km^2 centered on Santorini (Figure 5.1).

The travel time dataset includes over 200,000 first arrival times of crustal refractions (Pg) that were picked first automatically and then manually (see Heath et al. in prep. for more details). Data were picked on either the hydrophone, vertical, and/or a stack of the hydrophone and vertical channels using a causal

4th order Butterworth filter of 5-25 Hz. Tens of thousands of high signal-to-noise arrivals were picked automatically using opendTect (https://www.dgbes.com) and were assigned one-sigma errors of 10 msec. One-sigma errors for the manual picks were visually assigned and ranged from 5 msec to 30 msec. The data set includes travel time arrivals for shots with ranges up to 65 km, with high quality data between 10-30 km at many stations.

5.4 Tomographic inversion and results

We obtained a high-resolution seismic image of caldera structure at Santorini using a seismic tomography method to invert first-arriving compressional wave travel times for a P-wave velocity model that includes land-sea elevation (Toomey et al., 1994). In this paper we present a seismic velocity model (Figures 5.3 & 5.4) that is a 25 km x 25 km x 3 km subset of a tomographic velocity model that covers the entire domain of the PROTEUS seismic experiment (see Heath et al. in prep. for more details).

5.4.1 Inversion

Heath et al. (in prep.) inverted the Pg travel time arrivals using a tomographic method that minimizes the prediction error and penalizes the magnitude and roughness of model perturbations (Toomey et al., 1994). The travel times were calculated using a shortest path algorithm (Moser, 1991). The seismic slowness model was gridded at 200 m and extended 125 km x 45 km x 12 km in the horizontal (x parallel to the shot lines) and vertical directions. The slowness model was sheared vertically to include the bathymetry (Toomey et al., 1994) and water wave travel times to the seafloor were calculated on a 50 m by 50 m elevation grid (water velocity = 1.52 km/s). The perturbational grid for the inverse problem

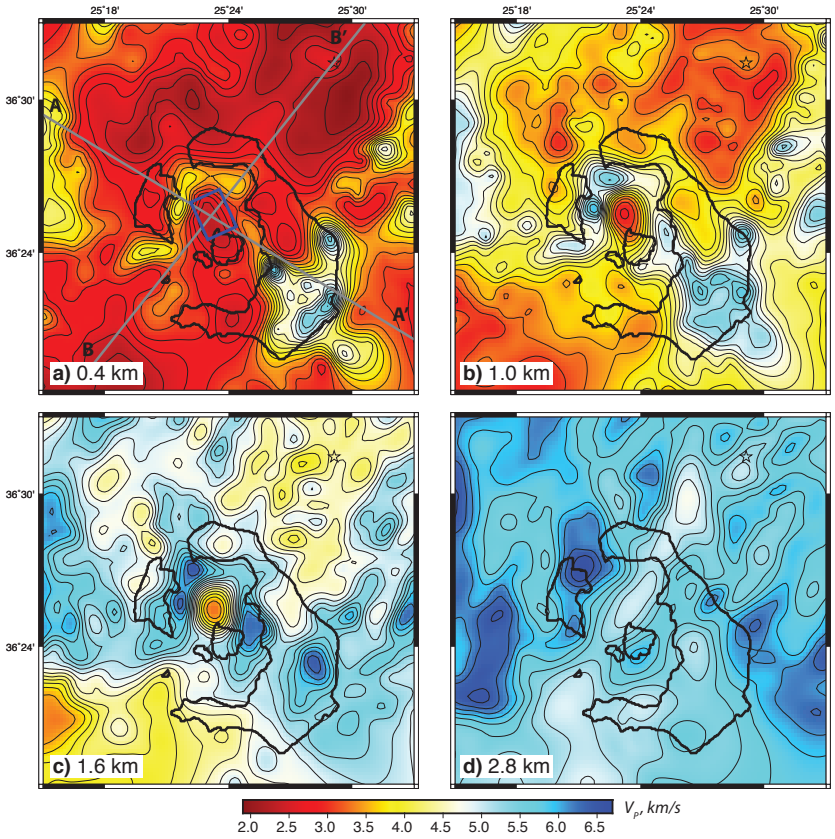

Figure 5.3. Maps of P-wave seismic velocity at Santorini. Depth slices through the tomographic model at 400 m (a), 1 km (b), 1.6 km (c) and 2.8 km (d) depth below the seafloor. Contour interval is 0.2 km/s. In (a) the grey lines show the profiles A-A' and B-B' in Figure 5.4 and the blue rectangle the area that was averaged to obtain the velocity-depth curve for the caldera profile in Figure 5.5a. Note the pronounced low-velocity anomaly between 1 and 2 km depth in the north-central caldera.

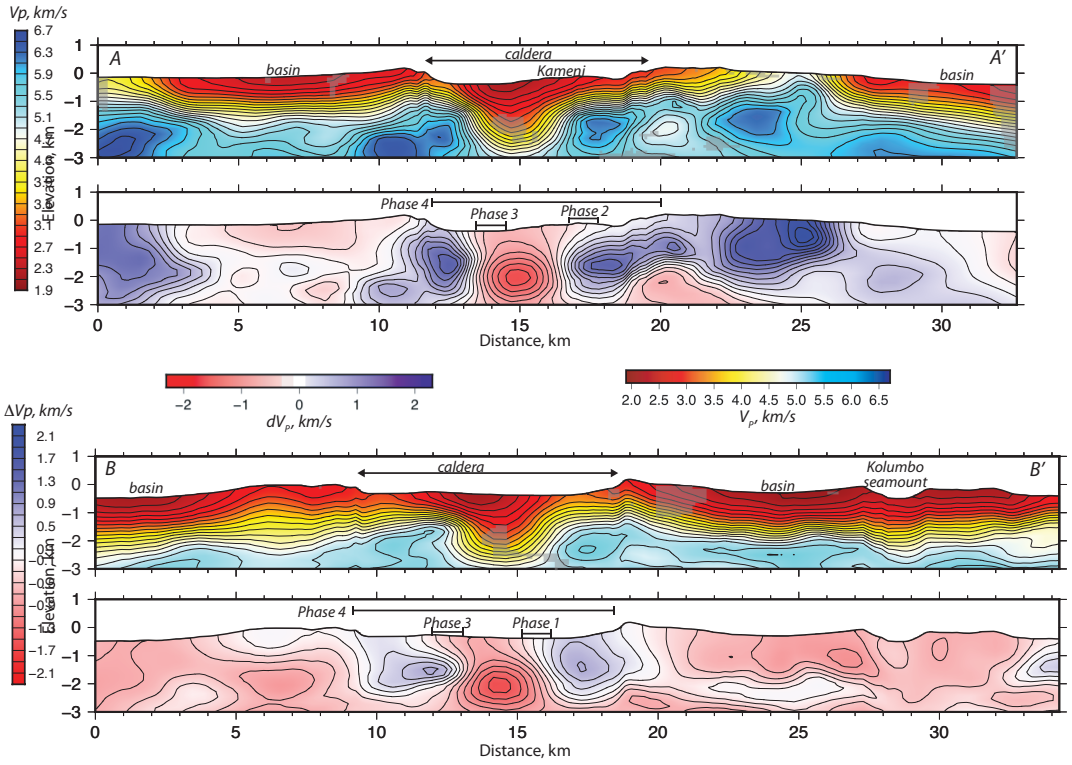

Figure 5.4. Cross-sections of seismic velocity along profile A-A' and B-B'. P-wave velocity and P-wave velocity anomalies relative to the velocity-depth structure of the Anydros metamorphic block (Figure 5.5a) along a NW-SE and a SE-NW profile. Contour interval is 0.2 km/s. Low velocities near the seafloor delineate sedimentary basins on the flanks of the volcano. The deeper low-velocity anomaly at 1-2 km depth north of the Kameni islands spatially correlate with the first three phases of the LBA eruption. The topographic caldera corresponds with phase 4 of the LBA eruption. Higher velocities are inferred to be due to metamorphic and/or plutonic rocks.

was spaced 400 m x 400 m x 200 m in the horizontal and vertical directions. New forward travel times are calculated after each iteration of the inverse problem (Toomey et al., 1994). Tens of inversions were conducted to determine the most appropriate inversion parameters. The final model used horizontal and vertical smoothing parameters of 200 and 100, respectively, and a penalty of 1 was used for model perturbations relative to the previous model. Each inversion consisted of 5 model iterations. The model presented here (Figures 5.3 & 5.4) was fit to a root mean squared misfit of 15 msec, which corresponds to a χ^2 of 2.2.

5.4.2 Synthetic tomography resolution tests

To analyze the resolution of features in the final model we conducted several synthetic tests. First, we superimposed sinusoidal checkerboard anomalies with horizontal wavelengths of 3 km and amplitude $\pm$0.25 km/s on top of the 1D velocity structure (Figure D.1). For the 1.6 and 2.8 km depth slices, the checkers had vertical wavelengths of 1 km and were centered at 1.6 km depth. Checkers were recovered with amplitudes 50-80% of the input values indicating that features of this size are well resolved. We note that the reversal of the sign of the velocity anomaly between 1.6 and 2.8 km depth is well recovered. For the 1.0 km depth slice the checkers had 2 km vertical wavelength and were centered at 1 km depth because the seismic rays average the structure above 1 km; recovery at this depth is 60-80%. Checkers beneath the center of eastern Santorini are not well recovered because of poor coupling of the island seismometers in the LBA ignimbrite deposits. Checkers south of Santorini are not well recovered because the seismic experiment did not sample this area.

In the second synthetic test we superimposed a cylinder with a 1 km/s velocity reduction at the location of the observed caldera low-velocity anomaly

(Figure D.2). The cylinder had diameter 3 km and height 4 km. Recovery is good down to about 3 km depth below which the recovery of the amplitude decreases. The width of the anomaly is reduced because the spatial smoothing constraint cannot recover the abrupt velocity change imposed in the synthetic model. Both resolution tests show that the magnitude of velocity anomalies will be under recovered in the tomographic inversion.

5.4.3 Tomography results

The seismic velocity structure of the uppermost crust at Santorini (Figures 5.3 & 5.4) reveals a pronounced cylinder of anomalously low velocities within the north basin of the caldera. Low velocities fill most of the upper ~400 m of the topographic caldera and their distribution reflects that of the three units of intra-caldera fill imaged using seismic reflection (Johnston et al., 2015) (Figure 5.3a & Figure D.3). The anomalous low-velocity cylinder lies below this (1-2 km depth) and is narrowly confined compared to the topographic caldera (diameters of 3 km and 10 km, respectively). It is located north of the Kameni islands and lies between the Kolumbo and Kameni lineaments (Figure 5.2b). The low-velocity anomaly extends down to 3 km depth, has a 3.0 ± 0.5 km diameter and, between 1 and 2 km depth, has a substantial velocity reduction of >2 km/s (VP ~3.2 km/s) compared to the surroundings (Figure 5.4). The velocity-depth gradient below 1 km differs from that of the surrounding metamorphic horsts (Figure 5.5a); velocities increase very slowly between 1 and 2 km depth, more rapidly from 2 to 2.5 km depth, followed by another gradual increase between 2.5 and 3 km depth (VP ~5.0 ±0.1 km/s). The low-velocity cylinder is unusual because it underlies only a portion of the caldera floor and has a significant reduction in velocity.

The low-velocity cylinder is surrounded by high-velocity rocks (VP of 5.7 - 6.5 km/s) (Figure 5.3). At depths less than 2.5 km, the high velocity regions are arc-shaped and contained within the northwest and southeast parts of the topographic caldera - a geometry indicative of solidified intrusives. At deeper depths high velocities extend beyond the caldera and are aligned NE, similar to the orientation of regional horsts of extended basement (Figure 5.3d). High velocities beneath southeast Santorini (5.5 km/s at 0.4 and 1 km depth) are located where metamorphic basement rocks outcrop at the surface (Figures 5.2a & 5.3a&b). Grabens between the associated horsts coincide with low-velocity sedimentary basins (Nomikou et al., 2016b; Piper and Perissoratis, 2003; Tsampouraki-Kraounaki and Sakellariou, 2018) northeast and southwest of the volcano (Figure 5.3 a&b). On the basis of these correlations, we infer that the anomalously high velocities are due to plutonic and metamorphic rocks.

5.5 Calculation of physical properties

To understand the subsurface structure of the Santorini caldera we infer physical properties from seismic velocity. Seismic velocities are controlled by various physical properties including composition, temperature, pressure, porosity, and the nature of the pore-filling material. We argue below that the observed low-VP anomaly between 1 and 2 km depth in the north central caldera is caused by increased porosity filled with hot seawater (Figure 5.5) and that the alternative where melt fills the pore spaces is unlikely.

We estimate the porosity required to explain the observed VP in the north central caldera by comparing the VP profile in the caldera to a reference VP profile for the basement (Figure 5.5 a & c). We first apply pressure and temperature corrections (Text D.1). While we take care to choose appropriate geotherms for

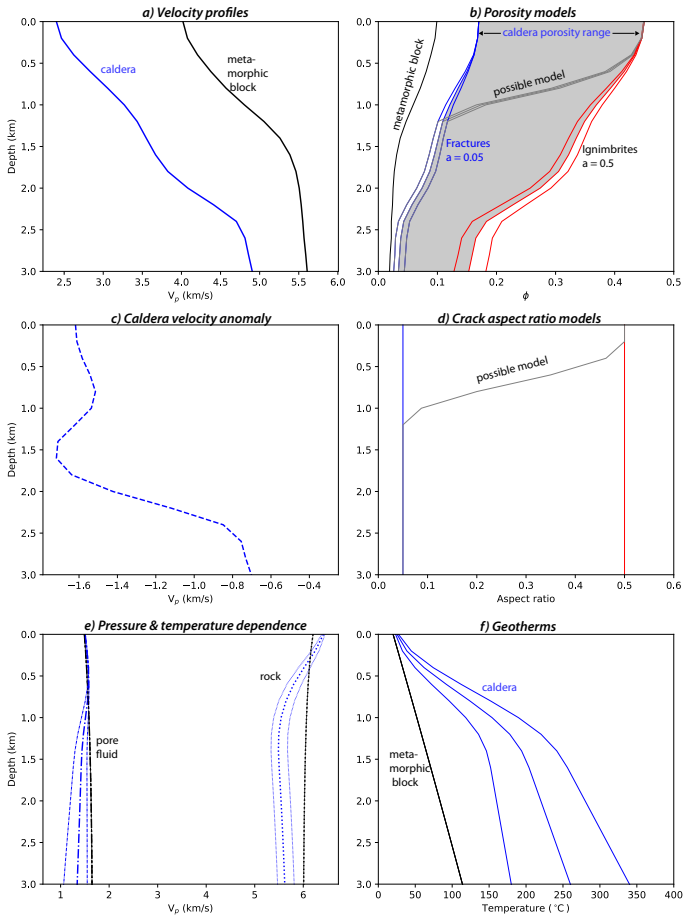

Figure 5.5. Predicted porosity for the northern caldera low-velocity anomaly and the reference metamorphic profile. (a) The velocity-depth structure of the caldera (blue) and the reference metamorphic profiles (black) obtained by averaging the velocity model over the blue and black rectangles in Figures 5.1 and 5.3, respectively. (c) The caldera velocity anomaly (dashed blue) is the difference between caldera and the reference metamorphic profiles in (a). (b) The porosity-depth structure is predicted for the reference profile (black) using a pore aspect ratio of 0.05 corresponding to cracks. The range of caldera porosity structures (grey field) corresponds to end-member pore aspect ratios from 0.5 (red) to 0.05 (blue) (d). A geologically motivated model where pore aspect ratio decreases with depth (grey) is also shown (b & d). (e) A correction to the predicted rock (dotted) and pore fluid (dot-dashed) velocities was applied for pressure and temperature effects of hot caldera (blue) and cooler reference (black) geotherms. (f) For the metamorphic profile we use 40^oC/km for a volcanic back arc. The hotter caldera geotherm is not well known and gradients that varied by $\pm 40^o$C/km (thin blue) and their corresponding effect on pore fluid and rock velocity and on predicted porosity are shown in (e) and (b), respectively. See Text D.1 for details.

the temperature correction the calculated porosities are far more sensitive to uncertainties in the pore aspect ratio than to uncertainties in the thermal structure (Figure 5.5). The reference metamorphic profile is generated using a rock of schists and limestones with VP = 6.5 km/s (Christensen and Stanley, 2003) and a background geotherm of 40°C/km. In the caldera we use a granitic rock with VP = 6.2 km/s (Christensen and Stanley, 2003) and a hotter geotherm estimated from measurements at Santorini and Milos. For the caldera geotherm, the pore fluid we model consists of hot seawater since the temperature remains below 370°C.

To estimate water-filled porosity we use a self-consistent effective medium approach that treats fluid inclusions as randomly oriented interconnected spheroids (Berryman, 1980). More recent treatments include anisotropy (e.g., Mainprice, 1997) or specific inclusions geometries (Jakobsen et al., 2000; e.g., Taylor and Singh, 2002) and are more complicated than warranted by our lack of knowledge of the subsurface microstructures. The elastic properties of the pore fluid are calculated for the temperature and pressure of each profile. For the metamorphic reference profile, we assume that the porosity is in the form of cracks with a pore aspect ratio of 0.05 and we obtain a porosity that decreases from 10% at the surface to 2% at 3 km depth (porosities between 1 and 2 km depth decrease from 7% to 3%) (Figure 5.5b).

For the caldera profile we consider two end-members for the porosity structure of the low-velocity anomaly (Figure 5.5b &d). In the first case we assume it consists of tuffs and ignimbrites with a pore aspect ratio of 0.5. This model is an upper bound for the porosity because of the low sensitivity of seismic velocity to relatively equant inclusions. We obtain a porosity of 37% to 27% between 1 and 2 km depth, which is an anomalous porosity relative to the reference profile by 30% to 24%. In the second case we assume that the low-velocity anomaly is due

to fractured igneous rocks with a pore aspect ratio of 0.05. This model provides a lower bound on the porosity because seismic velocity is very sensitive to crack-shaped inclusions. The resulting porosity is 12% to 7% between 1 and 2 km depth - an anomalous porosity relative to the reference profile of 5% to 4%. Using these two end members as bounds, the average anomalous porosity between 1 and 2 km depth ranges from 4 to 28% (Figure 5.5b).

A third geologically motivated structure might have pore aspect ratios that change with depth. One example is labelled “possible model" in Figure 5.5b & d and has ignimbrites and tuffs with aspect ratio 0.5 in the upper 750 m transitioning to fractured rocks with aspect ratio 0.05 beneath. The upper layer represents a ~150-m-thick layer of post-LBA deposits overlying a layer of ignimbrites and tuffs that is 200 to 600 m thick on the basis of seismic reflection imaging and geological models (Johnston et al., 2015; 2014). In this upper layer porosities are large, 45%, and the predicted porosity decreases rapidly at the depth where the pore aspect ratio becomes smaller. The unknown subsurface geology makes a range of models with depth-varying pore aspect ratios possible that would lie within the grey field in Figure 5.5. More accurate constraints on the physical properties and pore geometries can be obtained from joint analysis with shear waves (in particular Vp/Vs ratios), gravity modeling, and drilling within the caldera.

Although our preferred interpretation of the low-velocity volume at 1.5 km depth is water porosity at high temperature, a rhyolite or andesite partial melt could also explain the low VP. In this scenario we would attribute the VP anomaly to thermal effects up to the solidus and any further reduction of seismic velocity to melt using the same approach as above (Figure D.4). We isolate the portion of the VP anomaly in the caldera that cannot be explained simply with increased temperatures up to the solidus of andesite (800°C). For the pore fluid,

we use elastic properties for a silicic partial melt with a bulk modulus of 2.2 GPa and a density of 2300 kg/m^3. For melt we chose pore aspect ratios end-members of 0.05 and 0.2 for grain boundary and triple-junction geometries, respectively. This interpretation predicts melt fractions ranging from 13% to 26% at 1.5 km depth. For average porosities of 10% to 22% in a cylindrical volume, this implies 0.5 to 2.2 km^3 of melt between 1 and 2 km depth.

While some petrologic and geophysical studies have suggested shallow melt ponding at Santorini (Cottrell et al., 1999; Druitt et al., 2016; Saltogianni et al., 2014), we consider that a large volume of melt at shallow depths is inconsistent with most geological and geophysical observations of the current magmatic system. These observations include that: magma ponding depths of 4-6 km are inferred from melt inclusion saturation pressures for 726 AD Kameni lavas (Druitt, 2014); earthquakes extend down to at least 5 km depth during the recent unrest period (Konstantinou et al., 2013; Papadimitriou et al., 2015); and fluxes of magmatic gases and hydrothermal heat within the caldera are relatively low (Papadimitriou et al., 2015; Parks et al., 2013). Consequently, we infer the low-velocity anomaly beneath the north central caldera is caused by a cylindrical volume at 1-2 km depth with a porosity that is 4-28% higher than the local reference and is filled with high temperature water. This region is likely to be the main hydrothermal reservoir of Santorini (Tassi et al., 2013) and the potential for interaction between rising magma and water in the imaged high-porosity volume is a geo-hazard that needs to be further assessed.

5.6 Discussion

The discovery of an anomalous low-velocity, high-porosity cylinder at 1-2 km depth that is confined to the north central caldera (Figures 5.3 & 5.4) is new

and was not predicted by existing studies at Santorini. The seismic tomography and reflection data show the existence of two structures, respectively: (1) an inner cylinder of high porosity at 1-2 km depth, and (2) a surficial down-faulted zone of more coherent strata that is at most 200 m thick over the inner cylinder (Johnston et al., 2015). The geological observations show that over the history of the volcano there has been repeated intra-caldera growth followed by caldera collapse and that the vents for shield building and Plinian eruptions are located in the central caldera near the Kameni line. During the LBA eruption, phases 1 to 3 had vents located in the general area of the high-porosity cylinder and during phase 4 the caldera collapsed. These geologic observations may reflect the timing associated with the features in the seismic image.

Geological reconstructions of the pre-LBA caldera and its volcanic stratigraphy provide a starting structure that was modified during the LBA eruption and caldera formation (Figure 5.6a). This includes the remnants of the Skaros-Thirasia lava shields and their hyaloclastite cores that collapsed during the Cape Riva eruption to form the shallow pre-LBA caldera (Sparks and Wilson, 1990). We estimate a thickness of 400-600 m on the basis of the inferred 350-m elevation of the Skaros lava shield summit (Druitt et al., 1999; Heiken and McCoy, 1984). After the Cape Riva eruption and prior to the LBA eruption the Pre-Kameni island was built of black, glassy andesites and may also have had a hyaloclastite core. Most of the Pre-Kameni island is thought to have been ejected as lithics during the LBA eruption (Karátson et al., 2018). The primary low-velocity anomaly recovered in this study lies at 1-2 km depth and is located below these pre-existing deposits (Figure 5.6a).

The imaged low-velocity anomaly also lies between the Kolumbo and Kameni lineaments (KL2 and KL1, respectively in Figure 5.6a). These volcanic

alignments appear to be long-lived since numerous dikes lie parallel to the down-dropped graben of the Kolumbo line (Browning et al., 2015) and since earlier volcanic vents, both for intra-caldera effusive and Plinian explosive eruptions, lie near the Kameni line (Figure 5.2 a&b). These correlations suggest that the low-density column may have existed prior to the LBA event and be long-lived; to reflect this uncertainty we show it with a question mark in Figure 5.6a.

The observed seismic velocity structure correlates with the four phases of the LBA eruption as follows. The initial phase 1 and phase 2 vents (Druitt, 2014; Heiken and McCoy, 1984; Pfeiffer, 2001) are associated with the southeast boundary of the low-velocity cylinder (Figure 5.2c). The phase 3 vent is reconstructed within the shallow-water north caldera basin (Heiken and McCoy, 1984; Pfeiffer, 2001) approximately along the northern margin of the low-velocity cylinder (Figure 5.2c). Geological observations of several ignimbrite fans distributed around the caldera (Bond and Sparks, 1976; Druitt, 2014; Heiken and McCoy, 1984) and a diverse lithology of ejected rock debris (Druitt and Francaviglia, 1992) indicate that the entire topographic caldera subsided during phase 4 and we observe high velocities beneath the remainder of the caldera floor (Figure 5.2c). We argue that this last observation implies that the formation of the topographic caldera occurred by coherent down-drop of the larger caldera during the last phase of the LBA eruption (Figure 5.6c).

Below we explore three possible models for the formation of the inner seismic low-velocity anomaly (Figure 5.6b,d- f); the first two are motivated by the geological observations of the LBA eruption of Santorini, while the third is a general sequence for caldera formation. These scenarios are constructed as potential end-members and a combination of all three processes is possible.

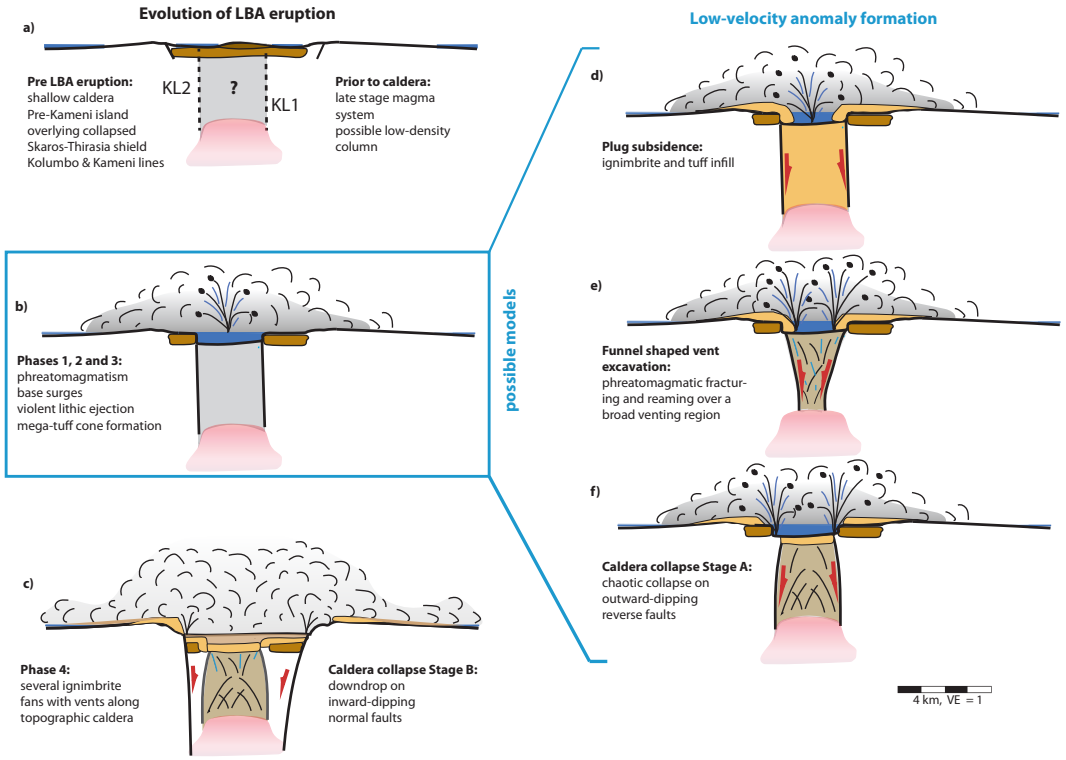

Figure 5.6. Conceptual model for the evolution of the LBA eruption and formation of the low-velocity anomaly. (a) Prior to the LBA eruption the Pre-Kameni island is located within a shallow caldera that overlies the collapsed Skaros-Thirasia shields with their hyaloclastite cores. The Kameni and Kolumbo lines (KL2 and KL1, respectively) exist and the magmatic system (red) is in a late stage of evolution. There may be a low-density column (grey) between KL2 and KL1. (b) The inner low-velocity anomaly at 1-2 km depth is spatially associated with phases 1, 2 and 3 of the LBA eruption that start Plinian and evolve to increasing magma-water interactions with violent lithic ejection and tuff formation. (c) Collapse of the topographic caldera and ignimbrite formation occurs during phase 4 of the LBA eruption. We infer the topographic caldera forms by down drop along inward-dipping normal faults potentially when accessing the deeper part of the magmatic system. Three possible models to form the inner low-velocity anomaly during phases 1 to 3 of the eruption are: (d) Subsidence of pre-existing caldera fill and infill with ignimbrites and tuffs; (e) Excavation by phreatomagmatic fracturing and reaming over a broad funnel-shaped venting region; (f) Inner caldera collapse along out-ward dipping reverse faults that fracture the pre-existing caldera fill.

5.6.1 Collapse plug filled with volcanic deposits

In the first scenario, the low-velocity cylinder is filled with tuffs and ignimbrite products (Figure 5.6d) and the average porosity between 1 and 2 km depth is high, ~32%. This interpretation requires extensive foundering of the low-velocity plug and infilling with eruptive products and is similar to that proposed for the larger Valles caldera (Lipman, 1997). Foundering and filling of this space may have happened entirely during the LBA eruption in which case pre-existing rock 3 km wide and 2 km deep (a cylindrical volume of 14 km^3) subsided into the collapsing magmatic system - an interpretation that is compatible with the volume erupted during LBA phases 1 to 3 (14 to 20 km^3 dense rock equivalent excluding the lithics (Karátson et al., 2018)). The correlation of the Kolumbo and Kameni lineaments with the margins of the low-velocity plug, suggests that these structural weaknesses could have facilitated large-scale foundering of the region between them accompanied by deposition of phreatomagmatic and pyroclastic products in the generated space. The inference that a tuff ring or mega-tuff cone ~600m tall grew within the caldera during phase 3 of the LBA eruption (Johnston et al., 2014) implies that the plug may have dropped at the end of phase 3 with a majority of the tuff products collapsing into it - in which case the stratigraphic layering observed in Unit 3 of the seismic reflection images of the LBA deposits within the caldera (Johnston et al., 2015) would correspond to overlying phase 4 ignimbrites.

Alternatively, the spatial association of earlier volcanic vents (Druitt et al., 1999) with the low-velocity cylinder, suggests that a tuff/ignimbrite-filled plug may have formed by repeated foundering and infilling of the same region over multiple eruptive cycles at Santorini. This interpretation is consistent with the apparent longevity of the Kolumbo and Kameni lines. In this case a lesser degree of foundering is needed during the LBA eruption and the structure is built up more

gradually. A further implication is that the margins of this pre-existing structure then provided pathways for, and localized, LBA vent formation during phases 1 through 3.

5.6.2 Phreatomagmatic rock breakup

Another possibility is that the high-porosity cylinder formed by rock breakup during the intensely phreatomagmatic phase 3 of the LBA eruption making a large diatreme-like structure (Figure 5.6e) (Escher, 1929; Sparks and Wilson, 1990). In this scenario, porosity is dominated by fractures and an average porosity of 9% between 1 and 2 km depth is inferred. Reaming and rock excavation undoubtedly took place given the energy required to eject up to 10 m lithics during phase 3 (Pfeiffer, 2001). The diatreme may also be the origin of the large tuff-ring proposed to explain deposition of phase 3 flows on the caldera rim (Sparks and Wilson, 1990). While analogue models of diatremes show that the ejected lithics are usually sourced from only a few 100 meters below the surface, it is possible that rock breakup from the powerful phreatomagmatic explosions as well as deep water penetration contributed to fracturing as deep as 1-2 km (Valentine et al., 2014). We consider this scenario less likely because the observed seismic anomaly (3 km wide at 1.5 km depth) is larger in spatial extent and depth than the largest studied diatremes, which are 2 km wide and 2 km deep and narrowing with depth(White and Ross, 2011).

However, this scenario has features that fit both the geology and the subsurface structure and more study is needed of the energy of large phreatomagmatic eruptions and how energy is partitioned between launching of material and sound waves into the atmosphere versus the spatial extent of hydrofracturing or damage by shock waves within the underlying rock. Numerical

simulations of rock damage by underground explosions suggest that damage extends well away from the cavity (e.g., Johnson and Sammis, 2001) and is more extensive below than above the explosion site (Ma et al., 2011). In addition, post-explosion well-logging studies reveal that explosions that are high in gaseous products or within water-filled media generate more extensive macrofractures (Stroujkova, 2018). Furthermore, studies of the mechanisms of deep-sea explosive eruptions show that, because the supercritical behavior of seawater is significantly different from that of fresh water, a vapor phase exists at super-critical pressures that is hydrodynamically unstable and results in explosive behavior at high pressures if the magma-water ratios and mixing mechanisms are right (Wohletz, 2003). Further understanding requires modeling of the accumulated damage pattern from repeated phreatomagmatic explosions and their spatial and depth extent given the inferred vent geometry and the fragmentation depth of phase 2 and 3 erupted products.

5.6.3 Multistage, nested caldera collapse

Our final scenario seeks to put the formation of both the intra-caldera, cylindrical, low-velocity region and the topographic caldera in a framework of evolving caldera deformation as magma continues to be withdrawn over the course of an eruption. In stage A of this scenario, chaotic collapse of the area between the phase 1, 2 and 3 vents occurred forming the high-porosity cylinder in the northern caldera (Figure 5.6f). We again speculate that either the vents formed along the Kolumbo and Kameni lines and consequently the area between them collapsed or that the cylindrical structure already existed and the LBA vents again formed along its boundaries during collapse (Figure 5.6f). Analogue studies show that instabilities during down drop of a 3D plug can cause vent location and eruptive

products to vary dramatically during subsidence (Kennedy et al., 2008), potentially explaining the temporal migration of vent locations during phases 1 through 3 and the variations in eruptive products during individual eruptive phases.

In the generalized caldera collapse models, the inner stage A involves breakup of the volume overlying the evacuating magma system by a number of reverse faults propagating upward (Figure 5.6f) (Roche et al., 2000; Scandone, 1990; Scandone and Acocella, 2007). If the volume between 1 and 2 km depth is dominated by fractured rock, the porosity is ~10%. If larger collapse blocks contribute more equant fractures the required porosity would be higher (Figure 5.5). Phase 4 ignimbrites likely fill the upper portion of the low-velocity collapse cylinder (Johnston et al., 2015) and the inferred porosity for a model where aspect ratio decreases with depth is illustrated in Figure 5.5. Alternatively, porosity may be higher from 1 to 2 km depth because of more intense brecciation below a transverse arch that develops within the collapsing column and acts to support the overlying material (Holohan et al., 2015; Scandone, 1990) (Figure 5.6f).

In stage B of this caldera formation scenario, the observation of high velocities beneath the remainder of the caldera (Figures 5.3 & 5.4) suggests that coherent subsidence of the entire topographic caldera to 500 m below sea level occurred during phase 4 of the eruption (Figures 5.6c). Resolved high velocities within the broader caldera could reflect down dropped Skaros-Thirasia shield lavas in the upper 500 m and/or igneous rocks along the caldera edges (Sakellariou et al., 2012).

In this scenario, the seismic and geological results from Santorini provide observational evidence for models of multistage, nested caldera formation during progressive caldera subsidence (Acocella, 2006). During stage A, the inner collapse column would be formed along outward-dipping reverse faults with breakup of the

roof rock (Figure 5.6g). During stage B, a new outer ring of collapse would cause subsidence of the entire topographic caldera and the opening of new vents during phase 4 (Figure 5.6d). This may also have caused an acceleration of the eruption by further pressurization of the magma system (Druitt and Sparks, 1984). In this scenario, the formation of the geologically distinctive LBA eruptive phases is a direct result of geological processes occurring during each stage of caldera formation (Figure 5.6).

It is quite possible that all three of the above scenarios (Figure 5.6 e-g) play a role in generating the inner cylinder of high porosities at Santorini. Thus, we consider it likely that rock breakup by reverse faulting during inner caldera collapse is accompanied by, or even promoted by, fracturing and reaming of the volcanic vent during violent magma-water interactions. In addition, the upper portions of the high-porosity cylinder are probably formed by the deposition of eruptive volcanic products including tuffs, pyroclasts, and ignimbrites.

5.6.4 Present day magma recharge

The spatial correlation of post-collapse volcanism with the upper crustal low-velocity volume suggests that present-day accumulation of magma in the upper ~5 km of the crust may be focused beneath the low-density column due to edifice stresses generated by both the low-density cylinder and the caldera topography (Figure 5.7). Since the 2011-2012 magmatic inflation episode (Parks et al., 2015) occurred directly beneath the low-velocity cylinder (Figure 5.2b), we suggest that a low-density cylinder within the caldera affects the dynamics of the underlying magmatic system. Previous authors have suggested that magma emplacement in the upper crust is influenced by stresses within the volcanic edifice due to topographic loads (Corbi et al., 2015; Muller et al., 2001; Pinel et al., 2017) and

internal structure (A. Gudmundsson, 1990; Karlstrom et al., 2009). Finite element calculations of edifice stress (Corbi et al., 2015) also show that volcano unloading caused by the topographic depression associated with caldera formation favors sill emplacement beneath the caldera floor because the least compressive stress becomes vertical. A low-density cylinder would unload the volcano in a similar way to caldera formation.

The relative importance of unloading by a low-density anomaly compared to that by caldera formation can be estimated from the lithostatic pressure at 4 km below sea level (Figure 5.7). We sum the contributions of the topography, the water column, and the crustal density calculated from seismic velocity using the relationships of Brocher (2005) at each grid point (Figure 5.7b-d). The predicted total lithostatic pressure varies from 85 to 120 MPa (Figure 5.7b) and has a minimum coincident with the seismic low-velocity anomaly. The topography of the volcanic edifice and the surrounding sea contribute variations of ~20 MPa to gravitational loading with a broad minimum throughout the caldera except beneath the Kameni islands (Figure 5.7c). The calculated differences in gravitational load due to density variations within the upper crust are ~14 MPa and have a pronounced low beneath the low-velocity anomaly (Figure 5.7d). While complete exploration of this idea requires modeling of edifice stresses, gravitational loading from internal density variations is likely to be important since the magnitude is comparable to that from topography (Figure 5.7c&d). The correlation of older volcanic vents with the low-velocity anomaly further suggests that a feedback between the internal structure of the volcanic edifice and localization of magma emplacement in the upper crust may have occured through several eruptive cycles at Santorini. Such a feedback would result in long-lived and actively, self-organized, centralized magmatic activity.

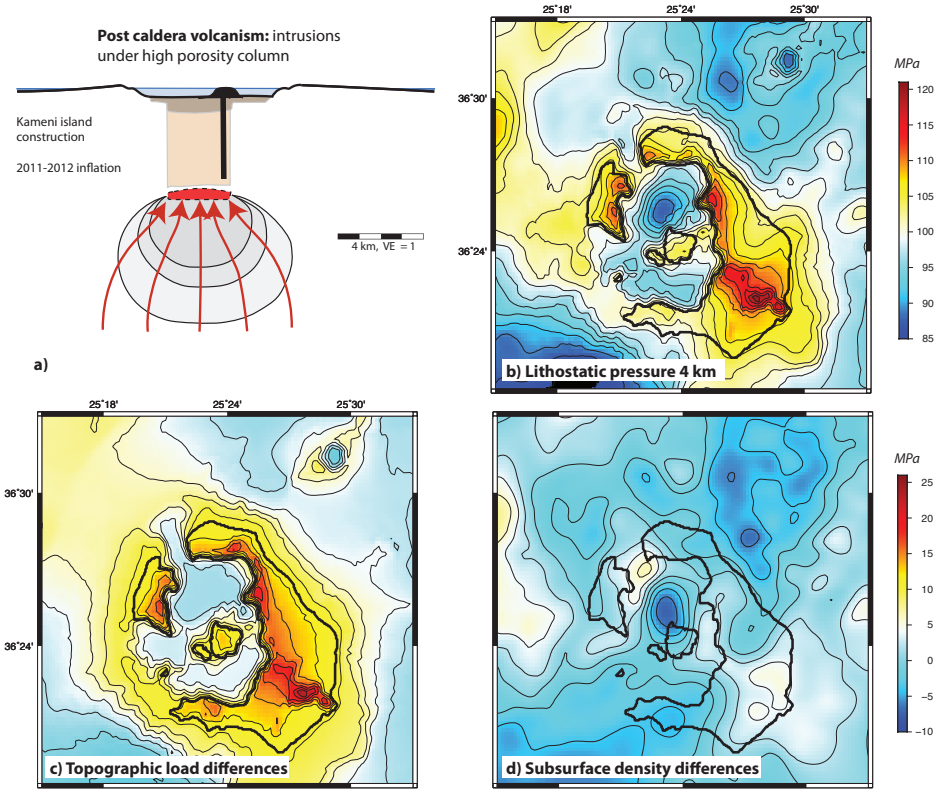

Figure 5.7. Comparison of the low-velocity anomaly with magma recharge during the 2011-2012 unrest and predicted lithostatic pressure at 4 km depth. (a) Conceptual model where unloading by the low-density column favors intrusion, such as the 2011-2012 inflation, beneath the low-density column. A simple lithostatic calculation suggests that spatial variations in unloading due to density variations in the upper crust are of similar magnitude to those due to unloading by the topography of the volcano. (b) Lithostatic pressure calculated from the seismic velocity model. The variations in gravitational load due the topography and the water column (c) are roughly equal to those from seismically-inferred crustal density variations (d). Contour interval is 2 MPa.

5.7 Conclusions

To understand caldera formation mechanisms at arc volcanoes we present a P-wave seismic velocity model of the upper crust at Santorini in the Hellenic volcanic arc of Greece. We find a low-velocity anomaly in the upper 1-2 km with diameter of 3 ± 0.5 km that is confined beneath the north-central portion of the caldera. We infer that this represents a volume of excess porosity of 4 to 28% filled with hot seawater and argue that the alternative where melt fills the pore spaces is unlikely. The Kolumbo and Kameni lineaments bound the margins of the anomaly and the locations of the vents for the first three phases of the Late Bronze Age eruption correlate with the imaged structure.

We combine our results with previous geological studies to infer that collapse of a limited area of the caldera floor resulted in a high-porosity, low-density cylindrical volume, which formed by either chaotic collapse along reverse faults, wholesale subsidence and infilling with tuffs and ignimbrites, phreatomagmatic fracturing, or a combination of these processes. Phase 4 eruptive vents are located along the margins of the topographic caldera and the velocity structure indicates that coherent down-drop of the wider topographic caldera followed more limited collapse in the northern caldera. This progressive collapse sequence is consistent with models for multi-stage formation of nested calderas along conjugate reverse and normal faults. If this model holds the geological processes during each stage of caldera formation produce the geologically distinctive eruptive phases of the LBA eruption. The pressure source of edifice inflation during 2011-2012 unrest lies at ~4.5 km directly beneath this cylindrical low-density anomaly and we hypothesize that sub-surface density anomalies influence present-day magma recharge.

The correlation of older volcanic vents with the low-velocity anomaly further suggests that this conduit vent system may be long-lived. We postulate that past

collapse mechanisms at Santorini influence magma focusing between eruptive cycles, an actively self-organized feedback process that may be important in other volcanoes.

CHAPTER VI

CONCLUSIONS

At Santorini, there is strong evidence for interaction between magmatism and tectonism. This evidence, outlined in Chapters 2 and 5, includes: i) localization of volcanic edifices within a basin structure, ii) arrangement of these edifices in a direction that parallels the strike of active faults, iii) correlation between regional fault orientation and the orientation of magmatic lineaments and dikes, iv) preferential localization of caldera centered vents between tectono-magamatic lineaments, v) a distinct brecciated region of caldera collapse/phreatomagmatic explosions that is bounded by these tectono-magmatic lineaments, vi) the association of a change in extensional direction with the initiation of magmatism, and vii) differing extensional styles depending on whether extension was accompanied or not by magmatism.

In Chapter 3, to investigate why tectonic activity and magmatism are correlated, I studied different scales of tectonic and magmatic interactions using anisotropic active source travel time tomography, a technique that distinguishes between regional scale faults (10s of km) and local faults/fractures (1s of km). Models for tectonic and magmatic interaction suggest that magmatic features may either increase local faulting/fracturing due to increased stresses or decrease faulting due to the accommodation of tectonic strain through diking. Here I find that regionally magmatic centers are uncorrelated with the magnitude of local scale faults/fractures, indicating that magmatism is neither inhibiting nor creating these faults/fractures. The orientation of magmatic lineaments and local scale faults/fractures, however, is approximately the same, indicating a shared response to broad stress patterns. I conclude, based on broad correlation between regions of magmatism and orientation and structure of regional faults, that the regional

stresses and regional faults control the emplacement of magma within the crust. Local scale faults/fractures, in turn respond to local-scale variations in this stress field. There is evidence that where local faults/fracture and magma intersect, magmatism is focused along the fault/fracture interface, however these results show that this is a passive process and that the intersection of magmatism and local faulting results from evolution of the regional stress field.

In Chapter 4, to investigate the temporal evolution of magmatic and tectonic interactions, I used Full Waveform Inversion (FWI) and anisotropic travel-time tomography, examining differences in the structure of basins that were associated/unassociated with time periods of magmatic activity, respectively. The structure of basins and horsts formed prior to the initiation of magmatism shows localization of both faulting and subsequent fault damage within the basin basement. In contrast, basins and horsts formed during time periods of magmatic activity show more distributed faulting, less focused deformation, and broader strain distribution. This distributed style of faulting can be due to the migration of faults resulting from a higher heat flux or due to an accommodation zone structure near Santorini that changes regional fault orientation/location and distributes strain over a larger area. Accommodation zones are often associated with volcanic centers, a feature thought to result from weakening of the crust from magmatism due to changes in rheologic properties, limiting the ability of the crust to form through-going normal faults.

These results outline styles of tectonic and magmatic interactions and their temporal evolution at Santorini. I highlight two of the most important aspects of tectonic and magmatic interactions. The first is that interaction between tectonic and magmatic activity is inherently scale dependent. Local-scale faults/stresses tend to have local impacts, regional scale faults/stresses exhibit regional impacts.

This likely holds true for magmatism as well. The second is that the style of interaction changes through time as systems evolve. Tectonism may focus and localize magmatic activity, magmatic activity may change tectonics through thermal and physical changes to the crust, this new tectonic activity may then further alter magmatism. To understand the current state of either tectonic or magmatic systems therefore requires understanding of the tectono-magmatic system.

APPENDIX A

APPENDIX CHAPTER II: TECTONISM AND ITS RELATION TO MAGMATISM AROUND SANTORINI VOLCANO FROM UPPER CRUSTAL P-WAVE VELOCITY

A.1 Description of Synthetics

: To analyze the resolution of features in the preferred model, we investigated ray path distribution and ran several synthetic models. We conducted checkerboard tests, superimposing sinusoidal checkerboard anomalies, with horizontal wavelengths of 3-10 km and vertical wavelengths of 1-4 km, on top of the 3-D velocity structure. 5 x 5 km checkers, with thickness 2 km and a velocity range of 0.5 km/s (+-0.25 km/s), were recovered well (Figure A.4). Checkerboards of similar anomaly magnitude and similar horizontal scale but that had a vertical scale of 1 km were well resolved at 2 and 3 km depths. However, in the basins, these checkers were poorly resolved above 2 km (e.g. Figure A.5, A.6) due to limited ray crossings and few rays turning at these depths (Figure A.8). In this case, the steep angle of incidence of waves through the upper two kilometers of the basins averages the opposite polarity of checkers from 0-1 and 1-2 km depth, respectively. Smaller checkers of 3 km by 3 km by 1 km were recovered in areas of dense ray coverage, areas that at shallow depths correspond to metamorphic horsts (Figure A.6, Figure 2.4).

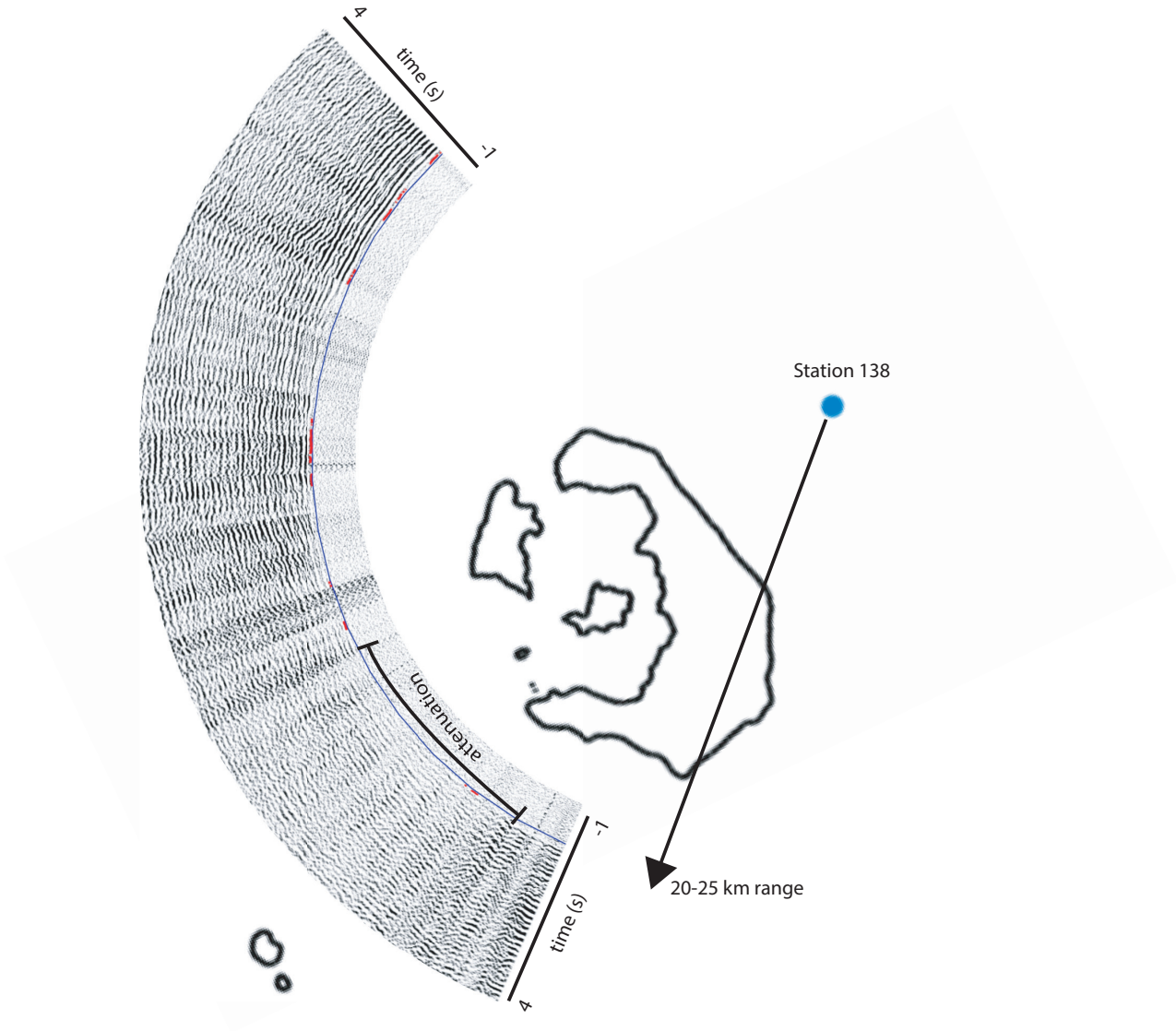

Figure A.1. Plot of recorded data for a station on the eastern side of Santorini (blue dot, station 138) with shots on the opposing side of Santorini at 20-25 km range. Shots going through the caldera show attenuation of first arriving energy. Data is filtered from 5 to 25 Hz and is aligned on the predicted arrival time from the 3-D velocity model (blue line) with picked arrival times shown (red dashes).

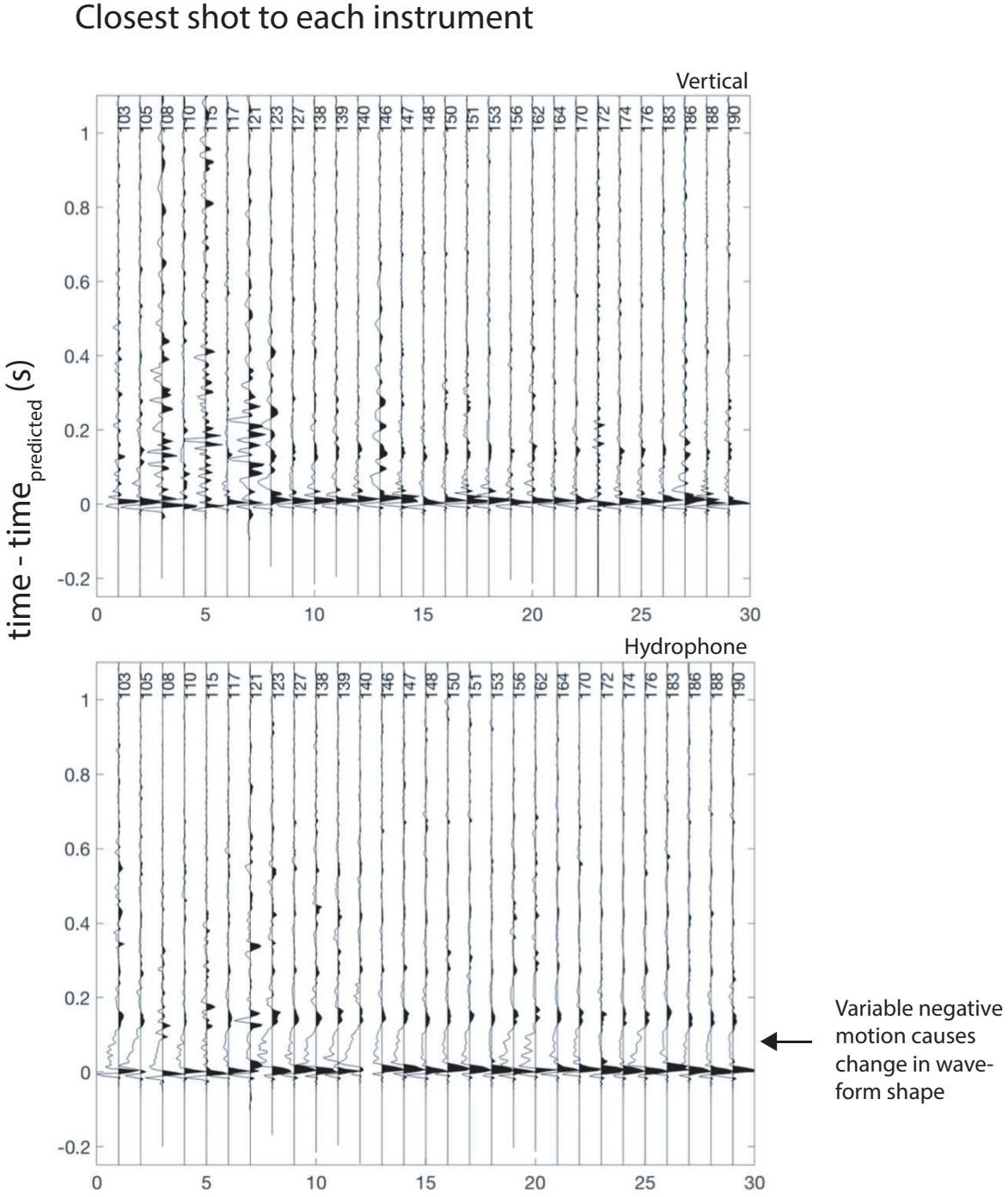

Figure A.2. First motions for closest shot (<1 km range) to each Woods Hole (WHOI) station, as recorded on both the unfiltered vertical and hydrophone channels, aligned on the predicted waterwave arrival time. Station number is plotted next to each trace. The vertical channel has a reasonably consistent signature whereas the hydrophone shows a variable amplitude negative pulse (labeled) after a high amplitude, high frequency positive pulse.

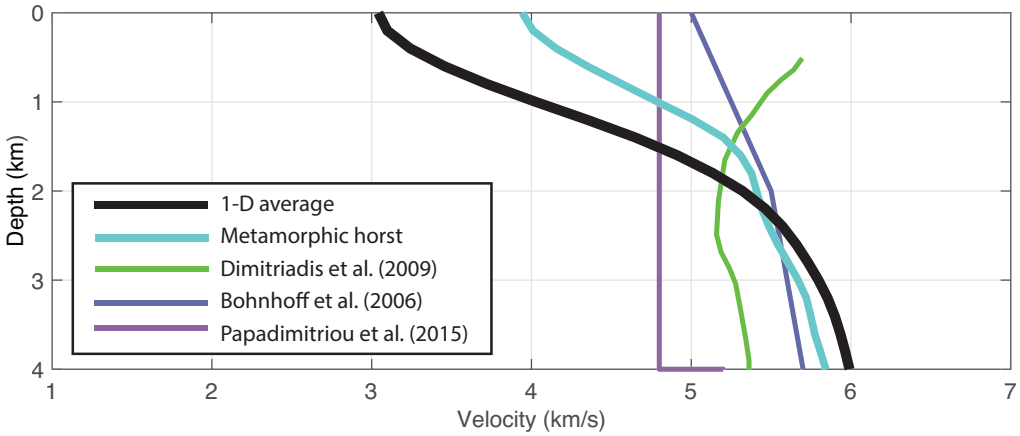

Figure A.3. Comparison between regional 1-D velocity profiles. This study (labeled 1-D average) has coverage in both the seimically slow basins and faster metamorphic horsts, whereas previous earthquake studies were biased against the seismically slow basins and thus had faster velocities at shallower depths. Comparison of recovered velocity of a metamorphic block (region shown in Figure 2.4) and previous velocity models from earthquake studies show greater agreement, although prior studies still tend towards faster velocities at shallow depths (0-2 km).

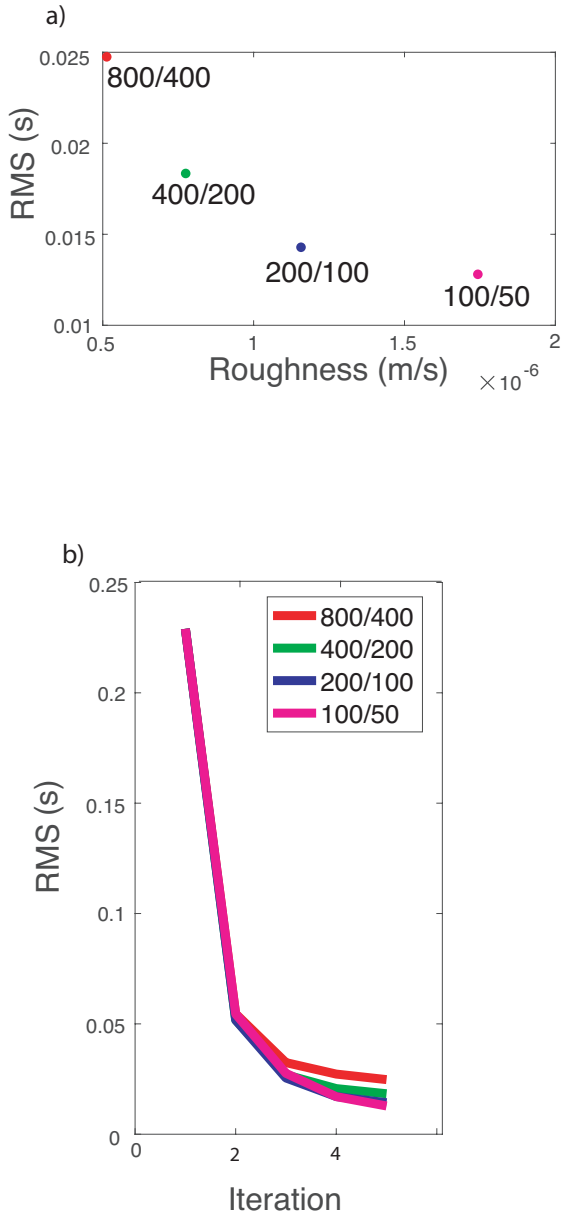

Figure A.4. Top: Roughness vs RMS of the travel time residual of the inversion for various smoothing weights (xy/z) shown by colored dots. Here roughness is measured using a Laplacian-style metric. Our preferred smoothing values are 200 and 100 for the xy and z values respectively. Bottom: Iteration vs RMS of the travel time residual of the inversion for various smoothing values (xy/z). The inversion converges towards a stable RMS after 5 iterations.

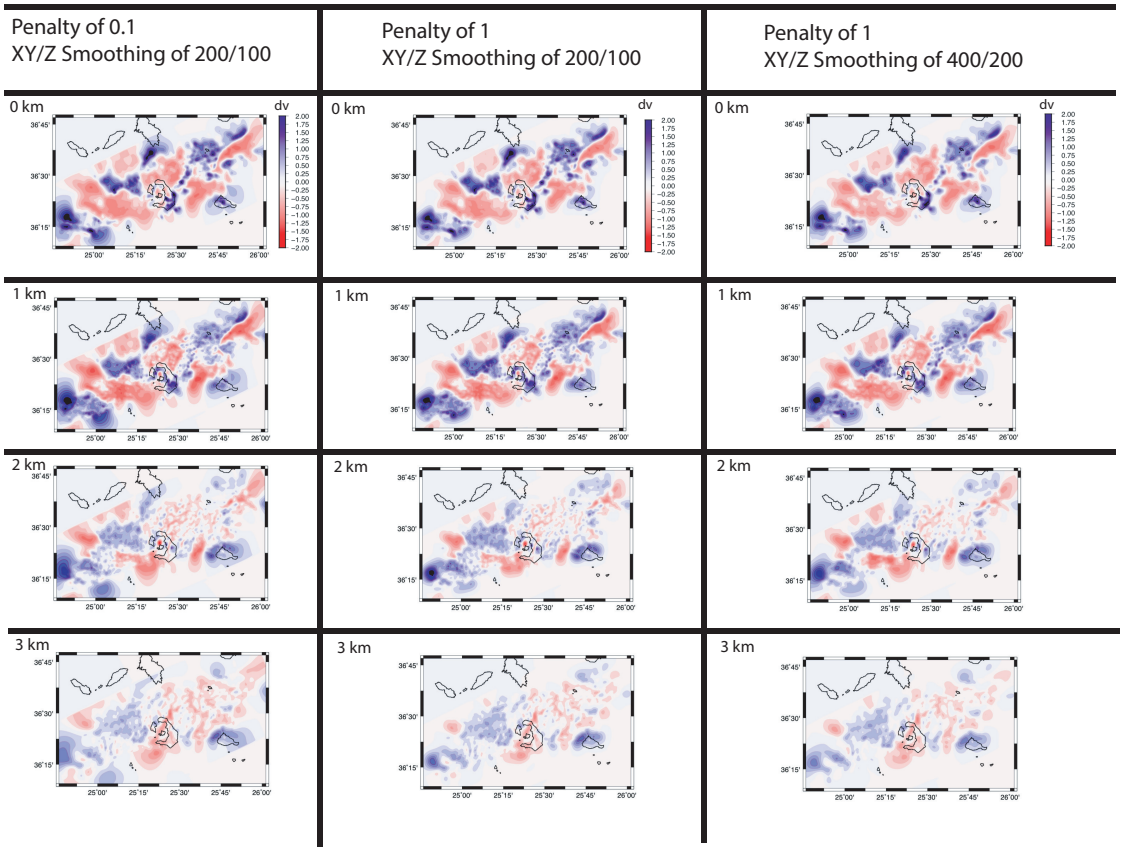

Figure A.5. Dv (km/s) variations at 0,1,2, and 3 km depth for an inversion where the penalty was varied (first column), an inversion following the preferred scheme (2nd column), and an inversion with higher smoothing (last column). The results across these distinct inversions are remarkably similar.

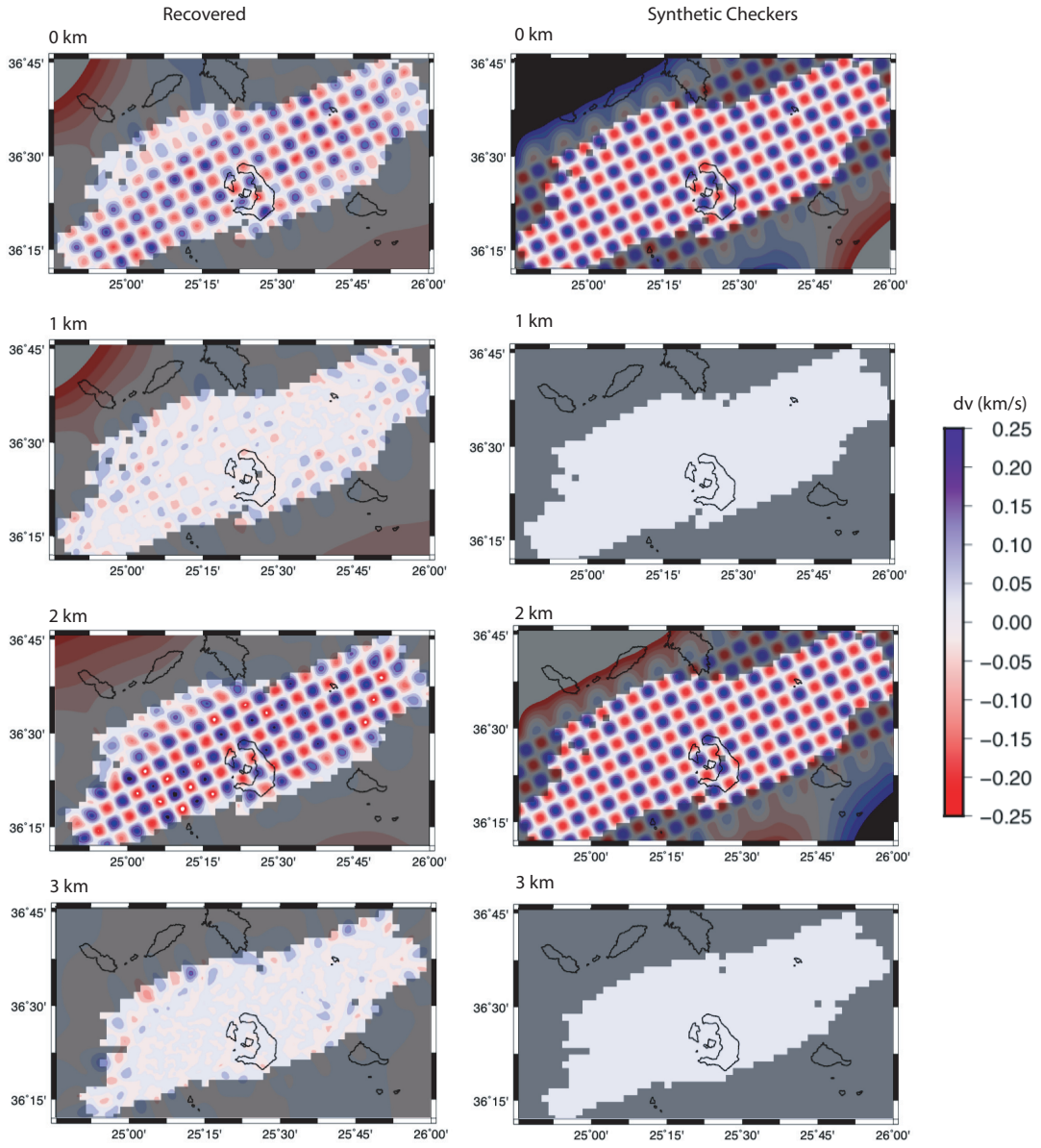

Figure A.6. Comparison between recovered and synthetic sinusoidal checkers with anomaly magnitude of +/- 0.25 km/s. Checkers are 5 km in the horizontal X and Y directions and 2 km in the vertical and were superimposed on the 3-D velocity structure (e.g., on Figure 2.5) and hence measure the resolvability to perturbations in the 3-D structure.

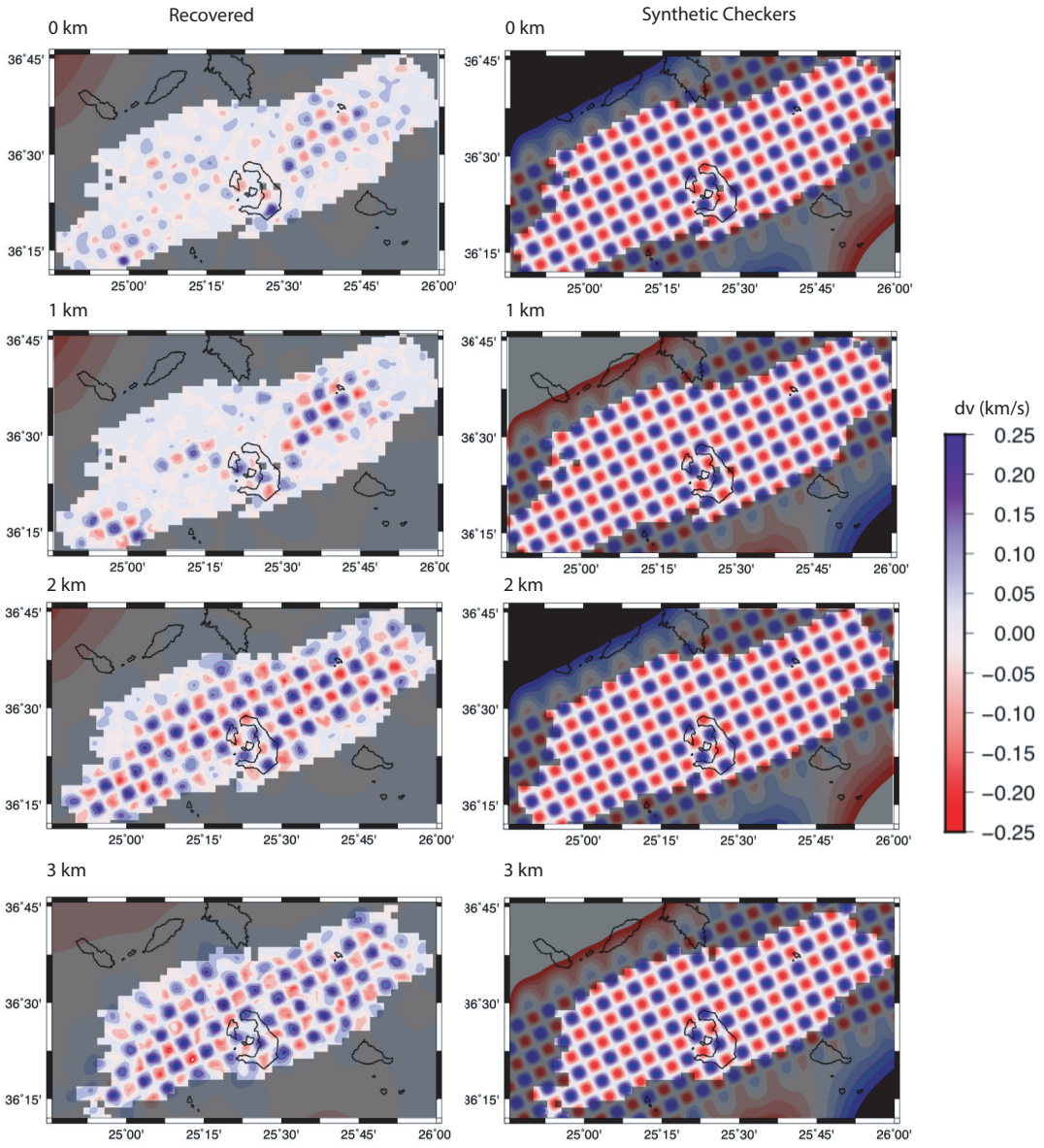

Figure A.7. Comparison between recovered and synthetic sinusoidal checkers with anomaly magnitude of +/-0.25 km/s and of size 5 km in the horizontal X and Y directions and 1 km in the vertical. Checker anomalies were superimposed on the recovered 3-D velocity structure. Coverage is poor at shallow 0-1 km depths due to poor ray coverage and near-vertical angle of incidence of rays in basin. Areas of good coverage at these depths correspond to areas of higher background velocity and shallower ray turning depths.

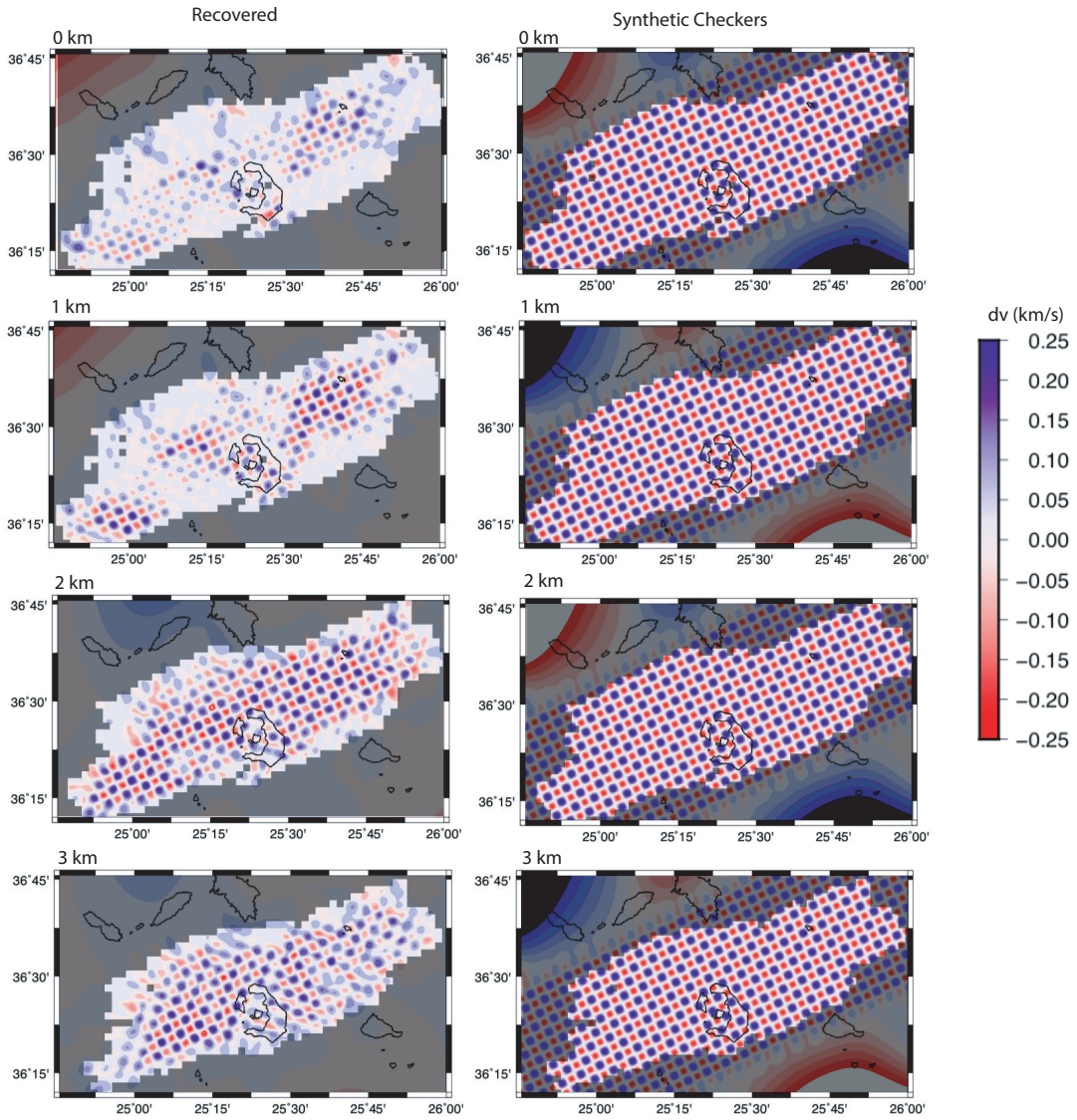

Figure A.8. Comparison between recovered and synthetic sinusoidal checkers with anomaly magnitude of +/- 0.25 km/s and of size 3 km in the horizontal X and Y directions and 1 km in the vertical. These tests show we are resolving most parts of the model at 2-3 km depth. The region around the caldera low velocity anomaly (e.g. Figure 2.10) does not show good coverage, a result of first arriving rays bending around the low-velocity anomaly.

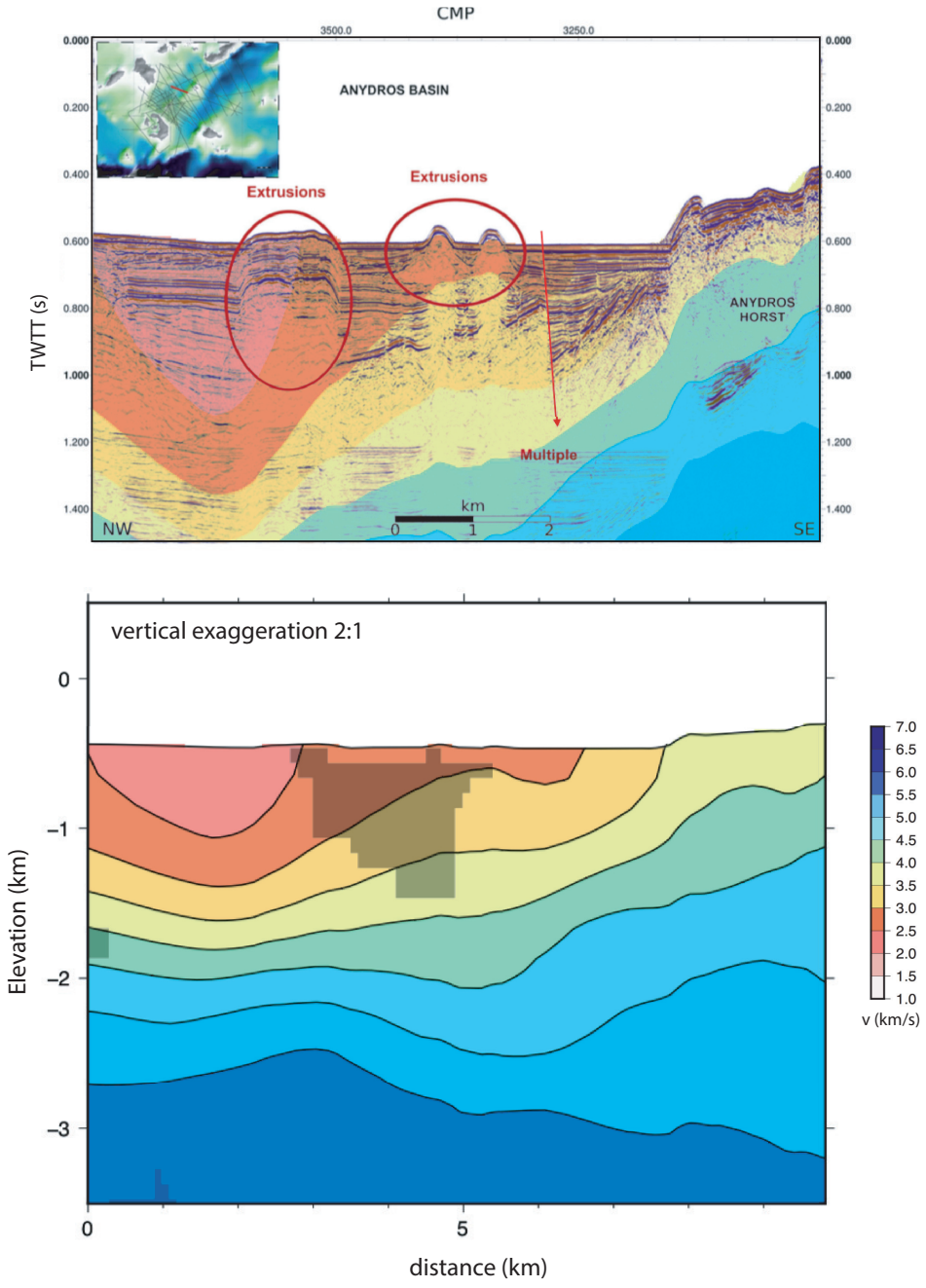

Figure A.9. a.) Comparison between the tomography velocity model (colored-overlay) and MCS reflection results along the Kolumbo volcanic chain. Tomography cross-section was converted from depth to two-way travel time (TWTT). MCS figure from *Nomikou et al.* (2016), Figure 5. b.) Results from tomography shown vs. elevation for the same area.

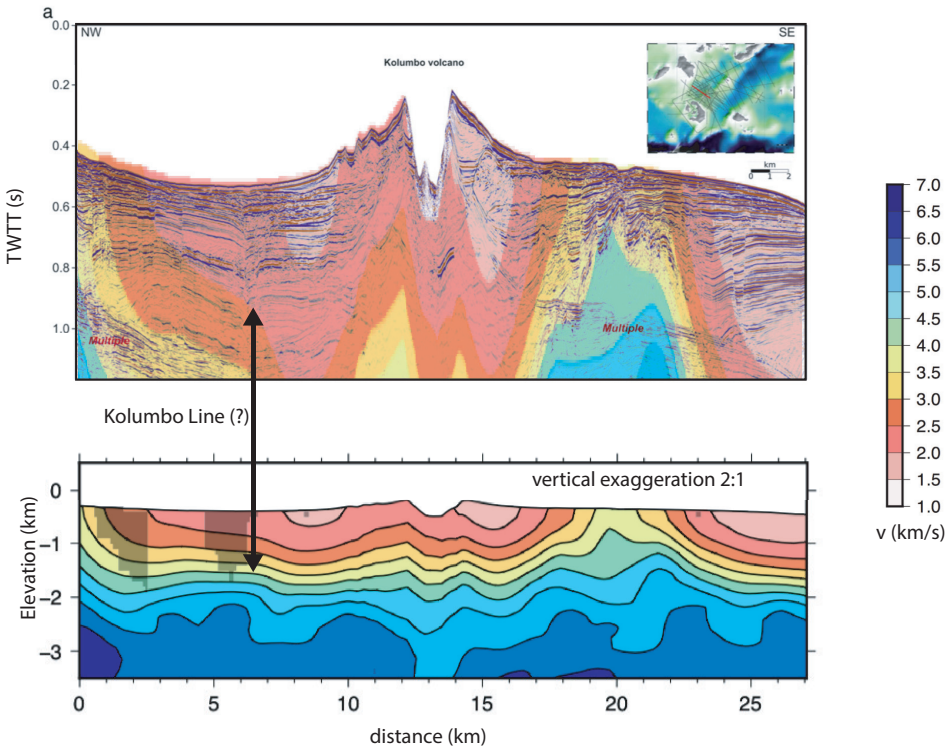

Figure A.10. a.) Comparison between the tomography velocity model (colored-overlay) and MCS reflection results crossing Kolumbo volcano. Tomography cross-section was converted from depth to two-way travel time. MCS figure from *Nomikou et al.* (2016), Figure 8. A small fault is observed in the MCS and tomography that may be related to the Kolumbo line, a tectono-magmatic line connecting the Santorini and Kolumbo volcanic systems. b.) Results from tomography, shown vs. elevation for the same area.

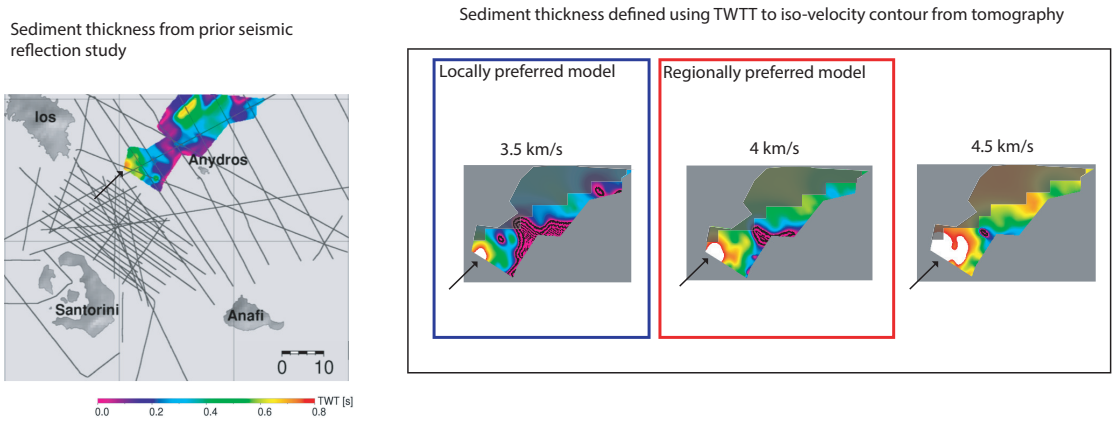

Figure A.11. Comparison of basin sediment thickness maps derived from the tomography model and a basin thickness map from a prior seismic reflection survey (*Nomikou et al.*, 2016). To define tomographic basin thickness we used the two-way travel time (TWTT) depth to an iso-velocity contour in the tomography model, using the the 3.5 km/s, 4 km/s and 4.5 km/s iso-velocity contours respectively. Black arrows show locations of small-scale changes in basin thickness observed in both the seismic reflection and tomography studies. While for this local area the 3.5 km/s iso-velocity best compares to the seismic reflection map, regionally the 4 km/s iso-velocity contour is favored.

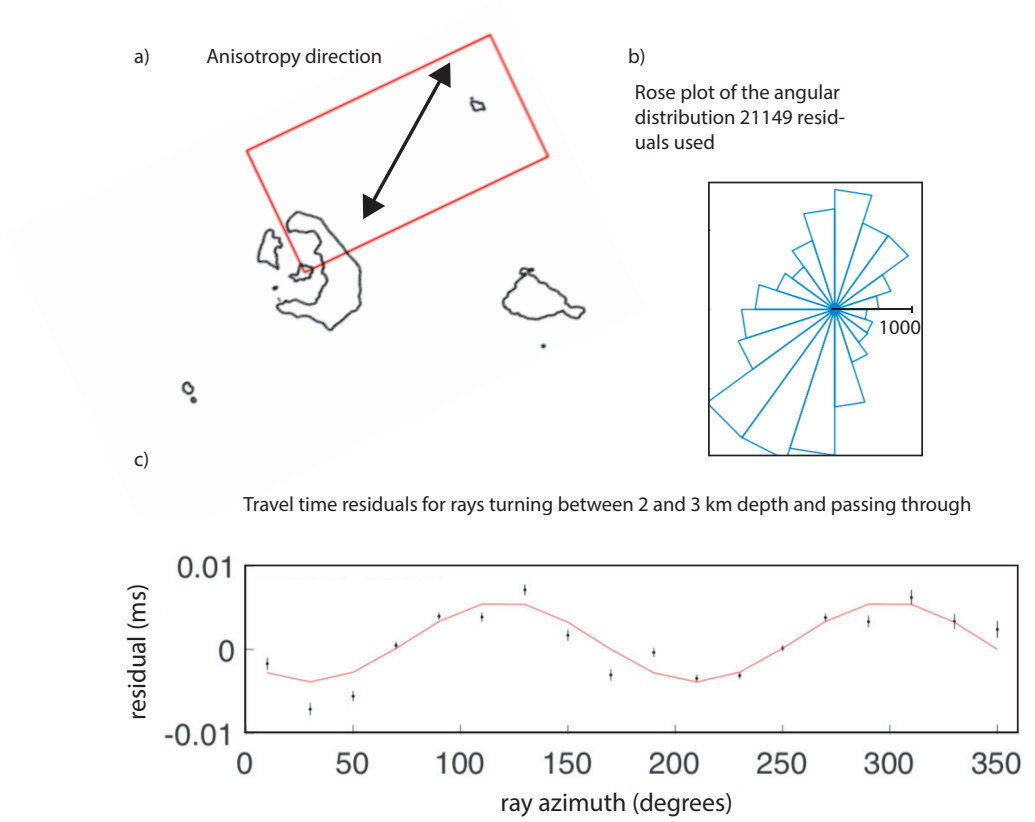

Figure A.12. To investigate anisotropy, we look for a $Acos(2\theta + \phi)$ pattern in the residuals of a subset of travel times. Here A relates to the magnitude of anistropy, θ represents ray azimuth and ϕ pertains to the azimuthal slow direction of anisotropy. a.) We use only residuals from rays that pass through the red box and have turning depths of 2-3 km. The recovered fast direction for anisotropy shown with arrow. b.) Rose plot showing the distribution of ray azimuths showing good azimuthal coverage. c.) Anisotropy plot showing mean and standard deviation of residuals from the tomographic inversion binned according to ray azimuth. Red line shows predicted anisotropy pattern (e.g., $Acos(2\theta + \phi)$ for fast direction shown with arrow in a).

Table A.1. Table showing the RMS of the travel time residuals for various smoothing weights and penalties. Rows 1-4 reflect inversions where the smoothing was varied. Rows 5-7 reflect inversions where the penalty was varied. Note the travel-time dataset used for rows 1-4 is different than that used from rows 5-7 and hence a direct comparison of RMS between these sets of inversions is not appropriate. Inversions marked with a * are shown in Figure A.5 and highlight the relatively small effect that reasonable smoothing weights and penalties have on the interpreted features in the tomography model.

Smoothing XY	Smoothing Z	Penalty	RMS
800	400	1	0.0235
400	200	1	0.0174*
200	100	1	0.0136*
100	50	1	0.0126
200	100	10	0.0151
200	100	1	0.0147
200	100	0.1	0.0157*

* Inversions shown in Figure A.5

APPENDIX B

APPENDIX CHAPTER III: RELATIONSHIP BETWEEN FAULTING AND MAGMATISM AROUND SANTORINI: SEISMIC ANISOTROPY RESULTS FROM A REFRACTION EXPERIMENT

B.1 Calculation of Resolution of Anisotropy

To calculate resolution of anisotropy, we look at azimuthal ray distribution across the experiment. We divide the model into 10 km x 10 km x-y grid. For each grid cell, we record the azimuth of the rays passing through it, assuming each ray is a straight line ray from source to receiver. Good anisotropy resolution in a grid cell is assumed to correlate with good azimuthal distribution, poor anisotropy resolution is assumed to correlate with poor azimuthal distribution. To quantify this azimuthal distribution, we bin the azimuths for the rays passing through each grid cell. An azimuthal bin is only considered "sampled" if it has a certain number of arrivals in it, defined as the *0.5(total arrivals in grid cell / total azimuthal bins)*, or half the number arrivals expected in each bin if the ray distribution was uniform. Bins with fewer than this threshold are considered empty. We calculate an azimuthal gap, which represents the largest range of consecutive bins for which we have no resolution. Azimuthal gaps $> 180^o$ for a given cell are considered to indicate no anisotropic resolution.

B.2 Applicability of Anisotropy Assumptions

In Figure B.1, I compare the applicability of equation 3.1 for measuring crack-induced anisotropy. I plot the true azimuthal velocities for a range of crack fractions (solid lines) and compare to modeled anisotropy using equation 3.1. At low fracture fractions, equation 3.1 almost perfectly reproduces the observed anisotropy. At higher fractions (e.g. $\epsilon = 0.5$) the fit is good and reproduces the

main structure of the anisotropy. These results validate the assumption of using equation 3.1 in modeling crack -induced anisotropy.

In Figure B.2, I model anisotropic velocities for a range of different anisotropy magnitudes and model their effective travel-times (assuming all waves travel 20 km). A $cos(2\theta)$ pattern is observed for all velocities (this is trivially a result of equation 3.1). However, only small anisotropy magnitudes show a $cos(2\theta)$ pattern in travel-times, a result of the fact that travel-time is inversely proportional to velocity.

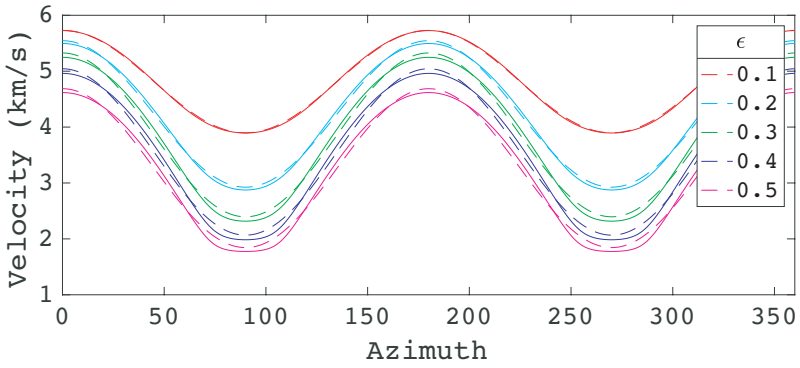

Figure B.1. Solid lines show velocities resulting from 0.1 aspect ratio oriented cracks embedded within a 6 km/s medium. Different colors represent different fractions of fractures. Dashed lines represent anisotropy approximated from equation 3.1. In general, there is good agreement between the approximated anisotropy and actual anisotropy.

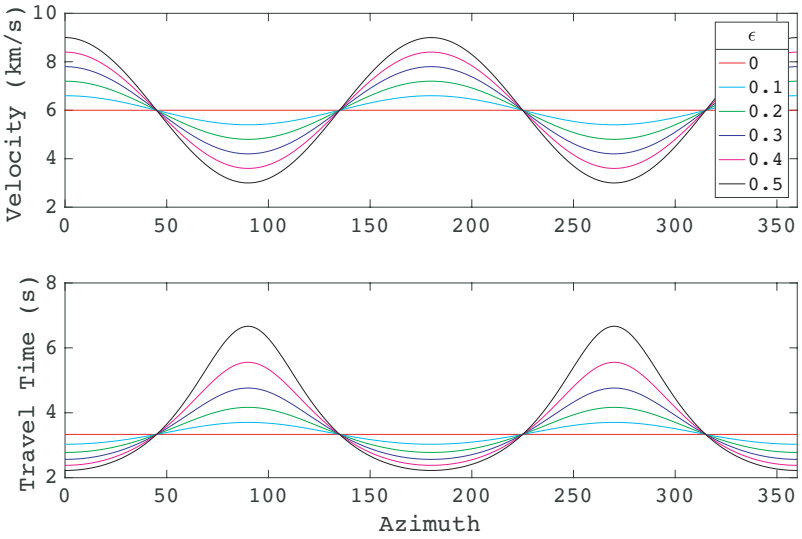

Figure B.2. Predicted velocities and travel-times as a function of azimuth for various different magnitudes of anisotropy. While velocities always show a $cos(2\theta)$ pattern, travel-times only exhibit a $cos(2\theta)$ pattern for small magnitude anisotropy.

APPENDIX C

APPENDIX CHAPTER IV: TECTONISM AND THE INFLUENCE OF INHERITED STRUCTURAL DEFORMATION AROUND SANTORINI FROM P-WAVE TOMOGRAPHY

C.1 Modeling Anisotropy

A simplified elliptical anisotropy system be written in the form (e.g. Dunn et al., 2005):

$$v = v_{iso}[1 + A\cos 2\theta + B\sin 2\theta] \tag{C.1}$$

where A and B are real numbers. Together A and B define a magnitude of anisotropy (ϵ) and a direction of anisotropy with respect to the x-axis (θ) through the following equations:

$$\epsilon = 2\sqrt{A^2 + B^2} \tag{C.2}$$

$$\theta_{x-axis} = tan^{-1}(B/A)/2 \tag{C.3}$$

To understand the role of fractures in determining the anisotropy magnitude and direction, we choose to solve a linear system of equations involving v_p, A and B (solving directly for ϵ and θ is not linear). We consider only forms of horizontal transverse isotropy (HTI) and consider only velocity variation in the horizontal plane. We can relate observed magnitude and direction of anisotropy as well as observed seismic velocity for $\phi = 0.1$ through the following equations:

$$\begin{aligned} v_p = v_{p_0} + \frac{\partial v_p}{\partial \phi_{\alpha=1}}\phi_{\alpha=1} + \frac{\partial v_p}{\partial \phi_{\alpha=0.1,\theta=\theta_1}}\phi_{\alpha=0.1,\theta=\theta_1} + \frac{\partial v_p}{\partial \phi_{\alpha=0.1,\theta=\theta_2}}\phi_{\alpha=0.1,\theta=\theta_2} + \\ \frac{\partial v_p}{\partial \phi_{\alpha=0.1,\theta=\theta_3}}\phi_{\alpha=0.1,\theta=\theta_3} + \frac{\partial v_p}{\partial \phi_{\alpha=0.1,\theta=\theta_4}}\phi_{\alpha=0.1,\theta=\theta_4} \end{aligned} \tag{C.4}$$

$$A = A_0 + \frac{\partial A}{\partial \phi_{\alpha=1}}\phi_{\alpha=1} + \frac{\partial A}{\partial \phi_{\alpha=0.1,\theta=\theta_1}}\phi_{\alpha=0.1,\theta=\theta_1} + \frac{\partial A}{\partial \phi_{\alpha=0.1,\theta=\theta_2}}\phi_{\alpha=0.1,\theta=\theta_2} + \frac{\partial A}{\partial \phi_{\alpha=0.1,\theta=\theta_3}}\phi_{\alpha=0.1,\theta=\theta_3} + \frac{\partial A}{\partial \phi_{\alpha=0.1,\theta=\theta_4}}\phi_{\alpha=0.1,\theta=\theta_4} \tag{C.5}$$

$$B = B_0 + \frac{\partial B}{\partial \phi_{\alpha=1}}\phi_{\alpha=1} + \frac{\partial B}{\partial \phi_{\alpha=0.1,\theta=\theta_1}}\phi_{\alpha=0.1,\theta=\theta_1} + \frac{\partial B}{\partial \phi_{\alpha=0.1,\theta=\theta_2}}\phi_{\alpha=0.1,\theta=\theta_2} + \frac{\partial B}{\partial \phi_{\alpha=0.1,\theta=\theta_3}}\phi_{\alpha=0.1,\theta=\theta_3} + \frac{\partial B}{\partial \phi_{\alpha=0.1,\theta=\theta_4}}\phi_{\alpha=0.1,\theta=\theta_4} + \tag{C.6}$$

To describe all possible values of the magnitude and direction of HTI anisotropy in the horizontal plane using a priori fractures requires a minimum of 3 sets of fractures. Each point in the $A - B$ parameter space represents a unique anisotropy field (magnitude and orientation). Each individual fracture can be thought of as a line in this $A - B$ space stretching from the origin to some point (A_0, B_0) which represents the anisotropy resulting from some fracture fraction. Because we are limited to the positive addition of fractures we can only move from the origin towards (A_0, B_0). Mathematically this corresponds to the requirement that ϕ is positive. Because of this limitation,we require a minimum of three sets of fractures to span the 2-D $A - B$ space. Here we assume 5 sets of fractures (one for each quadrant in $A - B$ space and one for v_p)) to define this anisotropy set. We discuss limitations of these assumptions below.

In the above equations, v_{p_0} represents the unaltered velocity, and A_0 and B_0 together inform the magnitude and fast direction of anisotropy of the unaltered metamorphic rock. We then impose 5 types of fractures at various fractions on this unaltered rock: $\phi_{\alpha=1}$ which represents randomly distributed fractures and which does not contribute to the overall anisotropy magnitude nor direction (e.g. aspect ratio of 1), $\phi_{\alpha=0.1,\theta=\theta_1}$ which represents 0.1 aspect ratio fractures oriented with fast direction in the θ_1 direction, $\phi_{\alpha=0.1,\theta=\theta_2}$ which represents 0.1 aspect ratio fractures oriented with fast direction in the θ_2 direction, $\phi_{\alpha=0.1,\theta=\theta_3}$ and $\phi_{\alpha=0.1,\theta=\theta_4}$. Here we

assume $\theta_1 = 130^o$, $\theta_2 = 90^o$, $\theta_3 = 30^o$ and $\theta_4 = 0^o$, all with respect to N. $\theta_1 = 130^o$ represents the fracture orientation of the boundary faults within the Christiana basin, $\theta_2 = 90^o$ represents the fracture orientation of deeper set faults within the Christiana basin and the inferred strike of faults associated with N-S extension, $\theta_3 = 30^o$ represents the orientation of faults in the Anydros basin (eastern side of Santorini) that are thought to extend through Santorini to the Christiana basin (Heath et al., 2019), and $\theta_4 = 0^o$ represents N-S oriented anisotropy to incorporate anisotropic effects resulting from inherited ductile N-S extension. These θ can be converted into θ_{x-axis} through $\theta_{x-axis} = 90 - \theta_{grid} - \theta$ where θ_{grid} is the counter clockwise rotation of the cartesian coordinate system around the z axis. These equations can be rewritten by solving for perturbations to the overall velocity and anisotropy:

$$\begin{bmatrix} \delta v_p \\ \delta A \\ \delta B \end{bmatrix} = \begin{bmatrix} \frac{\partial v_p}{\partial \phi_{\alpha=1}} & \frac{\partial v_p}{\partial \phi_{\alpha=0.1,\theta=130^o}} & \frac{\partial v_p}{\partial \phi_{\alpha=0.1,\theta=90^o}} & \frac{\partial v_p}{\partial \phi_{\alpha=0.1,\theta=30^o}} & \frac{\partial v_p}{\partial \phi_{\alpha=0.1,\theta=0^o}} \\ \frac{\partial A}{\partial \phi_{\alpha=1}} & \frac{\partial A}{\partial \phi_{\alpha=0.1,\theta=130^o}} & \frac{\partial A}{\partial \phi_{\alpha=0.1,\theta=90^o}} & \frac{\partial A}{\partial \phi_{\alpha=0.1,\theta=30^o}} & \frac{\partial A}{\partial \phi_{\alpha=0.1,\theta=0^o}} \\ \frac{\partial B}{\partial \phi_{\alpha=1}} & \frac{\partial B}{\partial \phi_{\alpha=0.1,\theta=130^o}} & \frac{\partial B}{\partial \phi_{\alpha=0.1,\theta=90^o}} & \frac{\partial B}{\partial \phi_{\alpha=0.1,\theta=30^o}} & \frac{\partial B}{\partial \phi_{\alpha=0.1,\theta=0^o}} \end{bmatrix} \begin{bmatrix} \phi_{\alpha=1} \\ \phi_{\alpha=0.1,\theta=130^o} \\ \phi_{\alpha=0.1,\theta=90^o} \\ \phi_{\alpha=0.1,\theta=30^o} \\ \phi_{\alpha=0.1,\theta=0^o} \end{bmatrix} \tag{C.7}$$

Here we follow the results from the previous chapter that look at anisotropy magnitudes resulting from various different orientation fractures, superimposed on a anisotropic metamorphic medium. We do not consider the relative interaction between superimposing two distinct fracture networks of distinct orientations and instead make the simplifying assumptions that their effects add linearly. Using

these results we can rewrite equation C.7:

$$\begin{bmatrix} \frac{\partial v_p}{\partial \phi_{\alpha=1}} & \frac{\partial v_p}{\partial \phi_{\alpha=0.1,\theta=\theta_{130^o}}} & \frac{\partial v_p}{\partial \phi_{\alpha=0.1,\theta=\theta_{90^o}}} & \frac{\partial v_p}{\partial \phi_{\alpha=0.1,\theta=\theta_{30^o}}} & \frac{\partial v_p}{\partial \phi_{\alpha=0.1,\theta=\theta_{0^o}}} \\ \frac{\partial A}{\partial \phi_{\alpha=1}} & \frac{\partial A}{\partial \phi_{\alpha=0.1,\theta=\theta_{130^o}}} & \frac{\partial A}{\partial \phi_{\alpha=0.1,\theta=\theta_{90^o}}} & \frac{\partial A}{\partial \phi_{\alpha=0.1,\theta=\theta_{30^o}}} & \frac{\partial A}{\partial \phi_{\alpha=0.1,\theta=\theta_{0^o}}} \\ \frac{\partial B}{\partial \phi_{\alpha=1}} & \frac{\partial B}{\partial \phi_{\alpha=0.1,\theta=\theta_{130^o}}} & \frac{\partial B}{\partial \phi_{\alpha=0.1,\theta=\theta_{90^o}}} & \frac{\partial B}{\partial \phi_{\alpha=0.1,\theta=\theta_{30^o}}} & \frac{\partial \theta}{\partial \phi_{\alpha=0.1,\theta=\theta_{0^o}}} \end{bmatrix} = \begin{bmatrix} -4 & -17 & -17 & -17 & -17 \\ 0 & -1.433 & 1.3845 & 0.7884 & -1.3845 \\ 0 & -1.6604 & -1.7097 & 2.0539 & 1.7097 \end{bmatrix} \tag{C.8}$$

The values for $\frac{\partial A}{\partial \phi}$ relate to $\frac{\partial \epsilon}{\partial \phi}$ through $\frac{\partial A}{\partial \phi} = \pm \frac{\partial \epsilon}{\partial \phi} 2(1 + \tan^2 2\theta_{x-axis})^{0.5}$, the sign of which depends on the anisotropy fast direction. The derivative for B is $\frac{\partial B}{\partial \phi} = \tan 2\theta_{x-axis} \frac{\partial A}{\partial \phi}$. Here $\frac{\partial \epsilon}{\partial \phi}$ is constant for $\alpha = 0.1$ and so the variation in $\frac{\partial A}{\partial \phi}$ and $\frac{\partial B}{\partial \phi}$ results entirely from differences in fault orientations. This indicates that the magnitude of anisotropy produced from given oriented cracks is not a function of crack orientation, but the fast-axis orientation of such a medium is a function of the orientation of the imposed cracks.

The matrix in equation C.8 is mathematically non-unique (we have 3 unknowns and 5 uncoupled variables). However, because we restrict all ϕ to be positive, we can individually exclude columns from C.8 to artificially make the matrix solvable. To span the entire anisotropy $A - B$ space using positive ϕ we need only 3 anisotropy producing variables (because the space the $A - B$ space is 2-D, uniqueness of a solution is not guaranteed). Here we have 4 anisotropy producing variables (the 5th variable $\phi_{\alpha=1}$ does not contribute to anisotropy). Because the orientations of fractures are geologically motivated, we choose to include all 4 variables at the expense of non-unique results.

To solve equation C.7, we choose to exclude two ϕ values. leaving 3 total variables. We select two anisotropy producing fractures for each anisotropy point: the closest fracture orientations in a clockwise and counterclockwise direction

in $A - B$ space to the anisotropic orientation of the point. Because we have 4 anisotropy producing variables that describe a 2-D space (and we only need 3 variables to entirely span this space), this artificial limitation of fracturing is inherently non-unique. We always include the $\phi_{\alpha=1}$ variable, which produces no anisotropy and only drops velocity.

There are several caveats to this approach. First, we are limited to anisotropy variation of the form shown in equation C.1. Secondly, we do not consider velocities outside of the vertical plane. This limits our ability to uniquely resolve fracture density. Third, we have made broad generalized assumptions about crack aspect ratio and have neglected non-vertically dipping fractures.

C.2 Modeling Styles of Extension

The style and mode of deformation is controlled by the changes to the thermal and physical state of the lithosphere. Following Buck (1991), we define the change due to extension acting on a piece of lithosphere. If the change in force is negative, the style of deformation favors either core complex mode or narrow rifting mode extension where by extension stays localized. If the change in force is positive, then the lithosphere has gotten stronger favoring the progressive migration of faulting.

This change in force is written:

$$dF = dF_{ys} + dF_{tb} + dF_{cb} \tag{C.9}$$

where dF is the change in force, dF_{ys} is the change in the yield strength (integrated crustal strength profile), dF_{tb} is the change in force due to temperature changes and dF_{cb} is the change in force due to crustal buoyancy.

Table C.1. Extensional Style Parameters

Symbol	Name	Value
ϵ	extension	0.25
$\dot{\epsilon}$	extension rate	model dependent
g	gravity	9.8 m/s^2
B	extensional brittle failure constant	
Z_c	thickness of brittle crust	model dependent
Z_m	thickness of brittle mantle	model dependent
h	crustal thickness	model dependent
α	coefficient of thermal expansion	
T_m	Moho temperatue	model dependent
T_S	Surface Temperature	273^oK
ρ_m	mantle density	3300 kg/m^3
ρ_c	crustal density	2700 kg/m^3
κ_f	effective crustal flow diffusivity	model dependent
X_e	width of pure shear zone	40 km
X_L	width of uniform lithosphere	250 km
$\Delta\rho^*$	density contrast	$p_c(p_m - p_c)/p_m$

While the general solution to equation C.9 requires a finite difference scheme to calculate changes in the thermal structure due to heat conduction and advection, approximate solutions from Buck (1991) can be written analytically as:

$$dF_{ys} = -[1 - exp(-2\epsilon)]\frac{gB}{2}[Z_c^2 + Z_m^2 - h^2] \qquad \text{for } Z_m > h,$$

$$dF_{ys} = -[1 - exp(-2\epsilon)]\frac{gB}{2}[Z_c^2] \qquad \text{for } Z_m < h,$$

$$dF_{tb} = -[1 - exp(-2\epsilon)]\frac{g\alpha\rho_m(T_m - T_S)Z_m^2}{6} \tag{C.10}$$

$$dF_{cb} = [1 - exp(-\epsilon)](g\Delta\rho^* h^2)F(\kappa_f, \dot{\epsilon}) \tag{C.11}$$

where $F(\kappa_f, \dot{\epsilon}) = erf(\frac{X_e}{4\sqrt{\kappa_f \epsilon/\dot{\epsilon}}}) - \frac{1}{2}erf(\frac{X_e + X_L}{4\sqrt{\kappa_f \epsilon/\dot{\epsilon}}}) - \frac{1}{2}erf(\frac{X_e - X_L}{4\sqrt{\kappa_f \epsilon/\dot{\epsilon}}})$.
with parameters defined in Table C.1.

APPENDIX D

APPENDIX CHAPTER V: SEISMIC IMAGING OF SANTORINI: SUBSURFACE CONSTRAINTS ON CALDERA COLLAPSE AND PRESENT-DAY MAGMA RECHARGE

D.1 Temperature and pressure corrections for velocity

We apply pressure and temperature corrections to the velocity profiles prior to interpreting the velocity in terms of porosity as a function of depth. We use a constant pressure derivative of 0.2 m/s per MPa (Rudnick and Fountain, 1995) and include the 4 MPa pressure of the overlying 400 m of seawater. We calculate a temperature correction accounting for both anharmonic and anelastic effects (Karato, 1993) assuming an activation enthalpy of 276 kJ/mol, an attenuation parameter Q=200, an anharmonic derivative dlnVP /dT = -8.1x10-5 K-1, and no frequency dependence (Paulatto et al., 2012). The elastic properties of the pore fluid are calculated for the temperature and pressure of each profile; we assume that pore pressure is between hydrostatic and lithostatic and used the formulas published by the International Association for the Properties of Water and Steam (Cooper and Dooley, 2007).

The reference VP profile for the basement is generated by applying a pressure and temperature correction to a rock of schists and limestones with VP = 6.2 km/s (Christensen and Stanley, 2003). We use a background geotherm of 40°C/km calculated using a heat flux of 62.8 mW/m^2 for a volcanic back arc (McKenzie and Sclater, 1967), a conductivity of 2.55 for schists, and a radiogenic heat production of 1.0 mW/m^3 (Eppelbaum et al., 2014).

In the caldera we use a granitic rock with VP = 6.5 km/s (Christensen and Stanley, 2003) and a hotter geotherm that we estimate from measurements in drill cores at Santorini (Fytikas et al., 1990) and from the neighboring Milos volcanic

center (Fytikas, 1989). It consists of a 200-m-thick upper layer where a gradual gradient of 40°C/km represents sea water mixing that keeps temperatures low within the porous intra-caldera sediments. This is followed by a steep temperature increase of 160°C/km from 200 to 1200 m depth and then a gentler increase of 50°C/km below. If there were magma at 4 km depth, we would expect a very steep thermal gradient directly above the magma system with temperatures reaching the solidus (e.g., Friðleifsson et al., 2013). We add $\pm$40°C/km to the caldera geotherm to assess the uncertainty in the temperature correction because the caldera geotherm is not well known. This temperature range changes the Vp correction by $\pm$0.2 km/s and is a small effect compared to the uncertainties in the pore aspect ratio (Figure 5.5).

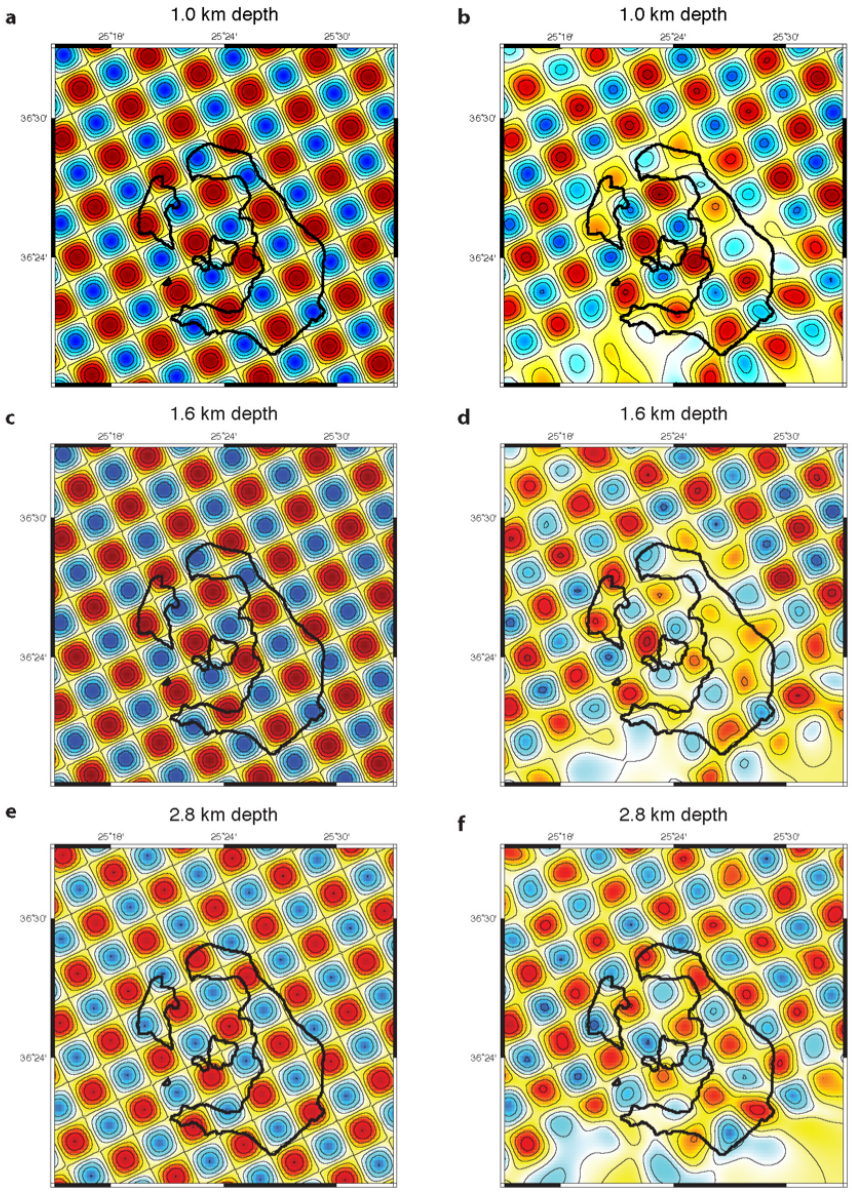

Figure D.1. Checkerboard resolution test. Checkers are sinusoidal with horizontal dimensions 3 x 3 km and ±0.25 km/s amplitude and superimposed on a 1D velocity profile. Left column (a, c, e) shows synthetic model, right column (b, d, f) shows recovered model. At 1.0 km depth (a, b) checks have vertical dimension 2 km and are centred at 1 km depth since rays average the upper 1 km. At 1.6 (c, d) and 2.6 (e, f) km depth checks have vertical dimension 1 km and are centred at 1.6 km depth. Contour interval is 0.05 km/s and anomalously low and high velocities are show as red and blue, respectively.

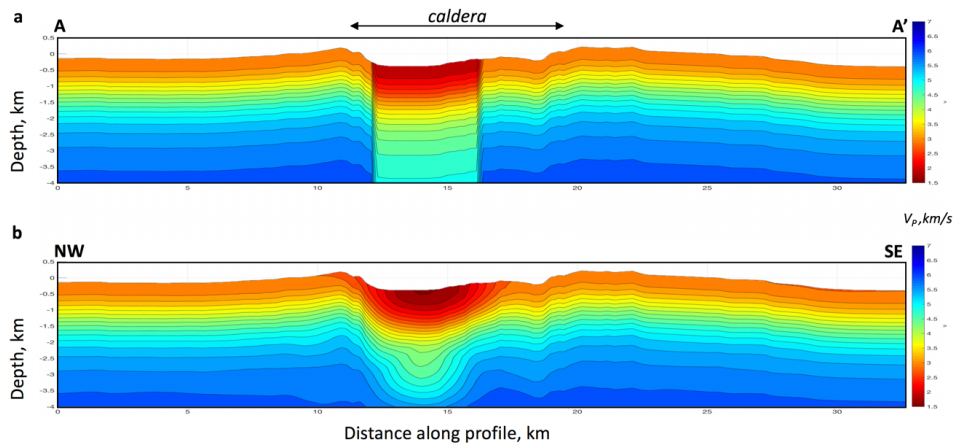

Figure D.2. Cylindrical low-velocity anomaly resolution test. (a) A cylinder with a -1 km/s velocity reduction is placed at the location of the caldera low velocity anomaly. The cylinder had radius 3 km and height 4 km. (b) Recovery is good down to about 3 km depth below which the recovery of the amplitude decreases. The width of the anomaly is reduced because the spatial smoothing constraint cannot recover the abrupt velocity change imposed in the synthetic model.

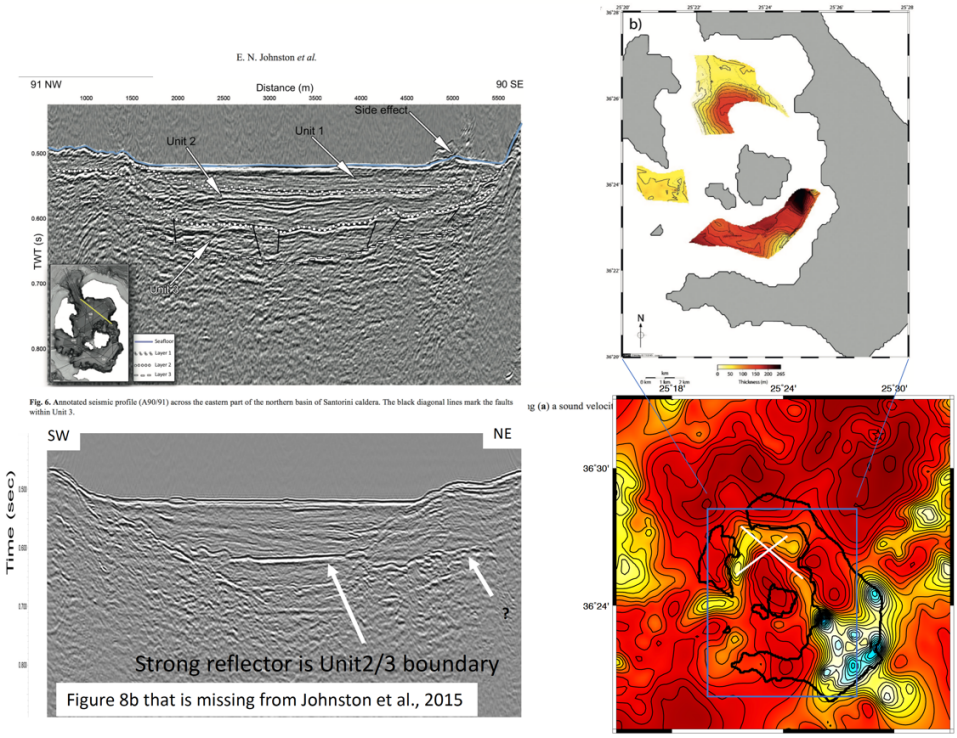

Figure D.3. Comparison of shallow tomography velocity model with seismic reflection profiles. (a) Seismic reflection profiles from (Johnston et al., 2015) oriented NW-SE and SW-NE on the left side. On the right side the mapped thickness of Unit 3 is compared to the seismic velocity in the 400 m depth slice from the seismic tomography model.

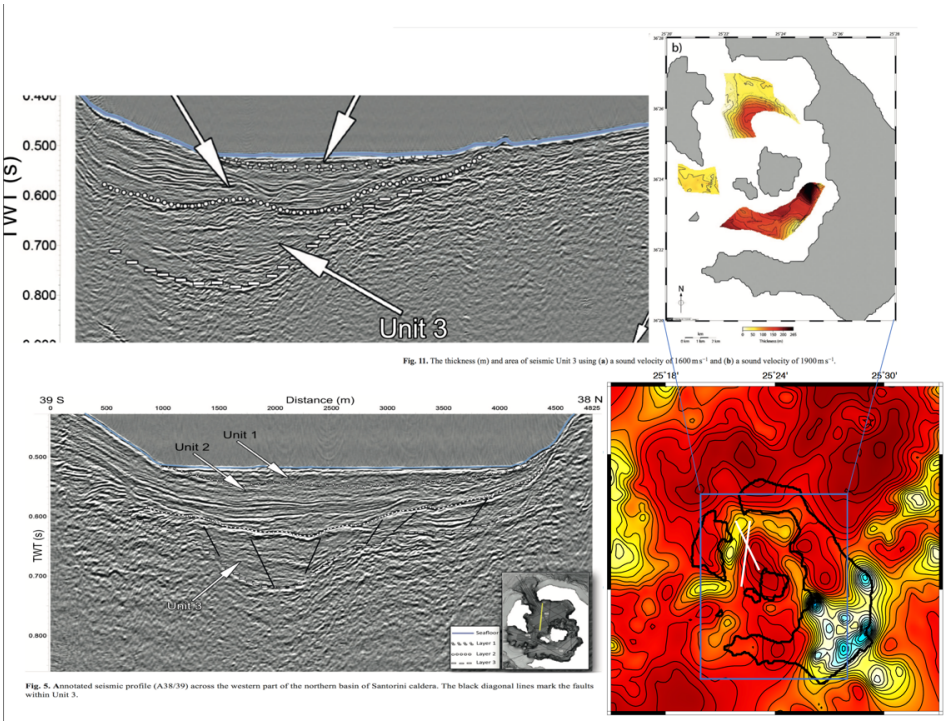

Figure D.4. Comparison of shallow tomography velocity model with seismic reflection profiles. (b) Seismic reflection profiles from (Johnston et al., 2015) oriented NNW-SSE and a N-S on the left side. On the right side the mapped thickness of Unit 3 is compared to the seismic velocity in the 400 m depth slice from the seismic tomography model.

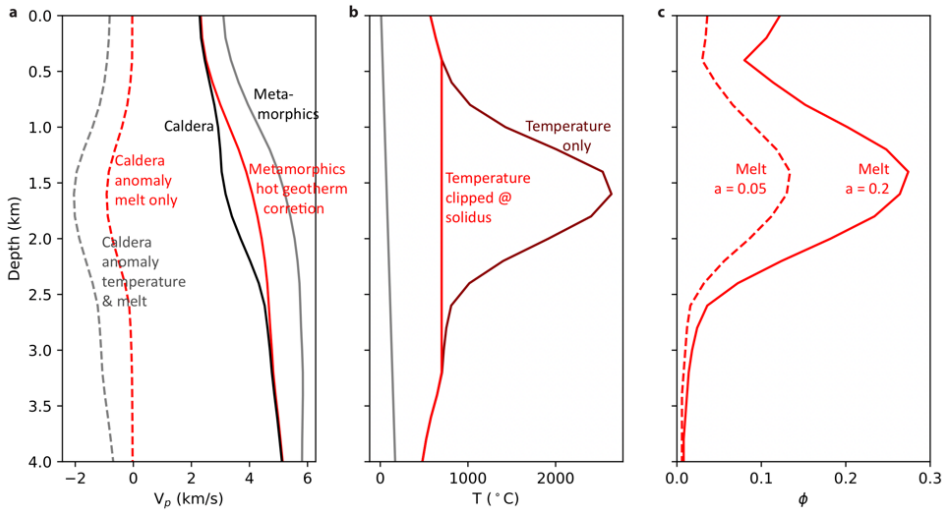

Figure D.5. Interpretation of the low VP anomaly if porosity were filled with partial melt. (a) The caldera VP anomaly (dashed grey) is the difference between the caldera profile (black) and the reference metamorphic profile (gray) with a correction applied for a hot geotherm (red); the caldera anomaly due to only melt (dashed red) isolates the portion of the anomaly that cannot be explained by temperature. (b) The temperature inferred from the caldera anomaly (dashed grey in (a)) assuming the entire anomaly is due to temperature alone (brown) yields unrealistically high temperatures and is clipped (red) at the solidus of andesite, 800°C. (c) The fractional melt porosity needed to account for the remaining VP anomaly is 13% and 26% for pore aspect ratios of 0.05 (dashed) and 0.2 (solid), respectively.

REFERENCES CITED

Acocella, V. (2006). Caldera types: How end-members relate to evolutionary stages of collapse. *Geophysical Research Letters*, *33*(18). doi: 10.1029/2006GL027434

Acocella, V., & Funiciello, F. (2010). Kinematic setting and structural control of arc volcanism. *Earth and Planetary Science Letters*, *289*(1-2), 43–53. doi: 10.1016/j.epsl.2009.10.027

Acocella, V., & Korme, T. (2002). Holocene extension direction along the Main Ethiopian Rift, East Africa. *Terra Nova*, *14*(3), 191–197. doi: 10.1046/j.1365-3121.2002.00403.x

Acocella, V., & Neri, M. (2009). Dike propagation in volcanic edifices: Overview and possible developments. *Tectonophysics*, *471*(1-2), 67–77. doi: 10.1016/j.tecto.2008.10.002

Anadón, P., Canet, C., & Friedrich, W. L. (2013). Aragonite stromatolitic buildups from Santorini (Aegean Sea, Greece): Geochemical and palaeontological constraints of the caldera palaeoenvironment prior to the Minoan eruption (\textit{ca} 3600 yr bp). *Sedimentology*, *60*(5), 1128–1155. doi: 10.1111/sed.12025

Anastasakis, G., & Piper, D. J. (2005). Late Neogene evolution of the western South Aegean volcanic arc: sedimentary imprint of volcanicity around Milos. *Marine Geology*, *215*(3-4), 135–158. doi: 10.1016/j.margeo.2004.11.014

Anderson, E. M. (1951). *The dynamics of faulting and dyke formation with applications to Britain*. Hafner Pub. Co.

Angelier, J., & Colletta, B. (1983). Tension fractures and extensional tectonics. *Nature*, *301*(5895), 49–51. doi: 10.1038/301049a0

Aramaki, S. (1984). Formation of the Aira Caldera, southern Kyushu, ˜22,000 years ago. *Journal of Geophysical Research*, *89*(B10), 8485. doi: 10.1029/JB089iB10p08485

Arnoux, G. M., Toomey, D. R., Hooft, E. E. E., & Wilcock, W. S. D. (2019). Seismic Imaging and Physical Properties of the Endeavour Segment: Evidence that Skew Between Mantle and Crustal Magmatic Systems Governs Spreading Center Processes. *Geochemistry, Geophysics, Geosystems*, *20*(3), 1319–1339. doi: 10.1029/2018GC007978

Arnoux, G. M., Toomey, D. R., Hooft, E. E. E., Wilcock, W. S. D., Morgan, J., Warner, M., & VanderBeek, B. P. (2017). Seismic evidence that black smoker heat flux is influenced by localized magma replenishment and associated increases in crustal permeability. *Geophysical Research Letters*. doi: 10.1002/2016GL071990

Athanassas, C. D., Bourlès, D. L., Braucher, R., Druitt, T. H., Nomikou, P., & Léanni, L. (2016). Evidence from cosmic ray exposure (CRE) dating for the existence of a pre-Minoan caldera on Santorini, Greece. *Bulletin of Volcanology*, *78*(5), 35. doi: 10.1007/s00445-016-1026-3

Backus, G. E. (1962). Long-wave elastic anisotropy produced by horizontal layering. *Journal of Geophysical Research*, *67*(11), 4427–4440. doi: 10.1029/JZ067i011p04427

Beachly, M. W., Hooft, E. E. E., Toomey, D. R., & Waite, G. P. (2012). Upper crustal structure of Newberry Volcano from P-wave tomography and finite difference waveform modeling. *Journal of Geophysical Research: Solid Earth*, *117*(B10). doi: 10.1029/2012JB009458

Ben-Zion, Y., Peng, Z., Okaya, D., Seeber, L., Armbruster, J. G., Ozer, N., Michael, A. J., Baris, S., & Aktar, M. (2003). A shallow fault-zone structure illuminated by trapped waves in the Karadere-Duzce branch of the North Anatolian Fault, western Turkey. *Geophysical Journal International*, *152*(3), 699–717. doi: 10.1046/j.1365-246X.2003.01870.x

Berg, S. S., & Skar, T. (2005). Controls on damage zone asymmetry of a normal fault zone: outcrop analyses of a segment of the Moab fault, SE Utah. *Journal of Structural Geology*, *27*(10), 1803–1822. doi: 10.1016/j.jsg.2005.04.012

Berryman, J. G. (1980). Long-wavelength propagation in composite elastic media I. Spherical inclusions. *The Journal of the Acoustical Society of America*, *68*(6), 1809–1819. doi: 10.1121/1.385171

Bohnhoff, M., Rische, M., Meier, T., Becker, D., Stavrakakis, G., & Harjes, H. P. (2006). Microseismic activity in the Hellenic Volcanic Arc, Greece, with emphasis on the seismotectonic setting of the Santorini-Amorgos zone. *Tectonophysics*, *423*(1-4), 17–33. doi: 10.1016/j.tecto.2006.03.024

Bond, A., & Sparks, R. S. J. (1976). The Minoan eruption of Santorini, Greece. *Journal of the Geological Society*, *132*(1), 1–16. doi: 10.1144/gsjgs.132.1.0001

Brocher, T. M. (2005). Empirical Relations between Elastic Wavespeeds and Density in the Earth's Crust. *Bulletin of the Seismological Society of America*, *95*(6), 2081–2092. doi: 10.1785/0120050077

Brocher, T. M., & Christensen, N. I. (1990). Seismic anisotropy due to preferred mineral orientation observed in shallow crustal rocks in southern Alaska. *Geology*, *18*(8), 737. doi: 10.1130/0091-7613(1990)018<0737:SADTPM>2.3.CO;2

Browning, J., Drymoni, K., & Gudmundsson, A. (2015). Forecasting magma-chamber rupture at Santorini volcano, Greece. *Scientific Reports*, *5*(1), 15785. doi: 10.1038/srep15785

Brownlee, S. J., Schulte-Pelkum, V., Raju, A., Mahan, K., Condit, C., & Orlandini, O. F. (2017). Characteristics of deep crustal seismic anisotropy from a compilation of rock elasticity tensors and their expression in receiver functions. *Tectonics*, *36*(9), 1835–1857. doi: 10.1002/2017TC004625

Brüstle, A., Friederich, W., Meier, T., & Gross, C. (2014). Focal mechanism and depth of the 1956 Amorgos twin earthquakes from waveform matching of analogue seismograms. *Solid Earth*, *5*(2), 1027–1044. doi: 10.5194/se-5-1027-2014

Buck, W. R. (1991). Modes of Continental Lithospheric Extension. *Journal of Geophysical Research*, *96*, 20161–20178. doi: 10.1029/91JB01485

Budetta, G., Condarelli, D., Fytikas, M., Kolios, N., Pascale, G., Rapolla, A., & Pinna, E. (1984). Geophysical prospecting on the Santorini Islands. *Bulletin Volcanologique*, *47*(3), 447–466. doi: 10.1007/BF01961218

Cao, Y., Jung, H., & Song, S. (2013). Petro-fabrics and seismic properties of blueschist and eclogite in the North Qilian suture zone, NW China: Implications for the low-velocity upper layer in subducting slab, trench-parallel seismic anisotropy, and eclogite detectability in the subduction z. *Journal of Geophysical Research: Solid Earth*, *118*(6), 3037–3058. doi: 10.1002/jgrb.50212

Caputo, R., Chatzipetros, A., Pavlides, S., & Sboras, S. (2012). The greek database of seismogenic sources (GreDaSS): State-of-the-art for northern greece. *Annals of Geophysics*. doi: 10.4401/ag-5168

Casey, M., Ebinger, C. J., Keir, D., Gloaguen, R., & Mohamed, F. (2006). Strain accommodation in transitional rifts: extension by magma intrusion and faulting in Ethiopian rift magmatic segments. *Geological Society Special Publication*, *259*(2003), 143–163. doi: 10.1144/GSL.SP.2006.259.01.13

Cashman, K. V., Sparks, R. S. J., & Blundy, J. D. (2017). Vertically extensive and unstable magmatic systems: A unified view of igneous processes. *Science*, *355*(6331), eaag3055. doi: 10.1126/science.aag3055

Christensen, N. I., & Stanley, D. (2003). 83 Seismic velocities and densities of rocks. In *International geophysics* (Vol. 81, pp. 1587–1594). doi: 10.1016/S0074-6142(03)80278-4

Cochran, E. S., Li, Y.-g., Shearer, P. M., Barbot, S., Fialko, Y., & Vidale, J. E. (2009). Seismic and geodetic evidence for extensive, long-lived fault damage zones. *Geology*, *37*(4), 315–318. doi: 10.1130/G25306A.1

Cooper, J. R., & Dooley, R. B. (2007). Revised release on the IAPWS industrial formulation 1997 for the thermodynamic properties of water and steam. *The International Association for the Properties of Water and Steam*, *1*, 48.

Corbi, F., Rivalta, E., Pinel, V., Maccaferri, F., Bagnardi, M., & Acocella, V. (2015). How caldera collapse shapes the shallow emplacement and transfer of magma in active volcanoes. *Earth and Planetary Science Letters*, *431*, 287–293. doi: 10.1016/j.epsl.2015.09.028

Corti, G., Bonini, M., Conticelli, S., Innocenti, F., Manetti, P., & Sokoutis, D. (2003). Analogue modelling of continental extension: A review focused on the relations between the patterns of deformation and the presence of magma. *Earth-Science Reviews*, *63*(3-4), 169–247. doi: 10.1016/S0012-8252(03)00035-7

Cossette, É., Audet, P., Schneider, D., & Grasemann, B. (2016). Structure and anisotropy of the crust in the Cyclades, Greece, using receiver functions constrained by in situ rock textural data. *Journal of Geophysical Research: Solid Earth*, *121*(4), 2661–2678. doi: 10.1002/2015JB012460

Cossette, É., Schneider, D., Audet, P., Grasemann, B., & Habler, G. (2015). Seismic properties and mineral crystallographic preferred orientations from EBSD data: Results from a crustal-scale detachment system, Aegean region. *Tectonophysics*, *651-652*, 66–78. doi: 10.1016/j.tecto.2015.03.014

Cottrell, E., Gardner, J. E., & Rutherford, M. J. (1999). Petrologic and experimental evidence for the movement and heating of the pre-eruptive Minoan rhyodacite (Santorini, Greece). *Contributions to Mineralogy and Petrology*, *135*(4), 315–331. doi: 10.1007/s004100050514

Creager, K. C., & Dorman, L. R. M. (1982). Location of Instruments on the Seafloor By Joint Adjustment of Instrument and Ship Positions. *Journal of Geophysical Research*, *87*(B10), 8379–8388. doi: 10.1029/JB087iB10p08379

Dempsey, E. D., Prior, D. J., Mariani, E., Toy, V. G., & Tatham, D. J. (2011). Mica-controlled anisotropy within mid-to-upper crustal mylonites: an EBSD study of mica fabrics in the Alpine Fault Zone, New Zealand. *Geological Society, London, Special Publications*, *360*(1), 33–47. doi: 10.1144/SP360.3

Deplus, C., Bonvalot, S., Dahrin, D., Diament, M., Harjono, H., & Dubois, J. (1995). Inner structure of the Krakatau volcanic complex (Indonesia) from gravity and bathymetry data. *Journal of Volcanology and Geothermal Research*, *64*(1-2), 23–52. doi: 10.1016/0377-0273(94)00038-I

Dimitriadis, I., Karagianni, E., Panagiotopoulos, D., Papazachos, C., Hatzidimitriou, P., Bohnhoff, M., Rische, M., & Meier, T. (2009). Seismicity and active tectonics at Coloumbo Reef (Aegean Sea, Greece): Monitoring an active volcano at Santorini Volcanic Center using a temporary seismic network. *Tectonophysics*, *465*(1-4), 136–149. doi: 10.1016/j.tecto.2008.11.005

Dimitriadis, I., Papazachos, C., Panagiotopoulos, D., Hatzidimitriou, P., Bohnhoff, M., Rische, M., & Meier, T. (2010). P and S velocity structures of the Santorini–Coloumbo volcanic system (Aegean Sea, Greece) obtained by non-linear inversion of travel times and its tectonic implications. *Journal of Volcanology and Geothermal Research*, *195*(1), 13–30. doi: 10.1016/j.jvolgeores.2010.05.013

Druitt, T., Edwards, L., Mellors, R., Pyle, D., Sparks, R., Lanphere, M., Davies, M., & Barreirio, B. (1999). *Santorini Volcano* (19th ed.). Geological Society London Memoir.

Druitt, T., & Francaviglia, V. (1992). Caldera formation on Santorini and the physiography of the islands in the late Bronze Age. *Bulletin of Volcanology*, *54*(6), 484–493. doi: 10.1007/BF00301394

Druitt, T. H. (2014). New insights into the initiation and venting of the Bronze-Age eruption of Santorini (Greece), from component analysis. *Bulletin of Volcanology*, *76*(2), 1–21. doi: 10.1007/s00445-014-0794-x

Druitt, T. H., Mercier, M., Florentin, L., Deloule, E., Cluzel, N., Flaherty, T., Médard, E., & Cadoux, A. (2016). Magma Storage and Extraction Associated with Plinian and Interplinian Activity at Santorini Caldera (Greece). *Journal of Petrology*, *57*(3), 461–494. doi: 10.1093/petrology/egw015

Dunn, R. A., Lekić, V., Detrick, R. S., & Toomey, D. R. (2005). Three-dimensional seismic structure of the Mid-Atlantic Ridge (35°N): Evidence for focused melt supply and lower crustal dike injection. *Journal of Geophysical Research: Solid Earth*, *110*(B9). doi: 10.1029/2004JB003473

Ebinger, C., & Casey, M. (2001). Continental breakup in magmatic provinces: An Ethiopian example. *Geology*, *29*(6), 527. doi: 10.1130/0091-7613(2001)029<0527:CBIMPA>2.0.CO;2

England, P. (1983). Constraints on extension of continental lithosphere. *Journal of Geophysical Research*, *88*(B2), 1145. doi: 10.1029/JB088iB02p01145

Eppelbaum, L., Kutasov, I., & Pilchin, A. (2014). The Thermal Field of the Earth. In *Applied geothermics* (pp. 1–98). Springer.

Escher, B. G. (1929). *On the formation of calderas.* BG Escher.

Fabbro, G. N., Druitt, T. H., & Scaillet, S. (2013). Evolution of the crustal magma plumbing system during the build-up to the 22-ka caldera-forming eruption of Santorini (Greece). *Bulletin of Volcanology*, *75*(12), 767. doi: 10.1007/s00445-013-0767-5

Farrell, J., Smith, R. B., Husen, S., & Diehl, T. (2014). Tomography from 26 years of seismicity revealing that the spatial extent of the Yellowstone crustal magma reservoir extends well beyond the Yellowstone caldera. *Geophysical Research Letters*, *41*(9), 3068–3073. doi: 10.1002/2014GL059588

Faulds, J. E., & Varga, R. J. (1998). The role of accommodation zones and transfer zones in the regional segmentation of extended terranes. *Special Paper 323: Accommodation zones and transfer zones; the regional segmentation of the Basin and Range Province*. doi: 10.1130/0-8137-2323-X.1

Faulkner, D., Jackson, C., Lunn, R., Schlische, R., Shipton, Z., Wibberley, C., & Withjack, M. (2010). A review of recent developments concerning the structure, mechanics and fluid flow properties of fault zones. *Journal of Structural Geology*, *32*(11), 1557–1575. doi: 10.1016/j.jsg.2010.06.009

Feuillet, N. (2013). The 2011-2012 unrest at Santorini rift: Stress interaction between active faulting and volcanism. *Geophysical Research Letters*, *40*(14), 3532–3537. doi: 10.1002/grl.50516

Flaherty, T., Druitt, T. H., Tuffen, H., Higgins, M. D., Costa, F., & Cadoux, A. (2018). Multiple timescale constraints for high-flux magma chamber assembly prior to the Late Bronze Age eruption of Santorini (Greece). *Contributions to Mineralogy and Petrology*, *173*(9), 75. doi: 10.1007/s00410-018-1490-1

Forster, M., & Lister, G. (2009). Core-complex-related extension of the Aegean Hthosphere initiated at the Eocene-Oligocene transition. *Journal of Geophysical Research: Solid Earth*, *114*(2), 1–36. doi: 10.1029/2007JB005382

Forster, M. A., & Lister, G. S. (1999). Detachment faults in the Aegean core complex of Ios, Cyclades, Greece. *Geological Society, London, Special Publications*, *154*(1), 305–323. doi: 10.1144/GSL.SP.1999.154.01.14

Friederich, W., Brüstle, A., Küperkoch, L., Meier, T., Lamara, S., & Working Group, E. (2014). Focal mechanisms in the southern Aegean from temporary seismic networks – implications for the regional stress field and ongoing deformation processes. *Solid Earth*, *5*(1), 275–297. doi: 10.5194/se-5-275-2014

Friedrich, W. L. (2006). Santorini Eruption Radiocarbon Dated to 1627-1600 B.C. *Science*, *312*(5773), 548–548. doi: 10.1126/science.1125087

Friedrich, W. L., Eriksen, U., Tauber, H., Heinemeier, J., Rud, N., Thomsen, M. S., & Buchardt, B. (1988). Existence of a water-filled caldera prior to the Minoan eruption of Santorini, Greece. *Naturwissenschaften*, *75*(11), 567–569. doi: 10.1007/BF00377720

Friðleifsson, G. Ó., Elders, W. A., & Bignall, G. (2013). A plan for a 5 km-deep borehole at Reykjanes, Iceland, into the root zone of a black smoker on land. *Scientific Drilling*, *16*, 73–79. doi: 10.5194/sd-16-73-2013

Fytikas, M., Kolios, N., & Vougioukalakis, G. (1990). Post-Minoan Volcanic Activivity of the Santroni Volcano. Volcanic Hazard and Risk, Forecasting Possiblities. In D. Hardy, J. Keller, V. Galanopoulos, N. Flemming, & H. Druitt, T (Eds.), *Thera and the aegean world iii, volume two* (pp. 183–198). London: The Thera Foundation.

Gautier, P., & Brun, J. P. (1994). *Ductile crust exhumation and extensional detachments in the central Aegean (Cyclades and Evvia Islands)* (Vol. 7) (No. 2).

Georgalas, G. C. (1953). L'éruption du volcan de Santorin en 1950. *Bulletin Volcanologique*, *13*(1), 39–55. doi: 10.1007/BF02596790

Górszczyk, A., Operto, S., & Malinowski, M. (2016). Toward a robust workflow for deep crustal imaging by FWI of OBS data: The eastern Nankai Trough revisited. *Journal of Geophysical Research: Solid Earth*. doi: 10.1002/2016JB013891

Gudmundsson, A. (1990). Emplacement of dikes, sills and crustal magma chambers at divergent plate boundaries. *Tectonophysics*, *176*(3-4), 257–275. doi: 10.1016/0040-1951(90)90073-H

Gudmundsson, A. (1995). Infrastructure and mechanics of volcanic systems in Iceland. *Journal of Volcanology and Geothermal Research*, *64*(1-2), 1–22. doi: 10.1016/0377-0273(95)92782-Q

Gudmundsson, M. T., Jónsdóttir, K., Hooper, A., Holohan, E. P., Halldórsson, S. A., Ófeigsson, B. G., Cesca, S., Vogfjörd, K. S., Sigmundsson, F., Högnadóttir, T., Einarsson, P., Sigmarsson, O., Jarosch, A. H., Jónasson, K., Magnússon, E., Hreinsdóttir, S., Bagnardi, M., Parks, M. M., Hjörleifsdóttir, V., Pálsson, F., Walter, T. R., Schöpfer, M. P. J., Heimann, S., Reynolds, H. I., Dumont, S., Bali, E., Gudfinnsson, G. H., Dahm, T., Roberts, M. J., Hensch, M., Belart, J. M. C., Spaans, K., Jakobsson, S., Gudmundsson, G. B., Fridriksdóttir, H. M., Drouin, V., Dürig, T., Aðalgeirsdóttir, G., Riishuus, M. S., Pedersen, G. B. M., van Boeckel, T., Oddsson, B., Pfeffer, M. A., Barsotti, S., Bergsson, B., Donovan, A., Burton, M. R., & Aiuppa, A. (2016). Gradual caldera collapse at Bárdarbunga volcano, Iceland, regulated by lateral magma outflow. *Science*, *353*(6296), aaf8988. doi: 10.1126/science.aaf8988

Heath, B. A., Hooft, E. E. E., Toomey, D. R., & Bezada, M. J. (2015). Imaging the magmatic system of Newberry Volcano using joint active source and teleseismic tomography. *Geochemistry, Geophysics, Geosystems*, *16*(12), 4433–4448. doi: 10.1002/2015GC006129

Heath, B. A., Hooft, E. E. E., Toomey, D. R., Papazachos, C. B., Nomikou, P., Paulatto, M., Morgan, J. V., & Warner, M. R. (2019). Tectonism and Its Relation to Magmatism Around Santorini Volcano From Upper Crustal P Wave Velocity. *Journal of Geophysical Research: Solid Earth*, *124*(10), 10610–10629. doi: 10.1029/2019JB017699

Heiken, G., & Mccoy, F. (1984). Caldera development during the Minoan eruption, Thira, Cyclades, Greece. *Journal of Geophysical Research*, *89*(B10), 8441. doi: 10.1029/JB089iB10p08441

Holohan, E., Schöpfer, M., & Walsh, J. (2015). Stress evolution during caldera collapse. *Earth and Planetary Science Letters*, *421*, 139–151. doi: 10.1016/j.epsl.2015.03.003

Hooft, E., Heath, B., Toomey, D., Paulatto, M., Papazachos, C., Nomikou, P., Morgan, J., & Warner, M. (2019). Seismic imaging of Santorini: Subsurface constraints on caldera collapse and present-day magma recharge. *Earth and Planetary Science Letters*, *514*, 48–61. doi: 10.1016/j.epsl.2019.02.033

Hooft, E. E., Nomikou, P., Toomey, D. R., Lampridou, D., Getz, C., Christopoulou, M.-E. E., O'Hara, D., Arnoux, G. M., Bodmer, M., Gray, M., Heath, B. A., & VanderBeek, B. P. (2017). Backarc tectonism, volcanism, and mass wasting shape seafloor morphology in the Santorini-Christiana-Amorgos region of the Hellenic Volcanic Arc. *Tectonophysics*, *712*, 396–414. doi: 10.1016/j.tecto.2017.06.005

Hübscher, C., Ruhnau, M., & Nomikou, P. (2015). Volcano-tectonic evolution of the polygenetic Kolumbo submarine volcano/Santorini (Aegean Sea). *Journal of Volcanology and Geothermal Research*, *291*, 101–111. doi: 10.1016/j.jvolgeores.2014.12.020

Huet, B., Labrousse, L., & Jolivet, L. (2009). Thrust or detachment? Exhumation processes in the Aegean: Insight from a field study on Ios (Cyclades, Greece). *Tectonics*, *28*(3). doi: 10.1029/2008TC002397

Huet, B., Le Pourhiet, L., Labrousse, L., Burov, E. B., & Jolivet, L. (2011). Formation of metamorphic core complex in inherited wedges: A thermomechanical modelling study. *Earth and Planetary Science Letters*, *309*(3-4), 249–257. doi: 10.1016/j.epsl.2011.07.004

Jakobsen, M., Hudson, J. A., Minshull, T. A., & Singh, S. C. (2000). Elastic properties of hydrate-bearing sediments using effective medium theory. *Journal of Geophysical Research: Solid Earth*, *105*(B1), 561–577. doi: 10.1029/1999JB900190

Ji, S., Shao, T., Michibayashi, K., Oya, S., Satsukawa, T., Wang, Q., Zhao, W., & Salisbury, M. H. (2015). Magnitude and symmetry of seismic anisotropy in mica- and amphibole-bearing metamorphic rocks and implications for tectonic interpretation of seismic data from the southeast Tibetan Plateau. *Journal of Geophysical Research: Solid Earth*, *120*(9), 6404–6430. doi: 10.1002/2015JB012209

Johnson, L. R., & Sammis, C. G. (2001). Effects of Rock Damage on Seismic Waves Generated by Explosions. *Pure and Applied Geophysics*, *158*(11), 1869–1908. doi: 10.1007/PL00001136

Johnston, E. N., Sparks, R. S. J., Nomikou, P., Livanos, I., Carey, S., Phillips, J. C., & Sigurdsson, H. (2015). Stratigraphic relations of Santorini's intracaldera fill and implications for the rate of post-caldera volcanism. *Journal of the Geological Society*, *172*(3), 323–335. doi: 10.1144/jgs2013-114

Johnston, E. N., Sparks, R. S. J., Phillips, J. C., & Carey, S. (2014). Revised estimates for the volume of the Late Bronze Age Minoan eruption, Santorini, Greece. *Journal of the Geological Society*, *171*(4), 583–590. doi: 10.1144/jgs2013-113

Jolivet, L., Faccenna, C., Huet, B., Labrousse, L., Le Pourhiet, L., Lacombe, O., Lecomte, E., Burov, E., Denèle, Y., Brun, J. P., Philippon, M., Paul, A., Salaün, G., Karabulut, H., Piromallo, C., Monié, P., Gueydan, F., Okay, A. I., Oberhänsli, R., Pourteau, A., Augier, R., Gadenne, L., & Driussi, O. (2013). Aegean tectonics: Strain localisation, slab tearing and trench retreat. *Tectonophysics*, *597-598*, 1–33. doi: 10.1016/j.tecto.2012.06.011

Karagianni, E. E., Papazachos, C. B., Panagiotopoulos, D. G., Suhadolc, P., Vuan, A., & Panza, G. F. (2004). Shear velocity structure in the Aegean area obtained by inversion of Rayleigh waves. *Geophysical Journal International*, *160*(1), 127–143. doi: 10.1111/j.1365-246X.2005.02354.x

Karato, S.-i. (1993). Importance of anelasticity in the interpretation of seismic tomography. *Geophysical Research Letters*, *20*(15), 1623–1626. doi: 10.1029/93GL01767

Karátson, D., Gertisser, R., Telbisz, T., Vereb, V., Quidelleur, X., Druitt, T., Nomikou, P., & Kósik, S. (2018). Towards reconstruction of the lost Late Bronze Age intra-caldera island of Santorini, Greece. *Scientific Reports*, *8*(1), 7026. doi: 10.1038/s41598-018-25301-2

Karlstrom, L., Dufek, J., & Manga, M. (2009). Organization of volcanic plumbing through magmatic lensing by magma chambers and volcanic loads. *Journal of Geophysical Research*, *114*(B10), B10204. doi: 10.1029/2009JB006339

Kennedy, B. M., Mark Jellinek, A., & Stix, J. (2008). Coupled caldera subsidence and stirring inferred from analogue models. *Nature Geoscience*, *1*(6), 385–389. doi: 10.1038/ngeo206

Kilias, S. P., Nomikou, P., Papanikolaou, D., Polymenakou, P. N., Godelitsas, A., Argyraki, A., Carey, S., Gamaletsos, P., Mertzimekis, T. J., Stathopoulou, E., Goettlicher, J., Steininger, R., Betzelou, K., Livanos, I., Christakis, C., Bell, K. C., & Scoullos, M. (2013). New insights into hydrothermal vent processes in the unique shallow-submarine arc-volcano, Kolumbo (Santorini), Greece. *Scientific Reports*, *3*, 1–13. doi: 10.1038/srep02421

Kim, E., Toomey, D. R., Hooft, E. E., Wilcock, W. S., Weekly, R. T., Lee, S. M., & Kim, Y. H. (2019). Upper Crustal Vp/Vs Ratios at the Endeavour Segment, Juan de Fuca Ridge, From Joint Inversion of P and S Traveltimes: Implications for Hydrothermal Circulation. *Geochemistry, Geophysics, Geosystems*, *20*(1), 208–229. doi: 10.1029/2018GC007921

Kim, Y. S., Peacock, D. C., & Sanderson, D. J. (2004). Fault damage zones. *Journal of Structural Geology*, *26*(3), 503–517. doi: 10.1016/j.jsg.2003.08.002

Klaver, M., Carey, S., Nomikou, P., Smet, I., Godelitsas, A., & Vroon, P. (2016). A distinct source and differentiation history for Kolumbo submarine volcano, Santorini volcanic field, Aegean arc. *Geochemistry, Geophysics, Geosystems*, *17*(8), 3254–3273. doi: 10.1002/2016GC006398

Kokkalas, S., & Aydin, A. (2013). Is there a link between faulting and magmatism in the south-central Aegean Sea? *Geological Magazine*, *150*(2), 193–224. doi: 10.1017/S0016756812000453

Konstantinou, K. (2010). Crustal rheology of the Santorini–Amorgos zone: Implications for the nucleation depth and rupture extent of the 9 July 1956 Amorgos earthquake, southern Aegean. *Journal of Geodynamics*, *50*(5), 400–409. doi: 10.1016/j.jog.2010.05.002

Konstantinou, K. I., Evangelidis, C. P., Liang, W.-T. T., Melis, N. S., & Kalogeras, I. (2013). Seismicity, Vp/Vs and shear wave anisotropy variations during the 2011 unrest at Santorini caldera, southern Aegean. *Journal of Volcanology and Geothermal Research*, *267*, 57–67. doi: 10.1016/j.jvolgeores.2013.10.001

Le Pichon, X., & Kreemer, C. (2010). The Miocene-to-Present Kinematic Evolution of the Eastern Mediterranean and Middle East and Its Implications for Dynamics. *Annual Review of Earth and Planetary Sciences*, *38*(1), 323–351. doi: 10.1146/annurev-earth-040809-152419

Li, Y. G., Vidale, J. E., & Cochran, E. S. (2004). Low-velocity damaged structure of the San Andreas Fault at Parkfield from fault zone trapped waves. *Geophysical Research Letters*, *31*(12). doi: 10.1029/2003GL019044

Lipman, P. W. (1997). Subsidence of ash-flow calderas: relation to caldera size and magma-chamber geometry. *Bulletin of Volcanology*, *59*(3), 198–218. doi: 10.1007/s004450050186

Lister, G. S., Banga, G., & Feenstra, A. (1984). Metamorphic core complexes of Cordilleran type in the Cyclades, Aegean Sea, Greece. *Geology*, *12*(4), 221. doi: 10.1130/0091-7613(1984)12<221:MCCOCT>2.0.CO;2

Ma, G., Hao, H., & Wang, F. (2011). Simulations of explosion-induced damage to underground rock chambers. *Journal of Rock Mechanics and Geotechnical Engineering*, *3*(1), 19–29. doi: 10.3724/SP.J.1235.2011.00019

MacLeod, N. S., & Sherrod, D. R. (1988). Geologic evidence for a magma chamber beneath Newberry Volcano, Oregon. *Journal of Geophysical Research: Solid Earth*, *93*(B9), 10067–10079. doi: 10.1029/JB093iB09p10067

Magee, C., Hunt-Stewart, E., & Jackson, C. A. (2013). Volcano growth mechanisms and the role of sub-volcanic intrusions: Insights from 2D seismic reflection data. *Earth and Planetary Science Letters*, *373*, 41–53. doi: 10.1016/j.epsl.2013.04.041

Mainprice, D. (1997). Modelling the anisotropic seismic properties of partially molten rocks found at mid-ocean ridges. *Tectonophysics*, *279*(1-4), 161–179. doi: 10.1016/S0040-1951(97)00122-4

Mainprice, D., & Casey, M. (1990). The calculated seismic properties of quartz mylonites with typical fabrics: relationship to kinematics and temperature. *Geophysical Journal International*, *103*(3), 599–608. doi: 10.1111/j.1365-246X.1990.tb05674.x

Makris, J. (1976). A dynamic model of the Hellenic Arc deduced from geophysical data. *Tectonophysics*, *36*(4), 339–346. doi: 10.1016/0040-1951(76)90108-6

Makris, J. (1978). The crust and upper mantle of the Aegean region from deep seismic soundings. *Tectonophysics*, *46*(3-4), 269–284. doi: 10.1016/0040-1951(78)90207-X

Manighetti, I., King, G., & Sammis, C. G. (2004). The role of off-fault damage in the evolution of normal faults. *Earth and Planetary Science Letters*, *217*(3-4), 399–408. doi: 10.1016/S0012-821X(03)00601-0

Marrett, R., & Allmendinger, R. W. (1992). Amount of extension on "small" faults: An example from the Viking graben. *Geology*, *20*(1), 47. doi: 10.1130/0091-7613(1992)020<0047:AOEOSF>2.3.CO;2

McClay, K. R. (1989). Analogue models of inversion tectonics. *Geological Society, London, Special Publications*, *44*(1), 41–59. doi: 10.1144/GSL.SP.1989.044.01.04

McClelland, E., Thomas, R., & Hardy, D. A. (1990). A palaeomagnetic study of Minoan age tephra from Thera. *Thera and the Aegean world III*, *2*, 129–138.

McClusky, S., Balassanian, S., Barka, A., Demir, C., Ergintav, S., Georgiev, I., Gurkan, O., Hamburger, M., Hurst, K., Kahle, H., Kastens, K., Kekelidze, G., King, R., Kotzev, V., Lenk, O., Mahmoud, S., Mishin, A., Nadariya, M., Ouzounis, A., Paradissis, D., Peter, Y., Prilepin, M., Reilinger, R., Sanli, I., Seeger, H., Tealeb, A., Toksöz, M. N., & Veis, G. (2000). Global Positioning System constraints on plate kinematics and dynamics in the eastern Mediterranean and Caucasus. *Journal of Geophysical Research: Solid Earth*, *105*(B3), 5695–5719. doi: 10.1029/1999JB900351

McKenzie, D. (1972). Active Tectonics of the Mediterranean Region. *Geophysical Journal of the Royal Astronomical Society*, *30*(2), 109–185. doi: 10.1111/j.1365-246X.1972.tb02351.x

McKenzie, D. P., & Sclater, J. G. (1969). Heat flow in the eastern Pacific and sea floor spreading. *Bulletin Volcanologique*, *33*(1), 101–117.

McVey, B., Hooft, E. E. E., Heath, B. A., Toomey, D. R., Paulatto, M., Morgan, J. V., Nomikou, P., & Papazachos, C. (2019). Magma Accumulation Beneath Santorini Volcano From P-Wave Tomography. *Geology*(In Press).

Melosh, H. J., & Williams, C. A. (1989). Mechanics of graben formation in crustal rocks: A finite element analysis. *Journal of Geophysical Research: Solid Earth*, *94*(B10), 13961–13973. doi: 10.1029/JB094iB10p13961

Mizera, M., & Behrmann, J. H. (2016). Strain and flow in the metamorphic core complex of Ios Island (Cyclades, Greece). *International Journal of Earth Sciences*, *105*(7), 2097–2110. doi: 10.1007/s00531-015-1259-y

Morgan, J., Warner, M., Arnoux, G., Hooft, E., Toomey, D., VanderBeek, B., & Wilcock, W. (2016). Next-generation seismic experiments – II: wide-angle, multi-azimuth, 3-D, full-waveform inversion of sparse field data. *Geophysical Journal International*, *204*(2), 1342–1363. doi: 10.1093/gji/ggv513

Morgan, J., Warner, M., Bell, R., Ashley, J., Barnes, D., Little, R., Roele, K., & Jones, C. (2013). Next-generation seismic experiments: wide-angle, multi-azimuth, three-dimensional, full-waveform inversion. *Geophysical Journal International*, *195*(3), 1657–1678. doi: 10.1093/gji/ggt345

Moser, T. J. (1991). Shortest path calculation of seismic rays. *GEOPHYSICS*, *56*(1), 59–67. doi: 10.1190/1.1442958

Muirhead, J. D., Kattenhorn, S. A., & Le Corvec, N. (2015). Varying styles ofmagmatic strain accommodation across the East African Rift. *Geochemistry, Geophysics, Geosystems*, *16*, 2775–2795. doi: 10.1002/2015GC005918.Received

Muller, J. R., Ito, G., & Martel, S. J. (2001). Effects of volcano loading on dike propagation in an elastic half-space. *Journal of Geophysical Research: Solid Earth*, *106*(B6), 11101–11113. doi: 10.1029/2000JB900461

Newman, A. V., Stiros, S., Feng, L., Psimoulis, P., Moschas, F., Saltogianni, V., Jiang, Y., Papazachos, C., Panagiotopoulos, D., Karagianni, E., & Vamvakaris, D. (2012). Recent geodetic unrest at Santorini Caldera, Greece. *Geophysical Research Letters*, *39*(6). doi: 10.1029/2012GL051286

Nomikou, P., Carey, S., Papanikolaou, D., Croff Bell, K., Sakellariou, D., Alexandri, M., & Bejelou, K. (2012). Submarine volcanoes of the Kolumbo volcanic zone NE of Santorini Caldera, Greece. *Global and Planetary Change*, *90-91*, 135–151. doi: 10.1016/j.gloplacha.2012.01.001

Nomikou, P., Hübscher, C., Papanikolaou, D., Farangitakis, G. P., Ruhnau, M., & Lampridou, D. (2018). Expanding extension, subsidence and lateral segmentation within the Santorini - Amorgos basins during Quaternary: Implications for the 1956 Amorgos events, central - south Aegean Sea, Greece. *Tectonophysics*, *722*, 138–153. doi: 10.1016/j.tecto.2017.10.016

Nomikou, P., Hübscher, C., Ruhnau, M., & Bejelou, K. (2016). Tectono-stratigraphic evolution through successive extensional events of the Anydros Basin, hosting Kolumbo volcanic field at the Aegean Sea, Greece. *Tectonophysics*, *671*, 202–217. doi: 10.1016/j.tecto.2016.01.021

Nomikou, P., & Papanikolaou, D. (2011). Extension of active fault zones on Nisyros volcano across the Yali-Nisyros Channel based on onshore and offshore data. *Marine Geophysical Research*, *32*(1-2), 181–192. doi: 10.1007/s11001-011-9119-z

Nomikou, P., & Papanikolaou, D. (2016). Bulletin of the Geological Society of Greece Faculty of Civil Engineering. *Bulletin of the Geplogica Society of Greece.*, *50*(2010), 656–664.

Nomikou, P., Papanikolaou, D., Alexandri, M., Sakellariou, D., & Rousakis, G. (2013). Submarine volcanoes along the Aegean volcanic arc. *Tectonophysics*, *597-598*, 123–146. doi: 10.1016/j.tecto.2012.10.001

Nomikou, P., Parks, M., Papanikolaou, D., Pyle, D., Mather, T., Carey, S., Watts, A., Paulatto, M., Kalnins, M., Livanos, I., Bejelou, K., Simou, E., & Perros, I. (2014). The emergence and growth of a submarine volcano: The Kameni islands, Santorini (Greece). *GeoResJ*, *1-2*, 8–18. doi: 10.1016/j.grj.2014.02.002

Okal, E. A., Synolakis, C. E., Uslu, B., Kalligeris, N., & Voukouvalas, E. (2009). The 1956 earthquake and tsunami in Amorgos, Greece. *Geophysical Journal International*, *178*(3), 1533–1554. doi: 10.1111/j.1365-246X.2009.04237.x

Okaya, D., Vel, S. S., Song, W. J., & Johnson, S. E. (2018). Modification of crustal seismic anisotropy by geological structures ("structural geometric anisotropy"). *Geosphere*, *15*(1), 146–170. doi: 10.1130/GES01655.1

Papadimitriou, P., Kapetanidis, V., Karakonstantis, A., Kaviris, G., Voulgaris, N., & Makropoulos, K. (2015). The Santorini Volcanic Complex: A detailed multi-parameter seismological approach with emphasis on the 2011–2012 unrest period. *Journal of Geodynamics*, *85*, 32–57. doi: 10.1016/j.jog.2014.12.004

Papadopoulos, G. A., & Pavlides, S. B. (1992). The large 1956 earthquake in the South Aegean: Macroseismic field configuration, faulting, and neotectonics of Amorgos Island. *Earth and Planetary Science Letters*, *113*(3), 383–396. doi: 10.1016/0012-821X(92)90140-Q

Papazachos, B. C., & Panagiotopoulos, D. G. (1993). Normal faults associated with volcanic activity arc. *Tectonophysics*, *220*(1-4), 301–308. doi: 10.1016/0040-1951(93)90237-E

Parks, M. M., Biggs, J., England, P., Mather, T. A., Nomikou, P., Palamartchouk, K., Papanikolaou, X., Paradissis, D., Parsons, B., Pyle, D. M., Raptakis, C., & Zacharis, V. (2012). Evolution of Santorini Volcano dominated by episodic and rapid fluxes of melt from depth. *Nature Geoscience*, *5*(10), 749–754. doi: 10.1038/ngeo1562

Parks, M. M., Caliro, S., Chiodini, G., Pyle, D. M., Mather, T. A., Berlo, K., Edmonds, M., Biggs, J., Nomikou, P., & Raptakis, C. (2013). Distinguishing contributions to diffuse CO2 emissions in volcanic areas from magmatic degassing and thermal decarbonation using soil gas 222Rn–δ13C systematics: Application to Santorini volcano, Greece. *Earth and Planetary Science Letters*, *377-378*, 180–190. doi: 10.1016/j.epsl.2013.06.046

Parks, M. M., Moore, J. D. P., Papanikolaou, X., Biggs, J., Mather, T. A., Pyle, D. M., Raptakis, C., Paradissis, D., Hooper, A., Parsons, B., & Nomikou, P. (2015). From quiescence to unrest: 20 years of satellite geodetic measurements at Santorini volcano, Greece. *Journal of Geophysical Research: Solid Earth*, *120*(2), 1309–1328. doi: 10.1002/2014JB011540

Parsons, T., & Thompson, G. A. (1991). The Role of Magma Overpressure in Suppressing Earthquakes and Topography: Worldwide Examples. *Science*, *253*(5026), 1399–1402. doi: 10.1126/science.253.5026.1399

Parsons, T., & Thompson, G. A. (1993). Does magmatism influence low-angle normal faulting? *Geology*, *21*(3), 247–250. doi: 10.1130/0091-7613(1993)021<0247:DMILAN>2.3.CO;2

Paulatto, M., Annen, C., Henstock, T. J., Kiddle, E., Minshull, T. A., Sparks, R. S. J., & Voight, B. (2012). Magma chamber properties from integrated seismic tomography and thermal modeling at Montserrat. *Geochemistry, Geophysics, Geosystems*, *13*(1). doi: 10.1029/2011GC003892

Perissoratis, C. (1995). The Santorini volcanic complex and its relation to the stratigraphy and structure of the Aegean arc, Greece. *Marine Geology*, *128*(1-2). doi: 10.1016/0025-3227(95)00090-L

Pfeiffer, T. (2001). Vent development during the Minoan eruption (1640 BC) of Santorini, Greece, as suggested by ballistic blocks. *Journal of Volcanology and Geothermal Research*, *106*(3-4), 229–242. doi: 10.1016/S0377-0273(00)00273-0

Pichon, X. L., & Angelier, J. (1979). The hellenic arc and trench system: A key to the neotectonic evolution of the eastern mediterranean area. *Tectonophysics*, *60*(1-2), 1–42. doi: 10.1016/0040-1951(79)90131-8

Pinel, V., Carrara, A., Maccaferri, F., Rivalta, E., & Corbi, F. (2017). A two-step model for dynamical dike propagation in two dimensions: Application to the July 2001 Etna eruption. *Journal of Geophysical Research: Solid Earth*, *122*(2), 1107–1125. doi: 10.1002/2016JB013630

Piper, D. J., & Perissoratis, C. (2003). Quaternary neotectonics of the South Aegean arc. *Marine Geology*, *198*(3-4), 259–288. doi: 10.1016/S0025-3227(03)00118-X

Piper, D. J. W., Pe-Piper, G., Perissoratis, C., & Anastasakis, G. (2007). Distribution and chronology of submarine volcanic rocks around Santorini and their relationship to faulting. *Geological Society, London, Special Publications*, *291*(1), 99–111. doi: 10.1144/SP291.5

Pyle, D. M., & Elliott, J. R. (2006). Quantitative morphology, recent evolution, and future activity of the Kameni Islands volcano, Santorini, Greece. *Geosphere*, *2*(5), 253–268. doi: 10.1130/GES00028.1

Reilinger, R., McClusky, S., Paradissis, D., Ergintav, S., & Vernant, P. (2010). Geodetic constraints on the tectonic evolution of the Aegean region and strain accumulation along the Hellenic subduction zone. *Tectonophysics*, *488*(1-4), 22–30. doi: 10.1016/j.tecto.2009.05.027

Ring, U., Glodny, J., Will, T., & Thomson, S. (2010). The Hellenic Subduction System: High-Pressure Metamorphism, Exhumation, Normal Faulting, and Large-Scale Extension. *Annual Review of Earth and Planetary Sciences*, *38*(1), 45–76. doi: 10.1146/annurev.earth.050708.170910

Rivalta, E., Corbi, F., Passarelli, L., Acocella, V., Davis, T., & Di Vito, M. A. (2019). Stress inversions to forecast magma pathways and eruptive vent location. *Science Advances*, *5*(7), eaau9784. doi: 10.1126/sciadv.aau9784

Roche, O., Druitt, T. H., & Merle, O. (2000). Experimental study of caldera formation. *Journal of Geophysical Research: Solid Earth*, *105*(B1), 395–416. doi: 10.1029/1999JB900298

Rudnick, R. L., & Fountain, D. M. (1995). Nature and composition of the continental crust: A lower crustal perspective. *Reviews of Geophysics*, *33*(3), 267. doi: 10.1029/95RG01302

Sakellariou, D., Sigurdsson, H., Alexandri, M., Carey, S., Rousakis, G., Nomikou, P., Georgiou, P., & Ballas, D. (2017). ACTIVE TECTONICS IN THE HELLENIC VOLCANIC ARC: THE KOLUMBO SUBMARINE VOLCANIC ZONE. *Bulletin of the Geological Society of Greece*, *43*(2), 1056. doi: 10.12681/bgsg.11270

Saltogianni, V., Stiros, S. C., Newman, A. V., Flanagan, K., Moschas, F., Stiros, S. C., Newman, A. V., Flanagan, K., & Moschas, F. (2014). Time-space modeling of the dynamics of Santorini volcano (Greece) during the 2011–2012 unrest. *Journal of Geophysical Research : Solid Earth*, *119*(11), 8517–8537. doi: https://doi.org/10.1002/2014JB011409

Savage, H. M., & Brodsky, E. E. (2011). Collateral damage: Evolution with displacement of fracture distribution and secondary fault strands in fault damage zones. *Journal of Geophysical Research*, *116*(B3), B03405. doi: 10.1029/2010JB007665

Scandone, R. (1990). Chaotic collapse of calderas. *Journal of Volcanology and Geothermal Research*, *42*(3), 285–302. doi: 10.1016/0377-0273(90)90005-Z

Scandone, R., & Acocella, V. (2007). Control of the aspect ratio of the chamber roof on caldera formation during silicic eruptions. *Geophysical Research Letters*, *34*(22), L22307. doi: 10.1029/2007GL032059

Schneider, D. A., Grasemann, B., Lion, A., Soukis, K., & Draganits, E. (2018). Geodynamic significance of the Santorini Detachment System (Cyclades, Greece). *Terra Nova*, *30*(6), 414–422. doi: 10.1111/ter.12357

Sigurdsson, H., Carey, S., Alexandri, G., Vougioukalakis, G. E., Croff-bell, K., Roman, C., Sakellariou, D., & Ana. (2006). Marine Investigations of Greece ' s Santorini Volcanic Field. *EOS, Transactions, American Geophysical Union*, *87*(34), 337–348. doi: 10.1029/2006EO340001

Smith, R. B., & Bruhn, R. L. (1984). Intraplate extensional tectonics of the Eastern basin-Range: Inferences on structural style from seismic reflection data, regional tectonics, and thermal-mechanical models of brittle-ductile deformation. *Journal of Geophysical Research: Solid Earth*, *89*(B7), 5733–5762. doi: 10.1029/JB089iB07p05733

Soukis, K. I., & Papanikolaou, D. J. (2004). CONTRASTING GEOMETRY BETWEEN ALPINE AND LATE- TO POSTALPINE TECTONIC STRUCTURES IN ANAFI ISLAND (CYCLADES). *Bulletin of the Geological Society of Greece*, *36*(4), 1688. doi: 10.12681/bgsg.16575

Sparks, R. S. J., & Wilson, C. J. N. (1990). The Minoan deposits: a review of their characteristics and interpretation. *Thera and the Aegean World III*, *2*, 89–99.

Stiros, S. C., Marangou, L., & Arnold, M. (1994). Quaternary uplift and tilting of Amorgos Island (southern Aegean) and the 1956 earthquake. *Earth and Planetary Science Letters*, *128*(3-4), 65–76. doi: 10.1016/0012-821X(94)90135-X

Stroujkova, A. (2018). Rock Damage and Seismic Radiation: A Case Study of the Chemical Explosions in New Hampshire. *Bulletin of the Seismological Society of America*, *108*(6), 3598–3611. doi: 10.1785/0120180117

Tassi, F., Vaselli, O., Papazachos, C. B., Giannini, L., Chiodini, G., Vougioukalakis, G. E., Karagianni, E., Vamvakaris, D., & Panagiotopoulos, D. (2013). Geochemical and isotopic changes in the fumarolic and submerged gas discharges during the 2011–2012 unrest at Santorini caldera (Greece). *Bulletin of Volcanology*, *75*(4), 711. doi: 10.1007/s00445-013-0711-8

Taylor, M. A. J., & Singh, S. C. (2002). Composition and microstructure of magma bodies from effective medium theory. *Geophysical Journal International*, *149*(1), 15–21. doi: 10.1046/j.1365-246X.2002.01577.x

Thomsen, L. (1986). Weak elastic anisotropy. *GEOPHYSICS*, *51*(10), 1954–1966. doi: 10.1190/1.1442051

Thomson, S. N., Ring, U., Brichau, S., Glodny, J., & Will, T. M. (2009). Timing and nature of formation of the Ios metamorphic core complex, southern Cyclades, Greece. *Geological Society, London, Special Publications*, *321*(1), 139–167. doi: 10.1144/SP321.7

Toomey, D. R., Solomon, S. C., & Purdy, G. M. (1994). Tomographic imaging of the shallow crustal structure of the East Pacific Rise at 9°30'N. *Journal of Geophysical Research: Solid Earth*, *99*(B12), 24135–24157. doi: 10.1029/94JB01942

Tsampouraki-Kraounaki, K., & Sakellariou, D. (2018). Seismic stratigraphy and geodynamic evolution of Christiana Basin, South Aegean Arc. *Marine Geology*, *399*(2017), 135–147. doi: 10.1016/j.margeo.2018.02.012

Valentine, G. A., Graettinger, A. H., & Sonder, I. (2014). Explosion depths for phreatomagmatic eruptions. *Geophysical Research Letters*, *41*(9), 3045–3051. doi: 10.1002/2014GL060096

Vanorio, T., Virieux, J., Capuano, P., & Russo, G. (2005). Three-dimensional seismic tomography from P wave and S wave microearthquake travel times and rock physics characterization of the Campi Flegrei Caldera. *Journal of Geophysical Research: Solid Earth*, *110*(3), 1–14. doi: 10.1029/2004JB003102

Virieux, J., & Operto, S. (2009). An overview of full-waveform inversion in exploration geophysics. *GEOPHYSICS*, *74*(6), WCC1–WCC26. doi: 10.1190/1.3238367

Walcott, C. R., & White, S. H. (1998). Constraints on the kinematics of post-orogenic extension imposed by stretching lineations in the Aegean region. *Tectonophysics*, *298*(1-3), 155–175. doi: 10.1016/S0040-1951(98)00182-6

Walker, G. P. L. (1984). Downsag calderas, ring faults, caldera sizes, and incremental caldera growth. *Journal of Geophysical Research*, *89*(B10), 8407. doi: 10.1029/JB089iB10p08407

Walsh, J., Watterson, J., & Yielding, G. (1991). The importance of small-scale faulting in regional extension. *Nature*, *351*(6325), 391–393. doi: 10.1038/351391a0

Warner, M., Ratcliffe, A., Nangoo, T., Morgan, J., Umpleby, A., Shah, N., Vinje, V., Štekl, I., Guasch, L., Win, C., Conroy, G., & Bertrand, A. (2013). Anisotropic 3D full-waveform inversion. *GEOPHYSICS*, *78*(2), R59–R80. doi: 10.1190/geo2012-0338.1

Wernicke, B., & Burchfiel, B. (1982). Modes of extensional tectonics. *Journal of Structural Geology*, *4*(2), 105–115. doi: 10.1016/0191-8141(82)90021-9

White, J., & Ross, P.-S. (2011). Maar-diatreme volcanoes: A review. *Journal of Volcanology and Geothermal Research*, *201*(1-4), 1–29. doi: 10.1016/j.jvolgeores.2011.01.010

Wilcock, W. S. D., Tolstoy, M., Waldhauser, F., Garcia, C., Tan, Y. J., Bohnenstiehl, D. R., Caplan-Auerbach, J., Dziak, R. P., Arnulf, A. F., & Mann, M. E. (2016). Seismic constraints on caldera dynamics from the 2015 Axial Seamount eruption. *Science*, *354*(6318), 1395–1399. doi: 10.1126/science.aah5563

Williams, H. (1941). Calderas and their origin. *Bull. Geol. Sci. Dep.*, *25*, 239–346.

Wohletz, K. H. (2003). Water/Magma Interaction: Physical considerations for the deep submarine environment. In J. D. White, J. L. Smellie, & D. A. Clague (Eds.), *Explosive subaqueous volcanism* (pp. 25–49). doi: 10.1029/140GM02

Xypolias, P., Spanos, D., Chatzaras, V., Kokkalas, S., & Koukouvelas, I. (2010). Vorticity of flow in ductile thrust zones: examples from the Attico-Cycladic Massif (Internal Hellenides, Greece). *Geological Society, London, Special Publications*, *335*(1), 687–714. doi: 10.1144/SP335.28

Yokoyama, I. (1981). A geophysical interpretation of the 1883 Krakatau eruption. *Journal of Volcanology and Geothermal Research*, *9*(4), 359–378. doi: 10.1016/0377-0273(81)90044-5

Zandomeneghi, D., Barclay, A., Almendros, J., Ibañez Godoy, J. M., Wilcock, W. S. D., Ben-Zvi, T., Godoy, J. M., Wilcock, W. S. D., & Ben-Zvi, T. (2009). Crustal structure of Deception Island volcano from P wave seismic tomography: Tectonic and volcanic implications. *Journal of Geophysical Research*, *114*(6), 1–16. doi: 10.1029/2008JB006119

Zong, J., Stewart, R. R., Dyaur, N., & Myers, M. T. (2017). Elastic properties of rock salt: Laboratory measurements and Gulf of Mexico well-log analysis. *GEOPHYSICS*, *82*(5), D303–D317. doi: 10.1190/geo2016-0527.1